

Earthquake Ground Motion Modelling from Crustal and Intermediate Depth Sources

Modellierung der Bodenbewegung von krustalen und mitteltiefen Erdbeben

Zur Erlangung des akademischen Grades eines
DOKTORS DER NATURWISSENSCHAFTEN

von der Fakultät für Physik der Universität (TH)

Karlsruhe

genehmigte

DISSERTATION

von

Dipl.-Geophys. Joachim Miksat

aus Riedlingen

Tag der mündlichen Prüfung:

15. Dezember 2006

Referent:

Prof. Dr. Friedemann Wenzel

Korreferent:

Prof. Dr. Karl Fuchs

Zusammenfassung

Computersimulationen sind ein wichtiger Bestandteil natur-, ingenieur- und sozialwissenschaftlicher Forschung. Da Prozesse wie die Kollision von Galaxien, die Klimaentwicklung und Erdbeben als Experiment nicht durchführbar sind, ist die Simulation mit Hilfe von Computern von besonderer Bedeutung. So helfen Simulationen vergangener Erdbeben die beobachtete Bodenbewegung zu verstehen und zu erklären. Zukünftige Erdbeben können mit Computern simuliert werden, um Aussagen über die Stärke der Bodenbewegung zu machen und besonders gefährdete Gebiete zu lokalisieren. In dieser Arbeit wird die Bodenbewegung des krustalen Kocaeli-Erdbebens von 1999 in der Türkei modelliert. Weiter werden die mitteltiefen Vrancea-Starkbeben in Rumänien simuliert. Die hier vorgestellten Beispiele zeigen das große Anwendungspotenzial von Computersimulationen vergangener und zukünftiger Erdbeben.

Kapitel 1: Modellierung der Wellenausbreitung in elastischen Medien

Die Ausbreitung von Wellen in elastischen Medien wird durch die linearisierte Impulsgleichung

$$\rho \frac{\partial^2 u_i}{\partial t^2} = f_i + \frac{\partial \tau_{ij}}{\partial x_j},$$

mit der Verschiebung u_i , dem Spannungstensor τ_{ij} und der Körperkraftdichte f_i beschrieben. Die verwendete lineare Spannungs-Dehnungsbeziehung für isotrope Medien lautet:

$$\tau_{ij} = (\lambda \delta_{ij} \delta_{kl} + \mu (\delta_{ik} \delta_{jl} + \delta_{il} \delta_{jk})) u_{k,l},$$

mit den elastischen Konstanten λ und μ . Um Wellenausbreitung für beliebige Verteilungen der elastischen Parameter zu simulieren, wird die Finite-Differenzen (FD) Methode auf die Bewegungsgleichung und die Spannungs-Dehnungsbeziehung angewendet. Hierbei werden die auftretenden räumlichen und zeitlichen Ableitungen durch FD-Quotienten ersetzt. Einschränkungen ergeben sich aus der auftretenden numerischen Dispersion, deren Einfluss mit steigenden Frequenzen und Laufwegen und mit kleiner werdenden minimalen S-Wellengeschwindigkeiten im Modell zunimmt. Um der numerischen Dispersion entgegen zu wirken, muss der Gitterpunktabstand reduziert werden. Dies bedeutet wiederum mehr Gitterpunkte und folglich einen erhöhten Speicherbedarf. Heutzutage können 2D FD-Simulationen der Wellenausbreitung

von Erdbeben für typische Modellgebiete von einigen 100 km Ausdehnung und minimalen S-Wellengeschwindigkeiten von etwa 1 km/s bis zu einigen Hz simuliert werden (Kebeasy and Husebye, 2003; Furumura and Kennett, 2005). 3D Modellierungen sind dagegen wesentlich speicherintensiver und sind selbst auf Großcomputern nur bis ungefähr 1.5 Hz durchführbar (Benites and Olsen, 2005; Olsen et al., 2006). Daher spielen 2D FD-Modellierungen eine wichtige Rolle für Modellierungen der Bodenbewegung in dem für Bauwerke interessanten Frequenzbereich bis 10 Hz. Quellen in 2D aber entsprechen senkrecht zum 2D Schnitt unendlich ausgedehnten Quellen in 3D. Deshalb müssen die in 2D simulierten Seismogramme korrigiert werden, um die entsprechenden Seismogramme für eine Ausbreitung in 3D zu erhalten. Die von Vidale and Helmberger (1987) angegebene Korrektur kann aber in Kombination mit dem verwendeten 2D FD-Programm (Karrenbach, 1995) nicht angewendet werden. Deshalb wird eine Korrekturmethode entwickelt, die es ermöglicht 2D FD-Simulationen des Programmes von Karrenbach (1995) wie auch anderer gängiger 2D FD-Programme zu korrigieren. Ausgeführte Testrechnungen unterstreichen die Anwendbarkeit des entwickelten Korrekturverfahrens.

Kapitel 2: Modellierung des Kocaeli-Bebens (Türkei)

Das Kocaeli-Erdbeben von 1999 forderte über 15000 Tote, etwa 400000 Obdachlose und verursachte Schäden von ungefähr 40 Mrd. US Dollar (EERI, 1999). Sechs seismische Stationen mit Abständen von höchstens 20 km zur Verwerfung zeichneten die Bodenbewegung auf. Makroseismische Intensitäten von X wurden im Epizentralgebiet entlang der südlichen Küste der Bucht von Izmit und im Adapazari Becken östlich des Epizentrums erreicht. Die aufgezeichneten Beschleunigungen scheinen aber im Vergleich zu den aufgetretenen Schäden und den zu erwartenden Beschleunigungen nach Boore et al. (1997), Campbell (1997) und Sadigh et al. (1997) zu gering zu sein. Die Bodenbewegung dieses Erdbebens wird mit einem 3D FD-Verfahren Olsen (1994) simuliert. Die für die etwa 120 km langen und 20 km tiefen Verwerfung invertierten Bruchprozesse von Bouchon et al. (2002) und Sekiguchi and Iwata (2002) werden in die Modellierung mit dem Verfahren von Miksat (2002) and Miksat et al. (2005) einbezogen. Bouchon et al. (2002) stützt sich auf die Daten von sechs Strong-Motion-Stationen innerhalb eines Bereiches von 20 km zur Verwerfung. Sekiguchi and Iwata (2002) verwenden Daten von Stationen mit Entfernungen von bis zu 50 km zur Verwerfung. Die Verteilung der Versätze und Anstiegszeiten zeigen deutliche Unterschiede zu Bouchon et al. (2002). Da für die Region des Kocaeli-Erdbebens kein publiziertes Untergrundmodell existiert, wird in Anlehnung an die Lage der Sedimente und die Geschwindigkeits- und Dichtewerte nach Ergin et al. (1998) and Karahan et al. (2001) ein vereinfachtes Modell entwickelt. Die Wellenausbreitung bis 1.5 Hz wird für insgesamt 75 s simuliert. Modellerte und beobachtete Seismogramme werden an den Stationen, die innerhalb des Modellgebietes liegen und die von Bouchon et al. (2002) und Sekiguchi and Iwata (2002) verwendet wurden, verglichen. In einem weiteren Schritt werden aus den synthetischen Seismogrammen basierend auf Sokolov (2002) makroseismische Intensitäten berechnet. Die Berechnung makroseismischer Intensitäten aus den simulierten Seismogrammen ermöglicht einen flächenhaften Vergleich zwischen Beobachtung und Modellierung.

Die modellierte Verteilung der maximalen horizontalen Geschwindigkeiten (PHV) zeigt ein sehr komplexes Bild. Unter der Verwendung des Bruchvorganges von Bouchon et al. (2002) werden nahe der großen Verschiebungen auf der Verwerfung große Amplituden erzeugt. Allgemein sind die großen PHV-Werte deutlich auf den Bereich der Sedimente begrenzt. Durch die bilaterale Bruchausbreitung führen Direktivitätseffekte zu großen PHV-Werten weit westlich und östlich der Verwerfung. Dieser Effekt wird in Richtung Osten durch die hohe Bruchgeschwindigkeit verstärkt. Weiter liegt die Ost-West orientierte Verwerfung in einem Sedimentband, das als Wellenleiter fungiert und durch welches die durch die Direktivität erzeugten Amplituden über große Entfernungen geführt werden. Bemerkenswert ist, dass keine der sechs Stationen in einem Bereich großer PHV-Werte liegt. Der Vergleich der Seismogramme an den Standorten der sechs Strong-Motion-Stationen, die von Bouchon et al. (2002) verwendet wurden, zeigt eine gute Übereinstimmung für die ersten 5 bis 10 s der Seismogramme. Die aus den modellierten Seismogrammen gewonnenen synthetischen makroseismischen Intensitäten beschreiben in einem Bereich von 10 - 20 km zur Verwerfung gut die beobachtete Verteilung. Die hohen Intensitäten von IX bis X entlang der südlichen Küste des Golfes von Izmit, die etwas geringeren Intensitäten von VIII zwischen Epizentrum und Adapazari-Becken, sowie Intensitäten von X im Adapazari-Becken werden durch die Modellierung gut wiedergegeben. Auch hier liegt keine Station im Bereich der Intensität X. Dies deutet darauf hin, dass die im Vergleich zu den Schäden zu geringen aufgezeichneten Beschleunigungswerte dadurch erklärt werden können, dass keine Station in einer Region maximaler Bodenbewegung stand.

Unter Verwendung des von Sekiguchi and Iwata (2002) invertierten Bruchprozesses zeigt sich wiederum ein komplexes Bild der Verteilung der PHV. Hier führen die sehr kurzen Anstiegszeiten im Bereich der großen Versätze auf der Bruchfläche zu sehr großen PHV-Werten. Das Bild unterscheidet sich aufgrund der Unterschiede in den Bruchdetails deutlich von der Modellierung mit dem Bruchprozess von Bouchon et al. (2002). Auch für die Modellierung mit dem Bruchvorgang nach Sekiguchi and Iwata (2002) werden die Seismogramme an den verwendeten Stationen im Modellgebiet in den ersten 5-10 s reproduziert. Die syntehtischen makroseismischen Intensitäten ergeben aber ein deutlich anderes Bild. Hier wird nur im Bereich des Epizentrums und des Adapazaribeckens die beobachtete Intensitätsverteilung richtig wiedergegeben. Auch hier liegt keine der Stationen in einer Region großer PHV und maximaler Intensität. Die Modellierung mit beiden Bruchprozessen (Bouchon et al., 2002; Sekiguchi and Iwata, 2002) reproduziert also gut die Seismogramme an den zur Inversion verwendeten Stationen. Die beobachteten makroseismischen Intensitäten werden aber nur unter Verwendung des Bruchprozesses nach Bouchon et al. (2002) wiedergegeben.

Die Modellierung des Kocaeli-Bebens zeigt, wie zuletzt auch die Beobachtungen des Parkfield-Bebens (Shakal et al., 2006), dass die Stärke der Bodenbewegung nahe der Verwerfungslinie starke räumliche Variationen aufweist und dort schwer durch Abminderungsfunktionen (z. B. Boore et al., 1997; Campbell, 1997; Sadigh et al., 1997) beschrieben werden kann. Vielmehr kann die Entwicklung von Abminderungsfunktionen aus den Daten des Kocaeli-Bebens zu einer gefährlichen Unterschätzung der möglich auftretenden Bodenbewegungen nahe der Bruchfläche führen.

Kapitel 3: Finite-Differenzen Modellierung der Vrancea-Erdbeben

Die Vrancea-Region in Rumänien ist Gegenstand des von der Deutschen Forschungsgemeinschaft geförderten Sonderforschungsbereiches 461 'Starkbeben: Von geowissenschaftlichen Grundlagen zu Ingenieurmaßnahmen' an der Universität Karlsruhe (TH). Pro Jahrhundert sind in dieser Region drei Erdbeben mit Magnituden größer als 7.2 zu erwarten, was eine große Gefährdung für Rumänien und die benachbarten Länder darstellt. So forderte das Erdbeben vom 4. März 1977 ($M_w=7.4$) in Bukarest 1570 Tote und 11300 Verletzte (Wenzel and Lungu, 2000; Cioflan et al., 2004). Alle mitteltiefen Vrancea-Beben treten in einem sehr kleinen Quellvolumen unterhalb des südöstlichen Karpatenbogens auf. Diese Seismizität wird mit einem subduzierten Lithosphärenstück in Verbindung gebracht, das sich im letzten Stadium der Subduktion entlang der osteuropäischen Plattform befindet (Sperner et al., 2001). Die Isoseisten aller Vrancea-Starkbeben zeigen eine Südwest-Nordost orientierte ovale Form. Die Entstehung dieser Form, die auch in der Verteilung der maximalen horizontalen Beschleunigungen (PHA) zu beobachten ist (Popa et al., 2005; Sokolov and Bonjer, 2006), wird kontrovers diskutiert. Während Mandrescu and Radulian (1999) den Einfluss der Quelle und die lokalen Standorteffekte verantwortlich machen, werden diese Effekte von Popa et al. (2005) ausgeschlossen und die beobachtete Verteilung auf die Variation der Dämpfung im oberen Mantel zurückgeführt. Um das Zustandekommen dieser ovalen Verteilung der Bodenbewegung zu ergründen, wird ein 2.5D und ein 3D FD-Verfahren zur Simulation der Wellenausbreitung angewendet. Da alle Vrancea-Starkbeben ähnliches Streichen, Fallen und einen ähnlichen Versatzwinkel aufweisen, wird repräsentativ das $M_w = 7.1$ Beben von 1986 modelliert. Die für FD-Rechnungen wichtige Struktur des Untergrundes von Südost-Rumänien ist sehr gut bekannt (Martin et al., 2005, 2006). Kennzeichnend sind die tiefen „forearc“ Sedimentbecken südlich und östlich der Karpaten. Um realistische Wellenformen zu simulieren, werden dem Untergrundmodell stochastische Geschwindigkeitsperturbationen nach Hock et al. (2004) überlagert. Die 2.5D Methode setzt sich aus der Simulation der Wellenausbreitung für mehrere 2D Schnitte, die um die Hypozentrums-Epizentrumsachse rotiert sind, zusammen. Dadurch kann die Bodenbewegung flächenhaft simuliert werden. Die einzelnen 2D Schnitte durch das Untergrundmodell sind 350 km lang und 131 km tief. Der Gitterpunktstand beträgt 140 m. Die Modellierung erfolgt für 64 s mit einem Zeitschritt von 8 ms. Aufgrund der numerischen Dispersion ergibt sich für eine minimale S-Wellengeschwindigkeit im Modell von ungefähr 1.7 km/s eine maximal zuverlässige Frequenz von 4.5 Hz. Die Wellenausbreitung wird für die speicherintensiveren 3D FD-Modellierungen für ein kleineres Modellgebiet mit einer Ausdehnung von 85 auf 85 km bis in eine Tiefe von 150 km ausgeführt. Mit einem Gitterpunktstand von 500 m ergibt sich aufgrund der numerischen Dispersion die maximal akzeptierte Frequenz zu 0.6 Hz. Die Erdbebenquelle wird als Punktquelle mit einer Herdzeitfunktion nach Beresnev and Atkinson (1997) beschrieben, wobei die Bruchdauer nach Brune (1970, 1971) mit einem statischen Spannungsabfall von 150 MPa skaliert wird. Die modellierte Verteilung der maximalen Beschleunigungen (PGA) zeigt deutlich die für die Vrancea-Erdbeben typische in Südwest-Nordost-Richtung orientierte, ovale Form, wobei die maximale Bodenbewegung etwa 70 km östlich des Epizentrums auftritt. Um die Entstehung dieser charakteristischen Form zu untersuchen, wird die Modellierung für verschiedene vereinfachte Untergrundstrukturen durchgeführt. Die Modellierung in einem horizontal geschichteten Modell macht den Einfluss

der Quellabstrahlung sichtbar, da die an den horizontalen Schichtgrenzen auftretende Refraktion punktsymmetrisch zum Epizentrum ist. Ausgehend von diesem horizontal geschichteten Modell wird der Untergrund verändert, indem die horizontalen Schichtgrenzen schrittweise durch die von Martin et al. (2005, 2006) gegebene Struktur ersetzt werden. Dies sind die Strukturen des Grundgebirges, der Conrad-Diskontinuität, der Moho-Diskontinuität und des Mantels. Die resultierende Verteilung der PGA-Werte im horizontal geschichteten Modell zeigt deutlich, dass allein die Quellabstrahlung ausreicht um eine Südwest-Nordost orientierte, ovale Verteilung der PGA-Werte zu erzeugen. Aufgrund der Quellabstrahlung treten Variationen der PGA von etwa 400 % auf. Nach der Einführung der Topographie des Grundgebirges ergeben sich für die Bereiche der tiefen „forearc“ Sedimentbecken eine Verstärkung der PGA um bis zu 150 %. Diese sehr großen Verstärkungen werden durch die Fokussierung der von unten einfallenden S-Welle in die konvex geformten Sedimentbecken erzeugt. An anderen Stellen treten Verminderungen der Amplituden durch Defokussierung aufgrund konkav geformter Basementstrukturen auf. Nach der Einführung der Conrad- und Moho-Diskontinuitäten ändert sich das Bild nur unwesentlich, da diese Strukturen im Modellgebiet nur geringe laterale Tiefenvariationen aufweisen und folglich die auftretenden Fokussierungs- und Defokussierungseffekte sehr klein sind.

Die 2.5D und 3D FD-Modellierungen zeigen deutlich, dass die ovalen Muster der PGA-Werte hauptsächlich durch die Abstrahlcharakteristik der Quelle verursacht werden. Die Sedimente östlich des Karpatenbogens verstärken lediglich diesen Effekt. Dass die Abstrahlung für Frequenzen bis zu 4.5 Hz zu beobachten ist, ist allerdings nicht selbstverständlich, da die Komplexität der Quelle und die Komplexität entlang des Laufweges den Einfluss der Quellabstrahlung verwischen. In verschiedenen Arbeiten wird die Abstrahlung bis zu Frequenzen von 3-6 Hz (Vidale, 1989), 0.5 Hz (Castro et al., 2006), 1 Hz (Takenaka et al., 2003) und 5 Hz (Siro and Chiaruttini, 1989; Sirovich, 1994) beobachtet. Um die Auswirkungen von Streukörpern auf die Wellenausbreitung abzuschätzen, wird für ein mit einer exponentiellen Autokorrelationsfunktion erstelltes stochastisches Modell mit konstantem Mittelwert der P-Wellengeschwindigkeit von 6 km/s, einer Korrelationslänge von 2 km und einer RMS Geschwindigkeitsabweichung von 5% die Wellenausbreitung simuliert. Im Vergleich zu einer Modellierung ohne stochastische Geschwindigkeitsfluktuationen führt die Streuung zu starken Amplitudenvariationen der Wellenfront. Dennoch ist die Abstrahlung bei Betrachtung der gesamten Wellenfront auch nach einem Laufweg von mehr als 100 km deutlich zu erkennen. Allerdings wird klar, dass bei Betrachten der Bodenbewegung an einigen wenigen Standorten, wie es bei Beobachtung realer Beben gegeben ist, die Abstrahlung aufgrund der starken Amplitudenvariationen entlang der Wellenfront nicht klar erkennbar sein kann. Für die Vrancea-Erdbeben kann der klare Einfluss der Abstrahlcharakteristik auch auf die hohen Spannungsabfälle von mehr als 100 MPa zurückgeführt werden, da hohe Spannungsabfälle kleine Bruchflächen im Vergleich zu krustalen Beben bedeuten. Folglich kann die Quelle wesentlich impulsivere und kohärentere Signale erzeugen als im Falle von niederen Spannungszuständen und Spannungsabfällen, bei welchen Rotationen des Versatzwinkels auftreten können (Spudich et al., 1998). Ein über einen weiten Frequenzbereich kohärentes und impulsives Quellsignal ermöglicht es, die Abstrahlcharakteristik über größere Distanzen und für höhere Frequenzen zu transportieren.

Kapitel 4: Verfahren zur Modellierung der Bodenbewegung für die Vrancea-Starkbeben

Das zur FD-Modellierung verwendete Untergrundmodell von Südost-Rumänien (Martin et al., 2005, 2006) enthält die sehr gut bekannten großräumigen Krustenstrukturen des Grundgebirges und der Conrad- und Moho-Diskontinuitäten. Der Einfluss der Standorteffekte, die durch die oberflächennahen Schichten mit meist sehr langsamen seismischen Geschwindigkeiten verursacht werden, ist somit in der FD-Simulation nicht enthalten. Diese genauere Struktur der oberen Schichten ist auch flächenhaft für Südost-Rumänien nicht bekannt. Aus diesem Grunde ist es nicht möglich, realistische Amplituden der Bodenbewegung mit FD-Verfahren zu simulieren. Selbst bei genauer Kenntnis der oberflächennahen Strukturen reicht eine FD-Simulation nicht aus, da für Modelle mit sehr niederen Geschwindigkeiten sehr kleine Gitterpunktabstände benötigt werden, um die Wellenausbreitung für einen bestimmten Frequenzbereich zu simulieren. Dies bedeutet aber einen extrem großen Speicherbedarf. Deshalb wird eine Methode verwendet, die FD-Simulation und den Einfluss der Standorteffekte verknüpft. In einem ersten Schritt wird die Wellenausbreitung vom Hypozentrum zur Oberfläche innerhalb des bekannten Mantel- und Krustenmodells (Martin et al., 2005, 2006) mit 2.5D und 3D FD-Verfahren simuliert. Dadurch fließt der Einfluss der Quelle und der Untergrundstruktur in die Modellierung ein. In einem zweiten Schritt werden die simulierten Seismogramme mit den Verstärkungsfaktoren der Standorteffekte nach Sokolov und Bonjer (2006) multipliziert. Sokolov und Bonjer (2006) geben für Südost-Rumänien innerhalb sechs charakteristischer Regionen frequenzabhängige Verstärkungsfaktoren an. Mit diesem kombinierten Verfahren wird die Bodenbewegung für das Starkbeben vom 30. August 1986 ($M_W = 7.1$) und das Erdbeben vom 27. Oktober 2004 ($M_W = 5.9$) modelliert. Um die Qualität der Modellierung zu überprüfen, werden die modellierten Fourier-Amplitudenspektren (FAS) an Stationen im Modellgebiet verglichen. Ein Vergleich der Seismogramme gestaltet sich schwierig, da die stochastischen Geschwindigkeitsperturbationen zwar realistische Wellenformen erzeugen, deren Form aber stark von der stochastischen und somit nicht unbedingt realen Struktur nahe der betrachteten Station abhängt. Der Vergleich der FAS ergibt an den meisten Stationen eine gute Übereinstimmung. Quantitativ werden die Abweichungen zwischen modellierten und beobachteten FAS innerhalb von fünf Frequenzbereichen zwischen 0.1 und 4.5 Hz verglichen. Die Abweichungen sind für beide Erdbeben ähnlich. Zusätzlich werden für das Erdbeben von 1986 aus der Modellierung makroseismische Intensitäten in Anlehnung an Sokolov (2002) berechnet. Die modellierte Intensitätsverteilung zeigt dieselben Südwest-Nordost orientierten Muster wie auch die beobachteten Intensitäten. Die maximal beobachteten Intensitäten von VII östlich des Epizentrums werden durch die Modellierung wiedergegeben. Im Bereich südlich und südöstlich des Epizentrums werden die beobachteten Intensitäten allerdings überschätzt. Dies deutet darauf hin, dass die entwickelte Methode zur Intensitätsbestimmung zu hohen Intensitäten neigt. Hier ist eine weitere Anpassung der ursprünglichen Methode von Sokolov (2002), die den Frequenzbereich bis 13 Hz auswertet, an den Niederfrequenzbereich sinnvoll.

Der Vergleich modellierter und beobachteter FAS zeigt, dass die entwickelte Kombination aus

FD-Modellierung und Berücksichtigung der Standorteffekte geeignet ist, um die Bodenbewegung für Vrancea-Erdbeben zu simulieren. Damit kann dieses Verfahren in die geplante Bestimmung von Abminderungsfunktionen für Südost-Rumänien im Rahmen des SFB 461 eingebunden werden (Gottschämmer et al., 2006).

Contents

Zusammenfassung	iii
Abstract	1
1 Wave Propagation Modelling in Elastic Media	3
1.1 Introduction	3
1.2 Equation of Motion in Elastic Continua	3
1.3 Finite Differences (FD)	5
1.4 The Seismic Moment Tensor	11
1.5 Source Implementation	15
1.6 Simulating Double Couple Sources with the 2D FD code of Karrenbach (1995)	19
1.7 2D to 3D Correction	20
2 Modelling of the 1999 Kocaeli Earthquake	29
2.1 Introduction	29
2.2 Observed Ground Motion	31
2.3 Modelling	32
2.4 Linking Ground Motion and Intensity	35
2.5 Applying the Rupture Process of Bouchon et al. (2002)	37
2.6 Applying the Rupture Process of Sekiguchi and Iwata (2002)	39
2.7 Comparison	40
2.8 Conclusions	45

3	Wave Propagation Modelling of the Vrancea Strong Earthquakes	47
3.1	Introduction	47
3.2	Historical Seismicity and Tectonics	48
3.3	Subsurface Structure	49
3.4	2.5D FD Modelling	57
3.5	3D FD Modelling	72
3.6	Discussion	74
3.7	Conclusions	85
4	Hybrid Modelling of Strong Ground Motions of the Vrancea Earthquakes	87
4.1	Introduction	87
4.2	Hybrid Modelling Method	88
4.3	Modelling of the 1986 Vrancea Strong Earthquake ($M_w = 7.1$)	91
4.4	Modelling of the 2004 Earthquake ($M_w=5.9$)	106
4.5	Summary & Conclusions	113
	Summary & Conclusions	116
	List of Figures	121
	List of Tables	124
	References	127
	Danksagungen/Acknowledgments	139
	Lebenslauf	142
	Hilfsmittel	143

Abstract

Computer simulations of natural processes are very important elements in science, engineering technology and social sciences. Simulations help to understand the real world and supplement or even substitute expensive and dangerous experiments like car crashes or nuclear explosions. Other experiments like galaxy collisions, climate change or earthquakes are simply impossible to perform. In these cases computer simulations are the only way to conduct experiments. The computer modelling presented in this work displays the application potential of ground motion simulations on the understanding of past and the modelling of future earthquakes. Wave propagation modelling for past earthquakes helps to understand the observed peculiarities and the gained knowledge helps to be prepared for future earthquakes. Furthermore, potential future earthquakes can be simulated and consequent precautions mitigate imminent damage. Wave propagation from the crustal 1999 Kocaeli (Turkey) earthquake ($M_W = 7.4$) and the intermediate-depth Vrancea (Romania) earthquakes is modelled by applying 2D and 3D Finite-Difference (FD) methods. Additionally, a method is developed to simulate strong ground motions for the Vrancea earthquakes by combining FD simulation and the knowledge of the amplification characteristics of the uppermost soft soil layers.

The theoretical principles applied in this work are described in chapter 1. 2D and 3D wave propagation is simulated numerically by applying the Finite Difference (FD) method on the equation of motion and the corresponding stress-strain relationship. A first benchmark publication by Alterman and Karal (1968) introduced the method into seismology. During the following decades the method was further improved. Important steps were the invention of the staggered grid scheme (Madariaga, 1976). Increasing computer capabilities allowed the application of schemes with a higher order of accuracy (Levander, 1988) and wave propagation modelling in 3D (Graves, 1996). Today, the available computer power allows the simulation of wave propagation from earthquakes in 2D for all frequencies of interest (Kebeasy and Husebye, 2003; Furumura and Kennett, 2005). Only 3D simulations are bounded to the low frequency range (Benites and Olsen, 2005; Olsen et al., 2006). Therefore, 2D FD modelling is usually performed to simulate wave propagation for frequencies larger than a few Hz. However, 2D FD modelling of wave propagation initiated by point sources corresponds to a line source in 3D. To get 3D seismograms the simulated 2D seismograms have to be corrected. Hence, many studies avoid to give absolute amplitudes (Kebeasy and Husebye, 2003; Furumura and Kennett, 2005). In this work, a correction method is developed and successfully tested, which is more easily applicable than the correction method given by Vidale and Helmberger (1987).

Ground motion modelling for the devastating 1999 Kocaeli (Turkey) earthquake is presented in

chapter 2. The Kocaeli ($M_W = 7.4$) earthquake killed about 15.000 people and destroyed large regions of NW Turkey. Six strong motion stations in the near fault range up to 20 km recorded the earthquake. Compared to the observed damage the recorded accelerograms seem to be very low. To analyse the earthquake two inverted rupture histories (Bouchon et al., 2002; Sekiguchi and Iwata, 2002) are implemented into the 3D FD modelling in order to introduce the real rupture on the extended fault plane. The simulated PHV patterns show very complex distribution of PHV, which is strongly correlated with the rupture process on the fault. Remarkably, no strong motion station is located within an area of large PHV. The simulated ground motions are also translated into macroseismic intensities. This allows not only point wise comparison between observation and modelling, but also an area-wide comparison of observed and modelled macroseismic intensities. Again, no strong motion station is located within an area of maximum intensity. This suggests that in the case of the 1999 Kocaeli earthquake the few strong motion stations were located by chance outside the areas of maximum ground motions. Consequently, taking the recorded acceleration as representative earthquakes of the strength of the Kocaeli event may yield to an underestimation of the real maximum accelerations of future earthquakes.

The Vrancea earthquakes in Romania impose significantly hazard on Romania and its neighboring countries. All Vrancea strong earthquakes produce typical SW-NE elongated patterns of observed macroseismic intensities. FD modelling of the 1986 $M_W = 7.1$ earthquake is performed in chapter 3 in order to explore the influence of the earthquake source and the subsurface structure on the resulting ground motion distribution. The intermediate-depth Vrancea earthquakes are implemented as point sources. The waveform of the source time function is adopted from Beresnev and Atkinson (1997) and the rupture time is scaled with the static stress drop. The subsurface structure is based on many different geophysical methods and was compiled by Martin et al. (2005, 2006). The modelling displays the interaction between source radiation and subsurface structure. Maximum S-wave amplitudes are radiated towards the deep sediments SE to E of the epicentre, where strong amplification occurs due to the convex shaped basin structures. In order to produce realistic seismograms, it is necessary to add stochastic velocity perturbations to the subsurface model. The wave propagation modelling shows that the source radiation pattern for frequencies up to 4.5 Hz is not completely blurred out after travelling from the hypocentre to the surface. This can be explained by the probable large stress drops and consequently small fault sizes of the Vrancea earthquakes, which are capable to produce strong coherent signals that preserve the source radiation pattern over long distances and for larger frequencies.

Chapter 4 presents a hybrid modelling of the ground motions for the Vrancea earthquakes. FD modelling of wave propagation through the mantle and the crust is combined with the knowledge of the site amplification characteristics of the uppermost soft soil layers after Sokolov and Bonjer (2006). To validate this method, the 1986 and 2004 Vrancea earthquakes are simulated and compared with observed data. Comparison between recorded and simulated Fourier amplitude spectra shows a very good agreement. In the case of the 1986 earthquake simulated ground motion are translated into macroseismic intensities. The modelling reproduces the observed intensity pattern. Therefore, the proposed hybrid method to simulate Vrancea earthquakes is an appropriate tool to simulate strong ground motions for potential Vrancea earthquakes. This allows the integration of the presented modelling method into the development of attenuation relationships for Romania (Gottschämmer et al., 2006).

Chapter 1

Wave Propagation Modelling in Elastic Media

1.1 Introduction

This chapter gives a brief overview on the theory of wave propagation in elastic media, which is described by the equation of motion in elastic continua. Applying the Finite Differences (FD) method to the equation of motion, seismic wave propagation can be simulated on computers. Also, the moment tensor formulation of an earthquake source is shown in this chapter. The implementation of an earthquake into the numerical scheme is explained and the scaling relations that connect the properties of the modelled and real earthquake are derived. Point source seismograms generated by 2D FD modelling have to be corrected in order to get 3D point source seismograms. The 2D to 3D mapping is developed and tested numerically. For a detailed review of the equation of motion and the concept of the seismic moment tensor see Aki and Richards (1980, chapter 3.3), Jost and Herrmann (1989), Lay and Wallace (1995, chapter 8.5), Stein and Wysession (2003, chapter 4.4), and (Udias, 1999, chapter 17). The application of FD in seismology is described in several papers which are cited in the next sections and in a more general, theoretical and technical manner in Cohen (2002), Durrant (1999), Marsal (1989) and Thomas (1995). For an introduction to FD see Aki and Richards (1980, p. 773), and Moczo et al. (2004).

1.2 Equation of Motion in Elastic Continua

To study wave propagation in seismology the concept of continuum mechanics is applied. Continuous means that the granular, molecular and atomic structure of the Earth is ignored. Within a continuous body density, force and displacement are continuous functions of spatial coordinates. Applying the conservation of momentum on a small volume dV within a continuous body yields to the equivalence between the rate of change of the momentum and the sum of all forces that

act on the volume dV (see Aki and Richards, 1980, chapter 2.1):

$$\frac{d}{dt} \int_V \rho \dot{u}_i dV = \int_V f_i dV + \int_V \frac{\partial \tau_{ij}}{\partial x_j} dV, \quad (1.1)$$

with the velocity \dot{u}_i , the body force density f_i and the stresses τ_{ij} acting on the surface of dV . Each index (i, j, k or l) indicate the x, y, z directions of a cartesian coordinate system. Eq. (1.1) can be written in differential form as:

$$\rho \frac{\partial^2 u_i}{\partial t^2} = f_i + \frac{\partial \tau_{ij}}{\partial x_j}, \quad (1.2)$$

which is called the linearised equation of motion. The total derivative with respect to time in eq. (1.1) is substituted by a partial derivative in eq. (1.2), which is valid if the amplitudes of the particle displacements are much smaller than the wavelengths of spatial fluctuations in the displacements and stresses. In this case, the Lagrangian and Eulerian formulations are equivalent (see Udias (1999) p.21 and Aki and Richards (1980) p. 18). For small deformations u_i the strain tensor e_{ij} is described by:

$$e_{ij} = \frac{1}{2} \left(\frac{\partial u_i}{\partial x_j} + \frac{\partial u_j}{\partial x_i} \right) = \frac{1}{2} (u_{i,j} + u_{j,i}). \quad (1.3)$$

For linear elasticity the relation between stress τ_{ij} and strains e_{ij} is given by Hooke's law:

$$\tau_{ij} = c_{ijkl} e_{kl}, \quad (1.4)$$

with the stiffness tensor c_{ijkl} . Substituting eq. (1.3) into eq. (1.4) yields to:

$$\tau_{ij} = c_{ijkl} u_{k,l}. \quad (1.5)$$

For general anisotropy, the stiffness tensor c_{ijkl} for a material has 21 independent elastic moduli (Aki and Richards, 1980, chapter 2.2). The elastic moduli are called elastic constants because they are independent of the strain e_{kl} but they vary with position in the Earth. For an isotropic medium there are only two independent elastic moduli, the so called Lamé constants λ and μ . The tensor of the elasticity coefficients for an isotropic media is:

$$c_{ijkl} = \lambda \delta_{ij} \delta_{kl} + \mu (\delta_{ik} \delta_{jl} + \delta_{il} \delta_{jk}), \quad (1.6)$$

with the Kronecker function δ_{ij} . The particle displacements u_i in eq. (1.2) travel as P- and S-waves through a body (Aki and Richards, 1980, p. 68). Within an isotropic medium P-waves show particle motion parallel to the direction of wave propagation and S-wave particle motion is perpendicular to the direction of wave propagation. Within a homogeneous isotropic body P-wave velocity α and S-wave velocity β depend on the Lamé constants λ and μ , and density ρ :

$$\alpha = \sqrt{\frac{\lambda + 2\mu}{\rho}}, \quad (1.7)$$

$$\beta = \sqrt{\frac{\mu}{\rho}}. \quad (1.8)$$

Using the equation of motion (1.2) and the relations between stresses and strains (eq. 1.4) wave propagation can be calculated. For arbitrary complicated media numerical solutions of these equations are the only way to simulate wave propagation. The next two sections describe the application of the concept of FD on eqs. (1.2) and (1.5).

1.3 Finite Differences (FD)

With growing computer capabilities the task of solving the equation of motion numerically was undertaken. The FD method is a popular method to solve differential equations numerically. The advantage of the explicit FD method, which is used in this work, over other numerical methods is that the propagation of the physical values from one time step to the next and from one grid point to the neighbouring points is calculated directly. Furthermore, complicated and therefore time consuming mathematical procedures like matrices inversions are not necessary. However, the disadvantage is the limited stability and the numerical dispersion of the schemes. The first important benchmark publications on the use of FD to calculate seismic wave propagation were Alterman and Karal (1968), Alford et al. (1974) and Kelly et al. (1976). Virieux (1984, 1986) used a second order accurate staggered grid scheme in 2 dimensions (2D), which was developed by Madariaga (1976). Levander (1988) improved the method from second order to fourth order. During the 90s the computer capabilities allowed the development and application of 3D FD schemes (Graves, 1996; Olsen, 1994). During the 1990's FD techniques developed to a standard tool to simulate earthquake wave propagation (Olsen et al., 1995; Olsen and Archuleta, 1996; Olsen et al., 1997; Graves, 1998; Sato et al., 1999). FD schemes are under steady development with respect to order of accuracy and technical optimisation, such as optimally accurate FD operators (Takeuchi and Geller, 2003), the rotated staggered grid (Saenger and Bohlen, 2004) and perfectly matched layers to improve the boundary conditions (Marcinkovich and Olsen, 2003). However, almost all of these "newer" schemes are in a state of development, are not yet developed to simulate earthquake wave propagation or are not freely available. Therefore, these schemes are not applicable for earthquake modelling and ground motion simulation.

1.3.1 Finite Difference Schemes

To simulate wave propagation, the concept of FD can be applied on eqs. (1.2) and (1.5). However, in this work the source is implemented by adding the stresses m_{ij} of the inelastic processes at the source rather than the body forces f_i . Therefore, the complete equations for the 2D and 3D cases are given in this section. In 2D, there are two systems of equations describing wave propagation because the P-SV-wave propagation with particle motion within the 2D plane is decoupled from SH-wave propagation, which shows particle motion perpendicular to the 2D plane (Lay and Wallace, 1995, p. 63-64). In this study a 2D FD code (Karrenbach, 1995) is used, which solves the system of equations given by eqs. (1.2) and (1.5). The system for P-SV-wave

propagation is:

$$\begin{aligned}\rho \frac{\partial^2 u_x}{\partial t^2} &= \left(\frac{\partial \sigma_{xx}}{\partial x} + \frac{\partial \sigma_{xz}}{\partial z} \right), \\ \rho \frac{\partial^2 u_z}{\partial t^2} &= \left(\frac{\partial \sigma_{xz}}{\partial x} + \frac{\partial \sigma_{zz}}{\partial z} \right),\end{aligned}\quad (1.9)$$

The FD code uses total stresses σ_{ij} to implement the source into the grid rather than the body forces f_i . The total stresses σ_{ij} comprises not only the pure elastic stresses τ_{ij} , which are used in eq. (1.2) and (1.5), but also the stresses due to the inelastic processes at the source m_{ij} . The relation between the strength of an earthquake and stresses needed for the FD modelling is shown in section 1.5. Stresses σ_{ij} are given by:

$$\begin{aligned}\sigma_{xx} &= (\lambda + 2\mu) \frac{\partial u_x}{\partial x} + \lambda \frac{\partial u_z}{\partial z} - m_{xx}, \\ \sigma_{zz} &= (\lambda + 2\mu) \frac{\partial u_z}{\partial z} + \lambda \frac{\partial u_x}{\partial x} - m_{zz}, \\ \sigma_{xz} &= \mu \left(\frac{\partial u_x}{\partial z} + \frac{\partial u_z}{\partial x} \right) - m_{xz}.\end{aligned}\quad (1.10)$$

The corresponding system for SH-wave propagation is:

$$\rho \frac{\partial^2 u_y}{\partial t^2} = \frac{\partial \sigma_{xy}}{\partial x} + \frac{\partial \sigma_{zy}}{\partial z}, \quad (1.11)$$

and:

$$\begin{aligned}\sigma_{xy} &= \mu \frac{\partial u_y}{\partial x} - m_{xy}, \\ \sigma_{zy} &= \mu \frac{\partial u_y}{\partial z} - m_{zy}.\end{aligned}\quad (1.12)$$

Eq. (1.10) and (1.12) build the so called displacement-stress formulation, which is a second order hyperbolic system. Other codes (Levander, 1988; Virieux, 1984, 1986) translate eq. (1.2) and (1.5) into a first order hyperbolic system, which is more suitable for a numerical procedure than the original second order hyperbolic differential equations. The 3D FD code used in this work was developed by Olsen (1994) and is based on the 2D scheme given by (Levander, 1988). This code uses the velocity-stress formulation for 3D (see Graves, 1996):

$$\begin{aligned}\rho \frac{\partial v_x}{\partial t} &= \frac{\partial \sigma_{xx}}{\partial x} + \frac{\partial \sigma_{xy}}{\partial y} + \frac{\partial \sigma_{xz}}{\partial z}, \\ \rho \frac{\partial v_y}{\partial t} &= \frac{\partial \sigma_{xy}}{\partial x} + \frac{\partial \sigma_{yy}}{\partial y} + \frac{\partial \sigma_{yz}}{\partial z}, \\ \rho \frac{\partial v_z}{\partial t} &= \frac{\partial \sigma_{xz}}{\partial x} + \frac{\partial \sigma_{yz}}{\partial y} + \frac{\partial \sigma_{zz}}{\partial z}.\end{aligned}\quad (1.13)$$

As above the stresses σ_{ij} refer to the total stresses, which include the pure elastic stresses τ_{ij} and the stresses at the source m_{ij} (see section 1.5):

$$\begin{aligned}
 \frac{\partial \sigma_{xx}}{\partial t} &= (\lambda + 2\mu) \frac{\partial v_x}{\partial x} + \lambda \left(\frac{\partial v_y}{\partial y} + \frac{\partial v_z}{\partial z} \right) - \frac{\partial m_{xx}}{\partial t}, \\
 \frac{\partial \sigma_{yy}}{\partial t} &= (\lambda + 2\mu) \frac{\partial v_y}{\partial y} + \lambda \left(\frac{\partial v_x}{\partial x} + \frac{\partial v_z}{\partial z} \right) - \frac{\partial m_{yy}}{\partial t}, \\
 \frac{\partial \sigma_{zz}}{\partial t} &= (\lambda + 2\mu) \frac{\partial v_z}{\partial z} + \lambda \left(\frac{\partial v_x}{\partial x} + \frac{\partial v_y}{\partial y} \right) - \frac{\partial m_{zz}}{\partial t}, \\
 \frac{\partial \sigma_{xy}}{\partial t} &= \mu \left(\frac{\partial v_x}{\partial y} + \frac{\partial v_y}{\partial x} \right) - \frac{\partial m_{xy}}{\partial t}, \\
 \frac{\partial \sigma_{xz}}{\partial t} &= \mu \left(\frac{\partial v_x}{\partial z} + \frac{\partial v_z}{\partial x} \right) - \frac{\partial m_{xz}}{\partial t}, \\
 \frac{\partial \sigma_{yz}}{\partial t} &= \mu \left(\frac{\partial v_y}{\partial z} + \frac{\partial v_z}{\partial y} \right) - \frac{\partial m_{yz}}{\partial t}.
 \end{aligned} \tag{1.14}$$

Eqs. (1.9) to (1.14) are transformed to a FD scheme by translating the derivatives with respect of space and time to finite difference expressions. For example, the derivative of a function g with respect to the spatial variable x is given by finite differences like:

$$\frac{dg}{dx} = \frac{g_{n+1} - g_{n-1}}{2\Delta x}. \tag{1.15}$$

Here, g_{n+1} and g_{n-1} are the values of function g neighboring to the point n on a grid, where the derivative is evaluated. The distance between two grid points is Δx . Eq. (1.15) is the so called central difference. Other expressions are the left or right finite differences (Durrant, 1999, p. 35). The finite difference expressions of the differential equation are substituted through a Taylor series expansions to approximate the solution for the neighboring points. The order of accuracy of a system is defined by the lowest power of Δx in the omitted Taylor series components. The 2D FD code of Karrenbach (1995) and 3D FD scheme of Olsen (1994), which are applied in this work, use a staggered grid. On a staggered grid the velocities and stresses are defined on nodes that are separated by half the grid increment. This reduction of grid spacing yields to an improved accuracy and to improved stability conditions because the stability does not depend on the Poisson's ratio (Madariaga, 1976; Aki and Richards, 1980, p. 777; Levander, 1988). The spatial accuracy of the applied 2D FD code (Karrenbach, 1995) is eight order and a second order accurate time operator is used. The used 3D FD code (Olsen, 1994) is fourth order accurate in space and second order accurate in time. The substitution of derivatives through finite differences, the Taylor series expansion and the choice of a proper grid (e.g. standard, staggered, rotated) are very important steps in the development of a FD scheme, because stability, numerical dispersion, accuracy and adaption to computer systems have to be taken into account.

1.3.2 Stability and Numerical Dispersion

A critical issue of FD schemes is the stability of the system. A system is unstable if small errors blow up and produce a numerical solution that increases more rapidly than the true solution. A standard method to explore stability is the Von Neumann analysis (Thomas, 1995, p. 117; Durrant, 1999, p. 43). The numerical solution at a time step is expressed as a finite Fourier series. The solution is stable if all Fourier coefficients are stable. The resulting stability condition is:

$$0 \leq \frac{\alpha_{max}\Delta t}{\Delta x} \leq A. \quad (1.16)$$

Here, α_{max} is the maximum wave speed, Δt the time discretisation, Δx the spatial discretisation within the model and A is a constant value. However, the Von Neumann method only gives a necessary condition and empirical values of A have to be chosen to ensure stability. For the 3D computations A is 0.45 and for the 2D case A is 0.5. Stability does not guarantee a good solution of the scheme for finite operators Δt and Δx . Only for $\Delta t \rightarrow 0$ and $\Delta x \rightarrow 0$ the exact solution would be computed. The accuracy of a scheme can only be checked by comparing the computed results with known analytical solutions for relatively simple problems. These are for example Lamb's problem (Lamb, 1904) or reflectivity solutions for layered models (Fuchs and Müller, 1971). Comparisons between numerical and analytical solutions are shown for example in Virieux (1984, 1986), Levander (1988), Graves (1996) and Coutant et al. (1995).

Numerical dispersion limits the accuracy of the applied FD scheme because different frequencies of a wave show different phase velocities. For non-dispersive waves the dispersion relation is given by:

$$\omega = c_0 k. \quad (1.17)$$

Here, ω is the angular frequency, k is the wavenumber and c_0 is the constant phase velocity. The spatial discretisation yields to a dispersion relation which depends on the grid spacing Δx and the applied time increment Δt . The error between the numerical phase velocity $c_{\Delta x}$ and the non-dispersive phase velocity c_0 is measured by the non-dimensional numerical dispersion coefficient q :

$$q = \frac{c_{\Delta x}}{c_0} = \frac{\omega_{\Delta x}}{\omega}. \quad (1.18)$$

To display the effect of spatial discretisation the dispersion relations for two FD formulations of the 1D wave equation are analysed. Fig. 1.1 shows the numerical dispersion coefficient for the central differences and staggered grid formulation of the 1D wave equation in dependence of the ratio $\Delta x/\lambda$. The numerical dispersion coefficient is calculated from the dispersion relations given by Aki and Richards (1980, eq. 13.134 and eq. 13.136). Only for a small grid spacing Δx compared to the wavelength λ , the numerical phase velocity approximates the non-dispersive case. The staggered grid scheme shows a better approximation than the central differences formulation. The dispersion relations for the 2D FD and 3D FD formulations are much more complicated in comparison to the 1D case, which is shown here. The numerical dispersion coefficient for 2D and 3D FD schemes are analyzed in several publications (Virieux, 1986; Levander, 1988; Graves, 1996; Saenger et al., 2000; Saenger and Bohlen, 2004). Additionally in 2D and 3D the phase

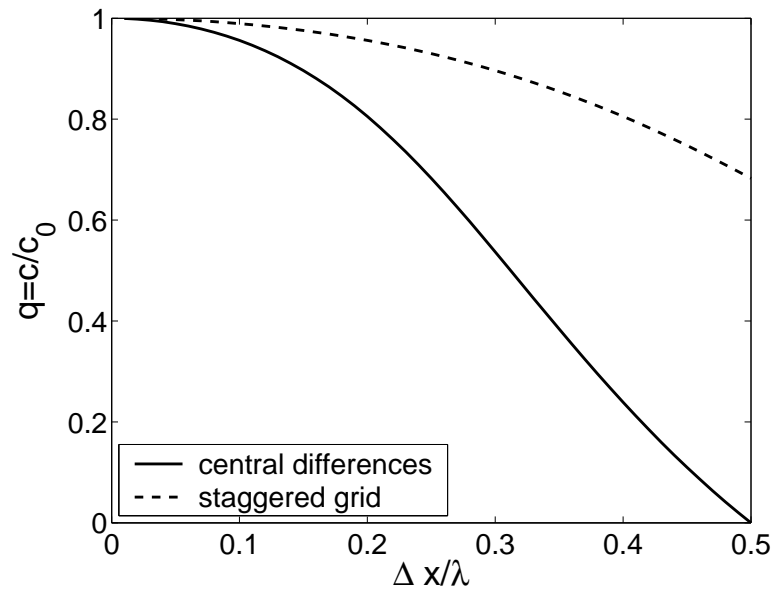


Figure 1.1: Numerical dispersion coefficient q for the central differences and staggered grid formulation of the 1D wave equation. The numerical schemes give a good approximation of the non-dispersive phase velocity c_0 for small grid spacings Δx compared to the wave length λ . The staggered grid formulation shows a good approximation for larger $\Delta x/\lambda$ than the central differences formulation.

speed of the waves depends on the direction between the grid and the wave front. This behaviour is called numerical anisotropy, which depends on the angle between the wavefront and the numerical grid. For waves travelling in the direction of the coordinate axes the numerical dispersion is larger than for waves travelling along the diagonal (Moczo et al., 2000). The error produced by numerical dispersion increases with increasing frequencies. Therefore, usually a relation for a specific FD scheme is given which states that the error due to numerical dispersion does not exceed a fixed limit for the used model size and the used spatial discretisation. These relationships have the following form:

$$\Delta x < \frac{\beta_{min}}{B f_{max}}, \quad (1.19)$$

with the grid spacing Δx , minimum shear wave velocity of the model β_{min} , maximum frequency f_{max} and a constant B that depends on the FD scheme. Constant B gives the minimum number of needed grid points per wavelength. Eq. (1.19) demands a maximum value Δx to get acceptable results for the frequency range up to f_{max} . In this study 6.5 grid points per wavelength are used for the 3D FD modelling. Thus, the dispersion error is less than about 12 % (Olsen, 1994; Olsen and Archuleta, 1996). For the 2D calculations B is 2.8. Table 1.1 summarises the constraints given by stability and numerical dispersion for the 2D and 3D FD schemes applied in this work. It is important to know that eq. (1.19) does not give a frequency range in which there is no numerical dispersion, rather it states that the error is below a predefined threshold. Even if the value is in the range allowed by eq. (1.19) numerical dispersion may significantly disturb the true solution if the modelled regions are larger than the models used to assess B . Eq. (1.19) implies

FD Code	A used in eq. 1.16 (stability)	B used in eq. 1.19 (num. dispersion)
2D (Olsen, 1994)	0.50	2.8
3D (Karrenbach, 1995)	0.45	4.5

Table 1.1: Values of A and B for eqs. (1.16) and (1.19), which are used for the 2D and 3D FD codes.

that for a given Δx the maximum frequency is set by β_{min} . To increase f_{max} it is necessary to reduce the grid spacing Δx . The use of half the grid spacing $\frac{\Delta x}{2}$ means 2^3 more grid points in 3D and therefore 8 times more of consumption of computational memory. Therefore, the available computer memory limits f_{max} . Today, 3D FD wave propagation on one of the world's largest computers, the Earth Simulator (Japan), can be calculated up to 3 Hz for a model of 512 km x 1024 km x 480 km size with a grid spacing of 0.5 km x 0.5 km x 0.25 km (Furumura and Kennett, 2005).

1.3.3 Boundary conditions

To calculate ground motions at the earth's surface a numerical free surface must be implemented. To include a free surface the boundary conditions have to be set explicitly along that border. In this study, the zero stress formulation is used (Levander, 1988; Graves, 1996). The stress vector at a free surface is zero. Hence, for a horizontal free surface with normal in z direction, following relation at the stress nodes along the free surface must be satisfied:

$$\tau_{zz} = \tau_{xz} = \tau_{yz} = 0. \quad (1.20)$$

The 3D code (Olsen, 1994) sets these free surface conditions at the nodes of the staggered grid, which are half a grid point below the position of the free surface. This implementation results in a higher accuracy in comparison to the application of eq. (1.20) directly at the free surface grid nodes (Gottschämmer and Olsen, 2001). Some codes use the vacuum method, which means that the elastic parameters of the material above the surface are almost set to zero (see Graves, 1996). Thus, the free surface boundary conditions are implicitly satisfied.

To avoid artificial reflections from the bottom and the sides of the model, which disturb the wave propagation within the model, special boundary conditions are implemented. The used codes apply damping and one way absorbing boundary conditions. To implement damping boundary conditions the sides and the bottom of the model is padded with an additional grid layer. Within this outer layer the amplitude of the waves is damped exponentially with distance to the inner model (Cerjan et al., 1985). Therefore, only a small part of the energy is reflected at the outermost edge of the model. The one way absorbing boundary conditions (Clayton and Enquist, 1977) allow the outward travelling of waves and reduce the travelling of waves back into the model. The performance of this method depends on the angle the waves impinge on the boundary.

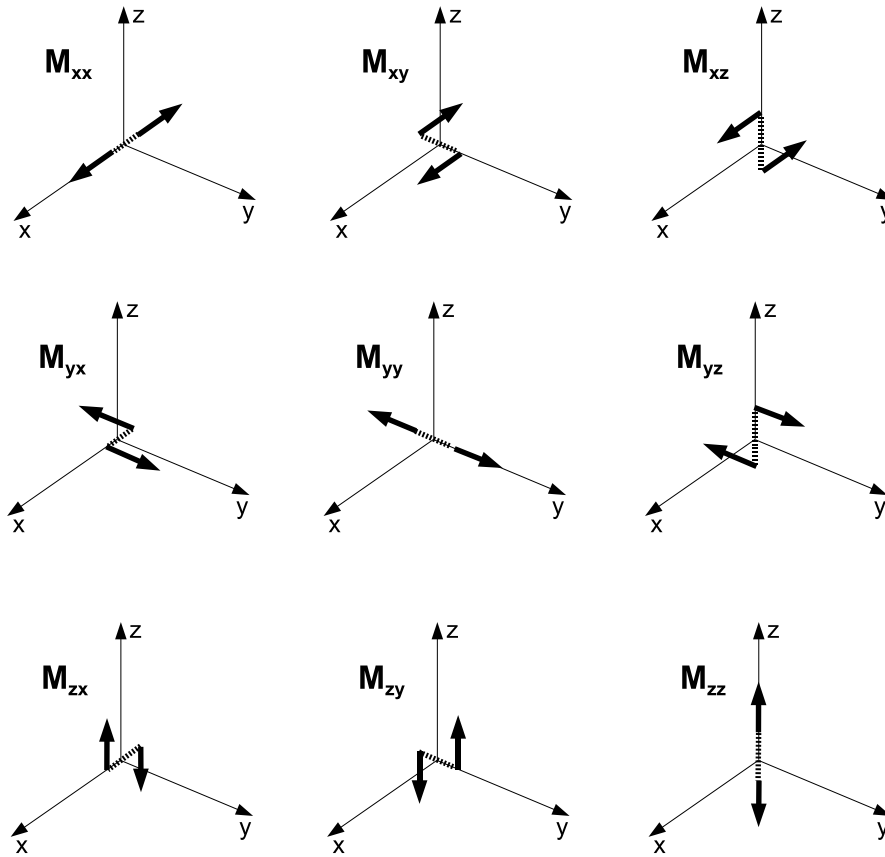


Figure 1.2: The nine force couples of the seismic moment tensor. Equivalent body forces for a dislocation discontinuity is given by a combination of different force couples.

1.4 The Seismic Moment Tensor

Seismic wave radiation due to displacement discontinuities within a body can be described by a combination of force couples. These force couples are referred to as equivalent body forces, which provide a simple model of the complex physical source processes. Fig. 1.2 shows the nine possible force couples that are the components of the seismic moment tensor:

$$M_{kj} = \begin{pmatrix} M_{xx} & M_{xy} & M_{xz} \\ M_{yx} & M_{yy} & M_{yz} \\ M_{zx} & M_{zy} & M_{zz} \end{pmatrix}. \quad (1.21)$$

The components M_{jj} are linear dipoles with arm and forces in the same direction. For explosion source all three linear dipoles are non zero and equal. The force couples M_{kj} ($k \neq j$) describe forces in $\pm k$ direction with a perpendicular arm in j direction. Tectonic earthquakes are produced by shear dislocations on fault planes. The equivalent body forces of shear dislocations are given by the two force couples (called double couple) M_{kj} and M_{jk} , which have to be equal because no

net torque occurs for shear dislocations on a fault.

The displacements due to a moment tensor point source are given by (see Udias, 1999, p. 324 and Aki and Richards, 1980, p. 53):

$$u_i = M_{kj} * G_{ik,j}, \quad (1.22)$$

where $*$ denotes convolution, M_{kj} is the seismic moment tensor and G_{ik} the Green's function, which depends on the characteristics of the medium and therefore "propagates" the displacements from the source to the receiver. The moment tensor for an arbitrary coordinate system is:

$$M_{kj} = M_0(l_k n_j + l_j n_k), \quad (1.23)$$

where the components of \vec{l} give the direction of the displacement discontinuity (slip) and \vec{n} is the normal to the fault plane. The size of an earthquake is given by the scalar moment:

$$M_0 = \mu AD. \quad (1.24)$$

M_0 depends on the Lamé constant μ , the average slip D and the fault area A . According to eq. (1.23) the seismic moment tensor gives the strength of an earthquake and its fault and slip orientation. Within the geographic coordinate system (x-axis to the North, y-axis to the East and z-axis positive downward) the fault orientation is given by the strike angle ϕ , which is the azimuth of the fault's projection onto the surface (Fig. 1.3). The dip angle δ is the angle from the surface to the fault plane. The strike is chosen in the way that the dip, measured from the negative \vec{Y} axis, is always less than 90° . The slip or rake angle λ gives the direction of the slip, which is the movement of the hanging wall relative to the foot wall. Angle λ is measured within the fault plane counterclockwise from the strike direction. The slip $D\vec{l}$ and the normal to the fault \vec{n} are:

$$\begin{aligned} D\vec{l} = & D(\cos \lambda \cos \phi + \cos \delta \sin \lambda \sin \phi)\hat{x} \cdots \\ & + D(\cos \lambda \sin \phi - \cos \delta \sin \lambda \cos \phi)\hat{y} \cdots \\ & - D \sin \delta \sin \lambda \hat{z} \end{aligned} \quad (1.25)$$

and

$$\vec{n} = -\sin \delta \sin \phi \hat{x} + \sin \delta \cos \phi \hat{y} - \cos \delta \hat{z}. \quad (1.26)$$

Then, M_{ij} with respect to a geographic coordinate system is described by (Lay and Wallace, 1995, p.343) and (Aki and Richards, 1980, box 4.4 on p. 117):

$$\begin{aligned} M_{xx} &= -M_0(\sin \delta \cos \lambda \sin 2\phi + \sin 2\delta \sin \lambda \sin^2 \phi) \\ M_{yy} &= M_0(\sin \delta \cos \lambda \sin 2\phi - \sin 2\delta \sin \lambda \cos^2 \phi) \\ M_{zz} &= M_0(\sin 2\delta \sin \lambda) \\ M_{xy} &= M_0(\sin \delta \cos \lambda \cos 2\phi + \frac{1}{2} \sin 2\delta \sin \lambda \sin 2\phi) \\ M_{xz} &= -M_0(\cos \delta \cos \lambda \cos \phi + \cos 2\delta \sin \lambda \sin \phi) \\ M_{yz} &= -M_0(\cos \delta \cos \lambda \sin \phi - \cos 2\delta \sin \lambda \cos \phi) \end{aligned} \quad (1.27)$$

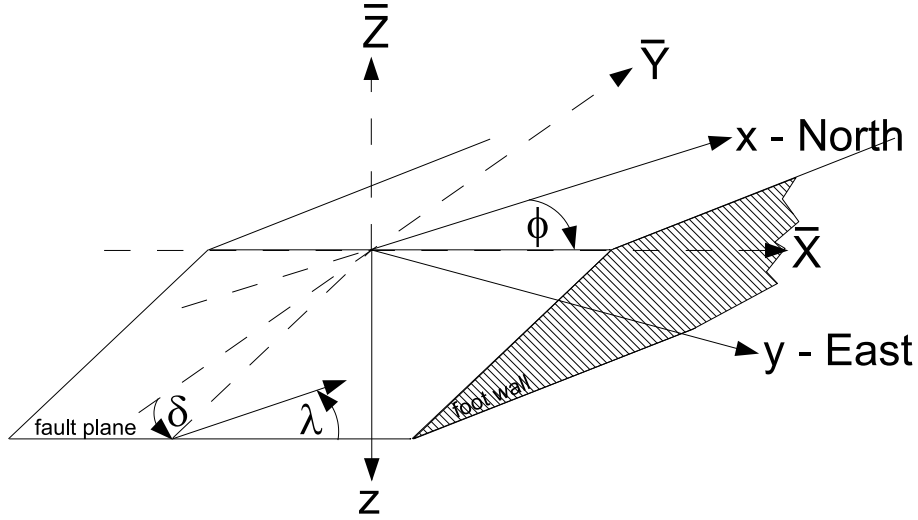


Figure 1.3: Foot wall of a fault with strike ϕ , dip δ and rake λ . The \bar{X} axis is oriented along the strike direction. The geographic coordinate system is given by the North (x), East (y) and z (positive downward) directions. The hanging wall is not shown.

The components of displacement for a double couple source are given by eq. (1.22). After (Aki and Richards, 1980, p. 79) the far field P- and S-displacements are given by:

$$\begin{aligned}
 u_i &= M_{kj} * G_{ik,j} = M_{kj} * G_{ik,j}^P + M_{kj} * G_{ik,j}^S \\
 &= \underbrace{\frac{\gamma_i \gamma_j \gamma_k}{4\pi\rho\alpha^3} \frac{1}{r} \dot{M}_{kj}(t - \frac{r}{\alpha})}_{\text{P-wave far field}} - \underbrace{\left(\frac{\gamma_i \gamma_k - \delta_{ik}}{4\pi\rho\beta^3} \right) \gamma_j \frac{1}{r} \dot{M}_{kj}(t - \frac{r}{\beta})}_{\text{S-wave far field}}.
 \end{aligned} \tag{1.28}$$

Distance between source and receiver is r , α and β are the P- and S-wave velocities and γ_i is the direction cosine r_i/r , where r_i is distance between source and receiver in i direction. Here, the time dependence of the seismic moment tensor is introduced. The pulse shape depends on the temporal derivation of the components of the seismic moment tensor \dot{M}_{kj} , at the retarded times $t - \frac{r}{\alpha}$ and $t - \frac{r}{\beta}$. Consequently, the P- and S-wave displacements after eq. (1.28) can only be nonzero for $t \geq r/\alpha$ or $t \geq r/\beta$, respectively. For a geographical reference system M_{kj} is expressed by eq. (1.27). Therefore, the time dependence of $M_{kj}(t)$ depends on the time dependence of $M_0(t)$. $M_0(t)$ is the seismic moment function and $\dot{M}_0(t)$ the seismic moment rate function or the source time function.

For 3D FD modelling all six independent components of M_{ij} are necessary. In 2D FD modelling the model is confined within the xz plane. According to eq. (1.28) the spatial derivatives of the P- and S-wave Green's functions depend on the direction cosines:

$$G_{ik,j}^P \sim \gamma_i \gamma_j \gamma_k, \tag{1.29}$$

$$G_{ik,j}^S \sim (\gamma_i \gamma_k - \delta_{ik}) \gamma_j. \tag{1.30}$$

In 2D r_y is zero and therefore the direction cosine $\gamma_y = r_y/r$ is also zero. Evaluating $G_{ik,j}^P$ (eq. 1.29) in 2D yields to:

$$G_{ik,j}^P = 0, \quad \text{if one index } i, k, j = y. \quad (1.31)$$

Following equations give the behaviour of $G_{ik,j}^S$ (eq 1.30) in 2D:

$$G_{ik,j}^S = 0, \text{ for} \quad (1.32)$$

$$(i) \ i \text{ or } k = y, \text{ if } i \neq k,$$

$$(ii) \ j = y. \quad (1.33)$$

The x component of the far field displacement \vec{u} in 3D is:

$$\begin{aligned} u_x = & M_{xx} * G_{xx,x} + M_{xy} * G_{xx,y} + M_{xz} * G_{xx,z} \\ & + M_{yx} * G_{xy,x} + M_{yy} * G_{xy,y} + M_{yz} * G_{xy,z} \\ & + M_{zx} * G_{xz,x} + M_{zy} * G_{xz,y} + M_{zz} * G_{xz,z}. \end{aligned} \quad (1.34)$$

After eqs. (1.31),(1.32) and (1.33) u_x in 2D is described by:

$$\begin{aligned} u_x = & M_{xx} * G_{xx,x} + M_{xz} * G_{xx,z} \\ & + M_{zx} * G_{xz,x} + M_{zz} * G_{xz,z}. \end{aligned} \quad (1.35)$$

The 3D far field displacement of the y component is given by:

$$\begin{aligned} u_y = & M_{xx} * G_{yx,x} + M_{xy} * G_{yx,y} + M_{xz} * G_{yx,z} \\ & + M_{yx} * G_{yy,x} + M_{yy} * G_{yy,y} + M_{yz} * G_{yy,z} \\ & + M_{zx} * G_{yz,x} + M_{zy} * G_{yz,y} + M_{zz} * G_{yz,z}. \end{aligned} \quad (1.36)$$

In 2D the far field displacement u_y is after eqs. (1.31),(1.32) and (1.33):

$$u_y = M_{yx} * G_{yy,x} + M_{yz} * G_{yy,z}. \quad (1.37)$$

The far field displacement u_z is:

$$\begin{aligned} u_z = & M_{xx} * G_{zx,x} + M_{xy} * G_{zx,y} + M_{xz} * G_{zx,z} \\ & + M_{yx} * G_{zy,x} + M_{yy} * G_{zy,y} + M_{yz} * G_{zy,z} \\ & + M_{zx} * G_{zz,x} + M_{zy} * G_{zz,y} + M_{zz} * G_{zz,z}. \end{aligned} \quad (1.38)$$

After eqs. (1.31),(1.32) and (1.33) u_z in 2D is described by:

$$\begin{aligned} u_z = & M_{xx} * G_{zx,x} + M_{xz} * G_{zx,z} \\ & + M_{zx} * G_{zz,x} + M_{zz} * G_{zz,z}. \end{aligned} \quad (1.39)$$

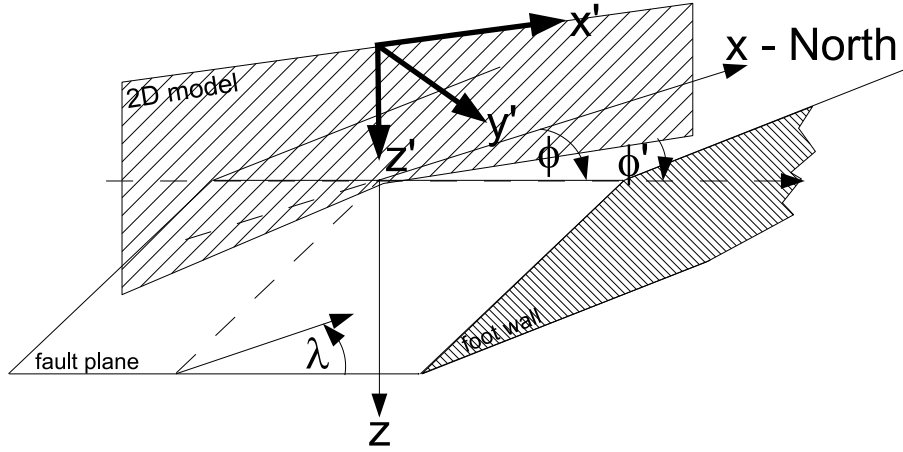


Figure 1.4: Fault orientation within a 2D model of azimuth ϕ' . Substitute ϕ with ϕ' in (1.27) to get the components M_{ij} for a 2D slice with azimuth ϕ' .

The u_x and u_z components in 2D represent the P-SV-wave propagation. After eq. (1.35) and (1.39) the components M_{xx} , M_{xz} , M_{zx} and M_{zz} of the seismic moment tensor are needed in 2D to initiate P-SV-wave propagation. The u_y component in 2D gives the SH wave displacements, which are fully decoupled from the P-SV-wave propagation. After eq. (1.37) the seismic source for SH-wave propagation in 2D is given by the moment tensor components M_{yx} and M_{yz} . Therefore, all components of the seismic moment tensor except of the M_{yy} component are necessary to describe a double couple source in 2D. The components of the seismic moment tensor are needed with respect to the orientation of the 2D model for which the wave propagation is simulated. This is done by substituting the azimuth ϕ with the angle ϕ' between the strike angle and the orientation of the 2D model in eq. (1.27) (see Fig. 1.4). This gives the moment tensor components in terms of an $x'y'z'$ coordinate system of the 2D model.

1.5 Source Implementation

A source can be implemented into a FD scheme by adding the corresponding source values at the displacement, velocity or stress nodes. Frankel (1993) and Graves (1996) translate the seismic moment into displacements/velocities values, which are added to the grid at the source location. In this work, the source is implemented by adding stress values, which imply the orientation and strength of the source, to the corresponding stress components of the staggered grid. The method is described for the 2D case in Coutant et al. (1995) and used by many FD codes (e.g Virieux, 1984, 1986; Levander, 1988; Olsen, 1994). This method is based on the fact that the moment tensor density m_{kj} or stress glut is the difference between the pure elastic stresses τ_{kj} , which are used in the equation of motion (1.2), and the total stresses σ_{kj} on the fault (Udias, 1999, chapter 17.1):

$$m_{kj} = \tau_{kj} - \sigma_{kj}. \quad (1.40)$$

The moment tensor density in a FD grid is equal to the seismic moment at the source node divided by the cell volume:

$$m_{kj} = \frac{M_{kj}}{\Delta x^3}. \quad (1.41)$$

Therefore, the implementation of an earthquake, which is defined by its moment tensor, is straightforward, as eqs. (1.40) and (1.41) relate the stress components needed for simulation to the seismic moment tensor, which gives the strength and orientation of the source. To simulate an earthquake with magnitude M_w , the seismic moment is calculated after Hanks and Kanamori (1979). The next step is the choice of proper time function for the seismic moment function and its translation into stress values after eq. (1.41), which can be added to the grid.

1.5.1 Source Scaling for Point Sources

A point source is used to simulate wave propagation for the Vrancea intermediate depth earthquakes (chapter 3). The source scaling is developed for a given seismic moment M_0 and stress drop $\Delta\sigma$. Assuming Brune's source model (Brune, 1970, 1971), which is valid for a circular fault, the static stress drop $\Delta\sigma$ is:

$$\Delta\sigma = \frac{7}{16} \frac{M_0}{r^3}, \quad (1.42)$$

with seismic moment M_0 and fault radius r . The corner frequency f_c is related with the fault radius r and the shear wave velocity β at the source (Brune, 1970, 1971):

$$2\pi f_c = 2.34 \frac{\beta}{r}. \quad (1.43)$$

Combining eq. (1.43) and eq. (1.42) yields to:

$$f_c^3 \approx 3.66 \frac{\Delta\sigma \beta^3}{\pi^3 M_0}, \quad (1.44)$$

with the rupture time $t_r = 1/f_c$. Static stress drop $\Delta\sigma$ is proportional to the cube of the corner frequency f_c . Therefore, doubling the corner frequency results in half the rupture time and eight times the stress drop. The stress drop of the Vrancea earthquakes is discussed in several publications (Gusev et al., 2002; Oncescu, 1989; Oth et al., 2006; Radulian et al., 2005; Wirth, 2004). Wirth (2004, p. 141) give an overview on derived stress drops for the 1977 $M_w = 7.4$ and 1986 $M_w = 7.1$ earthquakes. The derived stress drops of the Vrancea earthquakes vary from about 10 to 100 MPa. This variation most likely reflects the use of different source models to derive the stress drop (Oth et al., 2006). Eq. (1.44) relates the stress drop $\Delta\sigma$ and the rupture time t_r , which is necessary to construct a proper moment function for the modelling. In this work the source time function after Beresnev and Atkinson (1997) is used. They describe extended faults by adding the contributions of several subfaults. For the displacement at the subfaults they use:

$$D(t) = D(\infty) \left[1 - \left(1 + \frac{t}{\eta} \right) e^{-t/\eta} \right], \quad (1.45)$$

with the time derivative:

$$\dot{D}(t) = D(\infty) \frac{t}{\eta^2} e^{-t/\eta}. \quad (1.46)$$

The value $D(\infty)$ is the displacement D reached for infinite t . The characteristic time η controls the displacement increase and is therefore related to the rise time. The Fourier spectra (Beresnev and Atkinson, 1997, eq. 11) shows a ω^{-2} square frequency decay for frequencies larger than the corner frequency $1/\eta$. This is the same as derived by Brune (1970, 1971). Modelling extended sources as point sources means, that the total moment is released at a grid point or one subfault element, with dimension of the grid spacing. Therefore, η is chosen, so that the time to reach the final displacement corresponds to the rupture times of the Vrancea earthquakes rather than to the rise time of a subfault element. Eqs. (1.23) and (1.24) relate the displacement at the source and the moment tensor. Therefore, the time function for displacements (eq. 1.45) after Beresnev and Atkinson (1997) can be used to describe the seismic moment function:

$$M_0(t) = M_0(\infty) \left[1 - \left(1 + \frac{t}{\eta} \right) e^{-t/\eta} \right]. \quad (1.47)$$

A value of η is used so that 98% of the final seismic moment is reached after the rupture time $t_r = 1/f_c$. For the 1986 $M_w = 7.1$ event with $M_0 = 5 \cdot 10^{19}$ Nm and a stress drop of $\Delta\sigma = 100$ MPa, eq. (1.44) yield to a corner frequency f_c of 0.3 Hz. Fig. 1.5 shows the seismic moment tensor density function $M_0(t)/\Delta x^3$, which gives the stresses needed for the FD modelling. The orientation of an earthquake is implemented by applying eq. (1.41) with eq. (1.27). Using eq. (1.43) with $f_c = 0.3$ Hz, the fault radius is 7.61 km. Compared to the intermediate hypocentral depth of the Vrancea earthquakes the fault area is relatively small. Therefore, the use of a point source makes sense. Compared to real source time functions, the time function after Beresnev and Atkinson (1997) is rather smooth. However, since for the intermediate depth earthquakes the exact source process is unknown and the complexity along the travel path is much more important than the details of the rupture process the time function after Beresnev and Atkinson (1997) can be used to simulate the Vrancea earthquakes.

1.5.2 Source Scaling for Rupture Histories on Extended Faults

In chapter 2 the 1999 Kocaeli earthquake (Turkey) is modelled with 3D FD by applying inverted rupture processes. In contrast to the modelling of point sources (section 1.5.1) a extended fault is used. The number of subfaults N is given by the grid spacing Δx and the fault area A :

$$N = \frac{A}{\Delta x^2}. \quad (1.48)$$

The seismic moment is distributed over N subfaults and the seismic moment at a subfault is:

$$M_{ij}^N(T) = \int_{t=0}^{\infty} \dot{M}_{ij}^N(t) dt, \quad (1.49)$$

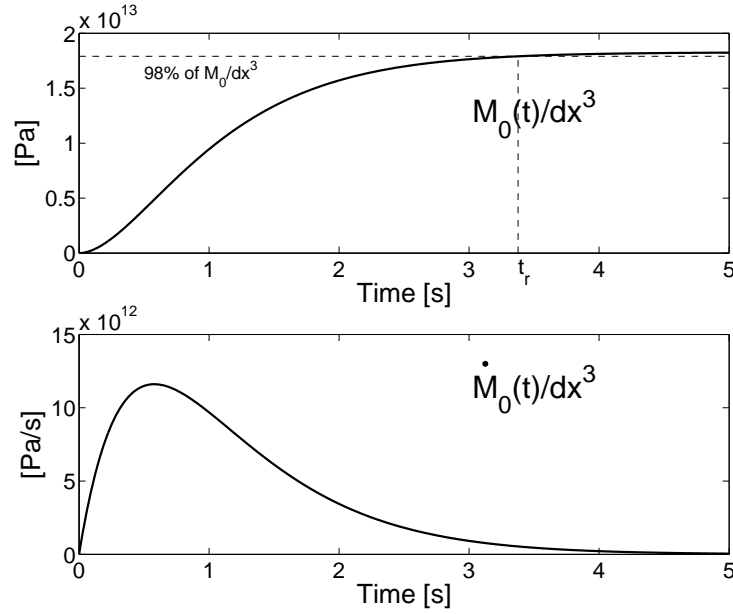


Figure 1.5: Top: Moment density function of the 1986 Vrancea earthquake for a static stress drop of 100 MPa. After $t_r = 1/f_c \approx 3.4$ seconds 98% of the final moment tensor density is reached. Bottom: Time derivative of the moment density function. This is the source time function divided by dx^3 . The wave form is given by Beresnev and Atkinson (1997).

where T is the rupture time at a subfault. The total seismic moment $M_{ij}(T)$ is given by the sum of all $M_{ij}^N(T)$ over all fault points:

$$M_{ij}(T) = \sum_1^N M_{ij}^N(T). \quad (1.50)$$

The 3D FD code (Olsen, 1994) translates the source time function \dot{M}_{ij}^N at a point of the fault into the seismic moment tensor density:

$$m_{ij}^N(t) = \Delta t \frac{\dot{M}_{ij}^N(t)}{\Delta x^3}. \quad (1.51)$$

For a subfault the source time function can be written after eq. (1.24) as:

$$\dot{M}_0^N(t) = \mu \Delta x^2 \dot{D}(t) = \mu \Delta x^2 v_{slip}(t). \quad (1.52)$$

Here, Δx^2 is the fault area for a small subfault, which surrounds a grid point, and v_{slip} is the particle velocity at the subfault. Inversions of earthquake rupture processes give the slip velocity v_{slip} in providing rise time and total slip for all subfaults. Using a geographical coordinate system the time derivative of eq. (1.27) calculates $\dot{M}_{ij}^N(t)$ from $\dot{M}_0^N(t)$ and eq. (1.51) gives the seismic moment tensor density at a subfault, which is added onto the FD grid. In chapter 2 the source time function is assumed as triangular (Fig. 1.6). The starting time of the rupture at a fault point is given by the inverted propagation of the rupture front.

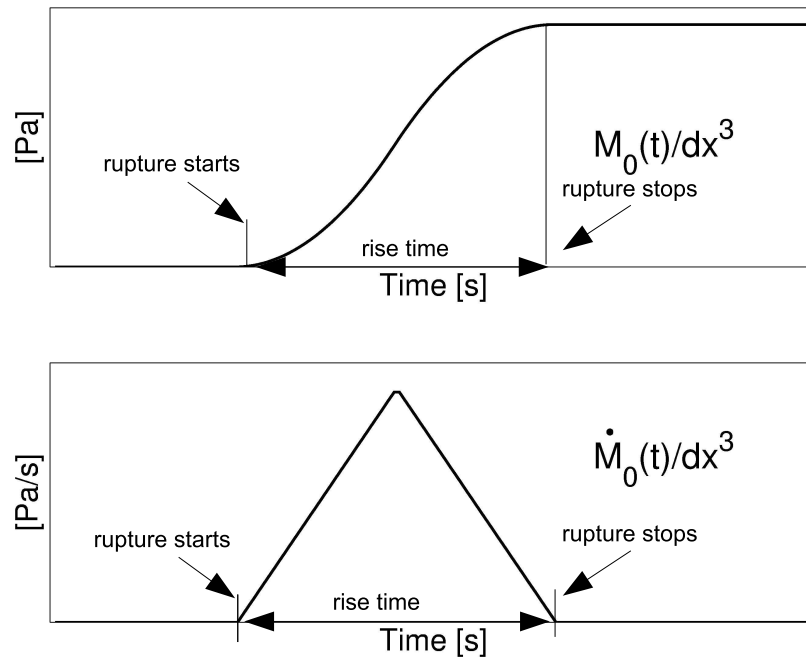


Figure 1.6: Top: Form of the moment tensor density function used at all fault points of the 1999 Kocaeli earthquake (chapter 2). Bottom: Used triangular shaped time derivative of the moment density function. The velocity at each fault point shows also this triangular behaviour, because the source time function is proportional to the slip velocity (eq. 1.52).

1.6 Simulating Double Couple Sources with the 2D FD code of Karrenbach (1995)

The 2D FD code (Karrenbach, 1995) was designed to use pressure sources, displacement sources, body force sources and stress sources. The stress source is the source type that is needed to incorporate double couple sources as described in section 1.4 and 1.5. However, the code is mainly used to model wave propagation initiated by pressure sources (Görtz, 2002; Sule, 2004). Therefore, first the functionality of the implementation of double couple sources by applying a stress source was tested. The simulated radiation results are compared to the theoretical source radiation given by eq. (1.28). Wave propagation within a homogeneous model for a double couple source with strike ϕ , dip δ and rake λ of the 1986 strong Vrancea earthquake is modelled. In Fig. 1.8 and 1.9 the modelled radiation for P- and S-waves within a 2D slice, which is orientated in EW direction, is compared to the theoretical radiation after eq. (1.28). It can be seen that the 2D FD code matches the theoretical source radiation pattern. Differences reflect the use of a staggered grid, where the stress components, which are used to simulate the source, are defined on different spacial locations of the grid. Additionally, the stress values of the source are distributed over a several grid points, which results in a small quadratic source rather than

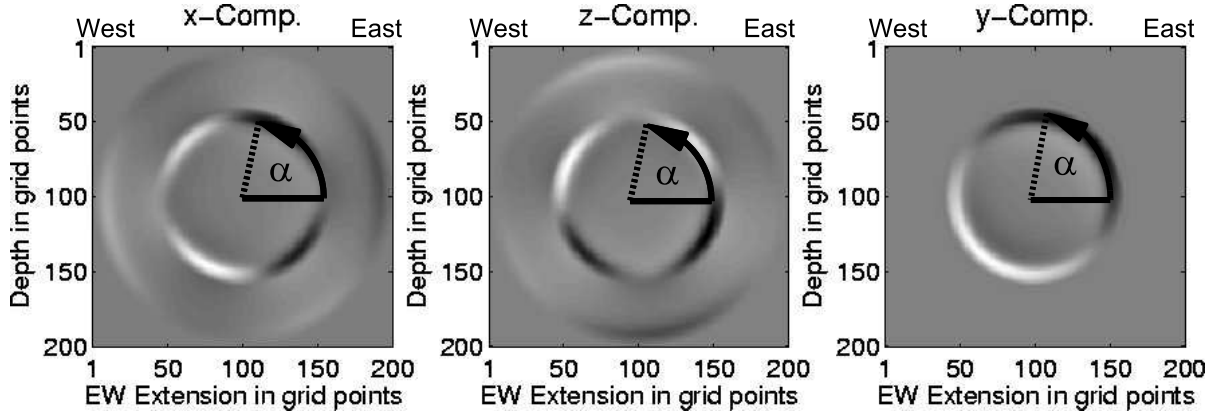


Figure 1.7: Snap shot of the wave field within an EW orientated 2D slice for a double couple source with strike, dip and rake of the 1986 Vrancea strong earthquake. In Fig. 1.8 and 1.9 the modelled and theoretical radiation patterns are compared. Angle α is measured counterclockwise from the East.

a point source. This is necessary to avoid numerical artefacts, which would be produced by the numerical operators (Schmidt-Aursch, 1998, p. 64).

1.7 2D to 3D Correction

In homogeneous media wave propagation initiated by a point source in 2D corresponds to wave propagation for a infinite line source in 3D. 3D line source seismograms have an infinite tail and the wavefield amplitudes decay with $1/\sqrt{R}$. In contrast, 3D point source seismograms have no tail and geometrical spreading is $1/R$. Therefore, seismograms obtained by 2D FD modelling can be corrected in order to simulate point source seismograms in 3D space. In this section, first the mapping between 2D seismograms and the corresponding 3D point source seismograms is derived. Next, the developed 2D to 3D mapping is tested numerically.

1.7.1 Theory

The far field Green's function G_{il} in the frequency domain for an elastic medium is given by Hudson (1980, p. 137):

$$G_{il} = \frac{1}{4\pi\rho} \left[\frac{\hat{x}_l\hat{x}_i}{\alpha^2R} e^{i\omega R/\alpha} + \frac{(\delta_{il} - \hat{x}_i\hat{x}_i)}{\beta^2R} e^{i\omega R/\beta} \right] = \frac{1}{4\pi\rho} \left[\frac{\hat{x}_l\hat{x}_i}{\alpha^2R} e^{ik_\alpha R} + \frac{(\delta_{il} - \hat{x}_i\hat{x}_i)}{\beta^2R} e^{ik_\beta R} \right]. \quad (1.53)$$

With the unit vectors \hat{x}_l and \hat{x}_i in l and i -direction. For simplicity the 2D to 3D correction is derived for an acoustic medium. However, the derived 2D to 3D correction is also valid for the

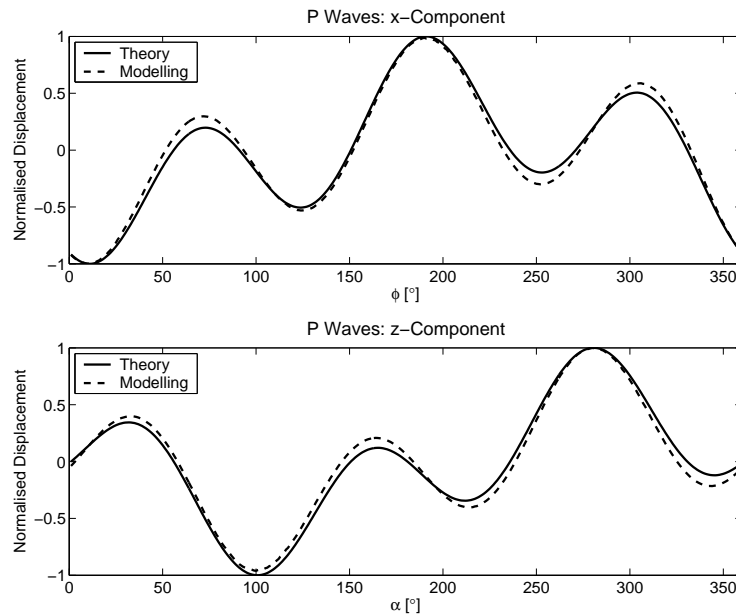


Figure 1.8: Comparison of theoretical and modelled P-wave radiation pattern of a point source. The strike, rake and dip values of the 1986 earthquake were used to model wave propagation within a homogeneous 2D model, which is orientated in EW direction. Differences occur because of the stress locations in the staggered grid and the use of small quadratic sources instead of a point source. Angle α is measured counterclockwise from the East (see Fig. 1.7)

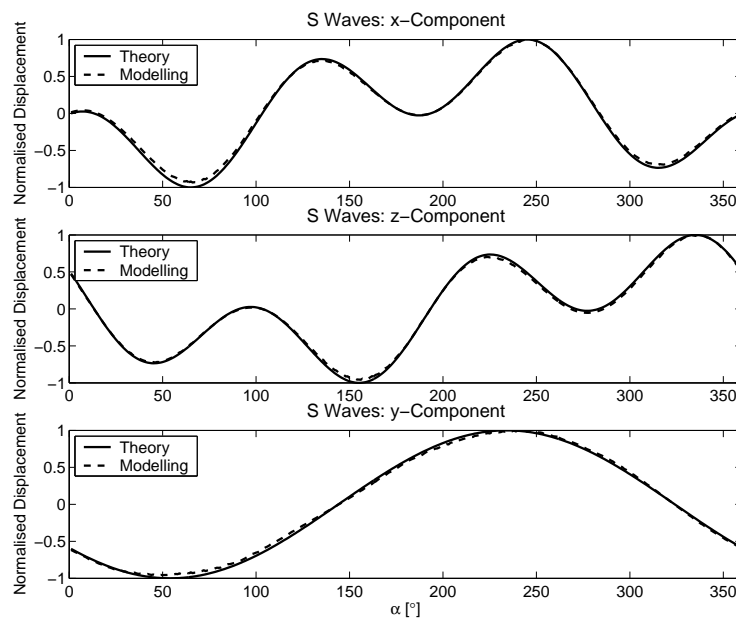


Figure 1.9: Comparison of theoretical and modelled S-wave radiation pattern for a source with strike, dip and rake of the 1986 strong Vrancea earthquake. Differences reflect the use of a small non circular source. Angle α is measured counterclockwise from the East (see Fig. 1.7)

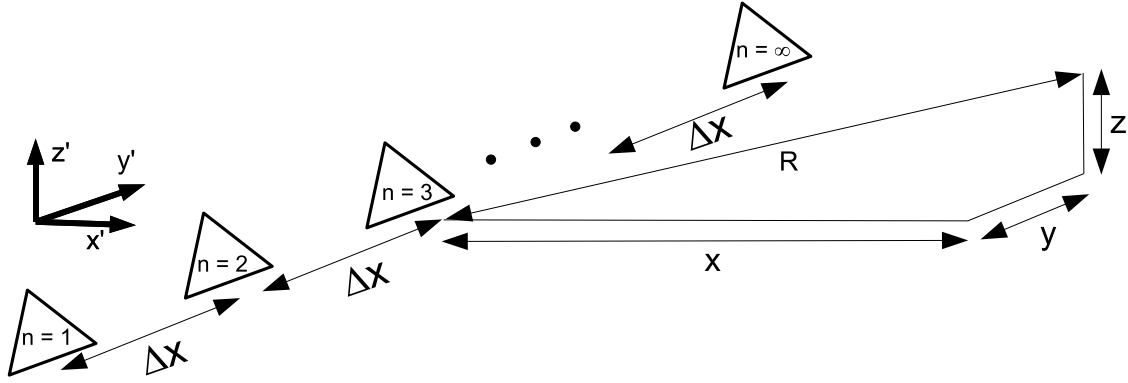


Figure 1.10: An infinite number of point sources in the y -direction build a line source. Distance between a point source and a receiver is given by: $R = \sqrt{x^2 + y^2 + z^2}$, where y can be expressed as $n\Delta x$ and $r^2 = x^2 + z^2$ is the square of the distance between source and receiver in the xz -plane.

elastic case because the Green's functions for both cases have the same wave function e^{ikR}/R . In the acoustic case the Green's function for the velocity potential in the Helmholtz equation is given by:

$$G_{point_3D}(\omega) = \frac{e^{ikR}}{4\pi R}, \quad (1.54)$$

with the wavenumber $k = \omega/c$, wave speed c and distance R between source and receiver:

$$R = \sqrt{x^2 + y^2 + z^2}. \quad (1.55)$$

In Fig. 1.10 an infinite number of point sources build a line source in y -direction. The response of a line source can be constructed by adding the contribution of an infinite number of point sources. Therefore, the response G_{line_3D} of the line source in Fig. 1.10 is given by:

$$G_{line_3D}(\omega) = \frac{1}{4\pi} \sum_{n=1}^{\infty} \frac{e^{ik\sqrt{r^2+n\Delta x}}}{\sqrt{r^2+n\Delta x}}, \quad (1.56)$$

where $y = n\Delta x$ and $r^2 = x^2 + z^2$, which is the square of the distance in the xz -plane between source and receiver. Applying the Fresnel approximation and writing the sum as an integral, eq. (1.56) transforms into:

$$G_{line_3D}(\omega) = \frac{e^{ikr}}{4\pi r} \frac{1}{\Delta x} \int_{-\infty}^{+\infty} e^{\frac{ikx^2}{2r}} dx. \quad (1.57)$$

The integral on the right hand side is given by:

$$\int_{-\infty}^{+\infty} e^{\frac{i\omega x^2}{2cr}} dx = \frac{e^{\frac{i\pi \text{sgn}(\omega)}{4}}}{\sqrt{|\omega|}} \sqrt{2\pi cr}. \quad (1.58)$$

Using eq. (1.58) the Green's function for a line source is given by:

$$G_{line_3D}(\omega) = \underbrace{\frac{e^{ikr}}{4\pi r}}_{G_{point_3D}(\omega) \text{ (see eq. 1.54)}} \underbrace{\frac{1}{\Delta x} \sqrt{\frac{2\pi cr}{|\omega|}} e^{\frac{i\pi \text{sgn}(\omega)}{4}}}_{C_{Line \rightarrow Point}^{-1}(\omega)}. \quad (1.59)$$

The first factor on the right hand side is the Green's function for a point source in 3D. Therefore, the 3D point source solution can be obtained by multiplying the line source solution (eq. 1.59) with:

$$C_{Line \rightarrow Point}(\omega) = \frac{\Delta x}{\sqrt{2\pi cr}} \sqrt{|\omega|} e^{-\frac{i\pi \text{sgn}(\omega)}{4}}. \quad (1.60)$$

Transforming eq. (1.60) into the time domain yields to:

$$C_{Line \rightarrow Point}(t) = \frac{\Delta x}{\pi \sqrt{2cr}} \frac{d}{dt} \frac{H(t)}{\sqrt{t}}. \quad (1.61)$$

Thus, the 2D FD line source seismogram $u_{line_2D}(t)$ can be translated into a 3D point source seismogram u_{point_3D} by applying operator (1.61) to $u_{line_2D}(t)$:

$$u_{point_3D} = \frac{\Delta x}{\pi \sqrt{2cr}} \left\{ \frac{d}{dt} \frac{H(t)}{\sqrt{t}} * u_{line_2D}(t) \right\}. \quad (1.62)$$

Vidale and Helmberger (1987) derived a formula without the factor $\Delta x/(\pi \sqrt{2c})$ to correct 2D FD seismograms:

$$u_{point_3D} = \frac{1}{\sqrt{r}} \left(\frac{1}{\sqrt{t}} * u_{line_2D} \right). \quad (1.63)$$

This equation is used by Igel et al. (2002) and Olsen et al. (1996) to transform 2D FD seismograms into 3D. However, eq. (1.63) is only valid for the source implementation technique used by Vidale et al. (1985) and Vidale and Helmberger (1987), which imposes the whole space, line source, first term asymptotic GRT (generalised ray theory) solution on the source grid points.

1.7.2 Numerical Tests

To validate eq. (1.62) 2D and 3D FD numerical tests are carried out with the 2D FD code of Karrenbach (1995) and the 3D FD code of Olsen (1994). A double couple source with the force couples in the xz-plane is used (Fig. 1.11). The source waveform is adopted from Beresnev and Atkinson (1997). In the next sections 3D FD point seismograms are compared with corrected 2D point seismograms for a homogeneous and a layered structure.

First, 3D and 2D FD wave propagation is simulated for a homogeneous model with $v_p = 6000$ m/s, $v_s = 3464$ m/s and density $\rho = 2500$ kg/m³ with a grid spacing of 140 m. The source wavelet and its frequency content is shown in Fig. 1.12. The maximum resolvable frequency of FD cal-

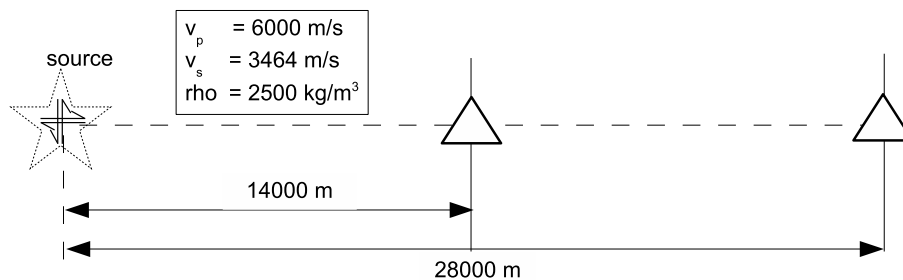


Figure 1.11: 2D and 3D wave propagation in homogeneous models is calculated for a double couple source with maximum SV radiation in x-direction. 3D and corrected 2D FD seismograms are compared for stations in a distance of 14000 m and 28000 m (Fig. 1.14).

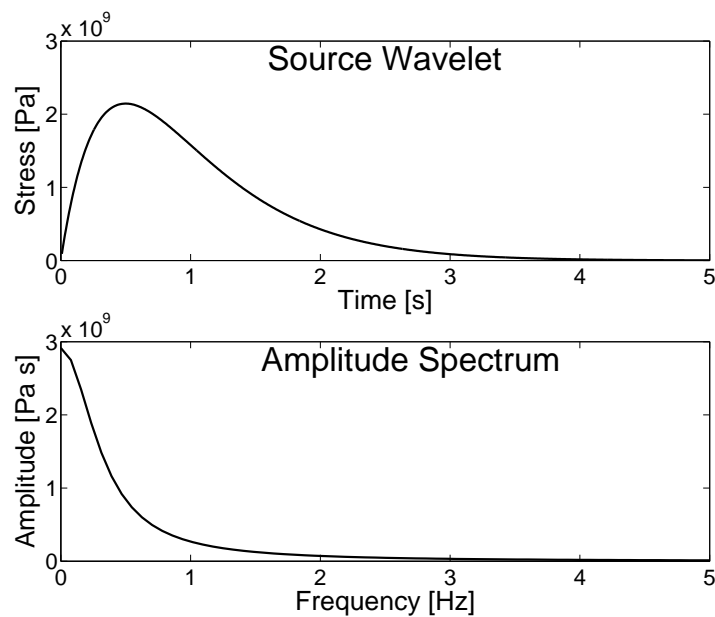


Figure 1.12: Top: Source wavelet after Beresnev and Atkinson (1997) used to test the 2D to 3D correction. Bottom: Fourier amplitude spectrum of the source wavelet. The frequency content of the source is below 5 Hz, which is the maximum frequency according to eq. (1.19) for $v_s=3464 \text{ m/s}$ and $B=5$.

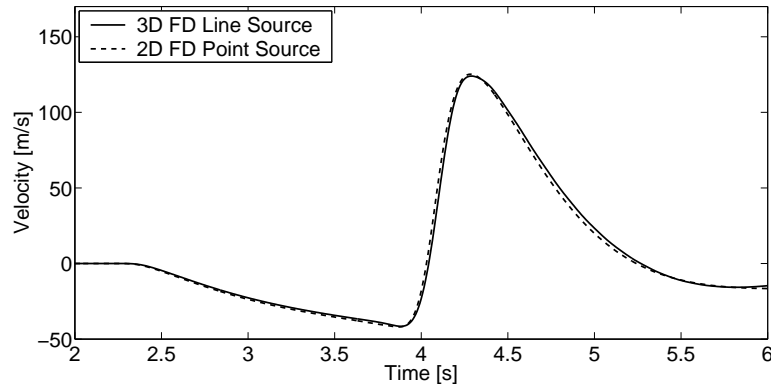


Figure 1.13: Comparison between a 3D line source seismogram and a 2D point source seismogram in a distance of 14000 m to the source. Differences are produced by the different accuracies of the two applied 2D and 3D FD schemes.

culations is limited by numerical dispersion. For a minimum of five points per wavelength and a minimum velocity of 3464 m/s, the maximum frequency according to eq. (1.19) is 5 Hz, which is higher than the frequency content of the source used here. The applied double couple source is indicated in Fig. 1.11. Fig. 1.13 shows the equivalence of a point source in 2D and a line source in 3D. The seismograms are compared in a x-distance of 14000 m to the source. In this direction the source radiates no P-waves and SV-wave radiation shows a maximum. Small differences are produced by the different numerical accuracies of the applied 2D FD (Karrenbach, 1995) and 3D FD (Olsen, 1994) codes. The 2D FD scheme is of eight order accuracy and the 3D FD scheme uses a fourth order accurate operator. Fig. 1.14 compares the seismograms of a point source in 3D and the 2D seismograms which are corrected according to eq. (1.62) in a x-distance of 14000 m and 28000 m to the source (Fig. 1.11). The amplitude difference between the corrected 2D FD seismogram and the 3D FD seismogram is about 10%. This difference occur because the schemes use operators of different numerical accuracy.

Eq. (1.62) is only valid for homogeneous models. The use of inhomogeneous structures results into non-straight ray paths and non-constant velocities. A 3D and 2D FD calculation is carried out for waves travelling from the source S to the stations A , B and C through a layered structure (Fig. 1.15). The source is the same double couple source as used above. To correct the 2D FD seismograms r is calculated after Snell's law and c is the average velocity along the ray path, which is given by r divided by the travel time. The comparison shows a good fit between the 3D FD calculations and the corrected 2D FD calculations (Fig. 1.16). The difference between the maximum amplitudes is about 10%. The numerical tests support the application of this methodology for inhomogeneous models to correct 2D FD seismograms. For inhomogeneous models a hybrid method of 2D FD modelling and ray tracing can be used to simulate 3D seismograms, which show the correct geometrical spreading for waves travelling through complex structures with curved interfaces. Ray tracing provides the distance r between source and receiver and the travel time t through an inhomogeneous structure. These values are necessary to compute the average velocity c for the 2D to 3D correction of the 2D FD seismograms (eq. 1.62). The use of a 2D FD technique, which is less computer intensive than 3D FD calculations, allows wave

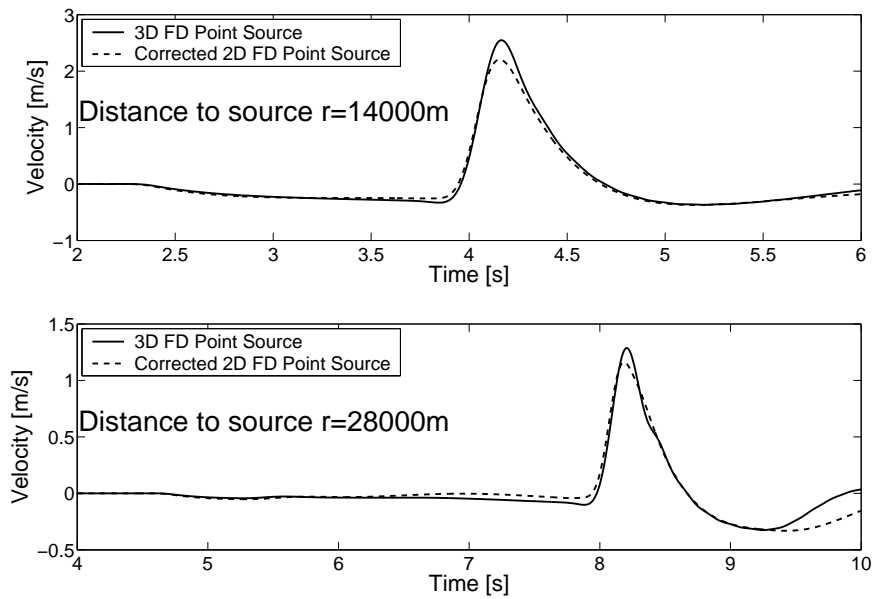


Figure 1.14: Comparison between a 3D point source seismogram and a corrected 2D point source seismogram in a distance of 14000 m and 28000 m to the source. Therefore, in eq. (1.62) $c = v_s = 3463$ m/s is used to correct the 2 FD seismograms. Amplitude differences of about 10 % are produced by the different accuracies of the two applied 2D and 3D FD schemes.

propagation simulation for larger frequencies compared to 3D FD calculations. Additionally, 2D FD simulations for many seismological problems can be carried out on today's desktop computers. This is an advantage if the access to powerful and expensive computers is limited. Of course, the simulation of 3D effects produced by complex 3D underground structures cannot be simulated with a 2D FD method. To simulate these 3D effects there is no other way than to simulate wave propagation in 3D. However, in many cases 2D FD methods reveal basic influences of underground structures on the wavefield. Consequently, it is convenient to use a 2D FD method before doing time consuming and therefore expensive 3D FD simulations on large computers (see Furumura and Kennett, 2005).

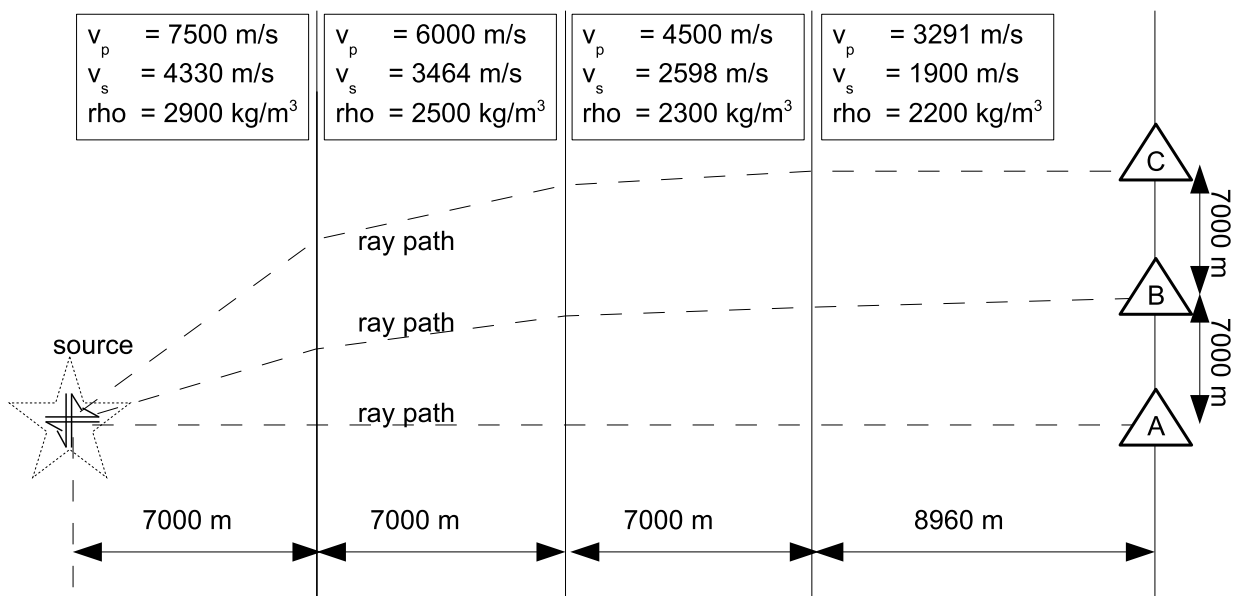


Figure 1.15: Layered model that is used to test the 2D to 3D correction for non straight ray paths through a layered structure.

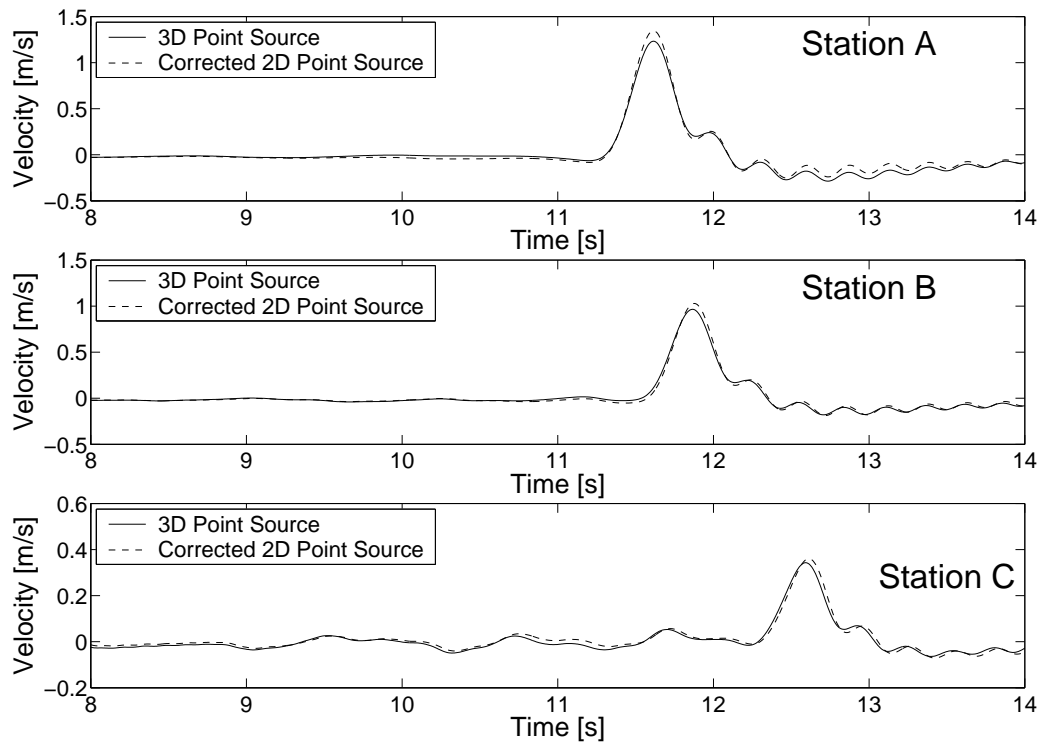


Figure 1.16: Comparison between 3D FD point source seismograms and corrected 2D FD seismograms for a layered model (Fig. 1.15). The vertical offset of stations A, B and C are 0 km, 7 km and 14 km, respectively. The seismograms are corrected by using the ray path after Snell's Law and the average velocity between source and receiver, which is travelpath r divided by traveltime. Amplitude differences of about 10 % between the 3D FD point source seismograms and the corrected 2D FD seismograms are found. A source of error are the different accuracies of the applied 2D and 3D FD schemes.

Chapter 2

3 FD Modelling of the 1999 Kocaeli Earthquake (Turkey)

2.1 Introduction

A 3D Finite-Difference (FD) method is used to simulate ground motions of the 1999 Kocaeli (Turkey) earthquake. The modelling generates an insight into the strong ground motions produced by this earthquake and helps to explain the observed peculiarities. The reliability of the used method and the adopted modelling parameters, such as source and underground structure, is shown by comparing the modelling results with the observed data. Therefore, this work may be a starting point for the modelling of a potential future large earthquake near Istanbul. The study in this chapter continues previous research, which is described in the author's diploma thesis (Miksat, 2002). During the diploma thesis the procedure to model earthquakes with complex rupture processes was developed and applied on the 1999 Kocaeli earthquake by using the rupture histories inverted by Yagi and Kikuchi (2000) and Bouchon et al. (2002). In this work an additional rupture history (Sekiguchi and Iwata, 2002) is used. The seismograms for the rupture histories of Bouchon et al. (2002) and Sekiguchi and Iwata (2002) are compared with the records at the stations that were used to invert the rupture. At these stations the synthetic seismograms show a good comparison with the observed seismograms. Furthermore, the translation of synthetic seismograms into macroseismic intensities, which directly describe damage, is performed. The synthetic intensity maps are compared with the observed intensity distribution. The FD modelling with Bouchon's rupture process reproduces the observed intensities for the near fault area. In contrast, the modelling with Sekiguchi's inversion results shows clear differences between the modelled and observed intensities. Consequently, applying different rupture inversions reproduce the seismograms at those stations which were used to invert the rupture process, but as the comparison between modelled and observed intensities showed, ground motions in between the stations are not necessarily reproduced. This study also points out that the near fault ground motion distribution for the Kocaeli earthquake and for large shallow earthquakes in general is quite complex and depends strongly on the rupture speed,

rise time and slip distribution on the fault. The lack of knowledge of a future rupture process makes it difficult to model future ground motions. Here, it is necessary to apply different rupture scenarios. This topic is further discussed in section 2.8.

The 1999 Kocaeli earthquake struck northwestern Turkey on August 17, 1999 at 03:02 a.m. The earthquake killed more than 15,000 people, at least 25,000 were injured and about 400,000 were left homeless EERI (1999). Approximately 75,000 buildings were damaged or destroyed and the direct damage was estimated at 40 billions US\$. During the earthquake a 120 km long part of the North Anatolian Fault (NAF) ruptured and produced a $M_w = 7.4$ event with horizontal surface ruptures up to about 5.2 m (Barka et al., 2002; Rockwell et al., 2002). The fault trace was divided into five different segments (Fig. 2.1), which are separated by releasing step-overs (Barka et al., 2002). A $M_w = 7.2$ event near Düzce followed the August 17 earthquake on November 11, 1999. These earthquakes were the latest of a sequence along the NAF, which started in 1939 near Erzincan in eastern Turkey and produced 12 events with magnitudes greater than $M_w = 6.7$. This sequence can be related to stress transfer (Stein et al., 1997) and consequently, the 1999 event increased the propability of a strong earthquake in the Sea of Marmara near the mega city of Istanbul (Parsons et al., 2000; Hubert-Ferrari et al., 2000).

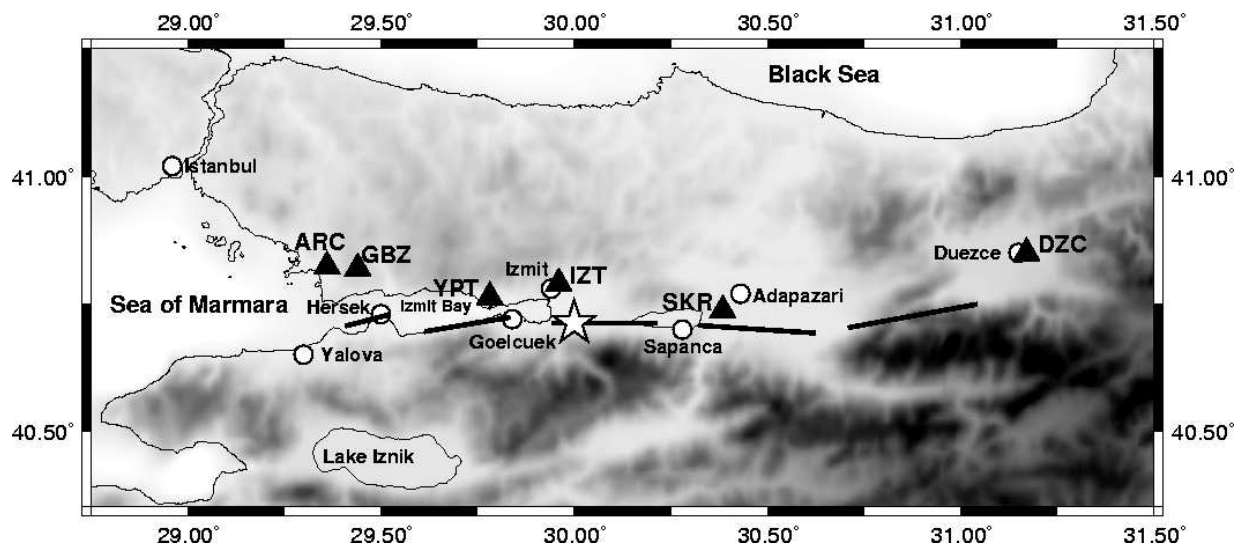


Figure 2.1: The map shows the five different segments of the August 1999 fault rupture after Barka et al. (2002). The triangles depict the six near fault (< 20 km) strong motion stations Gebze (GBZ), Yarimca (YPT), Izmit (IZT), Sakarya (SKR) and Düzce (DZC).

Figure 2.2 displays the 1200 km long NAF system from the junction with the East Anatolian Fault in the east to the Aegean Sea in the west. The NAF is the result of the collision of the the Asian and African Plates with Eurasia (Jackson and McKenzie, 1988). Africa and Asia move to the north with 10 mm/yr and 25 mm/yr, respectively (DeMets et al., 1994). The different plate velocities results in the left lateral movement along the Dead Sea Transform Fault. The Anatolian block is pushed to the relatively stable Eurasian plate which results in an escape movement

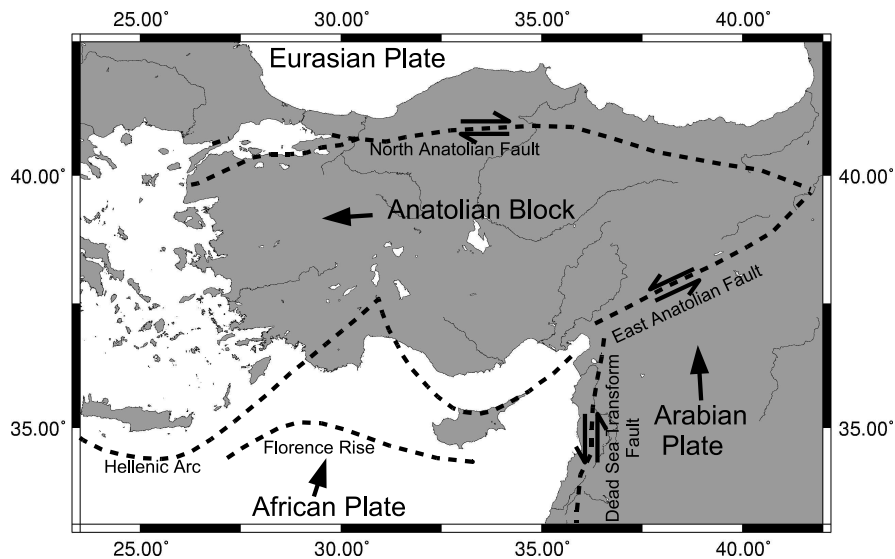


Figure 2.2: Tectonic map of Turkey with the location of the main tectonic features. It shows the Anatolian Block moving to the west due to to movement of the Arabian and African plates to the north. The escape tectonic behaviour of the Anatolian Block produces the right lateral (dextral) North Anatolian Fault and the left lateral (sinistral) East Anatolian Fault.

of Anatolia to the west (escape tectonics). Therefore, the NAF shows right lateral or dextral displacements and the East Anatolian Fault left lateral or sinistral displacements. Meade et al. (2002) and McClusky et al. (2000) found a movement of about 24 mm/yr for the NAF from GPS measurements.

2.2 Observed Ground Motion

The Kocaeli earthquake increased the world wide database of near fault strong motion records significantly, as prior to this event only 10 records for $M_w > 7$ within a distance of 20 km to the fault existed (EERI, 1999) . Six strong motion stations, operated by Kandilli Observatory and Earthquake Research Institute of the Bogazi University, Earthquake Research Department of the General Director of Disaster Affairs and Istanbul Technical University, within 20 km to the fault rupture recorded the earthquake. Table 2.1 gives distance to fault, PGA (Peak Ground Acceleration)and PGV (Peak Ground Velocity) for five stations. When comparing PGA at these stations with the prediction of the relationships proposed by Boore et al. (1997), Campbell (1997) and Sadigh et al. (1997) the observed PGAs seems to be very low (Table 2.2). The 1999 Chi-Chi Taiwan earthquake ($M_w = 7.6$) showed a similar behaviour with low PGA values, but high peak ground velocities (EERI, 1999; Tsai and Huang, 2000; Boore, 2001). Therefore, the Chi-Chi earthquake is characterised as a HV-LA (high PGV, low PGA) earthquake. However, for the Kocaeli earthquake only six strong motion records exist compared to the Chi-Chi event, for which several tens of records exist. For the spare data set of the Kocaeli event the results

Station	Distance to fault [km]	Component	PGA [g]	PGV [cm/s]
Sakarya (SKR)	3.20	EW	0.40	79.8
		NS	-	-
Yarimca (YPT)	3.28	EW	0.23	84.7
		NS	0.32	79.6
Izmit (IZT)	4.26	EW	0.22	54.3
		NS	0.16	32.0
Gebze (GBZ)	7.74	EW	0.14	34.7
		NS	0.26	45.6
Düzce (DZC)	17.06	EW	0.38	49.6
		NS	0.33	60.6

Table 2.1: PGA and PGV for five strong motion stations within 20 km to the rupture plane (after Akkar and Gülkan, 2002).

of the FD modelling provide an alternative explanation for the observed low PGA values. A macroseismic intensity map (MM scale) was published by the Earthquake Research Department of the General Director of Disaster Affairs on the world wide web (also included in Erdik, 2001). The observed macroseismic intensities show values up to X. Maximum intensity of X occur in the epicentral region and along the southern shore of Izmit Bay. Most parts of Izmit Bay show an intensity of VIII to IX. Intensity of IX and X is located in the Adapazari Basin region and near the Düzce fault segment. Intensity VII occur between the epicentral area, the Adapazari Basin and the Düzce basin.

2.3 Modelling

A fourth-order in space and second order in time 3D Finite-Difference (FD) method Olsen (1994) (see chapter 1) is used to model the wave propagation triggered by the Kocaeli earthquake. The modelled region is discretised with $dx = 230$ m and extends in east-west direction over 237 km, over 78 km in north-south direction and into a depth of 31 km. This leads to a total of 72.6 million grid points and approximately 3.5 GB of main memory is required for computing. Minimum shear wave velocity of 1.87 km/s and relation (1.19) yields to a maximum resolvable frequency of 1.25 Hz. The time discretisation according to eq. (1.16) is 15 ms and 5000 time steps are used to simulate wave propagation for 75 s.

The kinematic properties of a fault rupture are used to simulate wave propagation for complex rupture processes (Miksat, 2002). The kinematic parameters are displacements, rise times, rupture directions and rupture velocities on the fault plane. In the case of the Kocaeli earthquake there are several different inverted rupture histories (Bouchon et al., 2002; Delouis et al., 2000; Li et al., 2002; Sekiguchi and Iwata, 2002; Yagi and Kikuchi, 2000). In this study, the inversion results of Bouchon et al. (2002) and Sekiguchi and Iwata (2002) are implemented. Bouchon et al. (2002) applied the full frequency content of the strong motion records from five stations

Site Condition	Distance to fault	Attenuation relationships		
		Boore et al. (1997)	Campbell (1997)	Sadigh et al. (1997)
Moment Magnitude $M_w = 7.6$				
Rock	5 km	0.48 (0.29 - 0.81)	0.51 (0.35 - 0.77)	0.57 (0.39 - 0.84)
	10 km	0.35 (0.20 - 0.58)	0.40 (0.27 - 0.60)	0.44 (0.31 - 0.65)
Soil	5 km	0.62 (0.36 - 1.04)	0.5 (0.34 - 0.74)	0.46 (0.30 - 0.68)
	10 km	0.46 (0.27 - 0.75)	0.45 (0.31 - 0.67)	0.37 (0.25 - 0.57)
Moment Magnitude $M_w = 7.3$				
Rock	5 km	0.41 (0.24 - 0.69)	0.50 (0.34 - 0.74)	0.54 (0.37 - 0.80)
	10 km	0.29 (0.17 - 0.49)	0.38 (0.26 - 0.56)	0.40 (0.28 - 0.60)
Soil	5 km	0.53 (0.31 - 0.89)	0.48 (0.33 - 0.71)	0.44 (0.30 - 0.66)
	10 km	0.38 (0.22 - 0.64)	0.42 (0.28 - 0.62)	0.34 (0.23 - 0.51)
Moment Magnitude $M_w = 6.8$				
Rock	5 km	0.31 (0.18 - 0.53)	0.46 (0.31 - 0.68)	0.50 (0.32 - 0.77)
	10 km	0.22 (0.13 - 0.38)	0.31 (0.21 - 0.47)	0.34 (0.22 - 0.54)
Soil	5 km	0.40 (0.24 - 0.68)	0.44 (0.30 - 0.66)	0.40 (0.26 - 0.62)
	10 km	0.29 (0.17 - 0.49)	0.36 (0.24 - 0.52)	0.30 (0.19 - 0.46)

Table 2.2: PGA [g] mean values and ± 1 standard deviation (in parentheses) according to Boore et al. (1997), Campbell (1997) and Sadigh et al. (1997) for $M_w = 7.6$, $M_w = 7.3$ and $M_w = 6.8$.

(ARC, YPT, IZT, SKR and DZC), which are located all within the model used for the modelling. Sekiguchi and Iwata (2002) used the low frequency content up to 1 Hz of 10 strong motion stations, which is approximately the same frequency range as in our modelling. Fig. 2.3 displays the fault trace, final slip, rupture propagation and rise times on the 155 km long and 17 km deep fault used by Bouchon et al. (2002). Average slip is 2.9 m and maximal slip of 6.82 m occurs near SKR and 6.35 m near Gölcük. The rupture front between 0 and 50 km indicates the inverted super shear rupture velocity of about 4.8 km/s Bouchon et al. (2001). The inverted rise times vary between 1 and 5 s, and are about 3 s for the areas of large slip. The fault trace, slips, rupture front and rise times used and calculated by Sekiguchi and Iwata (2002) are displayed in Fig. 2.4. There are three fault areas with relative large final slip values. Maximal final slip of 7.5 m occurs west of the hypocentre in a depth of 15 km. A Slip of 6.5 m is derived 45 km east of the epicentre at the surface near the strong motion station SKR in the Adapazari Basin and a slip of about 5.6 m occurs at the fault's bottom 18 km east of the epicentre. Some parts show medium values and some no or very small slips. Average slip across the fault plane is 1.5 m. Average rise time is 2.2 s, but average rise time west of epicentre is larger than east of the epicentre. Rise time in the area of maximum slip west of the epicentre and at the fault's bottom 18 km east of the epicentre is about 4 s. The region of large slip at the surface near SKR shows a rise time of 2 s. The position of the rupture front gives larger rupture velocity of 5.4 km/s for the first 40 km east of the hypocentre compared to the propagation towards the west with 3.1 km/s. Because of restriction of the FD code to faults parallel to the FD grid only, the eastern north-east striking segment (Düzce segment) is omitted in both cases and the western segments are

assumed as one single east-west striking fault (indicated in Fig. 2.3 and 2.4). This simplification has a negligible influence on the ground motion in the centre and western parts, because the ground motion parameters, such as PGV and intensity, at a certain location are mainly controlled by the characteristic rupture features on the nearest parts of the fault plane. This is shown by Goto and Sawada (2004), and Goto et al. (2005) in modelling the special features of an observed strong motion record by using only the information of a relatively small fault element near the corresponding strong motion station.

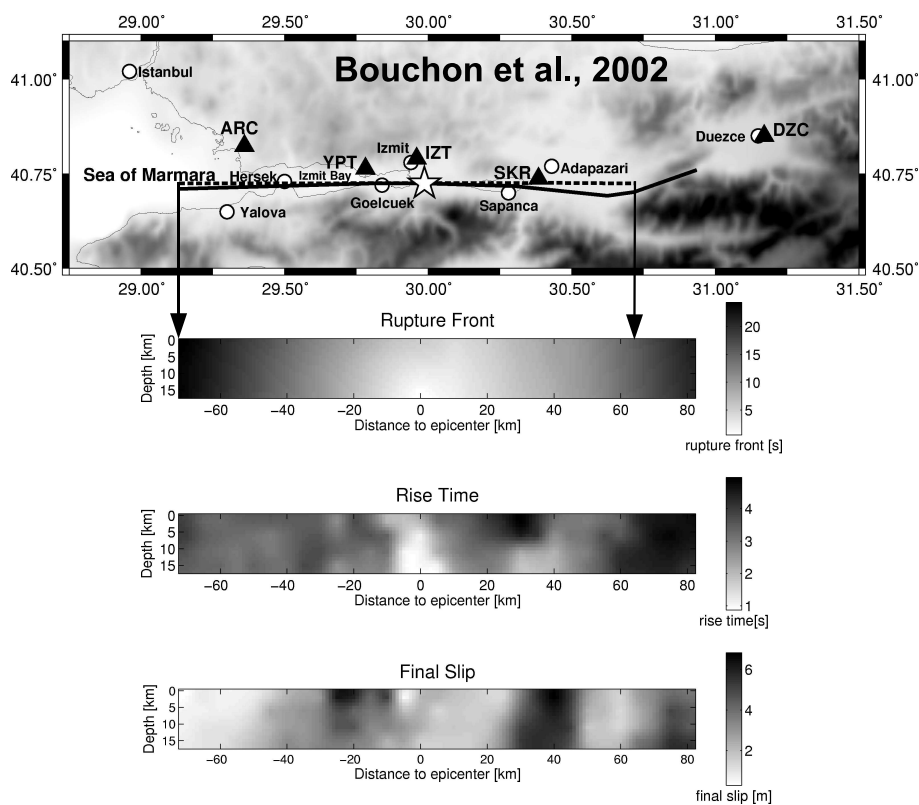


Figure 2.3: Fault trace used by Bouchon et al. (2002) (solid) and fault trace used for modelling (dashed). Black triangles depict strong motion stations. Propagation of rupture front, rise times and final slips on the fault derived are displayed at the same position as the fault plane. The arrows mark the part fault that is implemented into the modelling.

A simple elastic underground model was designed that comprises the large and characteristic structures of the region. These are the mountain (hardrock) regions, the sediments beneath the Sea of Marmara and beneath the Izmit Bay, the sedimentary Adapazari Basin and narrow sedimentary belt which connects the latter two (Fig. 2.5). The bedrock is dipping vertically in the south and depth decreases towards the north. The P-, S- wave velocities and the density (Table 2.3) are assigned after the horizontally layered model of Ergin et al. (1998), which is in good agreement with the 2D model of Karahan et al. (2001) that resulted from a refraction seismic

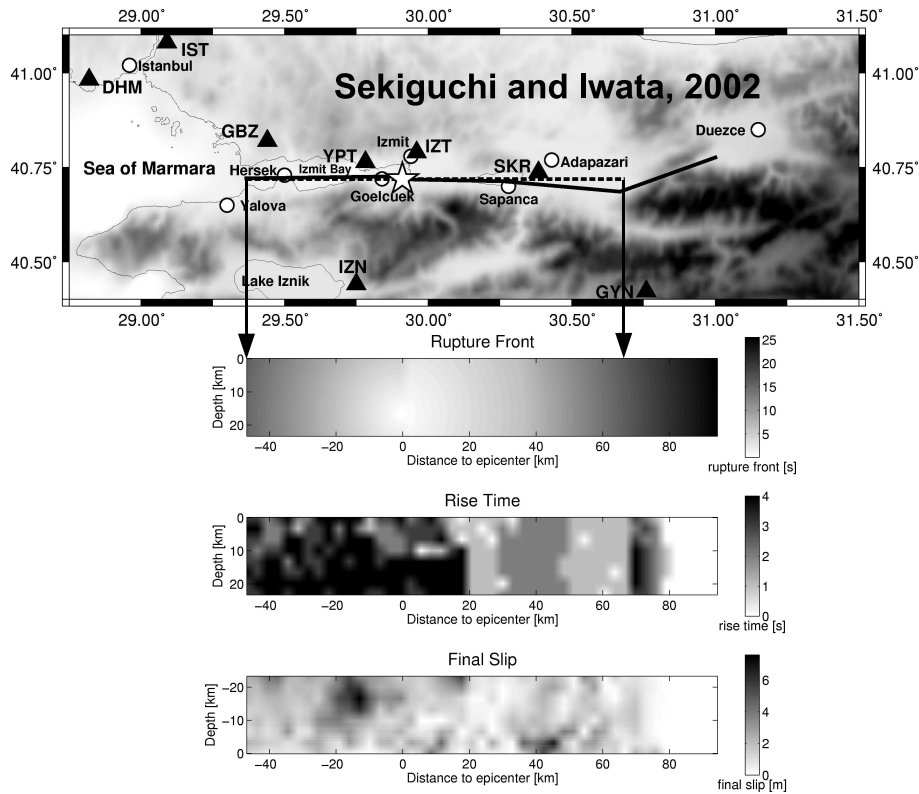


Figure 2.4: Fault trace used by Sekiguchi and Iwata (2002) (solid) and fault trace used for modelling (dashed). Black triangles depict strong motion stations. Propagation of rupture front, rise times and final slips on the fault derived are displayed at the same position as the fault plane. The arrows mark the fault extend used for the modelling.

campaign across the Adapazari basin. Due to the grid spacing of 230 m the shallow water layer of the Sea of Marmara can be neglected. The topography of the region cannot be considered by the FD code. This is no drawback as the topography is only important when modelling the accurate ground motion for a specific point in a mountain region, because topography influences the small scale (extend of mountain ranges and valleys up to 10 km) distribution and not the overall pattern, which is mainly influenced by large subsurface structures. Additionally, the low frequency range (< 1.5 Hz), which is used here, is not very sensitive to small topographic features.

2.4 Linking Ground Motion and Intensity

Many scaling relations linking parameters of accelerations and intensity have been developed (Trifunac and Brady, 1975; Murphy and O'Brien, 1977; Chernov and Sokolov, 1983; Aptikaev and Shebalin, 1983). After Sokolov (2002) macroseismic intensity (MM scale) is linked with the amplitudes of Fourier acceleration spectra (FAS) between 0.2 - 15 Hz. Each intensity value is

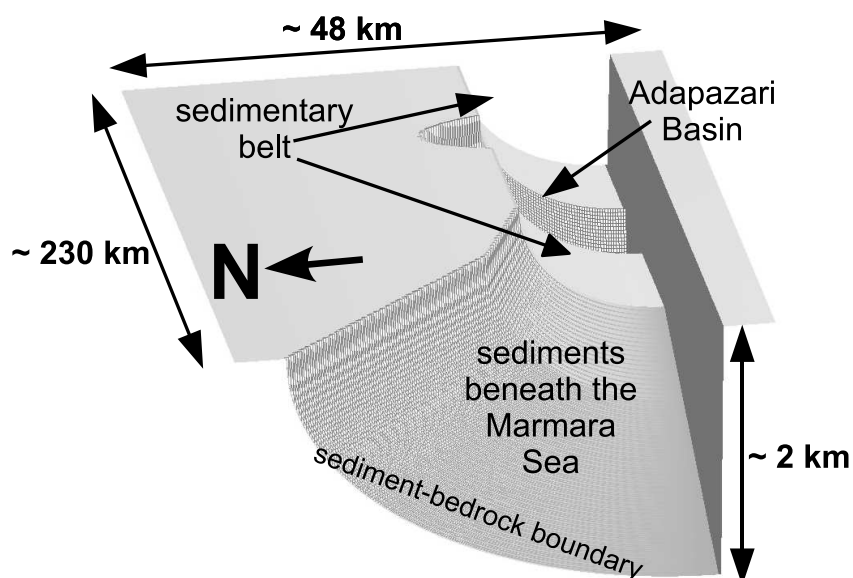


Figure 2.5: Uppermost part of the model of the region. The grey surface marks the boundary between sediments and bedrock. The model includes the sediments of the Sea of Marmara, the Adapazari Basin and a narrow east-west orientated sedimentary belt.

Layer	v_p [km/s]	v_s [km/s]	density [g/cm^3]
Sediment	3.34	1.87	2.2
Bedrock	5.94	3.32	2.4
13 km to 25 km depth	6.51	3.64	2.6
25 km to 32 km depth	6.66	3.73	2.8

Table 2.3: Velocities and densities of the 3D elastic model.

assigned to a certain frequency range ('representative frequencies'). Thus, intensities III-IV MM are connected to the representative frequencies between 5 - 10 Hz and for intensities VIII-IX MM the representative frequencies lay below 2 - 3 Hz. The standard algorithm for calculating macroseismic intensity needs the whole frequency range (0.13 - 12 Hz) (Sokolov, 2002; Sokolov and Wald, 2002). Here, the standard procedure cannot be used, because the maximum frequency of the synthetics is 1.25 Hz. In comparing the modelled and observed seismograms with the Fourier amplitude spectra of the different intensity values a simple straightforward way is used. However, the error for intensities more than VII MM does not exceed 0.5 intensity units. In Fig. 2.6 the observed and synthetic amplitude spectra at IZT is shown with the representative Fourier acceleration spectra. For all synthetic seismograms the Fourier amplitude spectra is compared with the reference spectra and an intensity value is assigned according to the level of the synthetic spectra.

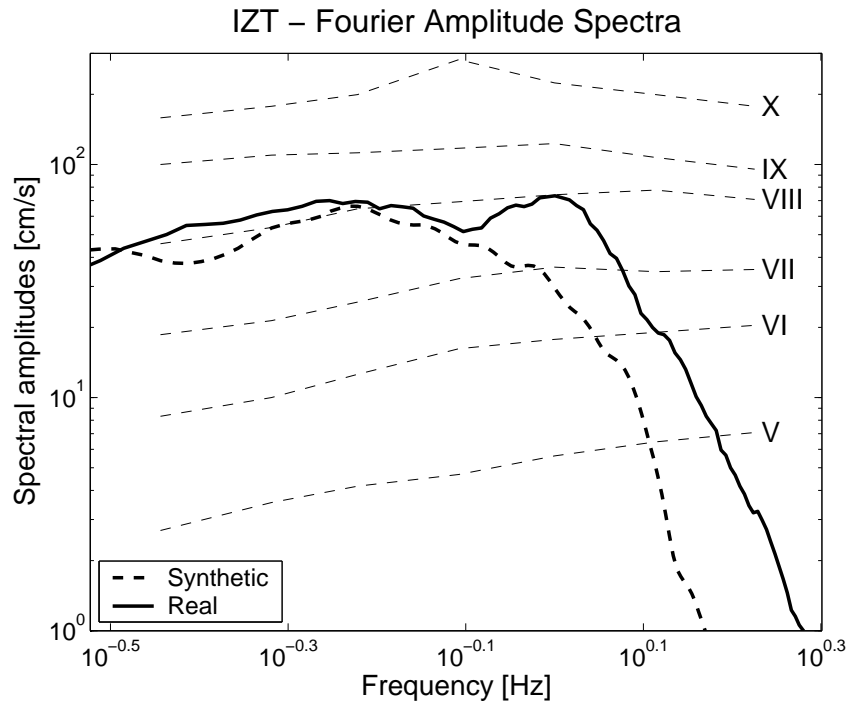


Figure 2.6: Fourier amplitude spectra for intensities V - X (MM) after Sokolov (2002) with the observed and synthetic spectra at IZT. The levels of both spectra indicate an intensity of VIII.

2.5 Modelled Ground Motions resulting from the Rupture Process of Bouchon et al. (2002)

The modelled PHV (peak horizontal velocities) map is shown in Fig. 2.7. The complex rupture process produces an inhomogeneous distribution of PHV values. The distribution is strongly influenced by the underground structure, slip amount and rupture velocity. The transition from sediment to bedrock in the south acts as a sharp boundary for the PHVs. Thus, PHV values decrease from 1.4 m/s to 0.8 m/s and 2 m/s to 1 m/s at the southern sediment bedrock boundary near Izmit and the Adapazari Basin, respectively. Slip of 5 m near Hersek Peninsula produces PHV values of about 2 m/s along the southern shore of Izmit Bay. Directivity effects due to the bilateral rupture process and large rupture velocities east of the epicentre produce relatively large ground motions east and west of the fault line. Within the Adapazari Basin maximum PHV is 2.3 m/s, which is due to large slip values of 5 to 6 m and the amplifying thick sediment cover. The sediment belt is orientated parallel to the fault and acts therefore as a perfect wave guide that transports the seismic energy over long distances.

The modelled PHV distribution shows that the rupture process controls the origin of strong ground motions. The sediments amplify and distribute the spatial distribution of ground shaking. Remarkably, none of the five strong motion stations is located within an area of large PHV. Even YPT and IZT, which are located very close to the fault, miss the areas of strong ground motion. This shows that the details of an earthquake rupture and the actual distribution of seismic stations

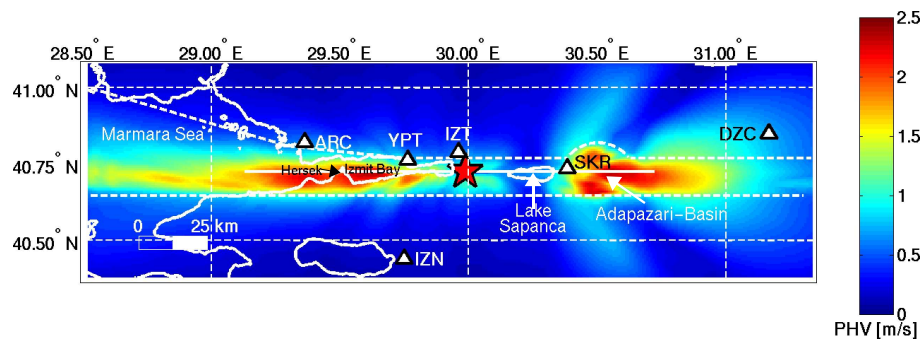


Figure 2.7: PHV distribution obtained by using the rupture process of Bouchon et al. (2002) for simulation. White dashed lines are the bedrock-sediment boundaries and the triangles depict strong motion stations. Rupture directivity and wave guide effects of the sediments yield to large values east and west of the fault. No strong motion station is located within an area of large PHV.

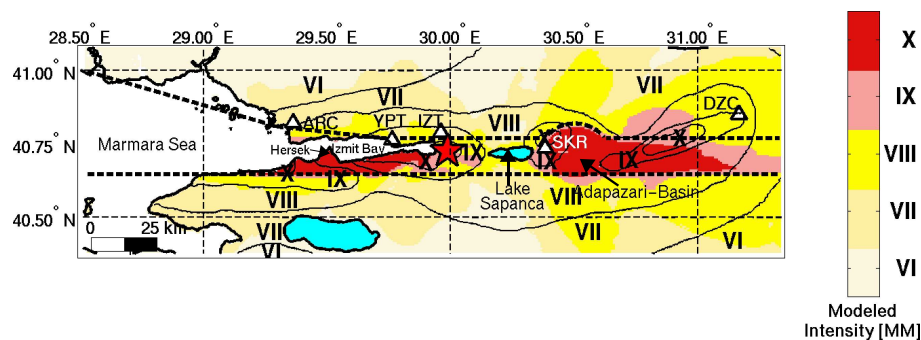


Figure 2.8: Calculated macroseismic intensities (coloured) estimated from Fourier Acceleration Spectra after Sokolov (2002). Comparison with the observed values (dashed lines) show a good fit in the epicentral region, the coast of Izmit Bay and the Adapazari Basin.

influence the observed ground motions and therefore the empirical database of near fault strong motion records, which anyway contains only a few near fault records for large earthquakes (see 2.2).

In Fig. 2.8 the observed and modelled/synthetic macroseismic intensities are compared. The observed macroseismic intensities were digitised from a map which was published by the Earthquake Research Department of the General Director of Disaster Affairs in Ankara (see Erdik, 2001). Large synthetic intensities are calculated for the Izmit Bay and the eastern part of the fault including the Adapazari Basin. Synthetic intensity in the epicentral area is IX, the observed value is X. The southern shore of Izmit Bay suffered from intensities between XIII and X, which is in good comparison with the modelled values (IX to X). Synthetic and observed intensity in the central part, between the epicentre and the Adapazari Basin, is VIII. Discrepancies between observation and modelling increase with increasing distance to the fault. East of the epicentre the observed and modelled intensities are comparable up to a distance of 25 km. In the central part the modelled intensities decrease more rapidly with distance to the fault than the observed ones.

Along the eastern part of the fault the modelled values decrease more rapidly than the observed intensities. Thus, the modelled intensities fit the observed ones up to a fault distance of 10 - 25 km along the whole fault trace, this is the same distance range as for the strong motion stations used for the rupture inversion.

Synthetic and observed seismograms are compared for the five stations, which were used by Bouchon et al. (2002) to invert the rupture process (Fig. 2.9). The records were provided by Prof. Polat Gülkan (Middle East Technical University, Ankara, Turkey) and the European Strong Motion Database (Ambraseys et al., 2000). The modelled seismograms must fit the observed records, which were used by Bouchon et al. (2002). But differences may occur because of the different velocity structures used for inversion and modelling. The synthetic and observed records are bandpassfiltered between 0.02 and 1.25 Hz. The first 5 s of the EW component at ARC show a good comparison. The modelled waveform of the NS component follows the observed one, but underestimates the amplitude. The horizontal components of YPT, IZT and SKR show a good comparison between the synthetic and observed data. The Z component of SKR also matches the recorded data. At DZC the waveforms fit only for the first 3 to 5 seconds and the observed amplitude are underestimated by the modelling. This is due to the neglect of the eastern fault segment that runs near this station. Generally, the maximum amplitudes and the waveforms during the first 5 to 10 seconds coincide.

2.6 Modelled Ground Motions resulting from the Rupture Process of Sekiguchi and Iwata (2002)

The PHV distribution produced by the rupture process of Sekiguchi and Iwata (2002) is shown in Fig. 2.10. Maximum PHV of about 5 m/s occurs in the Adapazari Basin. This large value is produced by the large final slip values at the fault's bottom 40 km east of the epicentre (Fig. 2.4). The whole area around the fault east of SKR is affected by large PHV values. The southern coast near Hersek Peninsula shows values up to 2.5 m/s and only moderate values up to 1.5 m/s occur between the Hersek Peninsula region and station SKR. The larger PHV are restricted to small regions because only small parts of the fault show large slip values (Fig. 2.4), which are capable to produce large PHV. Large PHV are restricted to the sediment belt. It acts as a wave guide that transports ground motion energy to the west and the east of the model area. Again, no station is located within an area of large ground motion. SKR is the only station that is located near an area of large PHV.

Macroseismic intensities between IX and X are calculated for the whole sedimentary region east of the epicentre. Calculated intensities vary between VIII and IX around Izmit Bay and values from VIII and X occur between 30°E and 30.5°E outside the sediment belt. Generally, intensities larger than VII occur in the whole model east of the epicentre, whereas the western part of the model shows significantly lower values. Except for the Adapazari Basin and the epicentral region there is no clear correlation between observed and modelled macroseismic intensities. Modelled intensity at SKR is IX and VI to VII for the other stations. Remarkably, there is no strong motion station within an region of maximum modelled intensity.

Eight of the strong motion stations used by Sekiguchi and Iwata (2002) for inversion are located within the modelled region. The observed and modelled seismograms at the digital stations (DHM, IST, SKR and YPT) are compared between 0.1 and 1 Hz (Fig. 2.12). All three components at DHM and IST show a good agreement between real data and modelling. At SKR the modelled velocities overestimate the observation, however they have the same pattern. At YPT the modelling underestimates the observation, but here Sekiguchi and Iwata (2002) used an extremely low surface velocity of 330 m/s compared to 1.87 km/s for the FD modelling. Therefore, it is not possible to reproduce the amplitudes generated by this low velocity layer. Modelled and real records for the analog stations are given in Fig. 2.13. The horizontal components at GBZ show a good fit, and the first seconds of the Z component. At GYN only the first seconds of the NS component give a good match and the horizontal components of IZN and IZT show similarities for the first 5 to 10 seconds. In most cases the modelling reproduces the observed amplitudes.

2.7 Comparison of Ground Motions resulting from Bouchon et al. (2002) and Sekiguchi and Iwata (2002)

The PHV distribution of both rupture models is strongly controlled by the rupture properties and therefore the modelling results in different PHV distributions. Sekiguchi's model shows two small areas with large PHV (up to 5 m/s) and in Bouchon's case a larger area is affected by large PHV with a maximum of 2.3 m/s. Looking at the inverted rupture parameters, Sekiguchi's model show extremely large slip values on small parts and in Bouchon's case a larger part shows relatively large slip values (Fig. 2.3 and 2.4). Amplitude of the radiated wave is controlled by particle velocity \dot{D} at a certain point of the fault (see eq. (1.28) with $\dot{M}_{kj} = \mu A \dot{D} (l_k n_j + l_j n_k)$ after eq. (1.23) for M_{kj} and eq. (1.24) for the scalar moment), which is slip divided by rise time. For the large slip areas near Gölcük (6.82 m) and near SKR (6.35 m), Bouchon's model show average rise times of 3 s. Therefore, the largest amplitudes are produced there. In Sekiguchi's model the rise time for the large slip region (up to 6.5 m) near SKR is only 2 s. Consequently, the particle velocity is larger than in Bouchon's model and the rupture produces seismic waves with larger amplitudes compared to Bouchon's model. In both cases the rupture velocity yield to directivity effects and therefore to the smearing of the ground motion from the large slip regions to the eastern and western fault ends. The modelled seismograms show a good fit with the observed data. Differences occur because of the different velocity models used for modelling and inversion and the simplified single fault segment in the modelling compared to the more detailed fault trace used for inversion. In terms of suitability of the modelling for hazard assessment it is important to notice that the modelling reproduces the observed maximum ground motion amplitudes.

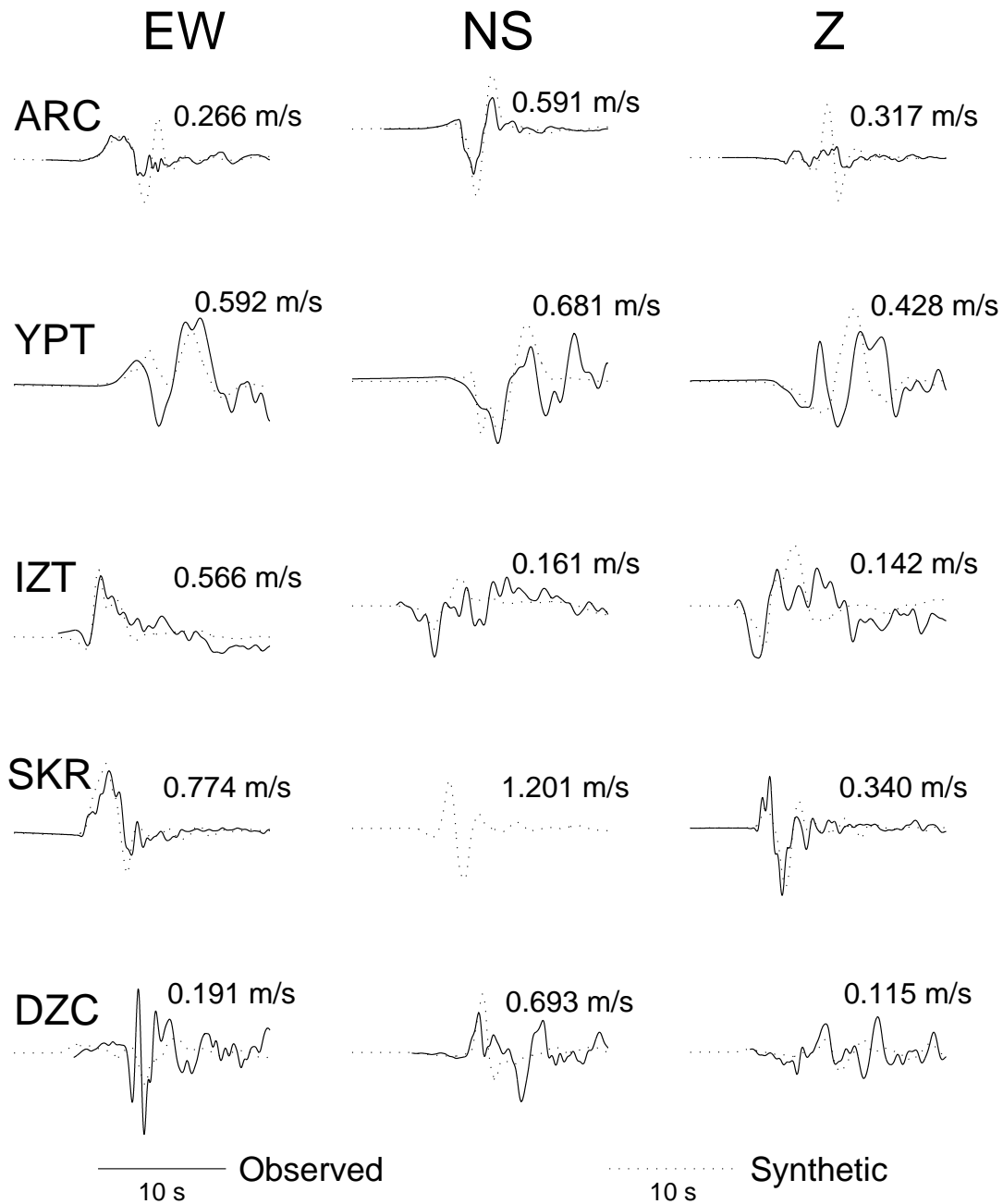


Figure 2.9: Comparison between the observed (solid) and modelled (dashed) seismograms at the strong motion stations used by Bouchon et al. (2002) to invert the rupture process. The numbers indicate the modelled peak velocity for each record. The horizontal components at YPT, IZT and SKR show a good fit, at ARC the first second coincide for the EW component and the waveform for the NS component. At DZC modelling and observation show a good fit for the first seconds only, because of the neglect of the eastern fault segment.

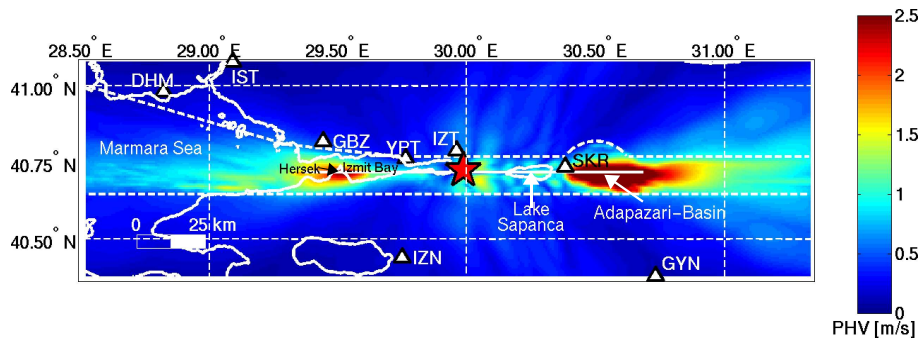


Figure 2.10: PHV distribution obtained by using the rupture process of Sekiguchi and Iwata (2002) for simulation. White dashed lines are the bedrock-sediment boundaries and the triangles depict strong motion stations. Rupture directivity and wave guide effects of the sediments yield to large values east and west of the fault. No strong motion station is located within an area of large PHV.

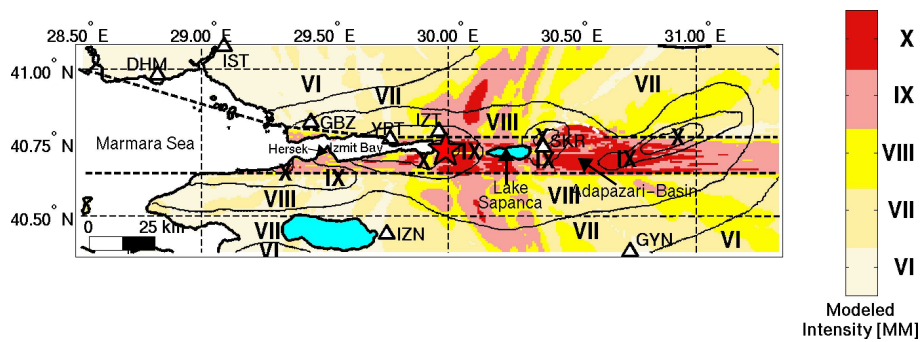


Figure 2.11: Calculated macroseismic intensities (coloured) from Fourier Acceleration Spectra Sokolov (2002). Comparison with the observed values (dashed lines) show a good fit in the epicentral region, the coasts of Izmit Bay and the Adapazari Basin.

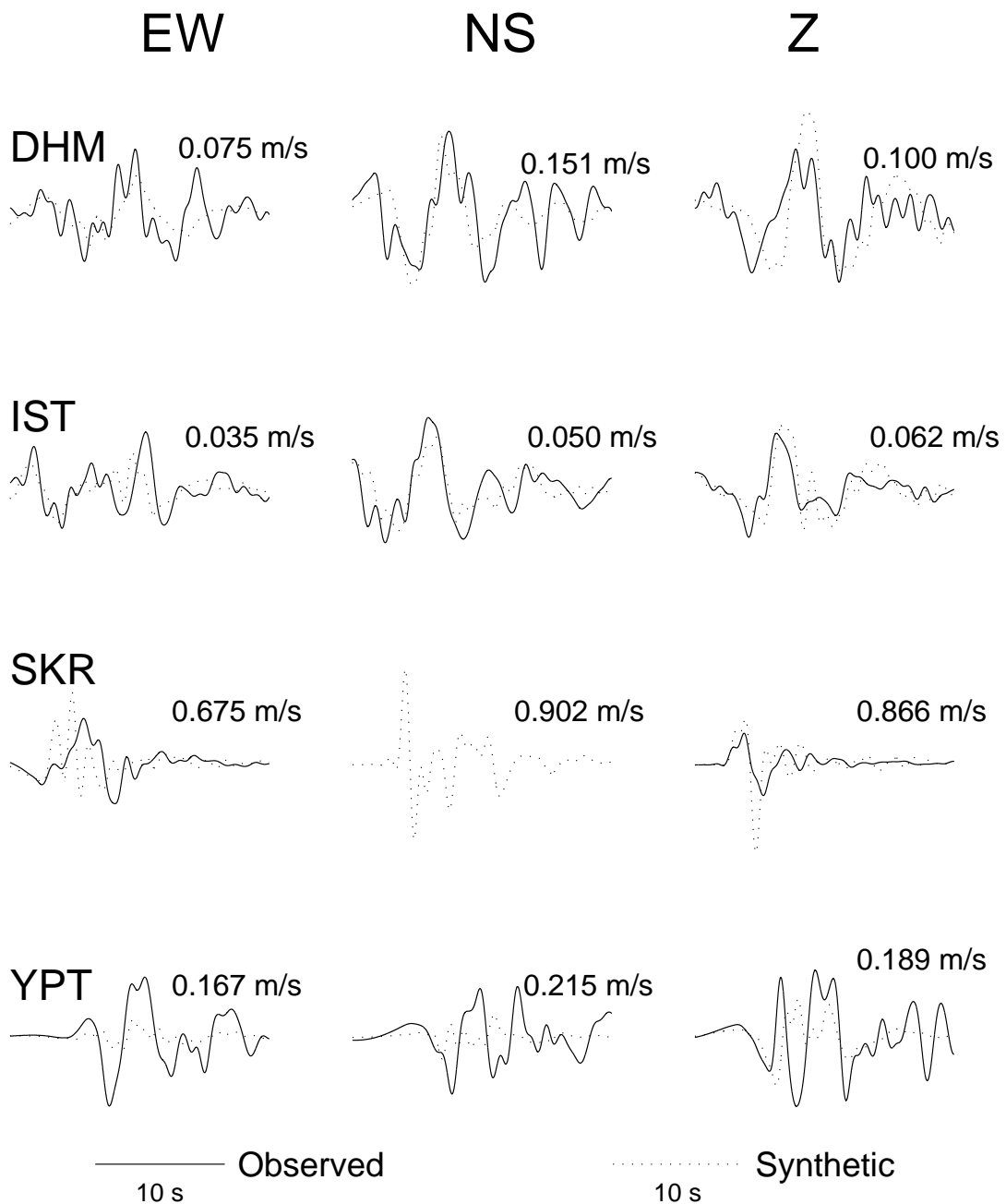


Figure 2.12: Modelled (dashed) and observed (solid) velocities with peak velocity of the modelled seismogram at the digital stations for the rupture process of Sekiguchi and Iwata (2002). At DHM and IZT all three modelled components match the records. At SKR the modelled velocities are too low and at YPT the modelled values overestimate the observation. At YPT this is due to the low surface velocity used for inversion.

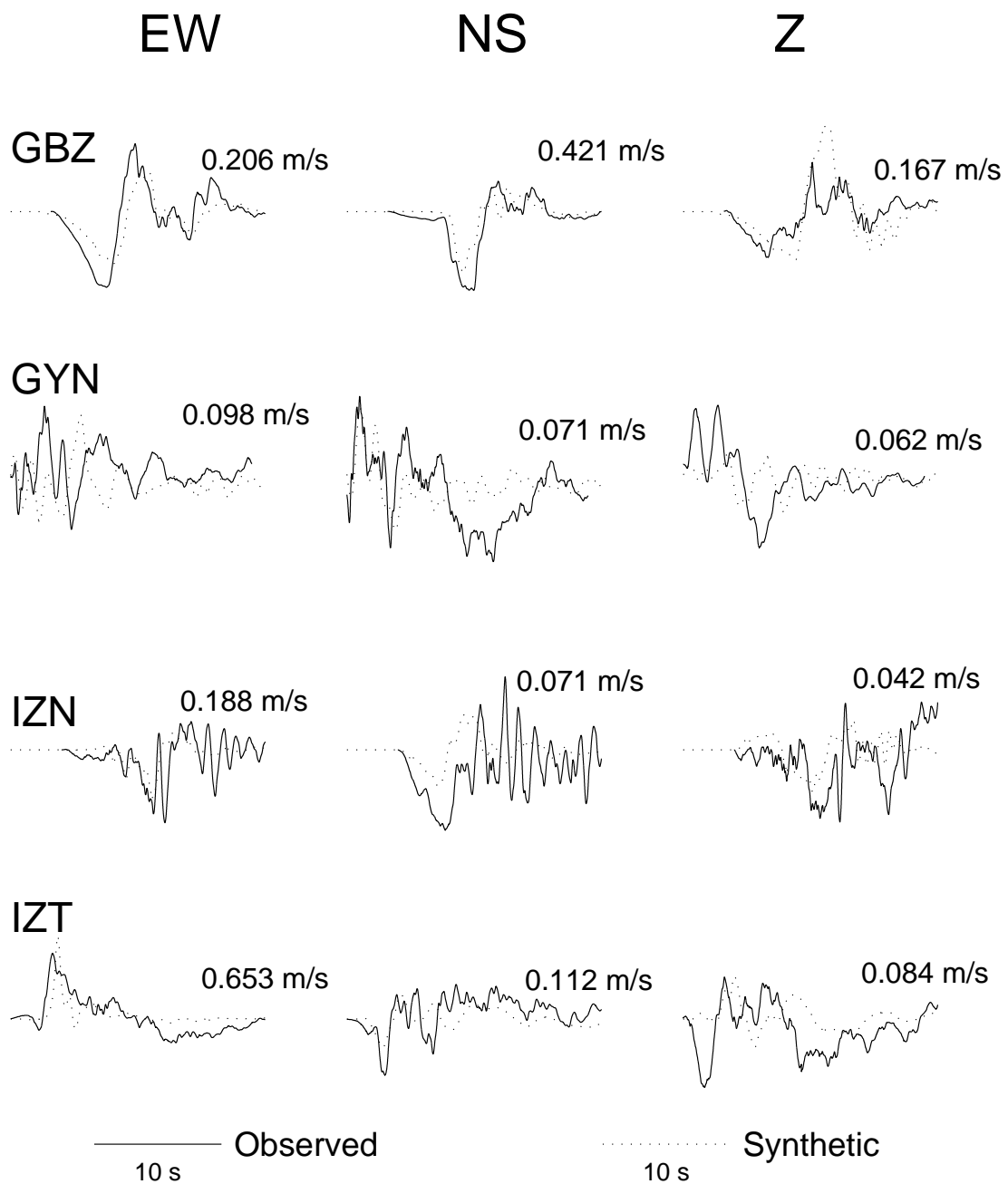


Figure 2.13: Synthetic (dashed) and observed (solid) seismograms at the analog stations for the rupture process of Sekiguchi and Iwata (2002). Peak values are given for the modelled velocities. Horizontal components of GBZ, IZN and IZT give a good comparison. At GYN the first seconds of NS component are comparable.

2.8 Conclusions

By applying inverted rupture histories the FD modelling reproduced the observed peak values and the seismograms at stations which were used to invert the rupture process. This shows the reliability of the modelling and the capability to simulate not only past but also potential future earthquakes. The calculations also demonstrate the complex near fault ground motion distribution produced by the Kocaeli earthquake, which means that some regions suffer from large ground motions whereas other areas, which might be located even closer to the fault trace, show almost no or moderate ground shaking. And remarkably, no strong motion station is located in an area of maximum ground motion. This might explain the observed surprisingly low PHA of the Kocaeli event. Recently, the observation of the Parkfield 2004 event (Shakal et al., 2006; Bakun et al., 2005) point into the same direction. This was the first time an earthquake was densely recorded in the near fault area with eight stations within 1 km of the rupture and 40 stations within 1 to 10 km. The observed ground motions also showed large spatial variations in the observed amplitudes. Therefore, the development of near fault attenuation relationships for large shallow earthquakes, which are based usually on observed strong motion data, has a large uncertainty of the expected ground motion for an specific scenario at a specific point. Thus, the development of attenuation relationships for the near fault part should be done with a stringent error estimate based on the uncertainties produced by the complex distribution of rupture parameters on the fault plane. The records of the Kocaeli earthquake, which doubled the database on near fault observations, should be used with great caution, because they may lead to an underestimation of expected ground motions in the near fault area.

For the modelling of future earthquakes, a detailed kinematic rupture history is naturally not available. Here, a homogenous rupture model can be used, but this gives only average ground motions at a specific point which may significantly under- or overestimate the ground motion during the real event. Another method is dynamic modelling (Peyrat et al., 2001), but here the resulting ground motions depend strongly on the exact knowledge of the stress distribution on the fault before the earthquake takes place and the applied friction laws. There are several studies how to develop rupture processes for scenario earthquakes which are consistent with observed past earthquakes (Mai and Beroza, 2002; Guatteri et al., 2003, 2004). As also shown in this study on the Kocaeli earthquake, Guatteri et al. (2003, 2004) emphasise that attenuation relationships (e.g. Boore et al., 1997; Campbell, 1997; Sadigh et al., 1997) are fully inadequate for the near fault area (<10 km) as the near fault strong ground motion strongly depends on the slip, rise time and rupture velocity distribution on the fault. Guatteri et al. (2003) suggest a physically consistent pseudo dynamic method to calculate rupture processes for scenario earthquakes. Starting from a generated stochastic slip distribution of a target earthquake, which is consistent with past earthquakes (e.g. after Mai and Beroza (2002)), they calculate physically consistent kinematic rupture properties (rupture speed, slip and rise time). This results in realistic rupture scenarios compared to a fully kinematic approach where the rupture velocities, slips and rise times are often set as independently and therefore not physically consistent. Therefore, the pseudo-dynamic method can be applied to develop likely scenarios of potential future earthquakes. Mai et al. (2006) started to develop source models for potential earthquakes in the Marmara Sea. It is important to note that

the exact distribution of the kinematic parameters of a future earthquake cannot be calculated in advance. Hence, modelling near fault strong ground motion for a future earthquake always means simulating several different rupture scenarios. By applying several likely rupture scenarios ground motion modelling can identify regions which may suffer from large ground motions and the modelling helps to find underground structures which influence wave propagation and the resulting surface ground motion distribution. Applying such a modelling procedure would help to be prepared for the ground motions expected for future earthquakes and in the Turkey case, for the expected earthquake near Istanbul.

Chapter 3

Wave Propagation Modelling of the Vrancea Strong Earthquakes

3.1 Introduction

This chapter presents a 2.5D and 3D FD wave propagation modelling method for the Vrancea strong earthquakes. As a case study, the simulation of the 1986 strong earthquake ($M_w = 7.1$) is performed and analysed. Valuable insights into the Vrancea strong earthquakes in general are gained by the modelling of the 1986 earthquake, as all earthquakes occur in a very confined volume, show similar focal mechanism and produce similar ground motion patterns. The subsurface structure of the region is adopted from Martin et al. (2005, 2006). In order to model realistic seismograms stochastic velocity perturbations are added to the model. To explore the influence of the subsurface structure and the source on the simulated ground motion, modelling is performed for varying underground models. The developed procedures to simulate 2.5D and 3D FD wave propagation, which are explained in this chapter, build the basis for the hybrid strong ground motion modelling of the Vrancea strong earthquakes presented in the next chapter.

A first seismogram modelling of a Vrancea strong earthquake was done by Hartzell (1979). He used a GRT (generalised ray theory) method to explain the seismograms in Bucharest of the 1977 earthquake. Due to the limitations of the method and the limited knowledge of the underground structure a simple layered subsurface model was used. In contrast, by applying a FD method, wave propagation can be modelled for arbitrary complicated subsurface structures. In this work 2.5D and 3D FD simulations are carried out for a very detailed underground structure, which is based on many different geophysical methods and campaigns (Martin et al., 2005, 2006). With the detailed knowledge of the underground structure FD simulations allow to understand wave propagation within this complex region formed of deep sedimentary basins, mountain roots and a subducted lithospheric slab in the mantle.

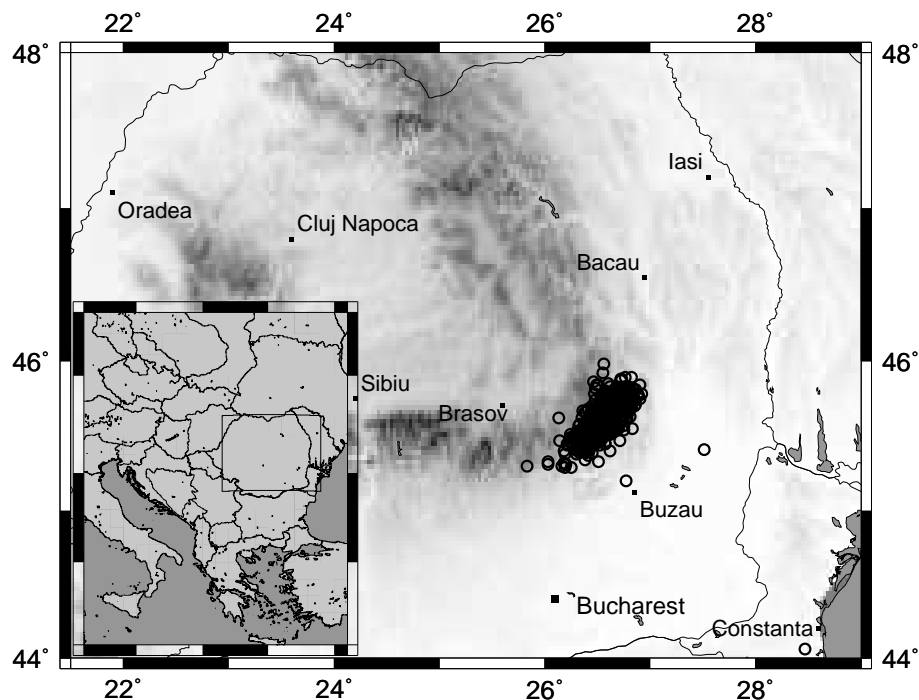


Figure 3.1: The map shows all earthquakes between Jan. 1, 2000 and 2004 that are deeper than 70 km. All these earthquakes occurred in a very confined volume beneath the SE Carpathian Arc.

3.2 Historical Seismicity and Tectonics

Seismicity in Romania is divided into a crustal domain with lower magnitudes and an intermediate depth domain, where all strong earthquakes are located. The mid depth earthquakes are confined to a small volume of 40 km to 80 km horizontal extension and to a depth between 70 km and 180 km beneath the Vrancea region in the SE Carpathians (Fig. 3.1). The seismicity beneath Vrancea is associated with a subducted and detached lithospheric slab. Sperner et al. (2001) describe the geodynamic evolution of the region beginning with active subduction along the whole Alpine-Carpathian belt during Cretaceous. The continent-continent collision in the Alps during Mid-Eocene stopped the subduction process there, but it continued eastwards in an embayment of the European platform (slab retreat). The embayment was filled by two separate blocks which collided with the East European Platform first in the North then in the South. Consequently, subduction stopped and slab break-off occurred first in the North and migrated to the SE. Today, beneath the SE Carpathians the last stage of the subduction process takes place with the detachment of a last segment (Sperner and the CRC 461 Team, 2005).

The Vrancea region in Romania shows the fourth highest seismic energy release rate in Europe (Wenzel et al., 1999). Past earthquakes caused many casualties and large damages. For example, the $M_w = 7.7$ event in 1977 produced large damage in the Romanian capital Bucharest where 1570 people were killed and 11300 were injured (Wenzel and Lungu, 2000; Cioflan et al., 2004).

Year	Day	Time (UTC)	Strike	Dip	Rake	M_w	Lat.	Lon.	Depth
1940	Nov. 10	01:39	224	62	76	7.7	45.8	26.70	150.0
1977	Mar. 4	19:21	225	65	85	7.4	45.77	26.76	94.0
1986	Aug. 30	21:28	226	64	107	7.1	45.52	26.49	131.0
1990	May 30	10:40	236	63	101	6.9	45.83	26.89	90.9

Table 3.1: Strong earthquakes during the 20th century with source parameters, longitudes, latitudes and depths (after Oncescu et al., 1999).

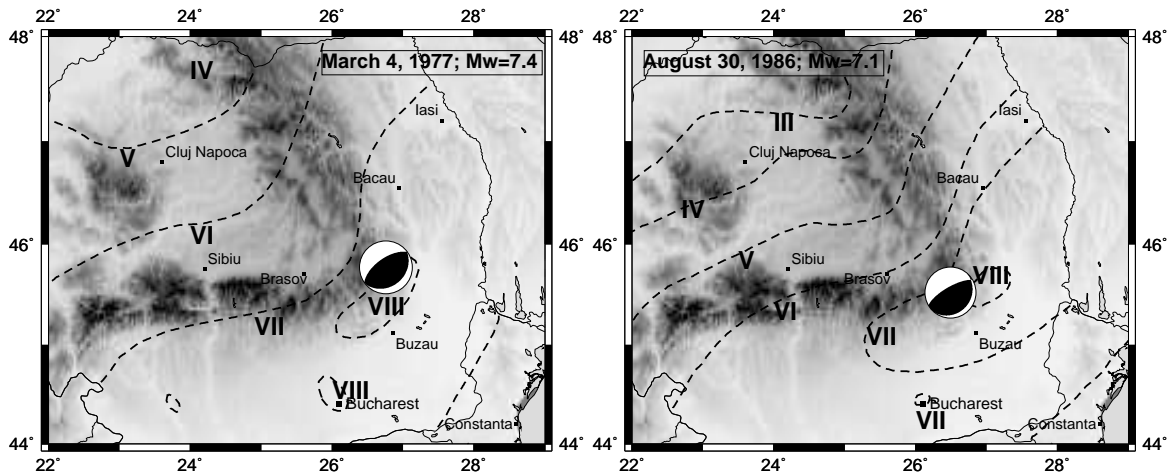
During the 20th century four strong earthquakes occurred with moment magnitudes from 6.9 to 7.4 (Tab. 3.1). Historical records show one to five earthquakes with $M_w \geq 7$ per century (Oncescu et al., 1999). All Vrancea events larger than $M_w = 7$ show reverse faulting with NE-SW striking faults compared to smaller earthquakes which also show NW-SE striking reverse faulting. All these strong events produced intensities of VIII about 50 to 100 km east of the epicentre (Fig. 3.2 after Radu et al., 1979, 1987; Radu and Utale, 1990). The Bucharest region was affected by intensities of VIII and VII during the 1977 and 1986 events, respectively. The isoseismals show an SW-NE elongated oval shape. A comparison of the intensities in SE and NW direction shows that the intensity decrease with distance is stronger towards the NW. It seems that the oval patterns during the 1977 earthquake is stretched to the SW, whereas the intensity pattern of the 1977 is stretched to the NE. This is probably produced by directivity effects due to the opposite rupture propagations during these earthquakes. Different directivity effects are also discussed for the 1940 and 1977 earthquakes (Hartzell, 1979).

3.3 Subsurface Structure

For FD simulation of wave propagation within isotropic media the knowledge of the Lamé constants (λ and μ) and of the density ρ is essential (see eqs. 1.13 and 1.14). The applied FD codes use eqs. (1.7) and (1.8) to calculate the Lamé constants from the P- and S-wave velocities. The P-wave velocity structure of SE Romania is described in the next section. The calculation of S-wave velocities and densities from the P-wave velocities is given in section 3.3.2. Section 3.3.4 shows the applied Q structure and explains the method used to implement intrinsic attenuation.

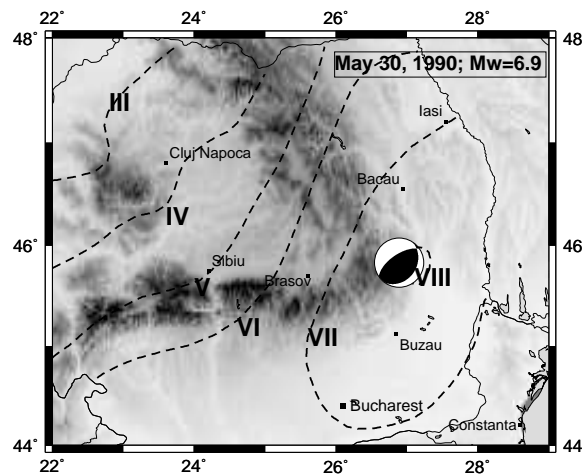
3.3.1 P-wave velocity structure

In the frame of the CRS 461 two deep seismic sounding experiments and a seismic tomography campaign were carried out to reveal the underground structure of SE Romania. During the deep seismic sounding experiments VRANCEA99 and VRANCEA2001, seismometers were



(a) Macroseismic Intensities; March 4, 1977

(b) Macroseismic Intensities; August 30, 1986



(c) Macroseismic Intensities; May 30, 1990

Figure 3.2: Maximum intensities were observed about 50 to 100 km east of the epicentre at all three Vrancea strong earthquakes during the 20th century. During the 1977 and 1986 earthquakes the Bucharest area was affected by an intensity of VIII and VII, respectively. The isoseismals of the Vrancea earthquake are elongated in SW-NE direction. Furthermore, the intensities show a stronger attenuation towards the NE direction compared to the SE direction.

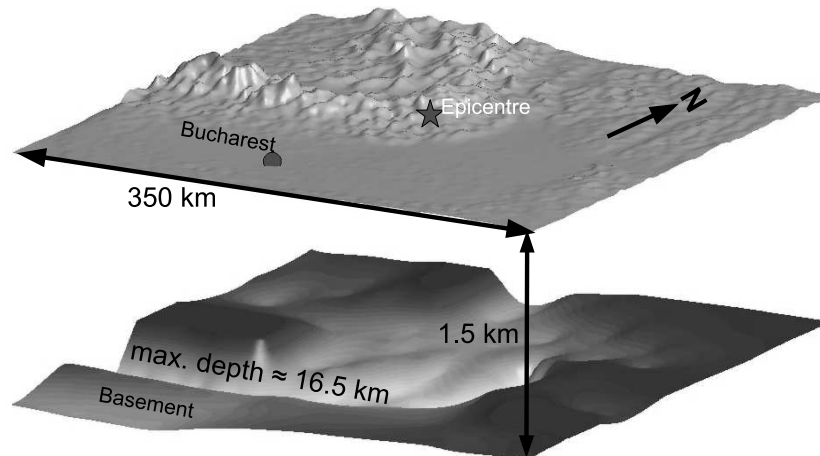


Figure 3.3: Topography and basement structure of SE Romania. The displayed topography and basement structures are 350 km x 350 km wide and centred at the epicentre of the 1986 Vrancea strong earthquake (star). A deep foreland basement is located south of the Carpathians and east of the SE Carpathian Arc. Maximum basement depth is about 16.5 km.

deployed along two profiles across the Carpathians. The resulting crustal structure is predominantly based on these long range seismic refraction lines (Hauser et al., 2001, 2002, 2003), 3D refraction tomography (Landes et al., 2004) and receiver function studies (Diehl et al., 2005). The results reveal Moho depths between 33 and 43 km along the seismic refraction profiles and depths between 28 and 46 km at the seismic stations used for receiver function analysis. Near-surface P-wave velocities show values of about 5.5 km/s across the Carpathians and 4 to 5 km/s in the foreland basins. Martin et al. (2005) combined the results of the different methods to compile a 3D P-wave velocity model of the crust. Fig. 3.3 shows the basement structure for a 350 km x 350 km wide area centred at the hypocentre of the 1986 Vrancea strong earthquake. A deep forearc basin is extended along the southern margin of the Carpathians towards the east of the Carpathian Arc. The maximum depth of the basin is about 16.5 km. The topography, basement, Conrad and Moho depths and the distributions of v_p at the surface and on the upper side of the basement are displayed in Fig. 3.4. The P-wave velocities between the surface and the basement are interpolated by assuming a velocity increase that is proportional to the square root of the depth (eq. (1) in Martin et al., 2005). This velocity depth relation is in good comparison with results of the seismic refraction studies (Fig. 6 in Martin et al., 2005). The P-wave velocities between basement and Conrad are interpolated linearly with depth from 5.9 km/s to 6.2 km/s and from 6.7 km/s to 7.0 km/s between Conrad and Moho. During the CALIXTO, 1999 seismic tomography campaign, 110 temporary and 18 permanent seismometers recorded local and teleseismic events over 6 months. Nonlinear teleseismic body wave tomography studies of Martin et al. (2005, 2006) and simultaneous inversion of teleseismic and global P-wave traveltime data (Weidle et al., 2005) reveal the structure of the mantle beneath the Vrancea region. In this work the results of Martin et al. (2005, 2006) are adopted. The results show a clear high velocity body beneath the SE Carpathians between 70 km and about 350 to 370 km depth. This high velocity

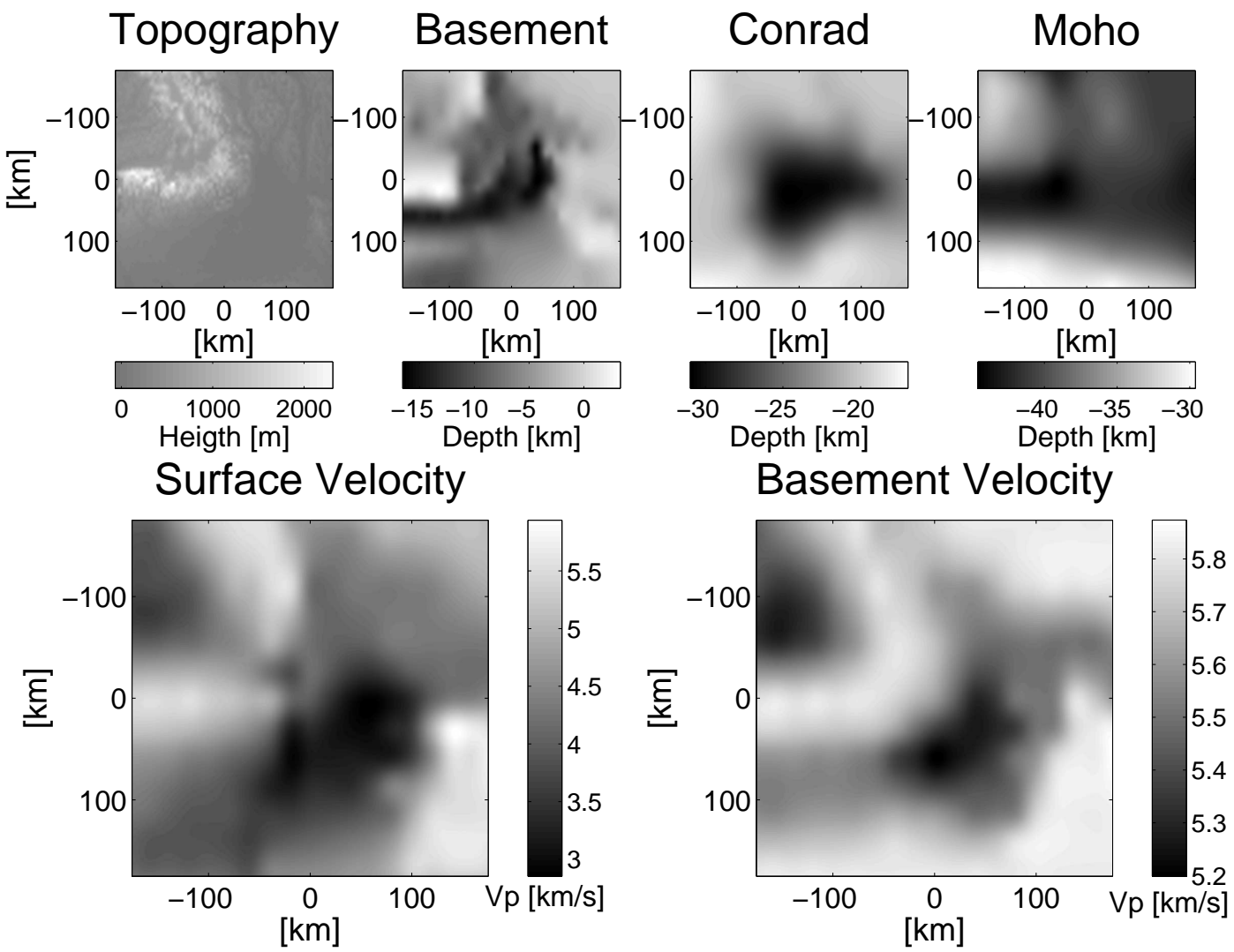


Figure 3.4: Topography, basement, Conrad, Moho structure and surface and basement velocities after Martin et al. (2005).

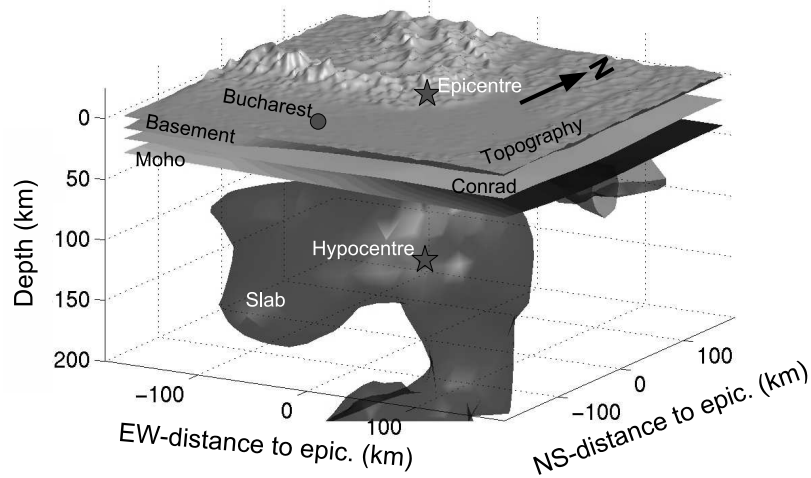


Figure 3.5: Topography, basement, Conrad and Moho with the slab beneath the SE Carpathian Arc after Martin et al. (2006). The slab above 200 km is elongated in NE-SW direction. Beneath 200 km the orientation changes by 90° to SE-NW.

body is interpreted as a lithospheric slab, which shows the last stage of the subduction process along the Alpine-Carpathian belt. For depths less than 200 km the slab shows a NE-SW orientation whereas for depths larger than 200 km the orientation changes to SE-NW. Fig. 3.5 displays topography, basement, Conrad, Moho and the uppermost part of the slab for a 350 km x 350 km wide region, which is centred at the epicentre of the 1986 Vrancea strong earthquake. The figure shows the NE-SW elongated shape of the slab between 50 km and 200 km depth and its change of orientation beneath 200 km. The given horizontal resolution of the P-wave velocities and depths of the crustal structures is about 1 km. The seismic tomography results have a horizontal resolution of 16 km and a vertical resolution of 40 to 50 km. These resolutions are interpolated to the grid spacing needed for the FD modelling by using MATLAB® and GMT (Wessel and Smith, 1998) interpolation routines.

3.3.2 Calculation of S-wave velocity and density

As described above, the Lamé constants λ and μ are calculated from v_p , v_s and ρ . S-wave velocity and P-wave velocity are connected with the Lamé constants by eqs. (1.7) and (1.8). S-wave velocities are calculated from the derived P-wave velocities by assuming $\lambda \approx \mu$, which is a good approximation for many Earth materials. This yields to:

$$v_s = \frac{v_p}{\sqrt{3}}. \quad (3.1)$$

Density values are calculated using the empirical relationship after Glaznev et al. (1996):

$$\rho(v_p) = a + b \ln(|v_p + c|), \quad (3.2)$$

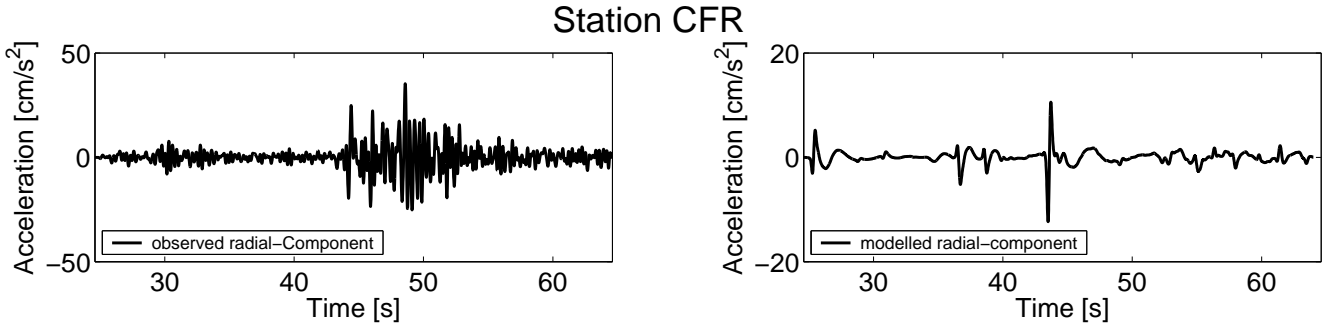


Figure 3.6: Comparison of the observed and modelled radial components at CFR. Due to the smooth velocity model, the modelled seismogram shows a very simple waveform.

with v_p in km/s and ρ in kg/m^3 . For $v_p \leq 5.5$ km/s the parameters a, b and c are:

$$\begin{aligned} a &= 2933, \\ b &= -518, \\ c &= -7.595. \end{aligned}$$

For $v_p > 5.5$ km/s the parameters a, b and c are:

$$\begin{aligned} a &= 1656, \\ b &= 1068, \\ c &= -3.180. \end{aligned}$$

3.3.3 Stochastic Velocity Perturbations

Compared to the observed seismogram at CFR (station location is indicated in Fig. 3.13), the modelled time-series shows very clear phases (Fig. 3.6). This is a direct result from the relatively smooth subsurface structure presented above. The real lithosphere is more complicated and shows small scale velocity perturbations (Sato and Fehler, 1998, chapter 1 and 2), which cannot be resolved by refraction seismology, refraction tomography and receiver functions (see section 3.3.1). Therefore, stochastic velocity perturbations are included into the smooth model to simulate realistic seismograms. Usually, stochastic velocity perturbations are mathematically described by autocorrelation functions (ACFs). To describe perturbations within the Earth the Gaussian, exponential and von Karman ACFs are very convenient (Sato and Fehler, 1998, chapter 2; Tittgemeyer, 1999, Anhang B, Haury, 2002, Kapitel 2). There are many studies on random heterogeneities in the lithosphere of Europe (Hock and M. Korn, 2000; Ritter et al., 1998; Ritter and Rothert, 2000; Hock et al., 2004). Unfortunately, there is no information available for Romania. Therefore, the stochastic properties were adopted from Hock et al. (2004). For a frequency range of 0.5 to 5 Hz, about the same range as in the 2.5D FD modelling, they obtain correlation lengths of 1 to 7 km and RMS velocity fluctuations of 3 to 7 %. In the presented work, the correlation length of crustal structures is chosen as 2 km with a RMS (root mean square)

Layer	Correlation length	Mean P-wave velocity	RMS velocity perturbation
Surface - Basement	2 km	5.05 km/s	5 %
Basement - Conrad	2 km	6.05 km/s	5 %
Conrad - Moho	2 km	6.85 km/s	5 %
Mantle	4 km	7.95 km/s	2 %

Table 3.2: Correlation lengths, mean P-wave velocities and RMS velocity perturbations used to build the stochastic velocity model. The values are based on Hock et al. (2004).

velocity perturbation of 5 %. Correlation length within the mantle is set to 4 km with 2 % RMS velocity perturbations. The RMS velocity perturbation of the mantle is chosen lower than the minimum of 2 % proposed by Hock et al. (2004) to avoid numerical instabilities (section 1.3.2) produced by large seismic wave velocities that would occur for RMS perturbations $> 3\%$. Even at a value of 2 % the velocity grows locally too large. In these cases, the maximum velocity is set to 8.75 km/s. Table 3.2 gives the correlation length, RMS velocity perturbations and mean velocities for all structures. The stochastic velocity perturbations have an exponential ACF and were produced with the help of the codes of Müller and Shapiro (2001), and Cirpka (2003). Fig. 3.7 shows the 2D slices through station CFR for the smooth and the stochastic model. The introduction of stochastic velocity perturbations results in a realistically shaped seismogram (Fig. 3.8).

3.3.4 Q Structure

The applied 2D and 3D FD codes do not consider intrinsic attenuation. Therefore, attenuation is added by applying the frequency dependent damping operator $D(\omega)$:

$$D(\omega) = e^{-\pi\omega t^*/(2\pi)}. \quad (3.3)$$

Where t^* is the sum of the traveltimes t_i through layers with different Q_i divided by Q_i :

$$t^* = \int \frac{dt}{Q} = \sum_{i=1}^N \frac{t_i}{Q_i}. \quad (3.4)$$

Damping is only applied to S-waves, which have usually the largest amplitudes in the seismograms and are therefore most important to simulate strong ground motion. A three layer Q model for Romania (Sokolov et al., 2004) is applied and the traveltimes through each layer are computed by assuming straight-line travel paths from the hypocentre to the receivers. Q is $150f^{0.80}$ for depths greater than 100 km, $400f^{0.90}$ between 40 and 100 km and $100f^{0.80}$ above 40 km. The synthetic seismograms $u(t)$ are Fourier transformed:

$$\tilde{U}(\omega) = A(\omega)e^{i\Phi(\omega)} = \int_{-\infty}^{+\infty} u(t)e^{i\omega t} dt, \quad (3.5)$$

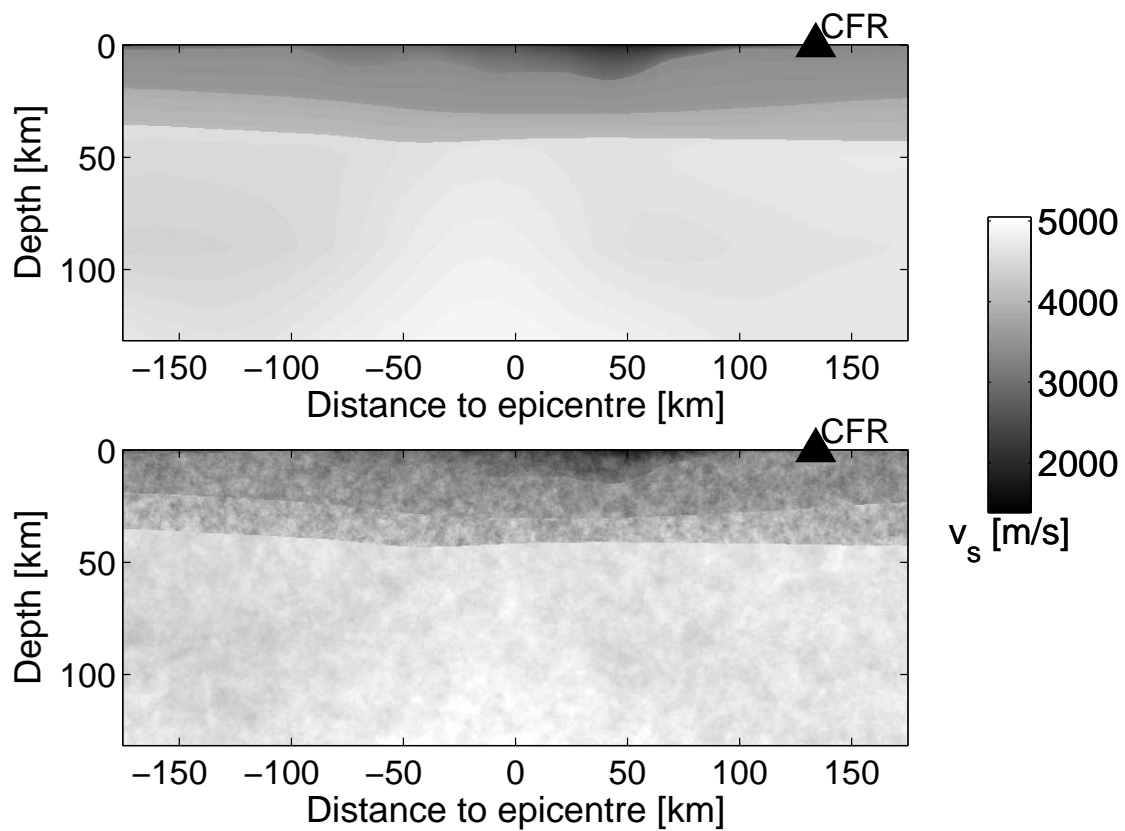


Figure 3.7: 2D slice through station CFR of the smooth model after Martin et al. (2005, 2006) and through the model with added stochastic velocity perturbations after Table 3.2.

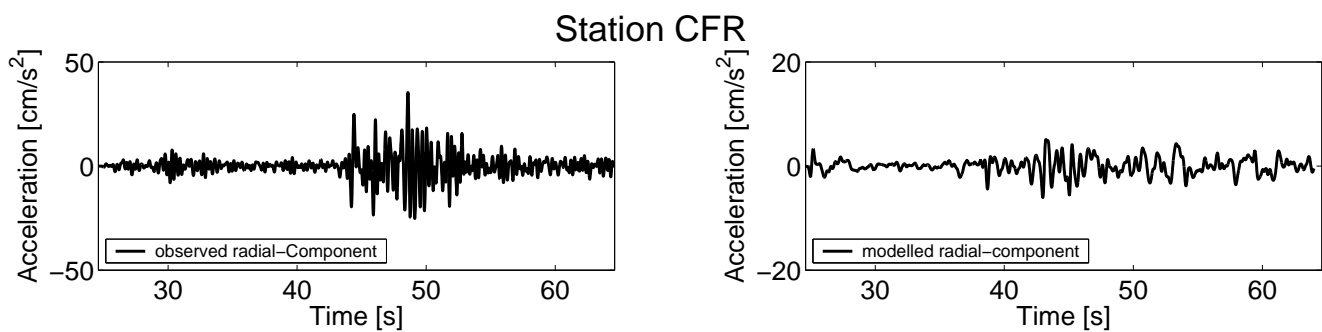


Figure 3.8: Comparison between the observed seismogram at CFR and the model with stochastic velocity perturbations. The resulting waveform is more realistic compared to the modelling without random velocity perturbations (see Fig. 3.6).

with the Fourier amplitude spectrum $A(\omega)$ and the phase $\Phi(\omega)$. Multiplication of the damping operator $D(\omega)$ with the Fourier amplitude spectrum yields to the damped spectrum $\tilde{U}_D(\omega)$:

$$\tilde{U}_D(\omega) = A(\omega)D(\omega). \quad (3.6)$$

Next, inverse Fourier transform is applied to obtain the damped seismograms $u_D(t)$:

$$u_D(t) = \frac{1}{2\pi} \int_{-\infty}^{+\infty} \tilde{U}_D(\omega) e^{i\omega t} d\omega. \quad (3.7)$$

This method modifies only the amplitude spectra, therefore the influence on the phase of the signal is ignored. Fig. 3.9 compares the undamped and damped seismogram at station CFR for the 1986 Vrancea strong earthquake. CFR is located at a distance of 134 km to the epicentre and the straight-line travel path from the hypocentre to the station is 187 km. The S-wave travel times through the deepest, middle and uppermost Q layers are 9.14 s, 18.52 s and 15.49 s, respectively. This gives a total travel time of 43.15 s. For the intermediate depth Vrancea earthquakes the S-waves have the maximum amplitudes in the seismograms. Therefore, the value of t^* is calculated for the travel time of the S-wave through the model to get realistic maximum amplitudes. But the applied damping is too large for waves arriving before the S-wave and too small for waves after the S-wave arrival. However, the sharp S-wave pulse in Fig. 3.9 is correctly damped. For the modelling with the stochastic velocity perturbations the S-wave is scattered over several seconds. Fig. 3.10 displays the transverse component at station CFR for a model with stochastic velocity perturbations. The solid line shows the seismogram which is corrected with the total traveltime of 43.15 s for the theoretical S-wave arrival. The last part of relatively large S-wave amplitudes arrives at about 46.35 s. Therefore, 3.2 s are added to the travel time through the uppermost Q layer to obtain a correctly damped seismogram (dashed) at 46.35 s. The comparison shows that the damping with the theoretical S-wave arrival is 0.07 m/s^2 too large at 46.35 s, which is about 10 % larger than the amplitude that is damped with the correct traveltime of 46.35 s. The scattered S-waves are not only produced in the uppermost layer but also in the deeper Q layers, which have large Q values and therefore produce less attenuation. Hence, for the transverse component of CFR the error of about 10 % is an upper bound.

3.4 2.5D FD Modelling

Wave propagation is modelled with a 2.5D FD method (Karrenbach, 1995). 2D slices with a horizontal extension of 350 km and a depth of about 90 km to 150 km, depending on the hypocentre depth, are extracted from the 3D model (section 3.3). Minimum shear wave velocity is about 1.6 km/s. The resulting grid spacing which depends on the available computer capacity and the numeric dispersion relation (1.19), is 140 m and the simulation of P-SV and SH-wave propagation takes 15 hours time. Wave propagation is simulated for 64 s by using 8000 time steps with a time interval of 8 ms to meet the stability criterion (eq. 1.16). 2D FD modelling is carried out for many slices, which are rotated around the epicentre-hypocentre axis. This 2.5D procedure

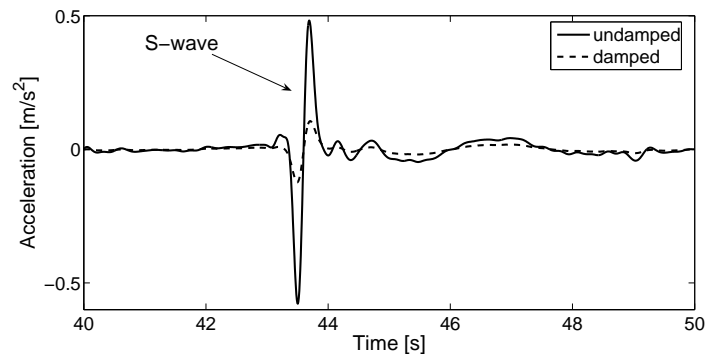
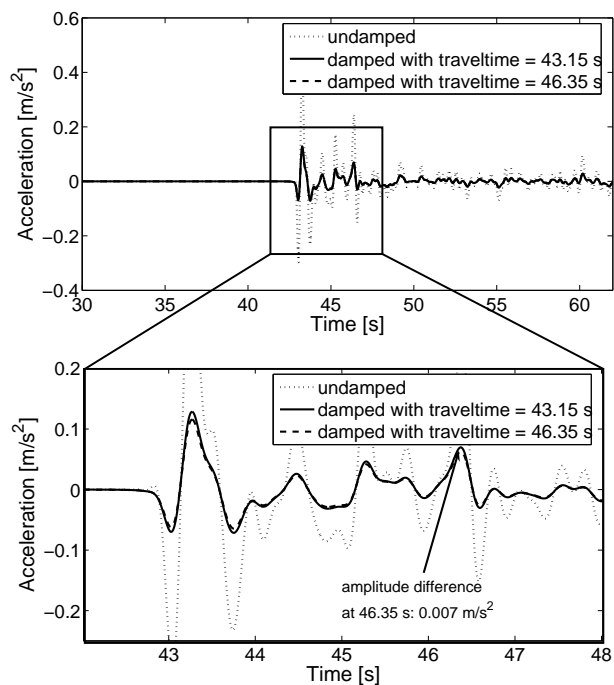


Figure 3.9: Undamped (solid) and damped (dashed) seismogram at station CFR east of the epicenter (see Fig. 3.13) for the Q-structure. The straight lined travelpath is 187 km and the theoretical S-wave arrival time is 43.15 s. The Q structure for SE Romania is adopted from Sokolov et al. (2004).

Figure 3.10: Seismogram at CFR for wave propagation through a model with stochastic velocity perturbations. In this case the S-wave arrivals are stretched over several seconds. Hence, the damping with the theoretical arrival time introduces an error for the S-waves which arrive after the theoretical S-wave. The undamped seismogram is shown with the seismogram damped with the travel time of the S-wave of 43.15 s (solid) and with a travel time that marks the end of large S-wave amplitudes at 46.35 s (dashed). The damping with the theoretical S-wave travel time is 0.007 m/s² to large, which is about 10 % of the correctly damped amplitude at 46.35 s.



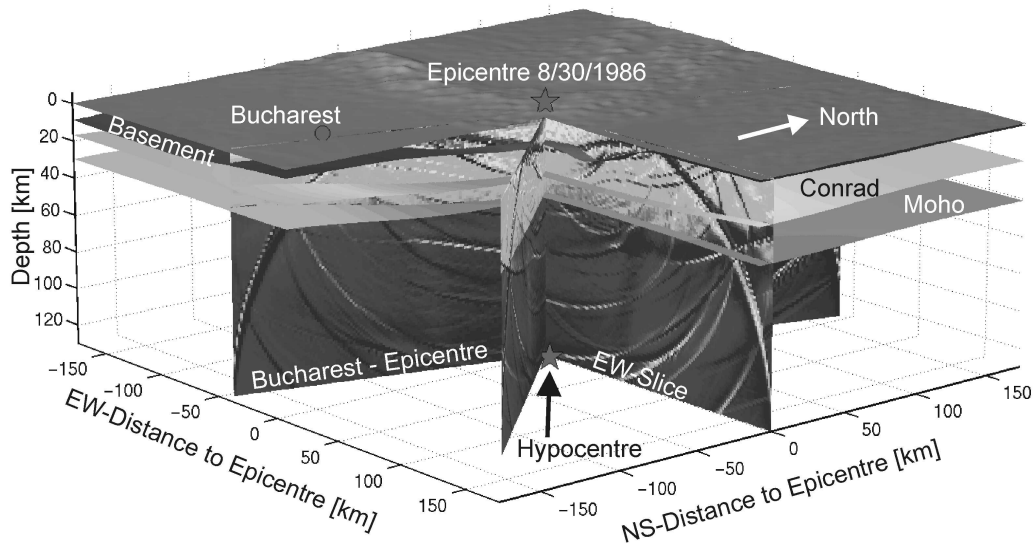


Figure 3.11: Wave propagation of the Vrancea earthquakes is modelled with a 2D FD method for different 2D slices through the underground structure. The slices are rotated around the epicentre-hypocentre axis. This 2.5D modelling procedure generates area-wide seismograms depending on the number of 2D slices. The figure shows the main crustal features, the epicentre and hypocentre of the 1986 August 30 earthquake and wave propagation on three 2D slices that are rotated around the epicentre-hypocentre axis.

allows the simulation of ground motions for the whole study region (Fig. 3.11). A double couple source is implemented as described in section 1.4. The earthquake is modelled as a point source with the source time function after Beresnev and Atkinson (1997) (see section 1.5.1). The use of a point source is no drawback because of the large hypocentre depth of 70 to about 150 km and the small fault sizes due to the large static stress drops of the Vrancea earthquakes (see section 1.5.1). The waveform of the source time function was adopted from Beresnev and Atkinson (1997) (see chapter 1.5.1). In comparison to a real source time function, the source time function after Beresnev and Atkinson (1997) is relatively smooth. This means that the modelling does not include the complexity of the source. Anyway, for the intermediate depth Vrancea earthquakes the source complexity is not known and therefore cannot be implemented in the modelling. Furthermore, for the minimum travel path length of about 100 km the complexity of the underground structure has the main influence on the waveforms of the modelled seismograms. The modelled seismograms are bandpass-filtered between 0.1 and 4.5 Hz to exclude high frequency numerical artefacts, which are produced by numerical dispersion and the source implementation. The next step is the conversion from line source seismograms produced by the 2D FD modelling to 3D point source seismograms after section 1.62. To include intrinsic attenuation the results of the FD modelling are damped as described in section 3.3.4.

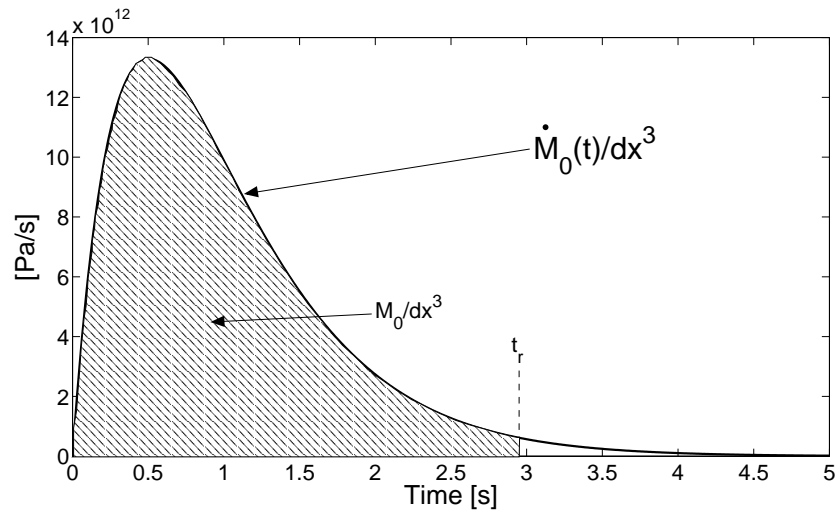


Figure 3.12: For a static stress drop $\Delta\sigma$ of 150 MPa the rupture time t_r is calculated after eq. (1.44). Next, the waveform of the moment density rate function after Beresnev and Atkinson (1997) is calculated so that 98 % of the final moment density M_0/dx^3 (shaded) is reached after the rupture time $t_r = 2.95$ s (see section 1.5.1).

3.4.1 2.5D Modelling of the August 30, 1986 Vrancea Earthquake ($M_W=7.1$)

Wave propagation is modelled for 22 2D slices through the underground structure. The horizontal extension of the 2D slices is 350 km, the vertical extension 131 km. Ten slices cross the locations of strong motion stations and the azimuths of the other 12 slices are chosen that the area is evenly covered. Fig. 3.12 shows the source wavelet used to model the 1986 earthquake. A detailed description of the calculation of the source wavelet is given in section 1.5.1. To model the 1986 earthquake a static stress drop $\Delta\sigma$ of 150 MPa is used. Using eq. (1.44) the rupture time $t_r = 1/f_c$ is 2.95 s. Fig. 3.12 displays the resulting moment density function with the waveform after Beresnev and Atkinson (1997). 98 % of the final moment density are reached after the rupture time $t_r = 2.95$ s. Fig. 3.13 shows peak ground accelerations (PGA) along the profiles of the 22 2D slices through the model without random velocity perturbations. The resulting PGA pattern is very smooth. It shows an oval form, which is elongated in NE-SW direction with a strong decrease in NW direction from 0.5 m/s^2 at the epicentre to 0.15 m/s^2 in a distance of 30 km. Maximum PGA of about 0.85 m/s^2 occurs east to southeast of the epicentre. The observed macroseismic intensities of the 1986 earthquake, and also the intensities of the 1977 and 1944 events, show an oval NE-SW elongated pattern with the maximum intensity about 50 to 100 km east of the epicentre (Fig. 3.2). These patterns are also observed for the PHA distributions (Popa et al., 2005; Sokolov and Bonjer, 2006). There are different explanations for this pattern. After Mandrescu and Radulian (1999) the observed pattern is generated by the source mechanism and the local site effects. Popa et al. (2005) emphasise the influence of attenuation variations in the upper mantle and exclude explicitly the influence of local site effects and source radiation. To

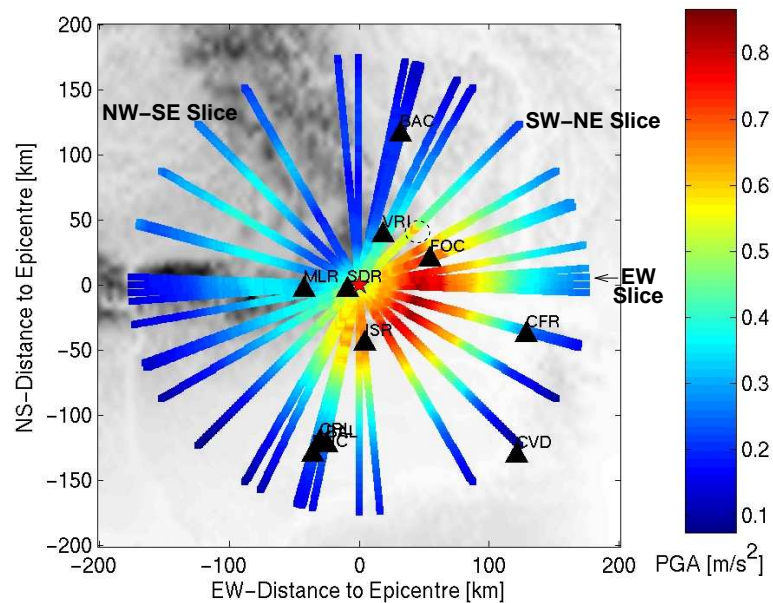


Figure 3.13: PGA distribution along the profiles of 22 2D slices through the model without stochastic velocity perturbations. The red star marks the 1986 epicentre. Strong motion stations, which recorded the earthquake are depicted by triangles. The grey background indicates the topography. The resulting PHA values show a simple pattern. Maximum PGA of about 0.85 m/s^2 occurs east of the epicentre. The PGA distribution shows an oval in NE-SW direction elongated pattern. In NW direction the PGA values show a strong decrease from about 0.5 m/s^2 to 0.15 m/s^2 over 30 km and again an increase to about 0.38 m/s^2 in a distance of 50 km. The large amplitudes within the dashed circle are explained in section 3.4.2.

address this question, FD modelling is an appropriate method. By simulating wave propagation for models where specific structures are included whereas others are omitted, the influence of the different underground structures can be studied. Therefore, in the next sections wave propagation is simulated for different models to explore the influence of the basement, Conrad, Moho and mantle structures on the wave propagation and the resulting ground motions at the surface.

3.4.2 2.5 FD Modelling - Influence of Underground Structure

Wave propagation is modelled for three 2D slices through the model without the stochastic velocity perturbations. This allows to study the influence of the main crustal boundaries. The three studied slices are orientated in EW, SW-NE and NW-SE direction (see Fig. 3.13). The EW slice runs through the deepest part of the basement, the SW-NE slice is parallel to the long axis of the oval PGA pattern and the NW-SE slice is oriented along the short axes of the oval pattern. Wave propagation is modelled for six different underground structures for each slice. For the horizontally layered model **LAY** the depths and velocities of the different structures are the average

Structure/Velocity	Average Depth/ Average Velocity
Basement	5.56 km
Conrad	22.55 km
Moho	38.64 km
Surface Velocity	4.37 km/s
Basement Velocity	5.64 km/s

Table 3.3: Average depths and velocities of the **layered model (LAY)**. The velocities between basement and Conrad and Conrad and Moho increase linearly from 5.9 km/s to 6.2 km/s and from 6.7 km/s to 7.0 km/s, respectively (see section 3.3.1)

Abbreviation	"Real" Structures (see section 3.3)	Simplified Structures
LAY	-	horizontal basement, Conrad, Moho homogeneous mantle
B	basement	horizontal Conrad, Moho homogeneous mantle
BC	basement, Conrad	horizontal Moho homogeneous mantle
BCM	basement, Conrad, Moho	homogeneous mantle
BCMM	basement, Conrad, Moho Mantle	-
BCMMs	basement, Conrad, Moho, Mantle with sharp boundary	-

Table 3.4: Abbreviations for the models used to explore the influence of the different underground structures on the resulting ground motion.

values of the structures within a 175 km x 175 km wide and 131 km deep 3D model (Table 3.3). Next the **basement** structure is added and the Conrad and Moho are kept as horizontal (model **B**). Then wave propagation is modelled for a model **BC** that contains the **basement** and **Conrad** structure. The fourth model **BCM** contains also the **Moho**. The mantle is homogeneous for all of these models. Then, the **mantle** structure after Martin et al. (2006) is added (model **BCMM**). The results of seismic tomography show a smooth image of the high velocity body in the mantle. However, the boundary between mantle and a descending slab is rather sharp than smooth. Therefore, wave propagation is also calculated for a slab with a **sharp boundary** (model **BCMMs**) to study the difference between wave propagation within a smooth mantle and a mantle with a discontinuity. Hereafter, the structures after Martin et al. (2005, 2006) are referred to as the "real" structures. Table 3.4 summarises the used model abbreviations.

SW-NE Slice

Wave propagation is simulated for six different underground structures of the SW-NE slice. Fig. 3.14 (a) shows these models with the snapshot of the resulting components of accelera-

tion after 8 s. Fig. 3.14 b displays a zoomed image of the resulting components of acceleration after 8 sec. The resulting component $a(t)$ is calculated as:

$$a(t) = \sqrt{a_r(t)^2 + a_t(t)^2 + a_z(t)^2}, \quad (3.8)$$

with the accelerations $a_r(t)$ is in radial direction, $a_t(t)$ in transverse direction and $a_z(t)$ in vertical direction. Hereafter, to describe the direction of radiation, angle γ is defined counterclockwise from the horizontal (indicated in Fig. 3.14 b). Fig. 3.15 shows the PGA (peak ground acceleration) along the profile of model LAY. PGA is defined as the resulting component (eq. 3.8) of the accelerations at the surface. There are no complicated underground structures that deflect the wavefield. The wavefront orientation is changed according to Snell's law and amplitude increase because of the impedance decrease for the upgoing waves. These two effects are point-symmetric to the epicentre. Therefore, the resulting PGA for the LAY model (solid line) displays mainly the influence of the source radiation. Fig. 3.14 (b) shows that the source radiates maximum S-waves in a direction between about 10° and 135° with a maximum for $\gamma \approx 77^\circ$. For model LAY maximum PGA of 0.61 m/s^2 occurs 35 km NE of the epicentre. This is about 1.3 times larger than the PGA 35 km SW of the epicentre with 0.46 m/s^2 . The PGA at 175 km is about 4.5 times larger than the PGA at the opposite site of the model at -175 km. This means that the source radiation produces amplitude variations up to a factor of 4.5 along the SW-NE profile. After implementing the basement structure (model B), the resulting PGA for model B is enhanced by about 25 % at 60 km (see also dashed circle in in Fig. 3.13). Between 65 km and 90 km the PGA of model B is lower than in LAY. Fig. 3.17 shows the snapshots for the S-waves travelling through the basin structure between 28 km and 98 km. It can be seen that, due to Snell's law, the convex basin edge at about 55 km produces focusing, which impinges on the surface at 60 km where large PGA occurred (Fig. 3.15). To the NE, between 65 km and 90 km model B results in lower PGA than in model LAY. The basin structure is concave in this range for the arriving wavefront, which is therefore defocused. Between 0 and 50 km the basement structure alternates between slightly concave and convex structures, which produce alternating focusing and defocusing. Next, the real Conrad and Moho structures are implemented. They show a negligible effect on the resulting PGA (Fig. 3.15 bottom) because compared to the basement structure the Conrad and Moho have minor lateral depth variations. Adding the real mantle structure (Model BCMM) the shape of the PGA distribution does not change, but the absolute value of PGA is reduced. The main difference to the previous models with homogeneous mantle is that the earthquake occurs in this case in a region with increased P-waves velocities. After eq. (1.28) the far field amplitudes of the P- and S-wave displacements in a homogeneous medium are:

$$u_i = \frac{\gamma_i \gamma_j \gamma_k}{4\pi\rho\alpha^3} \frac{1}{r} \dot{M}_{kj} - \frac{\gamma_i \gamma_k - \delta_{ik}}{4\pi\rho\beta^3} \gamma_j \frac{1}{r} \dot{M}_{kj}. \quad (3.9)$$

Consequently, the amplitudes u_i are connected with the P-wave velocity α as:

$$u_i \sim \frac{1}{\alpha^3}, \quad (3.10)$$

and with the S-wave velocity β as:

$$u_i \sim \frac{1}{\beta^3}. \quad (3.11)$$

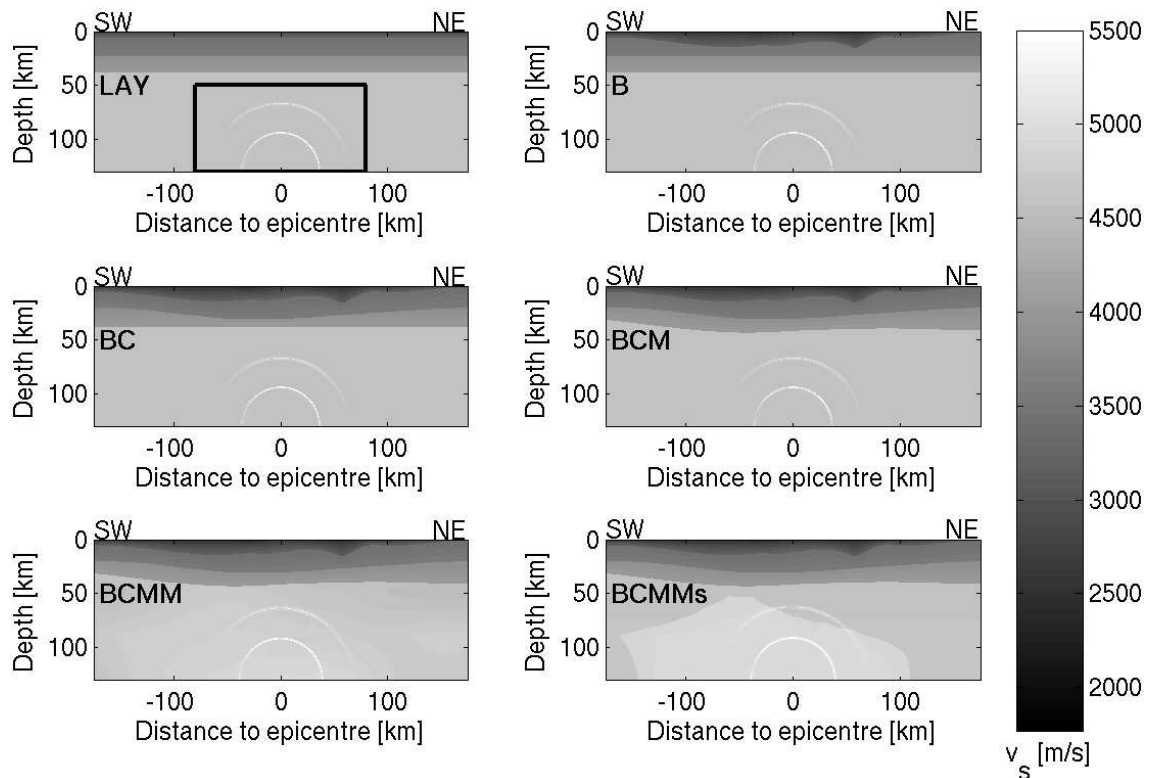
Displacements u_i that are initiated in the homogeneous models have therefore larger amplitudes compared to the waves that are produced in the high velocity slab. Subsequently, the waves which impinge on the different mantle and crustal structures have smaller amplitudes for models BCMM and BCMMs than for models LAY, B, BC and BCM. Consequently, the modelled amplitude at the surface for the models with the "real" mantle structures and the source in a high velocity area is also lower.

EW Slice

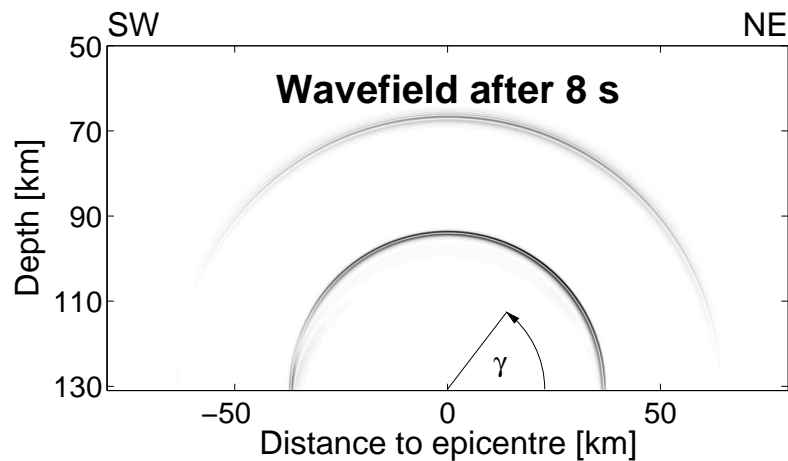
The different underground structures are given in Fig. 3.18 (a). Large S-wave amplitudes are mainly radiated to the East with a maximum for $\gamma = 60^\circ$. This is exactly the direction to the deepest part of the basin at 45 km with its convex structure. The PGA for model LAY (Fig. 3.19 top) displays the influence of the radiation pattern. Maximum PGA of 0.84 m/s^2 occurs 47.6 km east of the epicentre, which is 2.8 times larger than 47.6 km west of the epicentre. The basement structure between 40 km and 70 km focuses mainly the incoming S-waves and produce a maximum amplification of about 10 % compared to the PGA for model LAY. For the SW-NE slice the amplification was about 25 % because of the more pronounced convex structure. The concave basin structure between -25 km and -50 km produces also small defocusing. Despite of the relatively large S-waves radiated for $\gamma > 120^\circ$ the PGA level west of -85 km of model B drops beneath the level of model LAY. In this area, there are no basins and therefore no amplification due to decreasing impedance and focusing effects can occur. As for SW-NE slice the real Conrad and Moho have almost no influence on the PGA distribution (Fig. 3.19 bottom). For models BCMM and BCMMs the shape of the PGA remains (Fig. 3.20) but the absolute amplitude is reduced because the earthquake occurs in a high velocity region (eq. 3.9).

NW-SE Slice

Fig. 3.21 shows the models that are used to simulate wave propagation in NW-SE direction. Large S-wave amplitudes are radiated for $33^\circ < \gamma < 94^\circ$ and for $\gamma > 120^\circ$. The PGA for model LAY displays the strong influence of the source radiation (Fig. 3.22), as the PGA at 36.4 km is about four times larger than at -36.4 km at the opposite side to the epicentre. As in the previous two cases, large S-waves amplitudes impinge on the convex shaped deepest part of the basins. Therefore, maximum PGA due to focusing is observed at 43 km. The amplification compared to model LAY is about 10 %. Between -117 km and -150 km and to the east of 120 km there are no basins and therefore PGA for model B is lower than for model LAY. The Conrad and Moho structures have only a small influence on the resulting PGA. For models BCMM and BCMMs the hypocentre is located in a high velocity area. Therefore, PGA of these models is lower compared to the homogeneous mantle models.



(a) Different underground structures of the SW-NE slice



(b) Radiation pattern within the SW-NE slice

Figure 3.14: Top: Different models of the SW-NE slice that are used to examine the influence of different underground structures (see Table 3.4) on the wave propagation. Bottom: Detailed view of the snapshot of the resulting component of accelerations (eq. 3.8) after 8 s for the region indicated in the image of model LAY (black box). Maximum S-wave amplitudes are radiated for $\gamma = 77^\circ$.

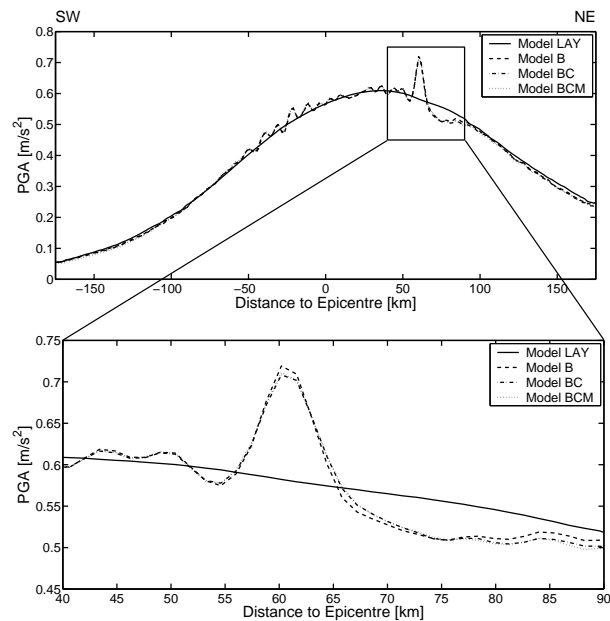


Figure 3.15: PGA along the SW-NE profile for model LAY and model B (top). Due to the source radiation the PGA for model LAY at 175 km is 4.5 times larger than at -175 km in the SW. After adding the basement structure (model B), PGA is increased by about 25 % at 60 km and decreased between 65 km and 90 km. As the snapshots (Fig. 3.17) show, this distinct feature is produced by focusing and defocusing at the basement. For models BC and BCM the resulting PGA (bottom) merely changes. The slight dips of the Conrad and Moho have only small effects on the resulting PGA.

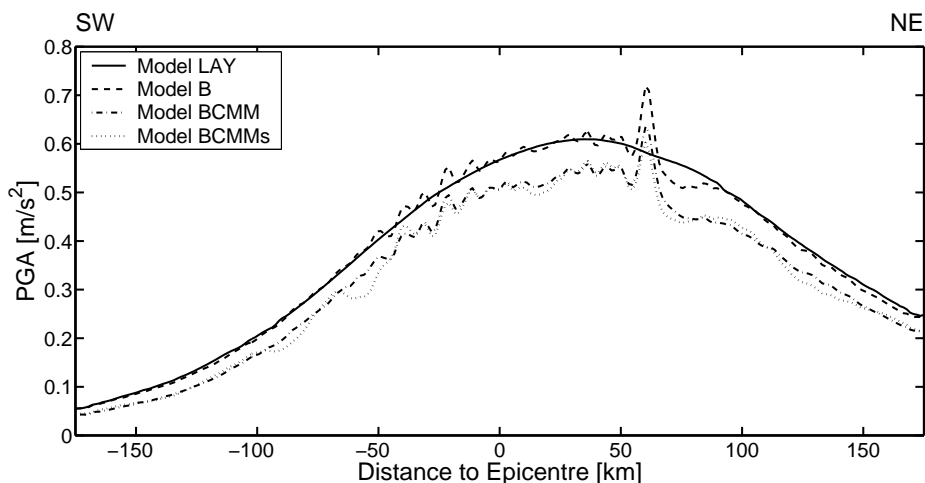


Figure 3.16: After adding the mantle structure (models BCMM and BCMMs) the shape of the PGA distribution along the SW-NE profile does not change but the amplitude is decreased. After eq. (3.9) amplitudes decrease because the source is located in a high velocity body.

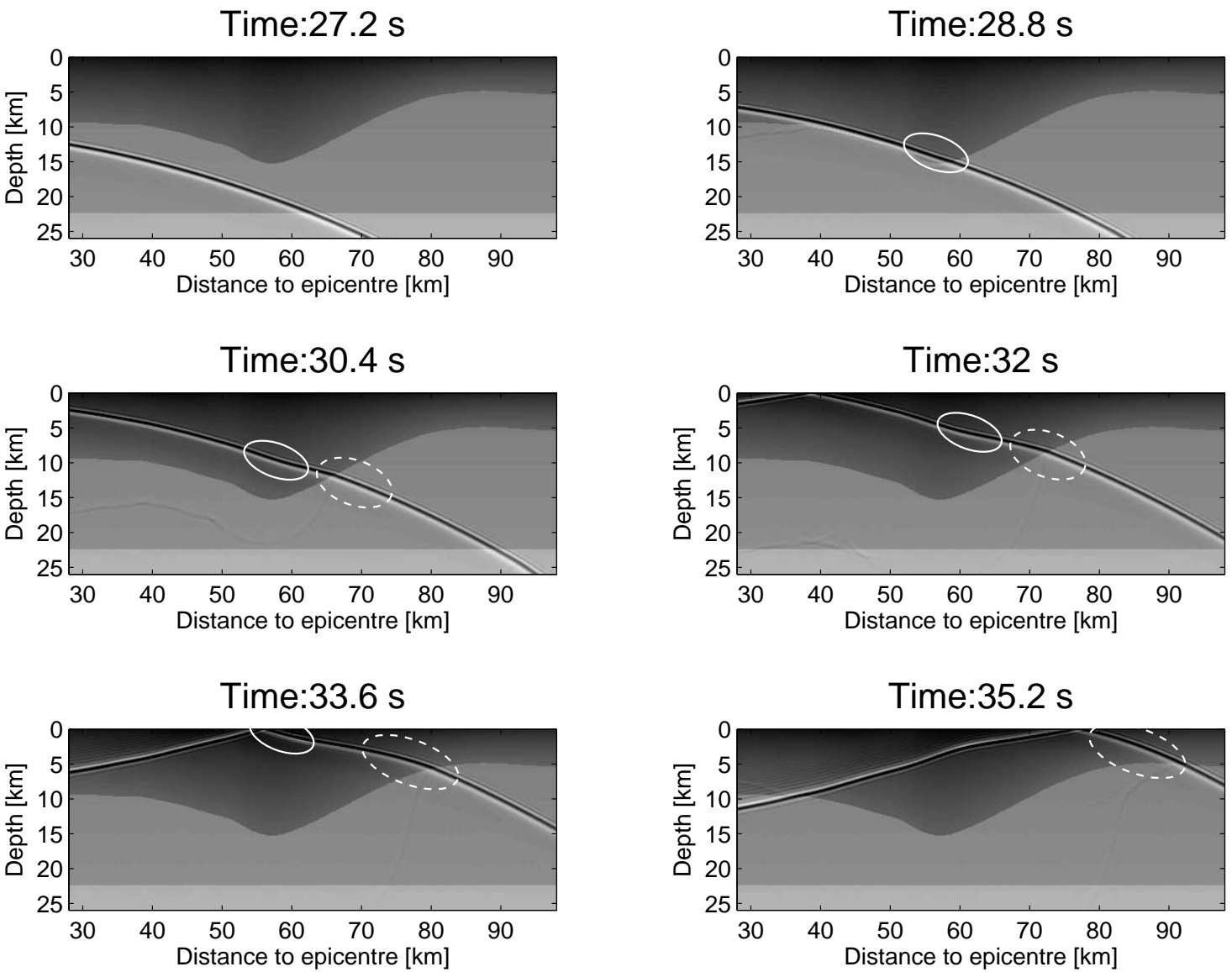
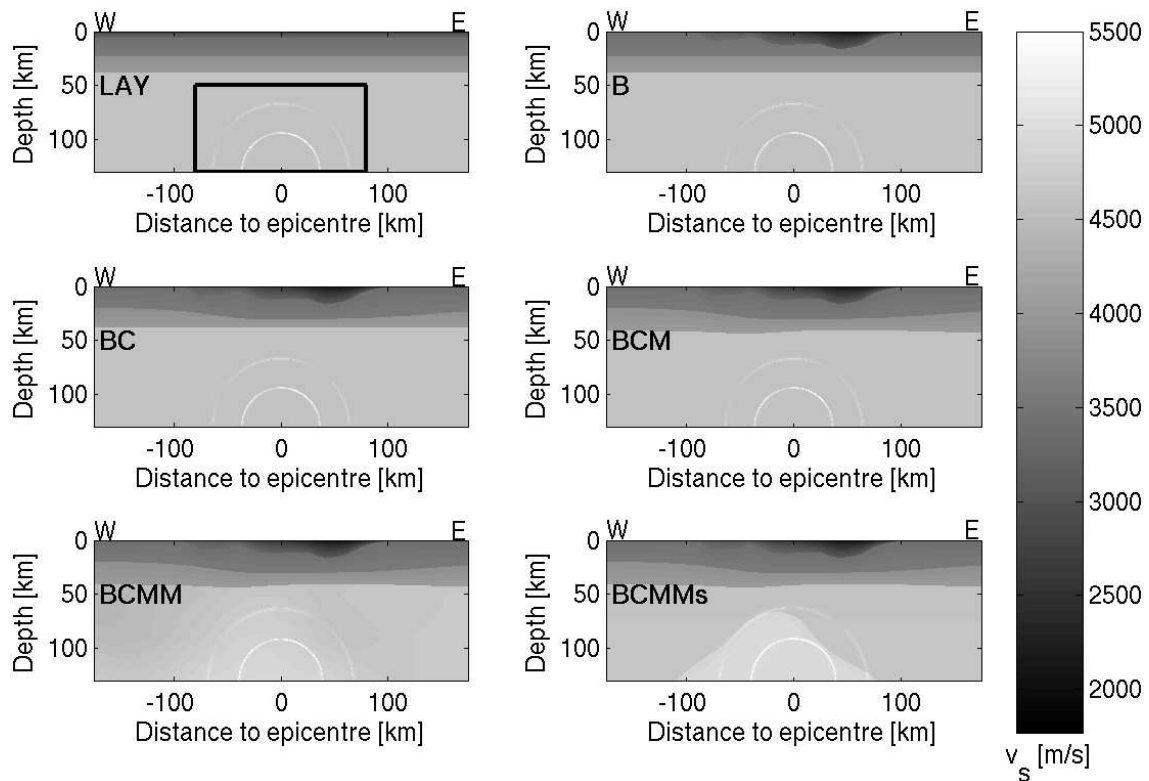
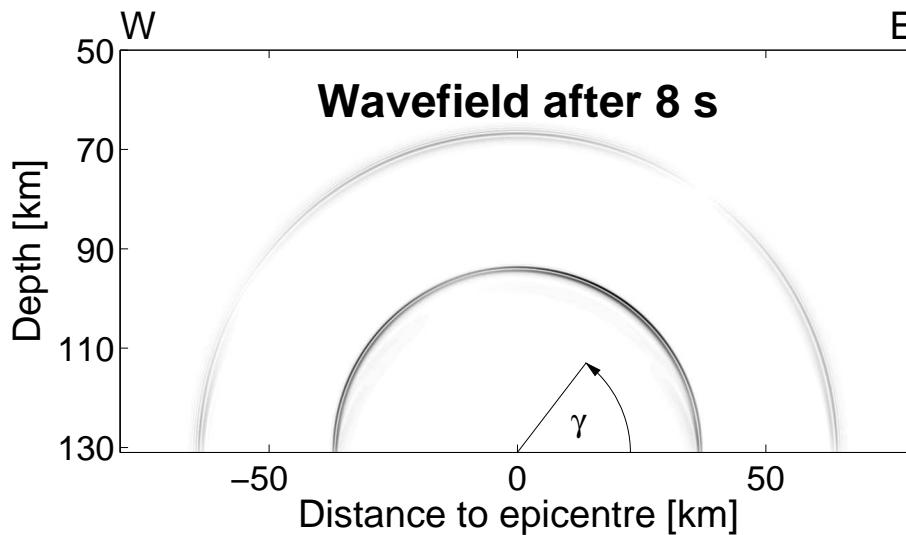


Figure 3.17: Snapshots of the wavefield in the basin between 28 km and 98 km between 27.2 s and 35.2 s. The solid white ellipse marks the focusing of the S-wavefront at the left basin edge. The focused S-waves impinge at 60 km on the surface. The defocused wavefront follows the defocused wavefront. Defocusing occurs because due to Snell's law the wavefront is stretched at the right boundary of the basin.



(a) Different Underground Structures of the EW slice



(b) Radiation pattern within the EW slice

Figure 3.18: Wave propagation is modelled for six different models of the EW slice (Table 3.4). The snapshot of the resulting component of acceleration is shown in more detail in (b) for the black box indicated in model LAY. Large S-waves travel mainly to the East, where the deep sedimentary basin is located.

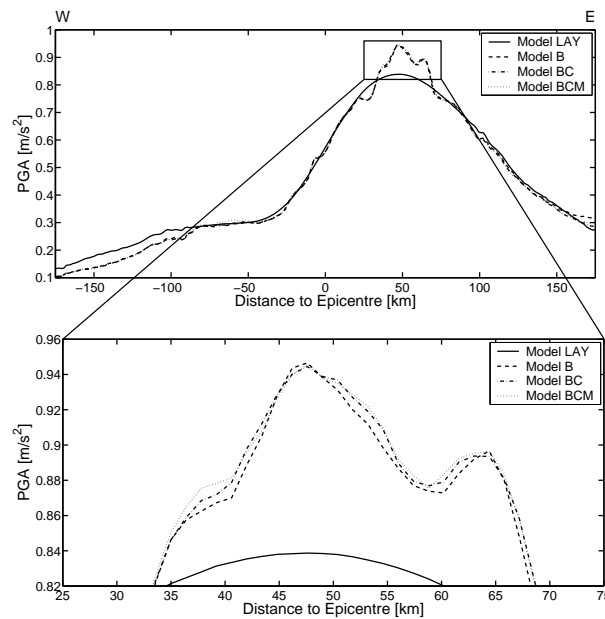


Figure 3.19: Top: Due to the source radiation maximum PGA for model LAY along the EW profile is simulated at 47.6 km, which is 2.8 times larger than the PGA on the opposite site of the epicentre at -47.6 km. The maximum radiated S-waves ($\gamma = 30^\circ$) impinge on the convex shape of the basin and are amplified by about 10%. To the east of -85 km the real model has no sediments and the PGA of model B is lower than in model LAY. Bottom: As the zoomed image shows, the introduction of the real Conrad and Moho merely changes the PGA distribution.

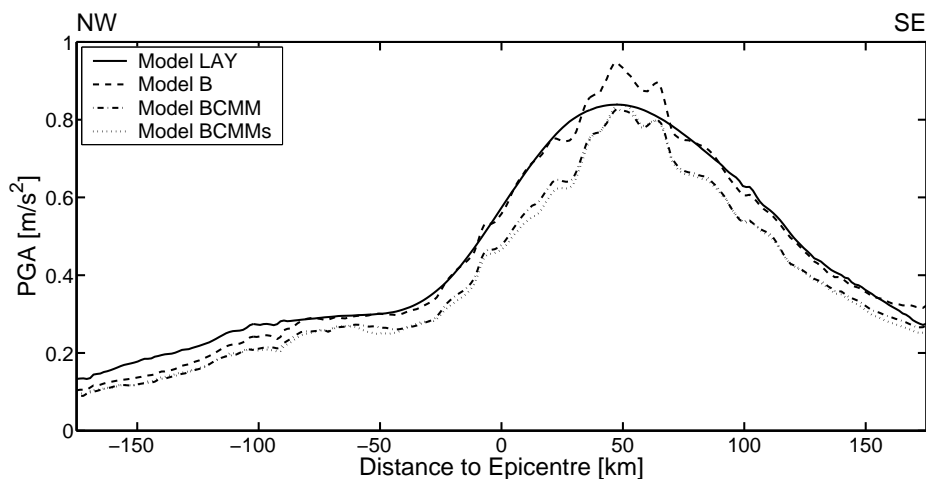
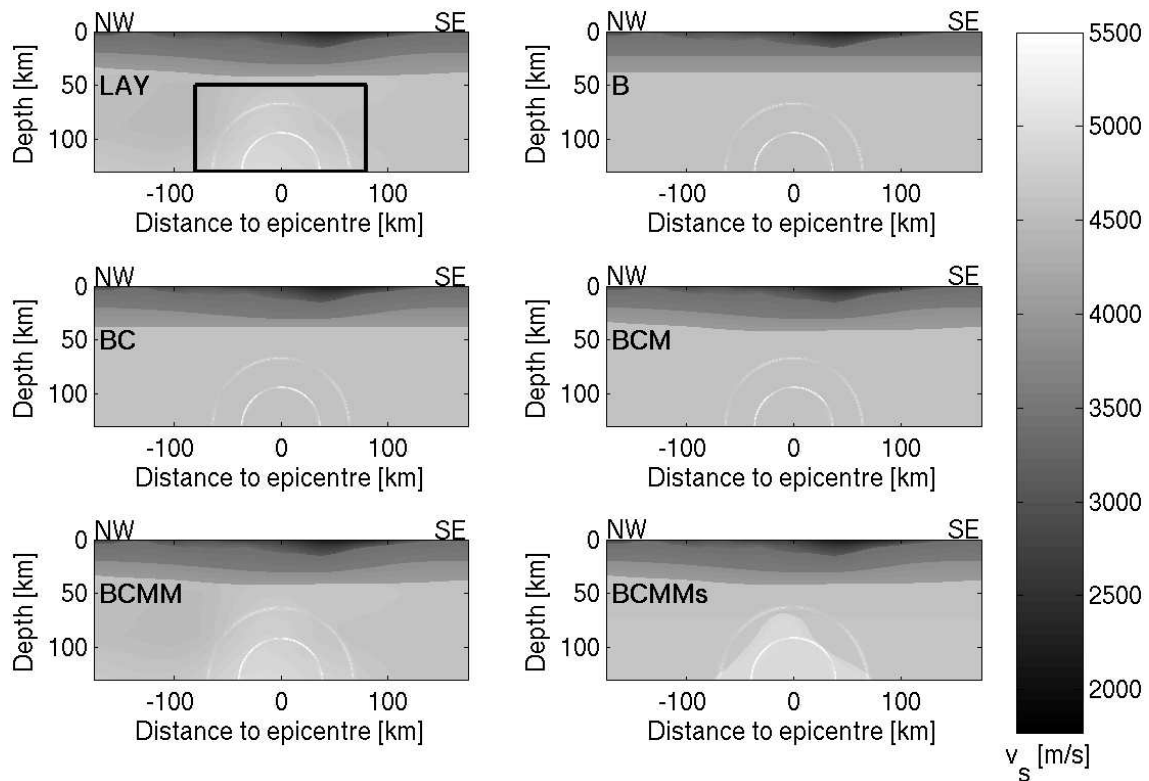
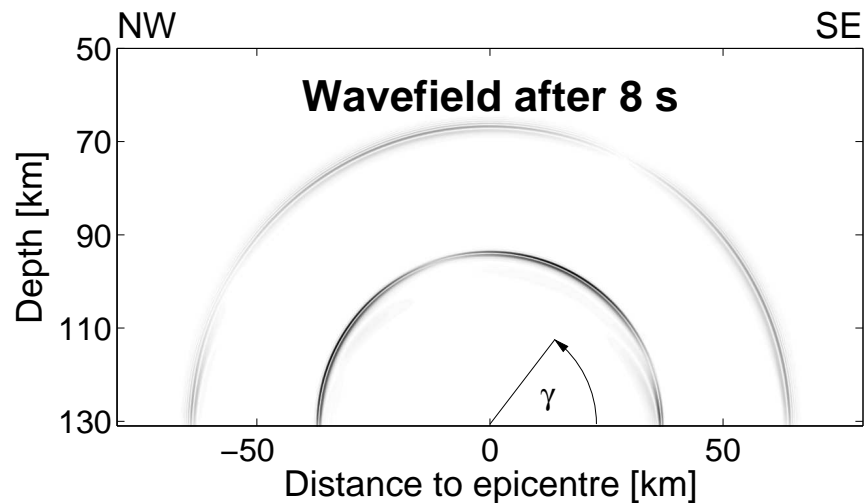


Figure 3.20: After simulating wave propagation for BCMM and BCMMs the form of the PGA distribution along the EW profile is conserved. In BCMM and BCMMs the earthquake source is located in the high velocity body. Therefore, the initiated amplitudes are lower than for the homogeneous mantle (see eq. 3.9).



(a) Different underground structures of the NW-SE slice



(b) Radiation pattern within the NW-SE slice

Figure 3.21: (a) Six different underground structures of the NW-SE slice with the snapshot of the wavefield after 8 s. For the model abbreviations see Table 3.4. (b): Detailed image of the snapshot after 8 s for the box indicated in model LAY. Maximum S-wave amplitudes are radiated for $\gamma = 61^\circ$.

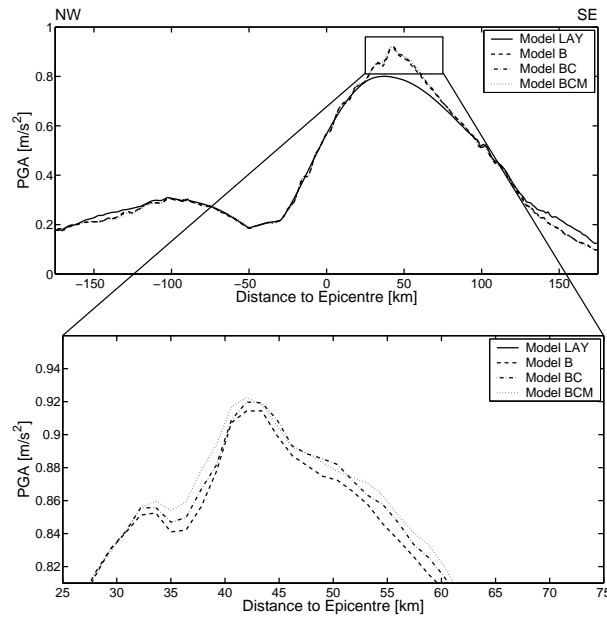


Figure 3.22: Top: PGA for model LAY (solid) model B (dashed) along the NW-SE slice. In model LAY the source radiation produces a difference of 400 % between the PGA at 36.4 km SE of the epicentre and 36.4 km NW of the epicentre. The basin SE of the epicentre focuses the incoming S-waves and amplify PGA by about 10 % compared to model LAY. PGA of model B is lower than of model LAY for the areas where no basins are located. Bottom: Zoomed view of the maximum PGA for model B, BC and BCM. The introduction of the real Conrad and Moho structures has only minor influence on the PGA.

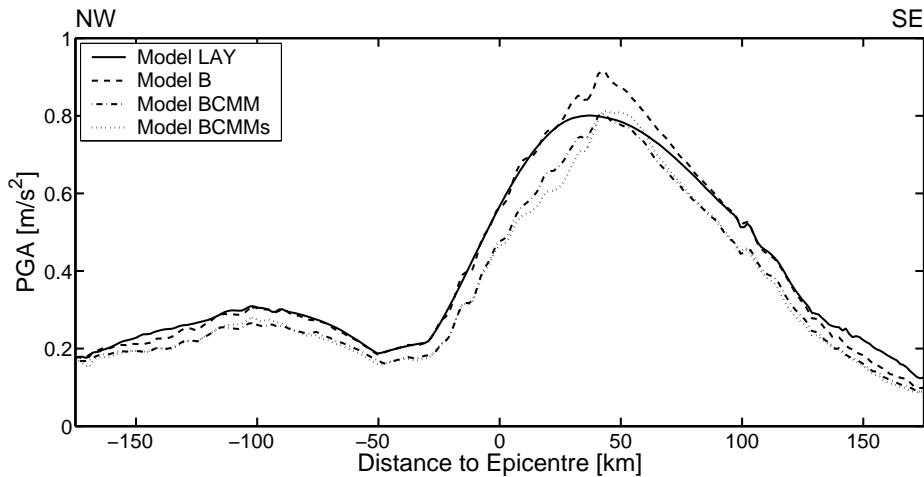


Figure 3.23: PGA for model LAY, B, BCMM and BCMMs. For models BCMM and BCMMs the PGAs are about 10 % percent lower compared to the models with the homogeneous mantle structure. In these models the earthquake source is located in the high velocity body. Therefore, the initiated amplitudes are lower than for the homogeneous mantle (see eq. 3.9).

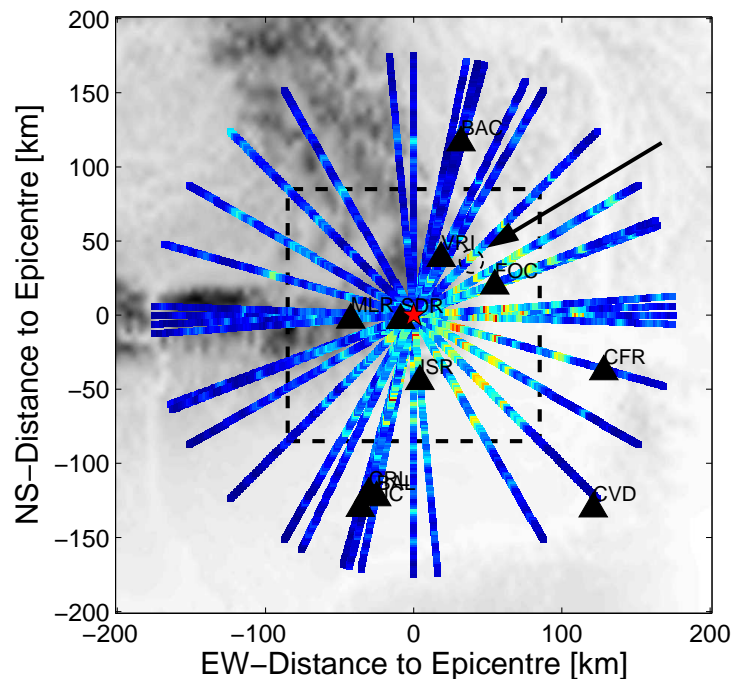


Figure 3.24: PGA distribution along 20 slices through the model with the imposed stochastic velocity perturbations. As in Fig. 3.13 for the PGA in the smooth model maximum PGA is observed east of the epicentre and the resulting PGA distribution is SW-NE elongated. The arrow indicates the PGA value produced by strong focusing at the convex shaped basins. The dashed square depicts the extension of the region used for the 3D FD modelling (section 3.5).

3.4.3 Model with Stochastic Velocity Perturbations

Fig. 3.24 shows the PGA distribution after adding the stochastic velocity perturbations to the smooth model (section 3.3.3). The PGA pattern is blurred compared to the PGA for the smooth model. However, the two main features, maximum PGA east of the epicentre and SW-NE orientation of the pattern, are the same. Even the small area with large PGA 60 km NE of the epicentre is still visible (arrow in Fig. 3.24). This points out that despite the stochastic velocity perturbations the influence of the crustal structures are necessary to explain the produced PGA distribution.

3.5 3D FD Modelling

It is not possible to simulate the influence of 3D structures with 2.5D FD simulations as the model properties in 2.5D are constant perpendicular to the corresponding 2D slice. Therefore, 3D wave propagation modelling is simulated by applying the 3D FD code of Olsen et al. (1995). However, the drawback of 3D FD calculations is that they are much more memory intensive.

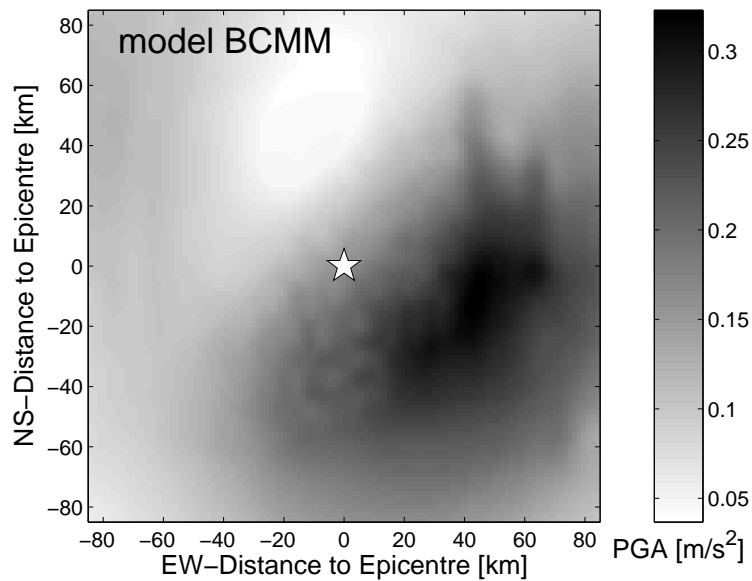


Figure 3.25: PGA of the 1986 strong Vrancea earthquake up to 0.6 Hz. The horizontal extension of the model is 85 km x 85 km. The white star depicts the 1986 epicentre. Maximum PGA of about 0.27 m/s^2 occur about 50 km east of the epicentre and the PGA distribution is SW-NE orientated. The "finger" shaped patterns are produced by the basement structure (see section 3.5.1).

Therefore, compared to the frequencies up to 4.5 Hz simulated with 2.5D FD in the previous sections, the maximum frequency considered in this section is 0.6 Hz. Grid spacing is 500 m. The horizontal extension is 401 x 401 grid points and 321 grid points vertically including absorbing boundaries. This corresponds to a 100 km x 100 km wide and 160 km deep model including the absorbing boundary layer. The minimal S-wave velocity is about 1.6 km/s. Hence, using the numerical dispersion relation (eq. 1.19) the maximum acceptable frequency is 0.6 Hz. Memory requirement is about 48 byte per grid point, which is 2.5 GB for the 520.000 used grid points. To ensure stability (eq. 1.16) of the FD scheme, time discretisation is 17 ms. Wave propagation is simulated for 7000 time steps (= 120 s), which needs about 12 hours on six processors on a SGI Origin 3200. The modelled seismograms are filtered between 0.1 and 0.6 Hz and corrected for intrinsic attenuation as described in section 3.3.4.

The 1986 Vrancea Earthquake ($M_w=7.1$) is modelled within a region centred at the epicentre (dashed square in Fig. 3.24). The applied source wavelet is the same as for the 2.5 FD modelling (Fig. 3.12). Fig. 3.25 shows the simulated PGA distribution for the 1986 earthquake. The PGA distribution looks similar as the distribution that results from the 2.5D modelling (Fig. 3.13). Maximum PGA occurs east of the epicentre and the pattern extends in SW-NE direction, which is the same pattern as in (Fig. 3.2) for the macroseismic intensity distribution. In the next section the subsurface structure is varied in order to reveal the mechanisms that produce this characteristic pattern.

3.5.1 3D Modelling - Influence of Underground Structure

As for the 2.5D FD modelling the influence of the underground structures on the resulting ground motion is studied by simulating wave propagation for simplified models. The used abbreviations of the models are listed in Table 3.4. The PGA distribution for model LAY (Fig. 3.26) reflects mainly the source pattern because the influence of Snell's law and the amplification increase due to impedance decrease is point-symmetric to the epicentre. Maximum amplitudes occur SE to east of the epicentre and the PGA pattern is SW-NE elongated. Maximum PGA SE of the epicentre is 0.28 m/s^2 . In the same distance to the North the PGA is 0.07 m/s^2 , which is four times lower than the maximum. Next, wave propagation is calculated for model B with the real basement structure and horizontal Conrad and Moho (Fig. 3.27). The PGA distribution outlines the influence of the basin structures. Main features are two "fingers" pointing to the North at 40 km east and 20 km north of the epicentre. The contour lines of the basin depth show that the western "finger" shaped PGA pattern is produced by the relatively narrow basin structure and the eastern "finger" shaped pattern occurs along the steep basin structure in the East. The western pattern corresponds to the observed large PGA values 60 km NE of the epicentre that is also visible in the 2.5D FD modelling (Fig. 3.13). The snapshots of the 2D wavefield (Fig. 3.17) show the strong focusing at the convex shaped basin. The largest PGA values occur about 5 km east of the deepest part of the basin because the waves are focused at the western edge of the basement and impinge about 5 km to the east on the surface. In Fig. 3.28 to 3.30 the PGA values for the SW-NE, EW and NE-SW profiles are shown. PGA for model LAY (solid) displays the influences of the source radiation. After adding the real basement structure, the PGA (dashed) along the profiles shows strong amplification. Amplification occurs at the same locations as for the 2.5D modelling at the top of the deep basins. Strong amplification occurs at 60 km on the SW-NE slice due to the relatively narrow and deep basin (Fig. 3.28). The amplification in comparison to model LAY is about 50 %. As in the 2.5D case the real Conrad and Moho structures have almost no influence on the resulting PGA. For all profiles the amplification is larger than in the 2.5D modelling. The contour lines of the basement depth in Fig. 3.27 show that for the three profiles (SW-NE, EW, NW-SE) the basins form 3D lenses, which focus S-waves from a larger part of the wavefield compared to the 2.5D case. After adding the real mantle structure (model BCMM) the amplitude of PGA drops. This is due to the larger P-wave velocity in the source region in comparison to the homogeneous mantle in models LAY, B, BC and BCM (eq. 3.9). After adding stochastic velocity perturbations the resulting PGA pattern is blurred. However, the main features, maximum PGA and SW-NE orientation, are still clearly visible.

3.6 Discussion

2.5D and 3D FD modelling of the 1986 Vrancea strong earthquake emphasises the influence of the sedimentary basins and the source radiation on the resulting ground motions. The simulations showed that the source radiation produces amplitude variations up to a factor of 4.5. Maximum S-wave amplitudes are radiated towards the deep sedimentary basins east of the epicentre. The

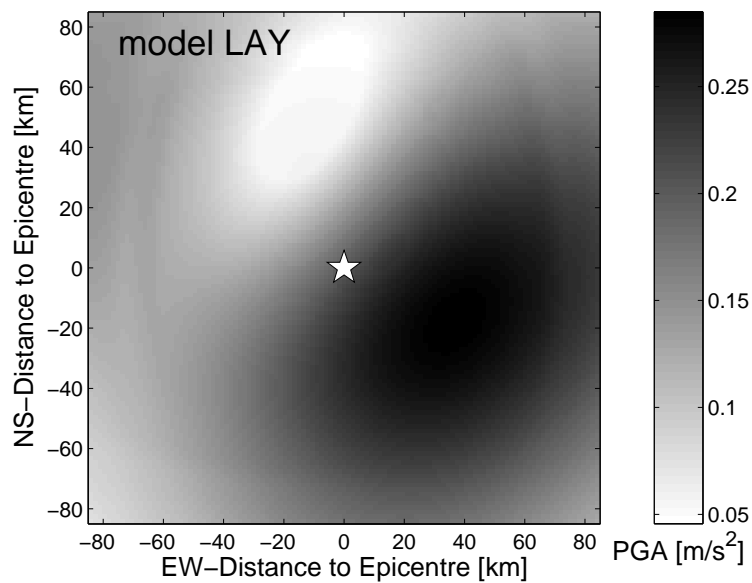


Figure 3.26: PGA distribution for model LAY. Due to the horizontally structured model the refraction at the layer boundaries is point-symmetric to the epicentre. Therefore, the PGA reflects the influence of the source radiation.

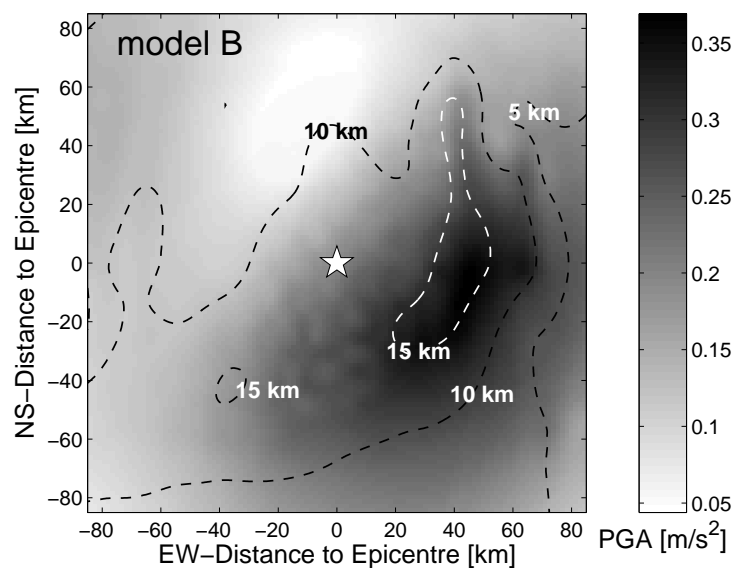


Figure 3.27: PGA distribution for model B. The contour lines (dashed) display the basement depth. Largest PGA values are found over the deepest part of the basement structure. Main features are two "fingers" pointing to the north at 40 km east and 20 km north of the epicentre. The western "finger" shaped PGA pattern is produced by the relatively narrow basin structure. The eastern "finger" shaped PGA pattern occurs along the steep basement structure in the East.

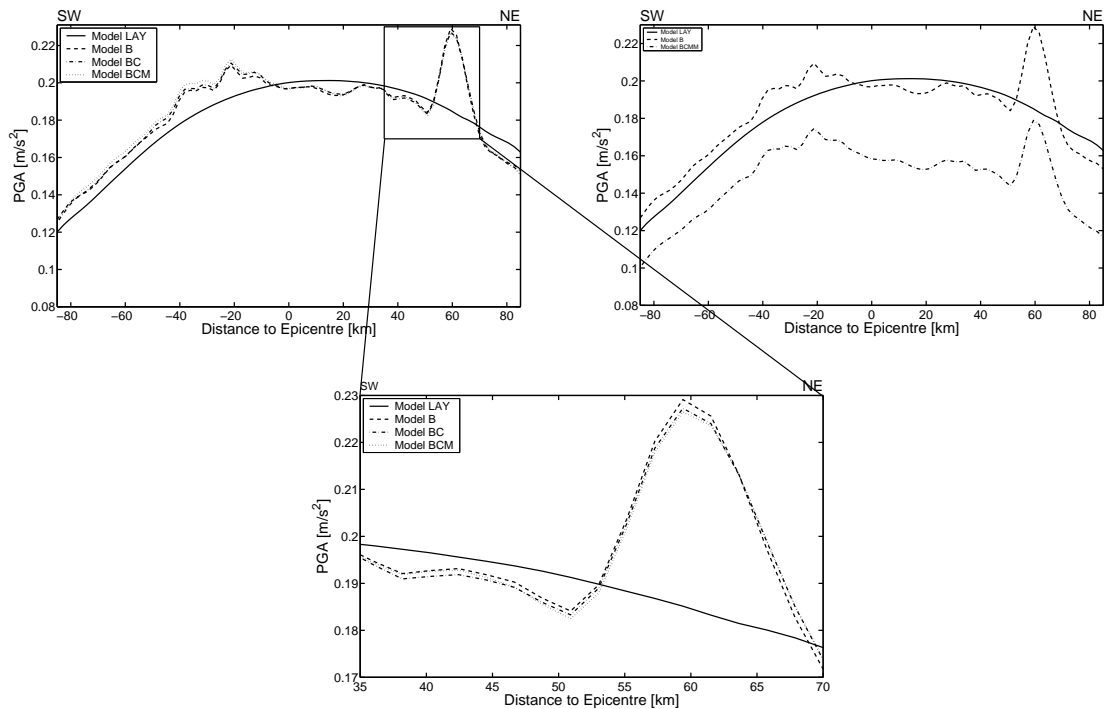


Figure 3.28: PGA along the SW-NE slice for model LAY (solid) indicates that maximum amplitudes due to the source radiation impinge at 20 km onto the surface. The PGA for model B (dashed) shows the strong focusing at 60 km produced by the narrow basin structure. For model BCMM the PGA values (dash-dotted) drop because the seismic wave velocities in the source region are large compared to the homogeneous mantle.

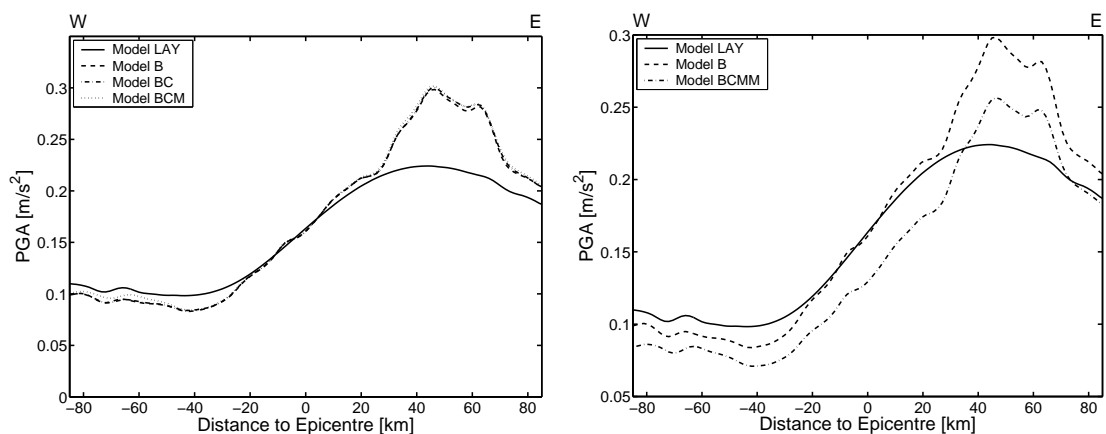


Figure 3.29: As can be seen from PGA of model LAY (solid) along the EW slice, the source radiates large amplitudes to 40 km east of the epicentre. There a deep basin focuses the incoming waves (dashed).

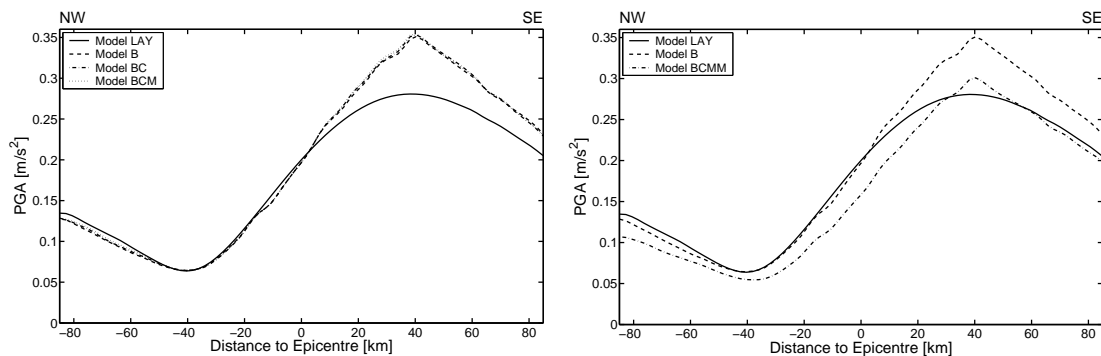


Figure 3.30: PGA for model LAY along the NW-SE profile show that large amplitudes are radiated to the SE of the epicentre. The deep basins in the Carpathian foreland focus the waves and produce maximum PGA 40 km SE of the epicentre.

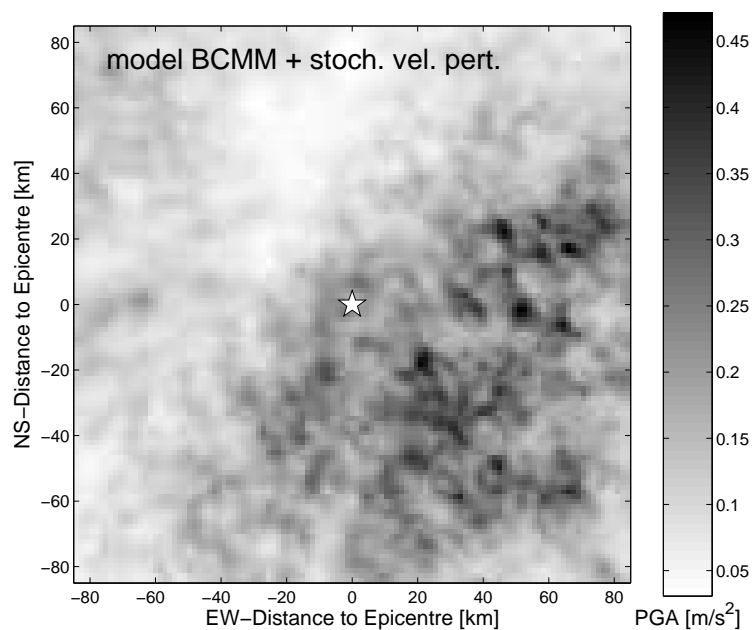


Figure 3.31: PGA distribution of the 1986 earthquake for the subsurface structure with stochastic velocity perturbations. The perturbations have an exponential ACF (autocorrelation function). The correlation length within the crust is 2 km with a RMS (root mean square) velocity perturbation of 5 %. Correlation length within the mantle is 4 km with 2 % RMS velocity perturbation. Compared to the model without perturbations (see Fig. 3.25), the PGA pattern is blurred. As in for the model without random perturbations, maximum amplitudes occur east of the epicentre and the PGA distribution is SW-NE orientated.

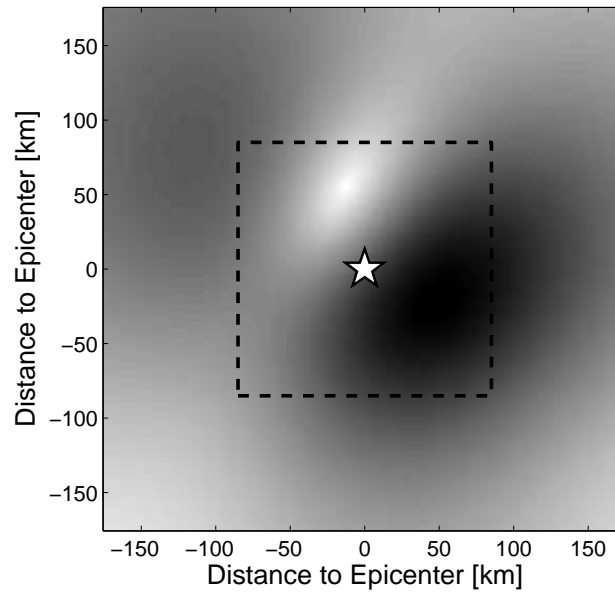


Figure 3.32: S-wave radiation pattern of the 1986 Vrancea earthquake. The pattern is calculated from the SV and SH radiation patterns after Aki and Richards (1980, eq. 4.85 and 4.86) and projected onto the surface. The figure covers the model area of the 2.5D FD modelling. The area of the 3D FD modelling is indicated by the dashed square.

convex basin shapes produce amplification up to 50 % compared to the layered model. Such focusing effects are modelled and observed for the 1994 Northridge earthquake (Gao et al., 1996; Alex and Olsen, 1998; Graves et al., 1998; Davis et al., 2000), where basin effects caused severe damage in Santa Monica. Focusing at convex shaped basins is also shown by Olsen et al. (2000). Additionally, resonance effects, the generation of surface waves at basins are observed and modelled for many earthquakes (e.g. Kawase, 1996; Joyner, 2000; Olsen, 2000; Benites and Olsen, 2005; Olsen et al., 2006). However, in the case of the modelling of the Vrancea earthquakes only the amplitude increase produced by focusing at the convex shaped basins is observed.

To display the influence of the focal mechanism the S-wave radiation F_{SV_SH} pattern is shown in Fig. 3.32. It is calculated from the dimensionless S-wave radiation patterns F_{SV} and F_{SH} after (Aki and Richards, 1980, eq. 4.85 and 4.86) as follows:

$$F_{SV_SH} = \frac{\sqrt{(F_{SH}^2 + F_{SV}^2)}}{R}. \quad (3.12)$$

Geometrical spreading is taken into account by division with distance R between hypocentre and surface. Straight-line travel paths are assumed to project F_{SV_SH} on the surface. The theoretical S-wave radiation pattern shows the same features as the modelled PGA distributions of the 2.5D and 3D FD simulations (Fig. 3.13 and 3.25). Maximum PGA is found east of the epicentre and the distribution is SW-NE orientated. At the top of the deep EW striking basin south of the Carpathians between -40 and -175 km (EW-distance) no notable PGA is modelled. According to the theoretical radiation pattern, no significant S-wave amplitudes are radiated into this region.

Consequently, the basins amplify the incoming waves radiated by the source significantly, but if only small amplitudes impinge on these structures, the resulting ground motion is also very low. This points out that the source radiation plays a major role on the distribution of strong ground motions of the Vrancea earthquakes. After introducing stochastic velocity perturbations, which is more appropriate for the real earth, the PGA patterns are blurred but the maximum values east of the epicentre and the SE-NW orientated pattern is retained. However, the influence of the source radiation for frequencies larger than 1 Hz is not self-evident for wave propagation within the real earth. The next sections discuss this topic and also the trade-off in the modelling between stress drop and applied damping structure. This is critical, because both parameters, stress drop and Q structure, are not well constrained for SE Romania.

3.6.1 Influence of Source Radiation

FD simulations of wave propagation within media with stochastic velocity perturbations are studied, for example, in Frankel and Clayton (1984, 1986), and Shapiro and Kneib (1993). These studies explore the influence of media with different ACFs, velocity perturbations, correlation lengths on arrival times, waveform changes and frequency dependence of the coda. The applied sources are pressure point and line sources. Therefore, no conclusion on the influence of random media on the radiation pattern can be made from these studies.

To display the influence of the stochastic velocity perturbations onto source radiation, 2D FD modelling is performed. Wave propagation is simulated for a 2D grid with 1500 x 1500 grid points and a grid spacing of 140 m. The simulations are carried out for a homogeneous model with $v_p = 6$ km/s, $v_s = 3.464$ km/s and $\rho = 2500$ kg/m³ and a random model with mean velocity values of the homogeneous model, correlation lengths of 2 km, RMS velocity perturbation of 5 % and an exponential ACF. The applied double couple source radiates maximum S-waves amplitudes of the x-component up and downwards and maximum S-wave amplitudes of the z-component to the left and right. The source time function is the same as for the 2.5D and 3D FD simulations of the 1986 Vrancea earthquake (Fig. 3.12). Fig. 3.33 show the snapshots of the wavefield of the radial and z-components for 9.6 s, 19.2 s, 28.8 s and 38.4 s. The stochastic velocity perturbations deflect and blur the wavefront. However, the radiation pattern is not completely disturbed and still visible at the top of the model in a distance of 140 km to the source. Fig. 3.34 shows the radial and z-components for four locations (triangles) directly above the source for the homogeneous and random model. In the homogeneous model the radial component of the S-pulse is clearly visible at each station. Because of the source orientation no S-wave is observed on the z-component. In the random model the radial component of the S-wave is also clearly visible at all stations. But in comparison to the homogeneous model a S-coda appears. Furthermore, the z-component shows also small amplitudes produced by the scattering of the initial P- and S-waves. Fig. 3.35 displays the peak values of the radial component along horizontal profiles with distances of 35 km, 63 km, 91 km and 119 km to the source. The PGA patterns show that the source pattern is not completely smeared out after propagating through the model. FD simulations produce ground motions for any location on the grid and therefore the overall pattern, even a blurred one, of the source radiation is visible. If,

as in reality, only seismograms of a few stations are available it may be more difficult to decide whether the source pattern is visible or not. However, the 2D modelling does not reflect the 3D case correctly because the waves cannot be scattered into the y-direction. But on the other hand, no energy coming from the y-direction is scattered into the 2D slice, which may compensate the lacking scattering into the y-direction.

The influence of the source radiation on observed ground motions is frequently discussed. Most of the studies deal with observations within 20 to 60 km to the earthquake source. Liu and Helmberger (1985) identify the SV and SH radiation pattern of an aftershock of the 1979 Imperial Valley earthquake for frequencies below 1 Hz but not for frequencies larger than 2 Hz. The maximum distance to the epicentre of the examined stations is about 20 km. Vidale (1989) indicated the double couple radiation pattern of another earthquake for frequencies of 3 to 6 Hz. He used stations with a distance up to 40 km. For local earthquakes in central Italy, the influence of the radiation pattern was found for frequencies up to 0.5 Hz (Castro et al., 2006). Takenaka et al. (2003) recognised radiation patterns for frequencies lower than 1 Hz and not for frequencies larger than 2 Hz. Siro and Chiaruttini (1989), and Sirovich (1994) recognised the radiation pattern on peak acceleration for frequencies between 0.1 and 5 Hz for the 1980 $M_L = 6.5$ event in southern Italy. They analysed stations with maximum distances to the fault of about 30 km and 60 km, respectively. For the same event, Panza and Cuscito (1982) computed successfully the observed isoseismals by mode summation for frequencies lower than 0.1 Hz from the focal mechanism. (Sato and Fehler, 1998, chapter 6) and Sato et al. (1997) explore the influence of the source radiation pattern on the S-wave coda theoretically. For large times the S-wave coda shows the same amplitudes irrespective of the source pattern. However, as their studies show, the amplitudes of the first arrivals depend on the station location with respect to the source. Only for increasing time after the direct arrival, the influence of the source on the coda vanishes. These studies indicate that the influence of the focal mechanism of the Vrancea strong earthquakes can also play an important role in the modelled frequency range. Additionally, in the case of the Vrancea earthquakes large stress drops are discussed, which corresponds to a relatively small fault area. Consequently, the earthquakes are able to produce a coherent narrow source time function with large amplitudes, which propagates the source pattern over larger distances compared to crustal earthquakes with significant lower stress drops and thus longer low amplitude and probable more complex source time functions. As shown by Spudich et al. (1998) for the 1995 Hyogo-ken Nanbu (Kobe) earthquake, rake rotation can occur for earthquakes on faults with small absolute stress values and small stress drops. Such rake rotation on small parts of the fault disturb the radiation pattern at high frequencies.

3.6.2 Trade-Off between Stress Drop and Damping Structure

In case of the Vrancea region, both the static stress drop and the damping structure are not well constrained.

From the stress drop $\Delta\sigma$ the rupture time t_r is calculated after eq. (1.44). For increasing stress drops the rupture time t_r decreases with $1/\sqrt[3]{\Delta\sigma}$. Therefore, the pulse width of the moment tensor

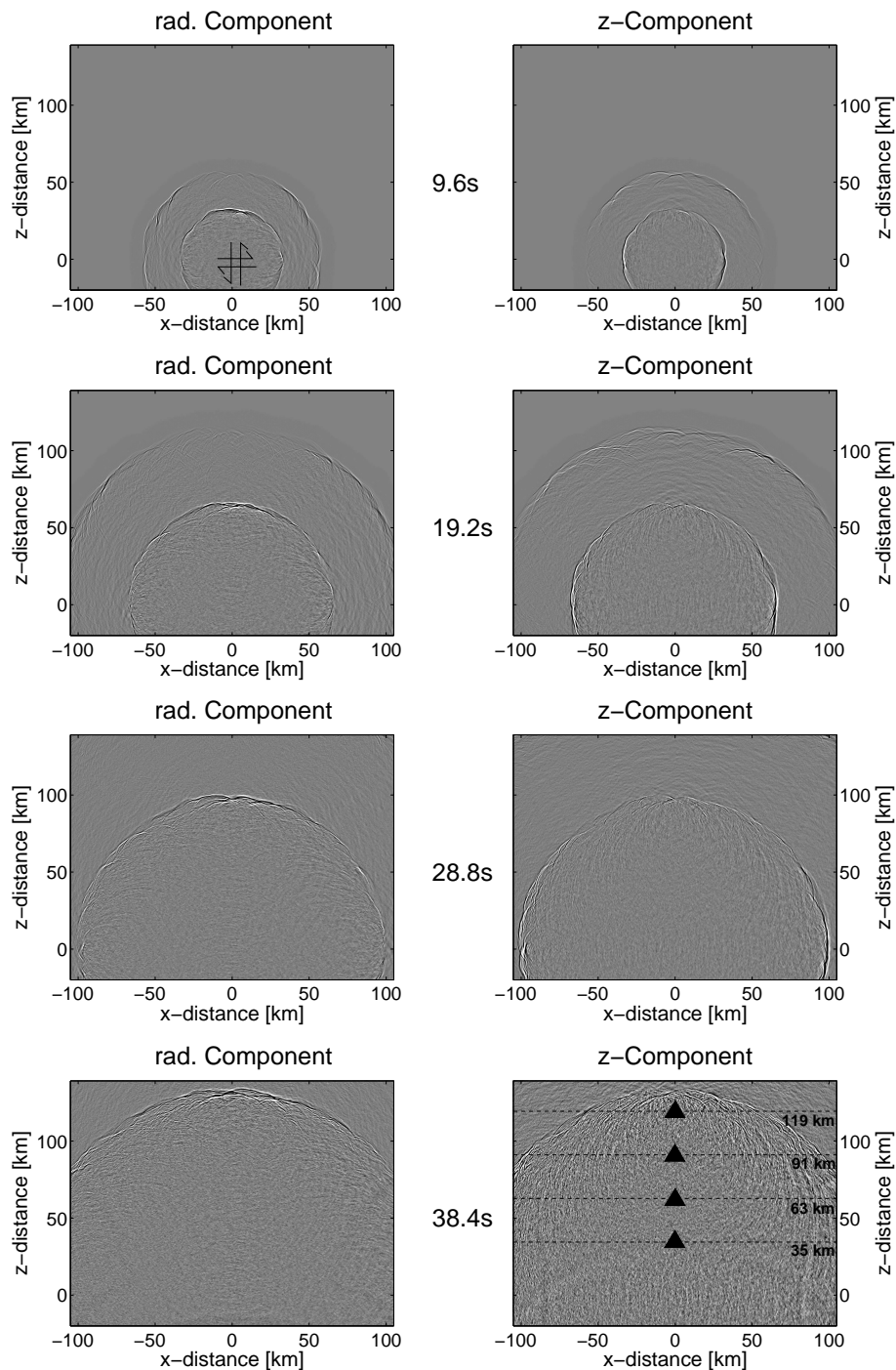


Figure 3.33: Snapshots of the x and z-components of the wavefield in the random model after 9.6 s, 19.2 s, 28.8 s and 38.4 s. The applied double couple source radiates maximum S-waves amplitudes upwards and downwards (x-component) and to the left and right (z-component). The seismograms at four stations (triangles) directly above the source are shown in Fig. 3.34. Peak values of the x-component along four profiles (dashed lines) are displayed in Fig. 3.35.

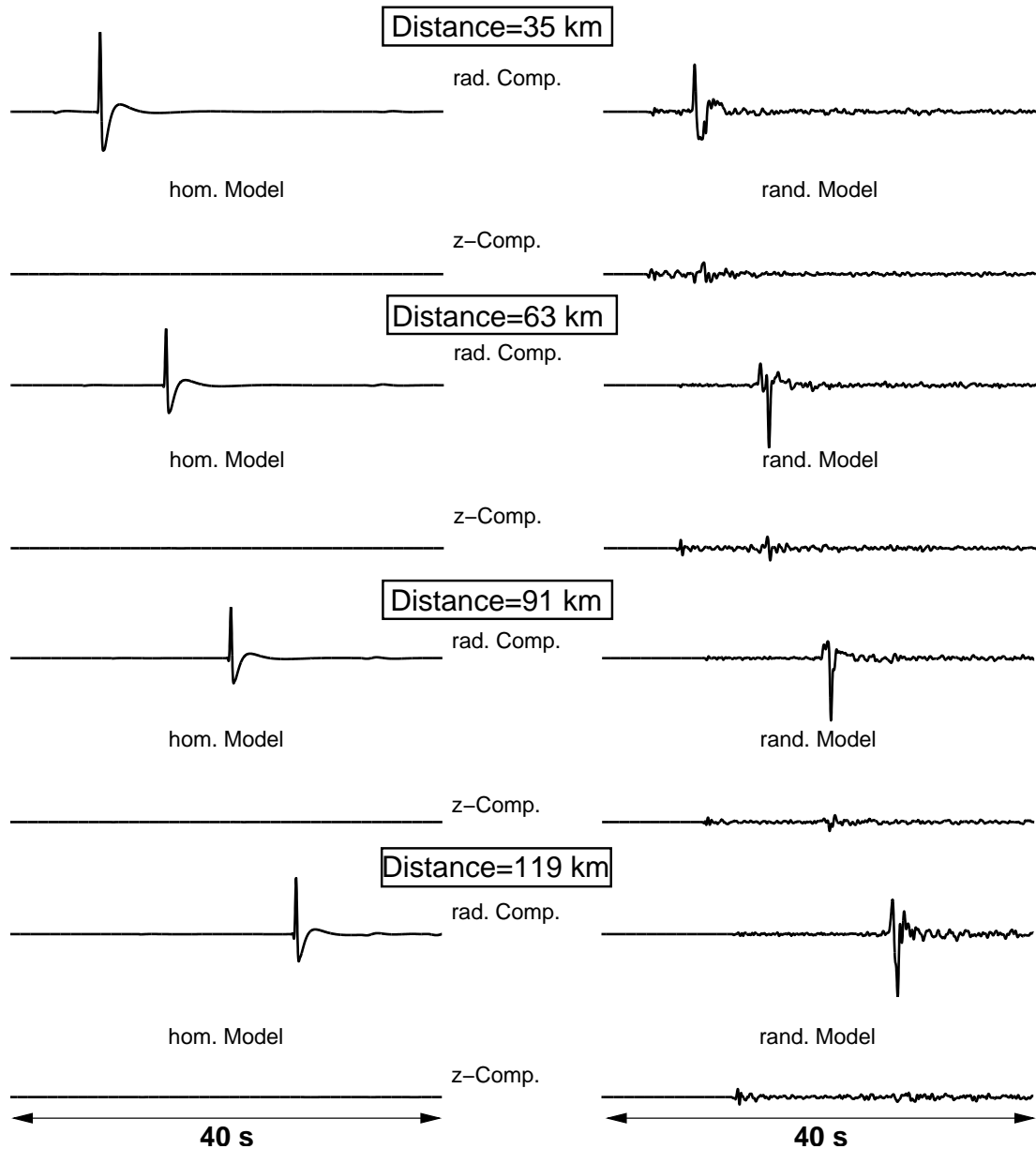


Figure 3.34: Accelerations at the station depicted in Fig. 3.33. For given distance all seismograms have the same scale. Because of the source orientation the S-wave is observed for the x-component and not for the z-components. In the random model a S-wave coda appears in the x-component. Compared to the homogeneous model small amplitudes, which are produced by the initial P- and S-waves, are also observable on the z-component.

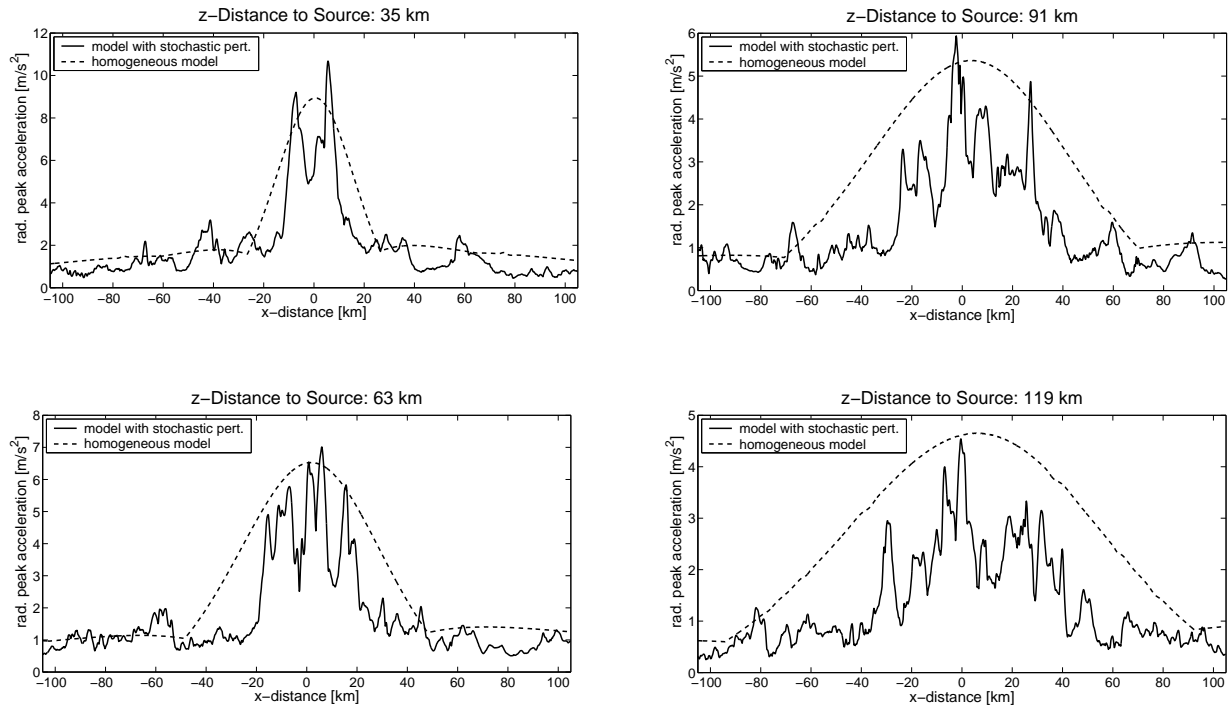


Figure 3.35: Peak values of the x-component along the four profiles indicated in Fig. 3.33 for the homogeneous and random models. The S-wave radiation pattern is clearly visible for the homogeneous case. Within the random model the radiation pattern is also visible but the amplitudes vary strongly. Consequently, the whole profiles reflect the source radiation, but if the amplitudes are only given for a few points, as it is the case for observations of real earthquakes, it is far more difficult to decide whether the radiation pattern is visible or not.

density function decreases and the amplitude increases. Fig. 3.36 shows the moment tensor density functions for $\Delta\sigma$ of 50 MPa, 100 MPa, 150 MPa, 200 MPa, 250 MPa and 300 MPa. The resulting accelerations at station BAL are shown in Fig. 3.37. The amplitude increase of the source wavelets is reflected in the modelled accelerations. To estimate the influence of changes in the damping structure, accelerations at station BAL (location indicated in Fig. 3.13) are modelled for the damping structure given in section 3.3.4 and for twice and half of the applied Q structure, $2Q$ and $0.5Q$ model, respectively (see Table 3.5). For the $2Q$ model the amplitudes increase as the attenuation decreases (see eqs. 3.3 and 3.4). For the $0.5Q$ model attenuation is decreased and therefore the amplitudes of the modelled seismogram increase.

From this it is clear that for the modelling either the stress drop or the damping structure can be changed in order to fit observed seismograms. The best fit was achieved with a stress drop of 150 MPa and applying the damping structure used by Sokolov et al. (2004). It is chosen to keep the damping structure used in Sokolov et al. (2004) to avoid the introduction of a new, also not well constrained, damping structure, which is only adapted to the modelling presented in this chapter. By keeping the damping structure, this work can be more easily compared to other studies, which are also based on the Q model used by Sokolov et al. (2004).

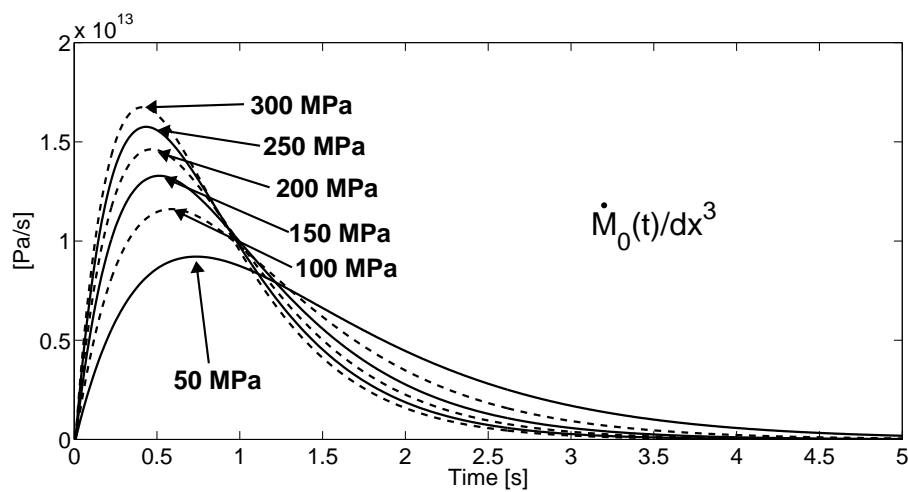


Figure 3.36: Moment tensor density rate function $\dot{M}_0(t)/dx^3$ for different stress drop values. For increasing stress drops rupture time decreases and the amplitude of the source wavelets increases. Because of $t_r \sim 1/\sqrt[3]{\Delta\sigma}$ the amplitude increase is larger between the source wavelets of 50 MPa and 100 MPa compared to the wavelets of 250 MPa and 300 MPa.

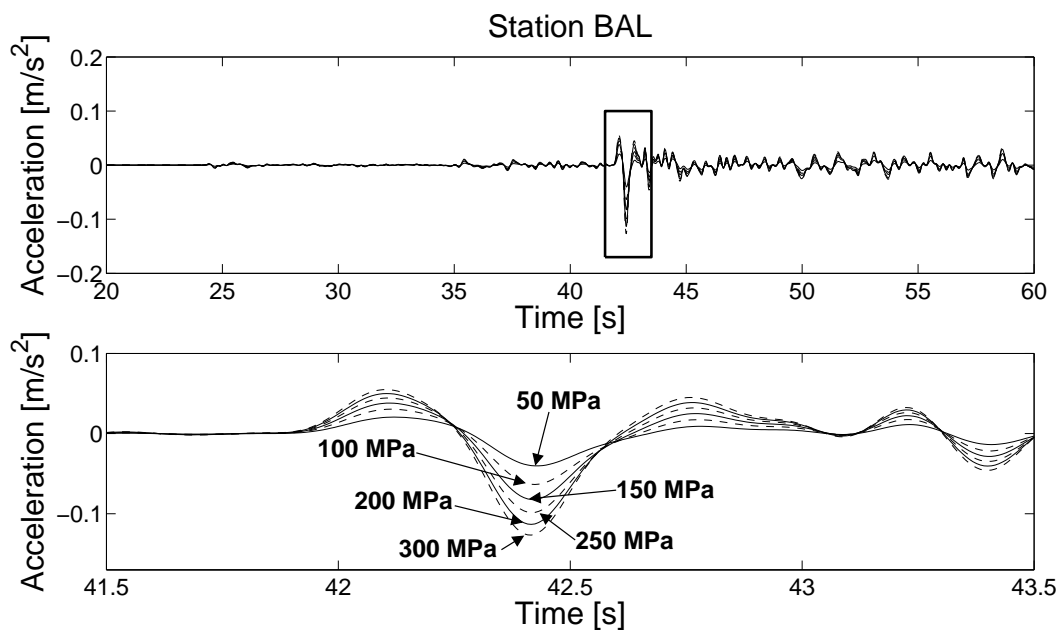


Figure 3.37: Seismogram at BAL for stress drops between 50 MPa and 300 MPa. The S-wave for all stress drops is shown in more detail (bottom).

Depth of Layer [km]	1Q model Sokolov et al. (2004)	0.5Q model	2Q model
0 - 40	$100 f^{0.8}$	$50 f^{0.8}$	$200 f^{0.8}$
40 - 100	$400 f^{0.9}$	$200 f^{0.9}$	$800 f^{0.9}$
> 100	$150 f^{0.8}$	$75 f^{0.8}$	$300 f^{0.8}$

Table 3.5: Accelerations for BAL are calculated for the original Q structure (Sokolov et al., 2004), for half and twice of these Q values.

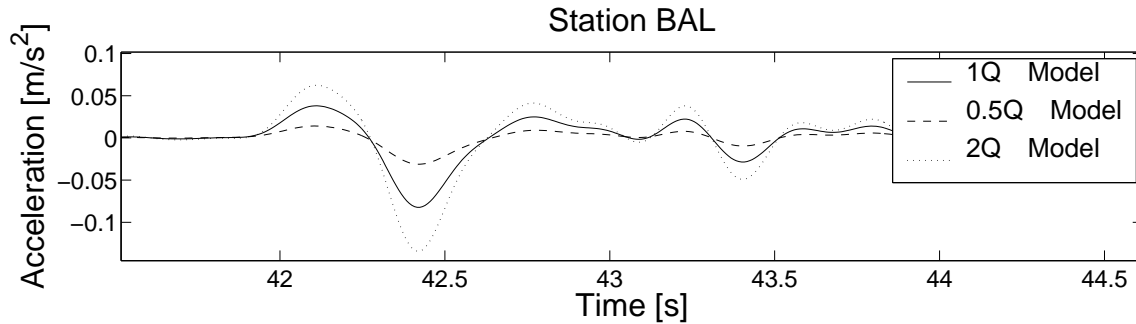


Figure 3.38: Acceleration at BAL is modelled for three different Q models (Table 3.5).

3.7 Conclusions

This chapter presented 2.5D and 3D FD modelling tools for the Vrancea strong earthquakes. 2.5D modelling is obtained by combining simulations for several 2D slices, which are rotated around the hypocentre-epicentre axis. Wave propagation is modelled and analysed for the known complex subsurface structure of SE Romania. The 2.5D and 3D FD simulations revealed that the source radiation in addition with the basement topography produces the typical SW-NE orientated ground motion pattern of the Vrancea strong earthquakes. PGA variations up to a factor of four occur due to influence of the source radiation. Additionally, the maximum S-wave amplitudes are radiated to the deep sedimentary basins east of the epicentre where distinct focusing and defocusing effects occur. Especially the narrow and deep basins in the Carpathian forearc are responsible for strong focusing effects up to a factor of 1.5. The 2.5D and 3D simulations produce similar PGA distributions but amplification varies at some locations significantly due to 3D effects, which cannot be simulated with a 2.5D method. The modelling revealed the remarkable and dominant influence of the source radiation pattern on the modelled ground motions. This is a striking result as in general the influence of the source for frequencies larger than 1 Hz is not necessarily anticipated. However, as discussed in section 3.6.1 studies on different earthquakes found that the influence of the source radiation pattern can be significant also for frequencies larger than 1 Hz. Additionally, the probable large stress drops and the consequently small fault sizes are able to generate a very coherent and strong source signal in contrast to crustal earthquakes. In the next chapter the presented modelling procedures are combined with a method to model the influence of the soft soil layers at the surface, which produce an amplification up to a factor of 2 to 16. This hybrid modelling tool allows the simulation of strong ground motions for past and future Vrancea strong earthquakes.

Chapter 4

Hybrid Modelling of Strong Ground Motions of the Vrancea Earthquakes

4.1 Introduction

In this chapter, a hybrid modelling method is presented, which combines FD simulation of wave propagation and the known site amplification characteristics of SE Romania (Sokolov and Bonjer, 2006). Due to computational limits and the lack of knowledge of the area-wide structure of the uppermost layers (several hundred meters), realistic ground motion cannot be calculated by only using FD. In a first step, wave propagation within the subsurface structure after Martin et al. (2005, 2006) is simulated by applying a FD method. Next, site amplification is added by applying frequency dependent site amplification ratios to the results of the FD simulation. The reliability of this method is shown by comparison of modelled and observed Fourier amplitude spectra (FAS) and macroseismic intensities for the 1986 ($M_W=7.1$) and the 2004 ($M_W=5.9$) earthquakes.

This modelling method is developed within the frame of the Collaborative Research Centre (CRC) 461 "Strong Earthquakes: A Challenge for Geosciences and Civil Engineering", which is located at Karlsruhe University and funded by the Deutsche Forschungsgemeinschaft (DFG). Geoscience and civil engineering institutes work together with their Romanian partners of the Romanian Group for Strong Vrancea Earthquakes (RGVE) to reveal the geophysical processes beneath Vrancea, to investigate past and future ground motions, to estimate the risk potential and to mitigate future losses (SFB461 (2005), <http://www-sfb461.physik.uni-karlsruhe.de>). The modelling presented here is used to complete the sparse database of observed Vrancea strong earthquakes. The simulated FAS (Fourier amplitude spectra) are used by Gottschämmer et al. (2006) to invert for the free parameters, which describe the FAS. These parameters will be used in future research to model ground motions for SE Romania with a stochastic method (Wenzel, 2004; Gottschämmer et al., 2006).

4.2 Hybrid Modelling Method

As outlined in section 1.3.2, the minimum shear wave velocity and the available computer capacity limit the maximum resolvable frequency of FD calculations. Therefore, minimum shear wave velocity of the applied subsurface structure is about 1.6 km/s, which is equivalent to hard rock conditions after the NEHRP (National Earthquake Hazards Reduction Program) classification (FEMA, 2003). Furthermore, even if enough computer capacities would be available, it would not be possible to use only FD because the detailed structure of the uppermost soft soil layers is not known for whole SE Romania. Therefore, after modelling wave propagation with FD from the hypocentre to the surface of the known structure, the influence of the soft soil layers is taken into account by applying average site amplification ratios.

4.2.1 Finite Differences (FD)

A detailed description of the applied 2.5D and 3D FD methods is given in chapter 3. Therefore, this section gives only a brief overview. Wave propagation is modelled from the hypocentre to the surface within the subsurface structure after Martin et al. (2005, 2006). Stochastic velocity perturbations after Hock et al. (2004) are added to the model (see section 3.3.3). The correlation length within the crust is 2 km with a RMS (root mean square) velocity perturbation of 5 %. Correlation length within the mantle is 4 km with 2 % RMS velocity perturbations. 2.5D FD modelling (Karrenbach, 1995) is performed for 350 km wide and about 90 to 131 km deep, depending on the hypocentre depth, 2D slices, which are rotated around the hypocentre-epicentre axis. Grid spacing is 140 m. This yields with the minimum shear wave velocity of about 1.6 km/s to a maximum reliable frequency of about 4.5 Hz (see eq. 1.19). For stability reasons the time increment is chosen as 8 ms (see eq. 1.19). Wave propagation is simulated for 8000 time steps, which corresponds to 64 s. The 2D to 3D correction is performed as described in section 1.7. 3D FD wave propagation is simulated by applying the code of Olsen (1994). Grid spacing is 500 m and consequently the maximum reliable frequency is about 0.6 Hz. The horizontal extension of the models is 170 km with a depth of 150 km. Wave propagation is simulated for 7000 time steps with a time increment of 17 ms. Intrinsic attenuation is included into the 2.5D and 3D modelling as described in section 3.3.4. The modelling in chapter 3 showed that the source radiation is responsible for PGA variations up to a factor of four and the basin structure produces an amplification up to a factor of 1.5. The site amplification ratios are introduced in the next section.

4.2.2 Site Effects

Sokolov et al. (2004) calculated for 26 K2 (Bonjer and Grecu, 2004; Bonjer et al., 2000) permanent network stations and 35 CALIXTO (Carpathian Arc Lithospheric X-Tomography) temporary stations (Martin et al., 2005, 2006) frequency dependent site amplification ratios. This

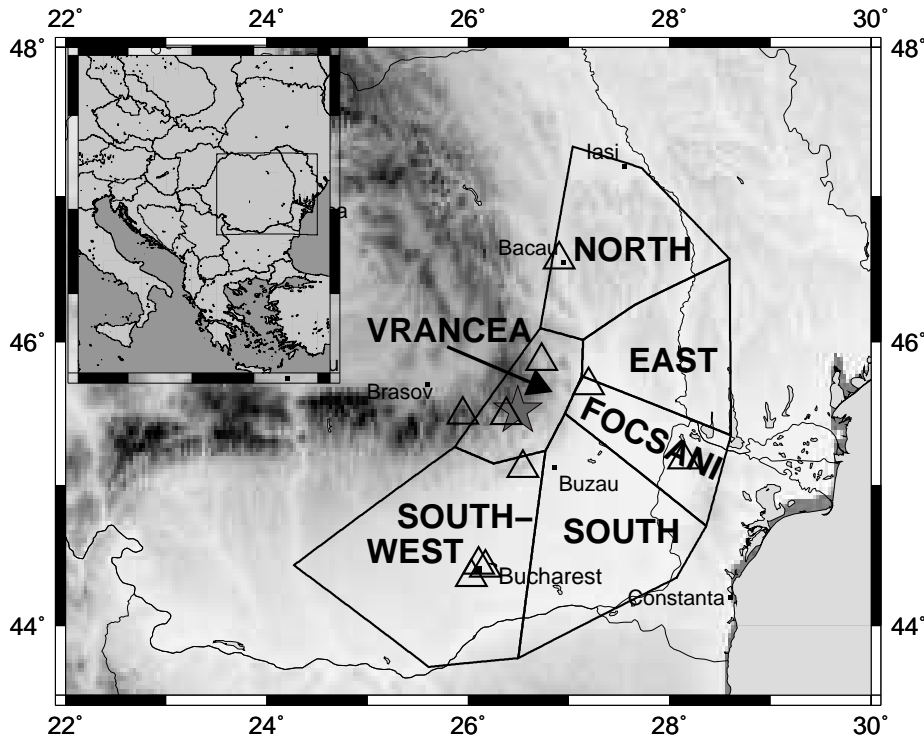


Figure 4.1: The map indicates the six regions for which average site amplification ratios are given by Sokolov and Bonjer (2006). The site amplification ratios are displayed in Fig. 4.2. Observed and modelled seismograms are compared at the stations depicted by triangles.

was done by simulating the FAS with known source and propagation parameters at the locations of seismic stations. The simulated FAS are classified as "very hard rock" (VHR)-FAS as no assumption on the local site effects is made. By comparing the calculated VHR-FAS with records of real earthquakes, frequency site amplification ratios are derived for each station (Sokolov et al., 2004). Based on these data average amplification ratios are given in Sokolov and Bonjer (2006) for six regions in SE Romania (Fig. 4.1 and 4.2). To include the site amplification in the modelling, the FAS of the seismograms produced by the FD modelling are multiplied by the corresponding region dependent amplification ratios. Next, inverse Fourier transformation yields to the corresponding signal in the time domain. This procedure modifies only the amplitude spectra, therefore the influence on the phase of the time series is ignored. For comparison between modelled and observed seismograms and spectra at specific stations, the site specific ratios are applied, if they are given by Sokolov and Bonjer (2006). Fig. 4.3 shows the seismogram resulting from the FD simulation and the amplified seismogram after applying the frequency dependent amplification ratios. Best fit between modelling and observation is obtained by applying the mean plus one standard deviation of the amplification ratios. Therefore, all seismograms and spectra given in this chapter are amplified in this way. The applied amplification ratios vary between 2 and 10 for the frequency range between 0.1 and 2 Hz. For frequencies between 2 and 4.5 Hz, which is the maximum frequency of the modelling, the amplification ratios are 5 to 17.

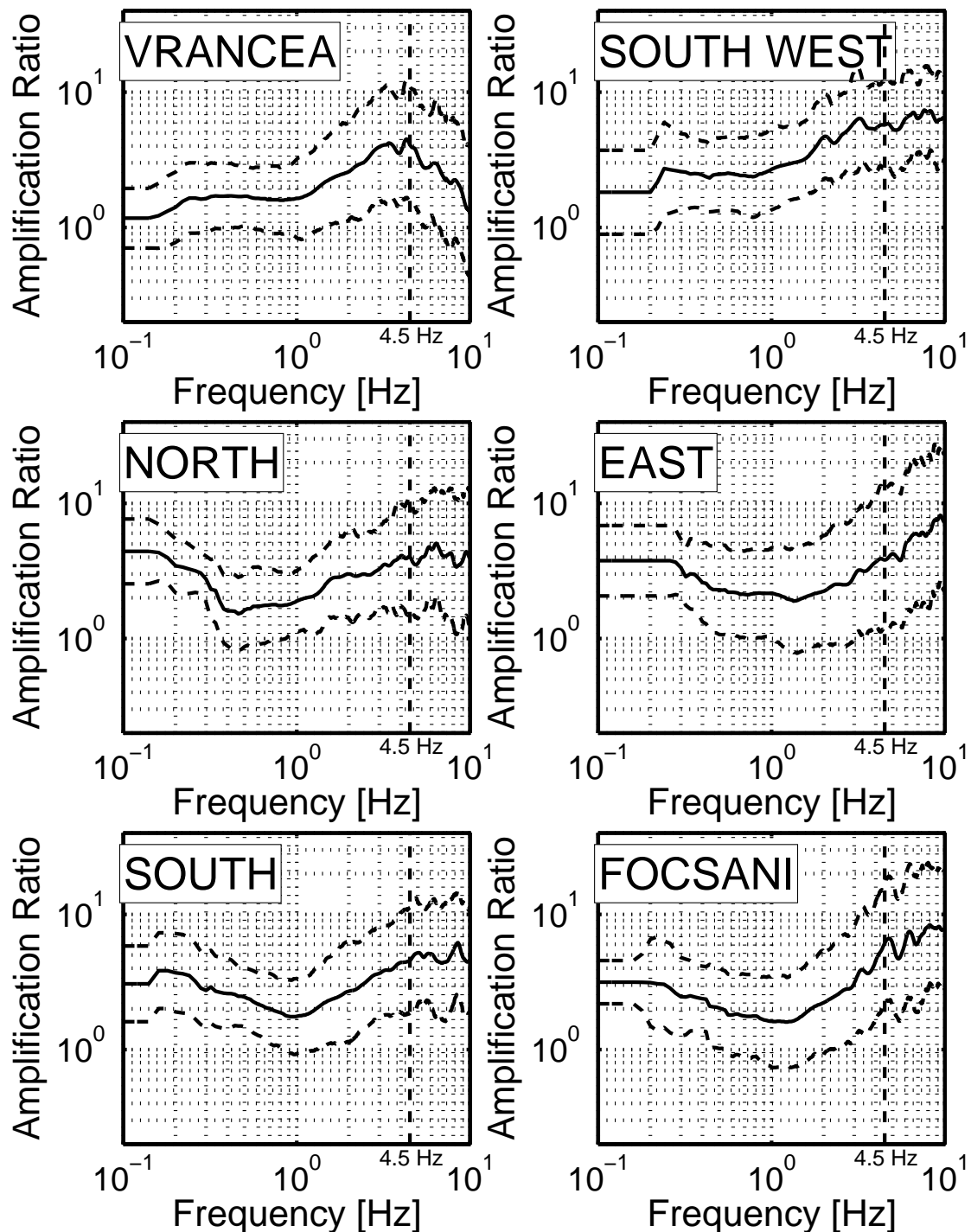


Figure 4.2: Mean frequency dependent site amplification ratios between 0.2 and 10 Hz with mean \pm 1 standard deviation after Sokolov and Bonjer (2006). The locations of the regions are shown in Fig. 4.1. In this work the mean+1 standard deviation is used to amplify the modelled seismograms. For the frequency range between 0.1 and 2 Hz the amplification ratios vary between 2 and 10. For frequencies between 2 and 4.5 Hz, which is the maximum frequency of the modelling, the amplification ratios are 5 to 17.

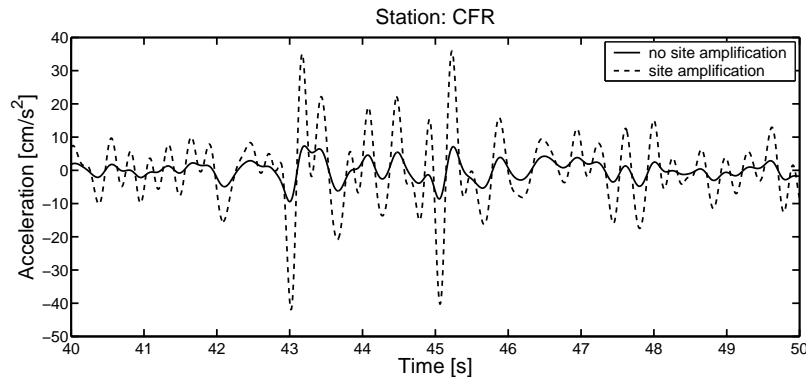


Figure 4.3: The solid signal displays the radial component at CFR modelled by FD. The dashed line shows the seismogram after adding the corresponding site amplification for region FOCSANI.

Azimuth [°]	0.0	11.7	14.4	15.1	15.8	25.6	40.0	45.0	60.0	68.7
Station	-	BAL	CRL	BAC	BUC	VRI	-	-	-	SDR
Azimuth [°]	69.9	85.8	88.00	90.0	92.0	105.9	120.0	135.0	150	174.6
Station	FOC	MLR	-	-	-	CFR	-	-	-	ISR

Table 4.1: Azimuths of the 2D slices used to model the 1986 earthquake. Ten slices cross the location of seismic stations.

4.3 Modelling of the 1986 Vrancea Strong Earthquake ($M_W = 7.1$)

Fig. 4.4 displays the location of the stations and the focal mechanism of the 1986 earthquake. The 1986 strong earthquake was recorded by twenty stations. In contrast, for the 1977 earthquake only records from station INC exist. Therefore, the 1986 event is used to validate the hybrid modelling method. The source is modelled as a point source and it is scaled after section 1.5.1 with a stress drop of 150 MPa. The resulting moment density rate function is displayed in Fig. 3.12. The strike, dip and rake angles of the 1986 earthquake are given in Table 3.1.

4.3.1 2.5D FD Modelling

Wave propagation is simulated for 20 2D slices, which are rotated around the hypocentre-epicentre axis (section 3.4 and Fig. 3.11). The azimuths of the 20 2D slices are given in Table 4.1. Seismograms are modelled for 10 stations. These are seven stations BAC, CFR, FOC, ISR, MLR, SDR and VRI outside Bucharest and three stations BAL, BUC and CRL within Bucharest. The station locations are indicated in Fig. 4.4. The observed and modelled accelerograms are bandpass-filtered between 0.1 and 4.5 Hz. The observed components are rotated in radial and transverse direction, which corresponds to the components modelled by the 2.5D FD modelling.

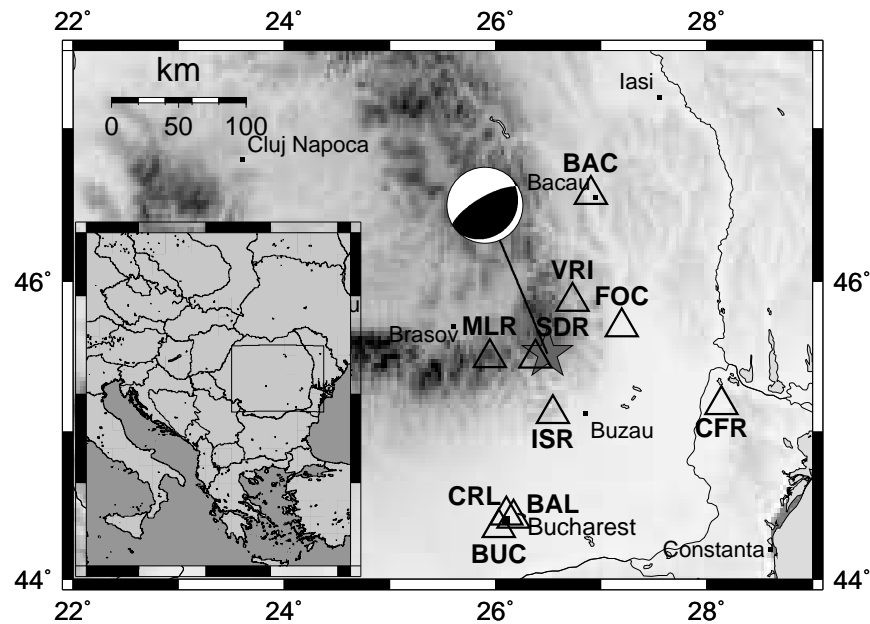


Figure 4.4: Focal mechanism and location of the 1986 earthquake. Seismograms are simulated for the stations indicated by triangles.

Fig. 4.5 to 4.9 display the observed radial, transverse and vertical components. On most seismograms the P- and S-wave arrivals are clearly visible. The transverse component of the modelled seismograms does not show P-waves as in 2D, the transverse component corresponds to pure SH-waves. The modelled and observed amplitudes are in all cases similar. However, the shape of the seismograms, especially the coda, differ on several components. For stations BAC, BUC and FOC, the observed seismograms show distinctive codas compared to the modelling. The shapes of the S-wave codas are similar at stations BAL, CFR, and SDR. A good fit between the observed and modelled seismogram would mean that the modelling reproduces the waveform and the maximum amplitude of the observed time series. Here, it is necessary to point out that the random velocity fluctuations, which are introduced into the model, produce realistic wave form shapes, but depend strongly on the actual model of random fluctuations beneath the corresponding station. This means that simulation of wave propagation for a set of different random generated fluctuations may produce significantly different waveforms at specific positions. Consequently, it is more appropriate to look at the FAS, which are linked with macroseismic intensity (Sokolov, 2002) and therefore with damage. Furthermore, the spectra are the parameters that can be used by the procedure proposed by Gottschämmer et al. (2006) to invert for the parameters, which give the best description of the spectra. Therefore, the quality of the modelling is described in this chapter by comparing modelled and observed FAS. Fig. 4.10 to 4.11 show the arithmetic mean of the FAS of the radial and transverse components. Additionally, the reference spectra for intensity VI to X after Sokolov (2002) are plotted. The representative frequencies of these intensities are in the frequency range of the modelling up to 4.5 Hz. The modelled and observed spectra at BUC, CFR, CRL, VRI and SDR are in good comparison with the observed spectra, which means

Frequency Range [Hz]	0.11 - 0.23	0.23 - 0.48	0.48 - 1.02	1.02 - 2.13	2.13 - 4.48
Centre Frequency [Hz]	0.1586	0.3333	0.7003	1.4720	3.0931

Table 4.2: Frequency ranges and centre frequencies (in the logarithmic space) used to calculate SR.

Station	BAC	BAL	BUC	CFR	CRL	FOC	ISR	MLR	SDR	VRI
SSR	0.086	0.098	0.022	0.025	0.049	0.037	0.12	0.032	0.027	0.014

Table 4.3: 2.5D modelling of the 1986 earthquake: Summarised square residual (SSR) for all stations (see eq. 4.2). Stations VRI, BUC and CFR show the lowest misfits.

that the intensity deviation is clearly smaller than one intensity unit. At BAC the modelled spectrum shows slightly smaller amplitudes than the real spectrum. At BAL the modelled values are larger than the observed spectrum. At BAC and BAL the deviation is about one intensity unit. Good comparison is achieved at FOC for frequencies of about 0.5 and 1.5 Hz and for frequencies higher than 3.1 Hz. At ISR the modelling overestimates the observation, except for frequencies between about 1.4 and 2.8 Hz. Maximum intensity deviation of two intensity units is found for frequencies larger than 2.8 Hz. However, comparing the whole spectra the maximum deviation can be estimated as one intensity value. The modelling shows the same intensities at five of the ten stations and at two stations the FAS are reproduced for smaller frequency ranges. To give a quantitative measurement of the quality of the modelling, the misfit between observed and modelled spectra is calculated for five frequency ranges. Table 4.2 gives the frequency ranges and the corresponding centre frequencies. The misfit for each frequency range is defined as the square residual SR between the logarithmic average observed and modelled spectral values $\log_{10}(S_{obs})$ and $\log_{10}(S_{mod})$ within each frequency range:

$$SR = (\log_{10}(S_{obs}) - \log_{10}(S_{mod}))^2. \quad (4.1)$$

The summarised square residual SSR describes the misfit for the whole frequency range and is calculated as follows:

$$SSR = \sum_{n=1}^N \frac{(\log_{10}(S_{obs}) - \log_{10}(S_{mod}))^2}{N}, \quad (4.2)$$

with $N = 5$ as five frequency ranges are considered. Fig. 4.12 displays the residuals of all stations at the centre frequencies of the considered frequency ranges and the average values for each frequency range. The values show a large scatter for each frequency range. The average values lay between 0.03 and 0.07. Minimum average value is calculated for the frequency range between 0.48 and 1.02 Hz. Table 4.3 lists the SSR for each spectra. As the above given visual comparison of the FAS showed, stations VRI, BUC and CFR show the lowest misfits. The largest SSR are calculated for stations ISR and BAL.

Fig. 4.13 displays the modelled peak horizontal acceleration (PHA). PHA is calculated as the maximum of the resulting horizontal component a_{hor} :

$$a_{hor}(t) = \sqrt{a_r(t)^2 + a_t(t)^2}, \quad (4.3)$$

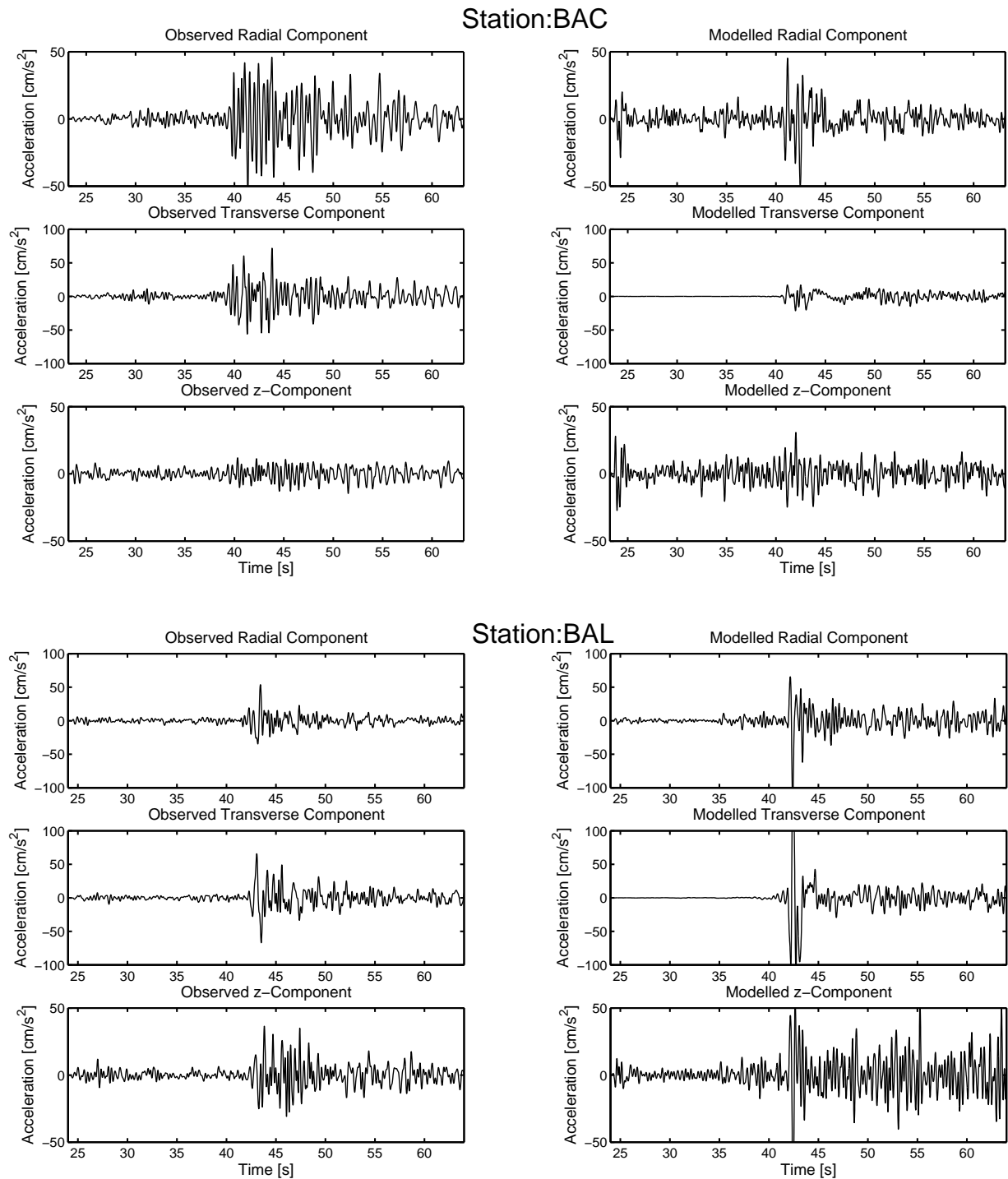


Figure 4.5: Observed (left) and modelled (right) seismograms at BAC and BAL. The modelled amplitudes at BAC are smaller than the observed accelerations. At BAL the modelling overestimates the observation but the modelled length of the S-wave pulse is similar to the observation.

4.3 Modelling of the 1986 Vrancea Strong Earthquake ($M_W = 7.1$)

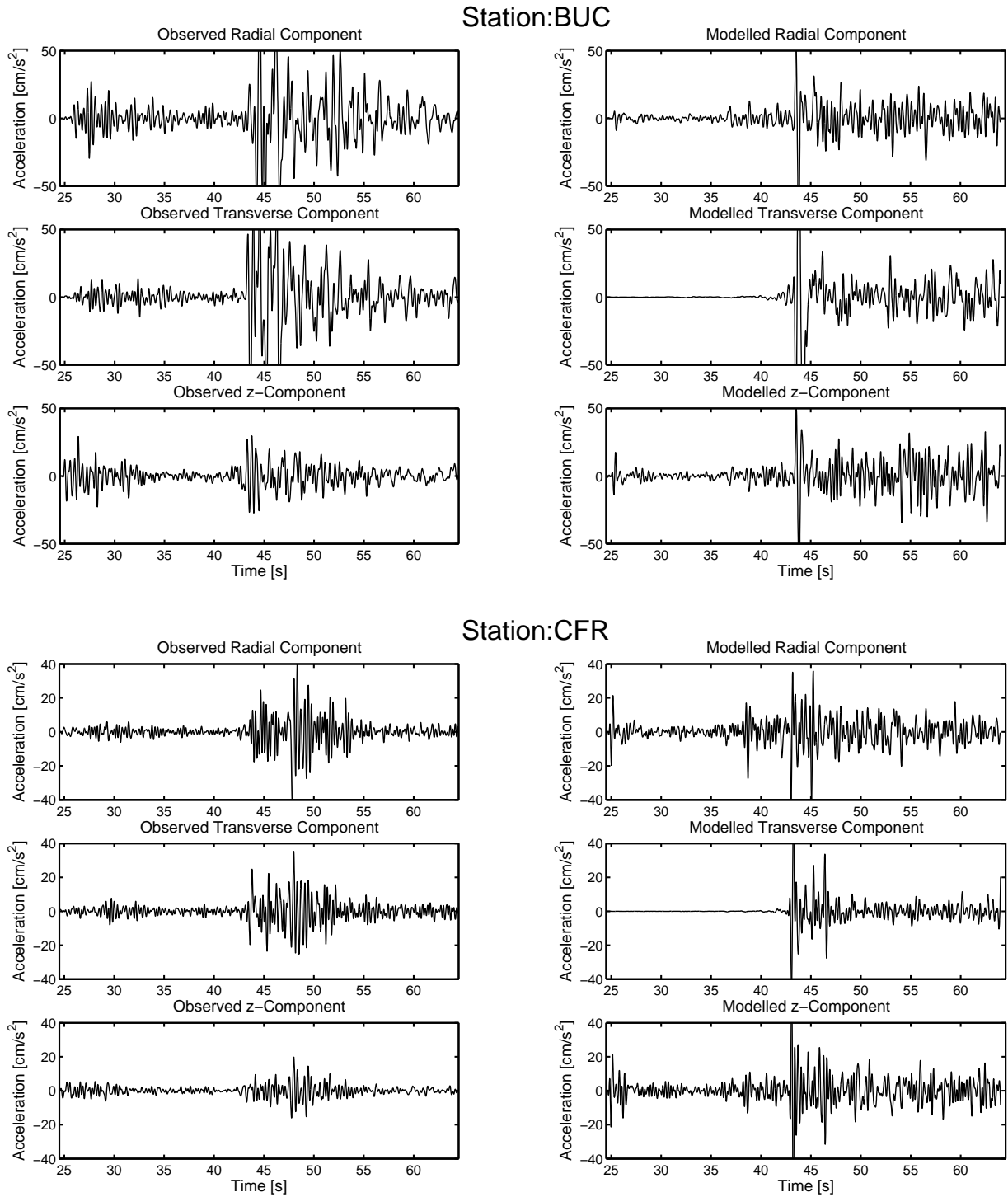


Figure 4.6: Observed (left) and modelled (right) seismograms at BUC and CFR. The observed waveforms at BUC show larger scattering than the modelling. At CFR the modelled and observed horizontal components show similar maximum amplitudes.

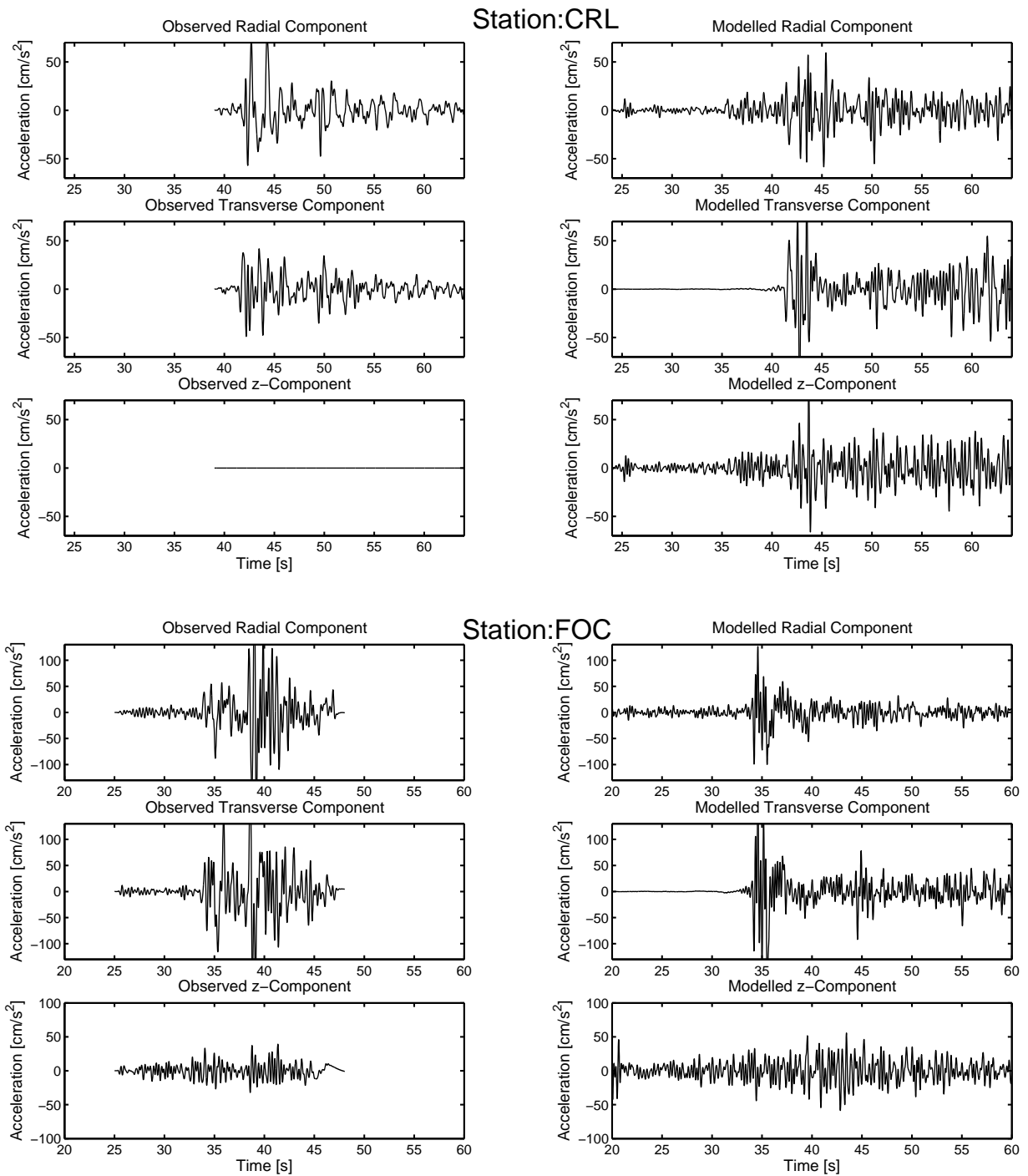


Figure 4.7: Observed (left) and modelled (right) seismograms at CRL and FOC. At both stations the modelling reproduces the maximum amplitudes. The observed and modelled horizontal components at CRL show a phase arrival about 5 s after the S-wave. At FOC the observed signal is more scattered than the observed time series. The modelled and observed vertical components at FOC show a similar pattern.

4.3 Modelling of the 1986 Vrancea Strong Earthquake ($M_W = 7.1$)

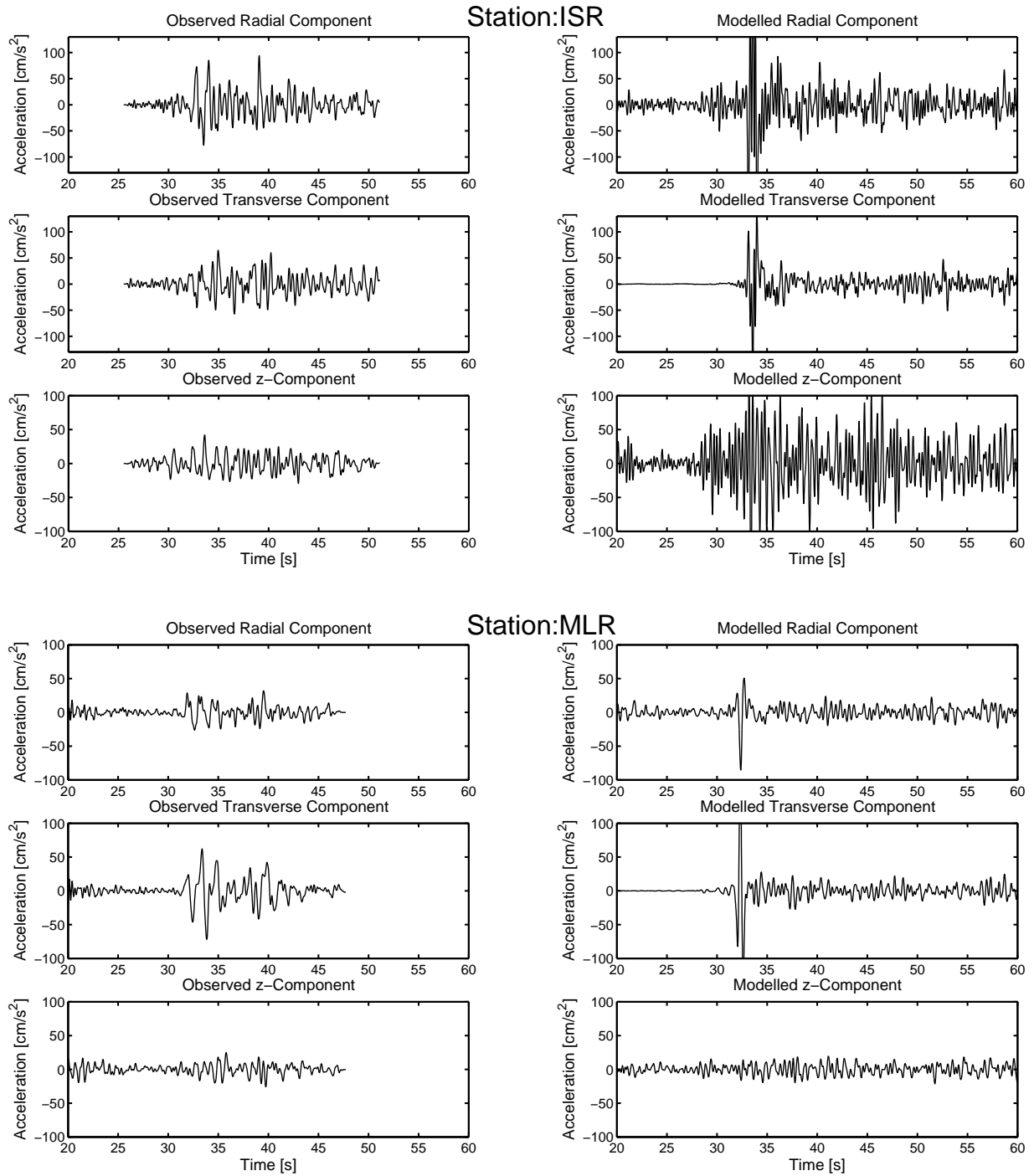


Figure 4.8: Observed (left) and modelled (right) seismograms at ISR and MLR. At ISR the modelled amplitudes are larger than the observed amplitudes for all three components. At MLR the modelled S-wave pulse shows a very sharp form compared to the observation. The modelled and observed vertical components at MLR are very similar.

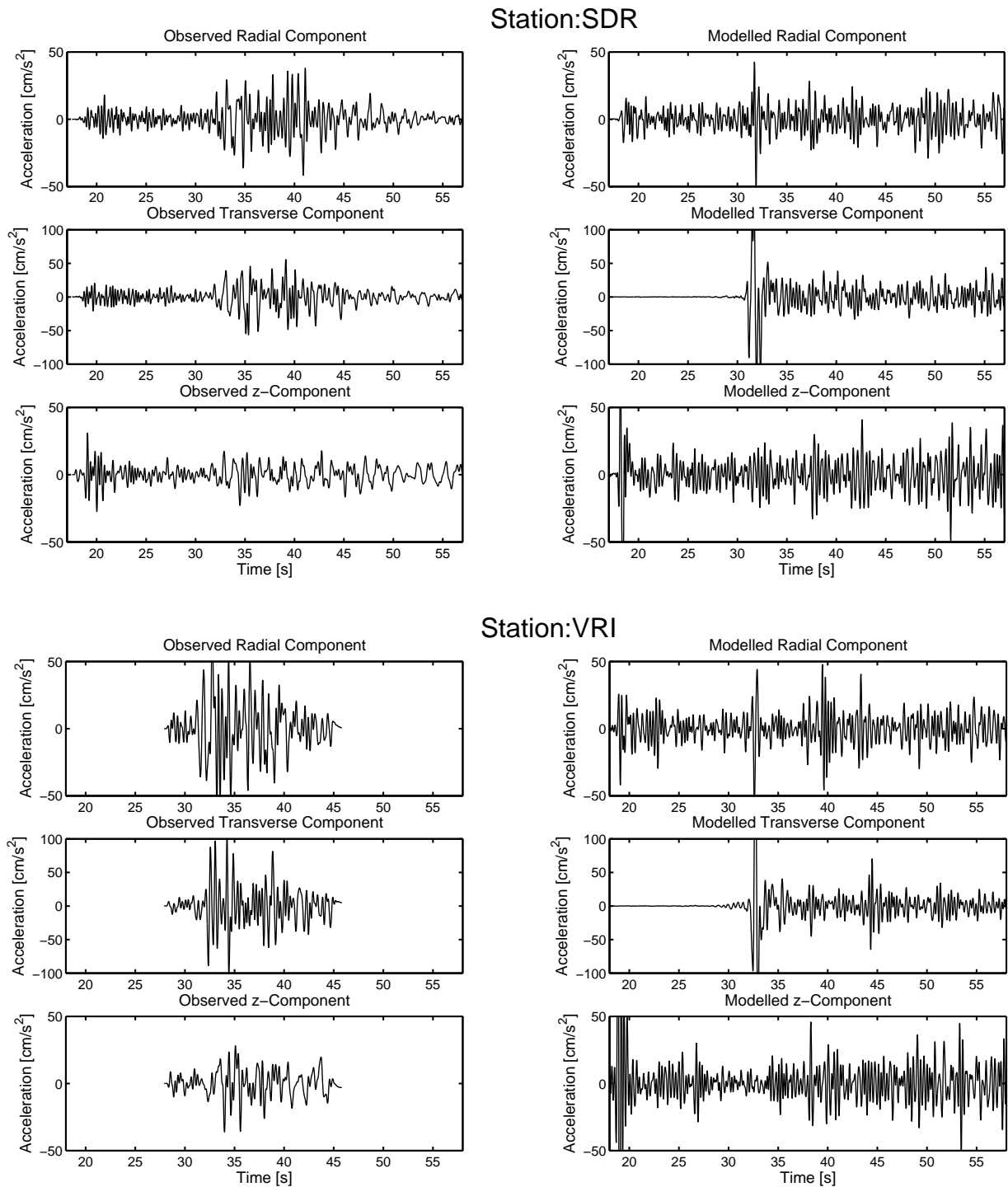


Figure 4.9: Observed (left) and modelled (right) seismograms at SDR and VRI. For both stations the modelled and observed time series show similar amplitudes but the waveforms are very different.

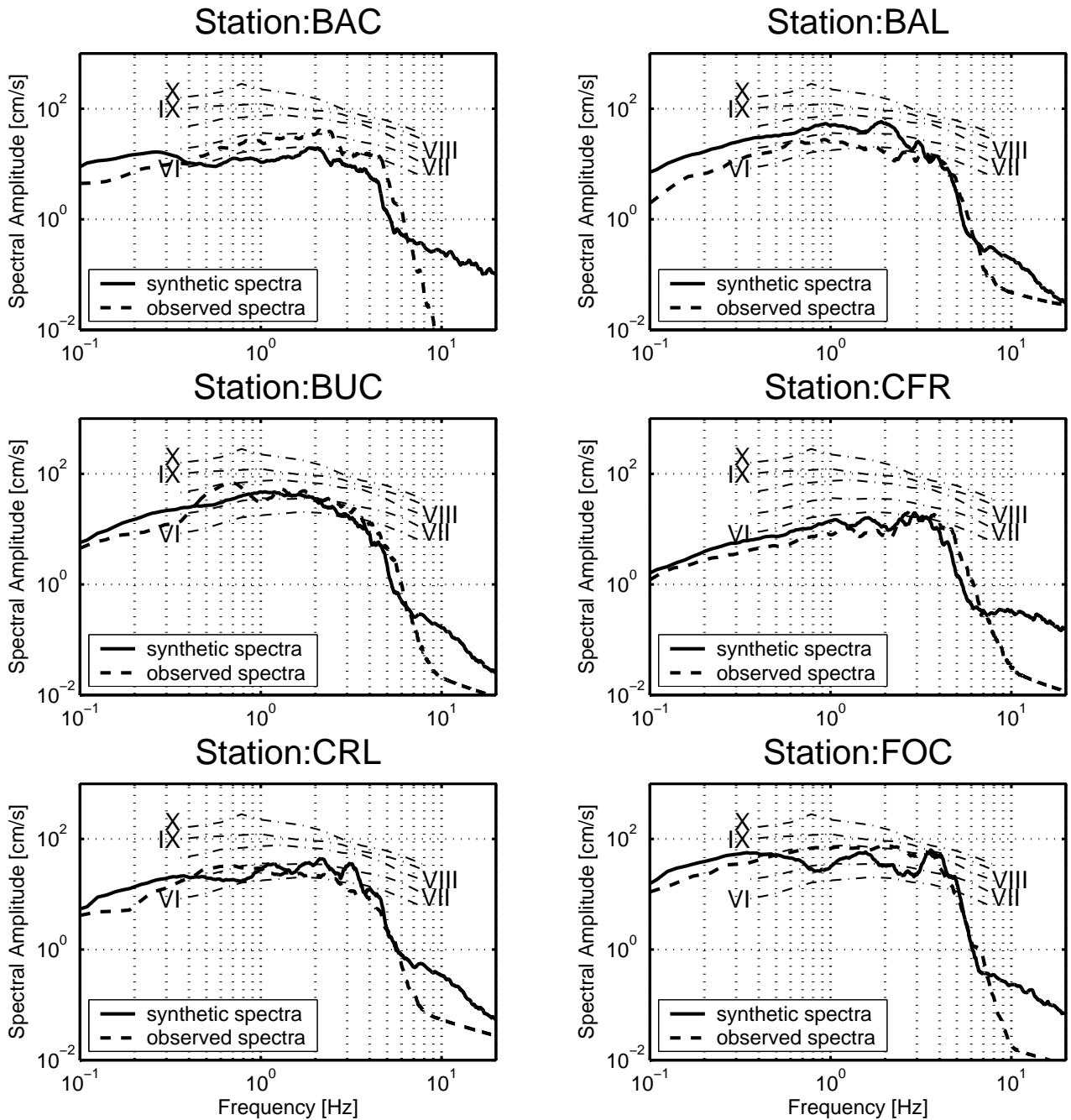


Figure 4.10: 2.5D modelling of the 1986 earthquake: Modelled and observed Fourier amplitude spectra (FAS) at BAC, BAL, BUC, CFR, CRL and FOC and reference spectra for macroseismic intensities VI to X after Sokolov (2002). The modelling fits the observation at BUC, CFR and CRL. At BAC the modelling underestimates the observations. Only for frequencies higher than 3.2 Hz the observed amplitudes are reproduced. At BAL the modelled amplitude is too large. For BAC and BAL the intensity deviation is about one intensity unit. At FOC modelling and observations show about the same amplitude at 0.5 Hz, 1.5 Hz and for frequencies higher than 3.1 Hz. Maximum intensity deviation is about one intensity unit at FOC.

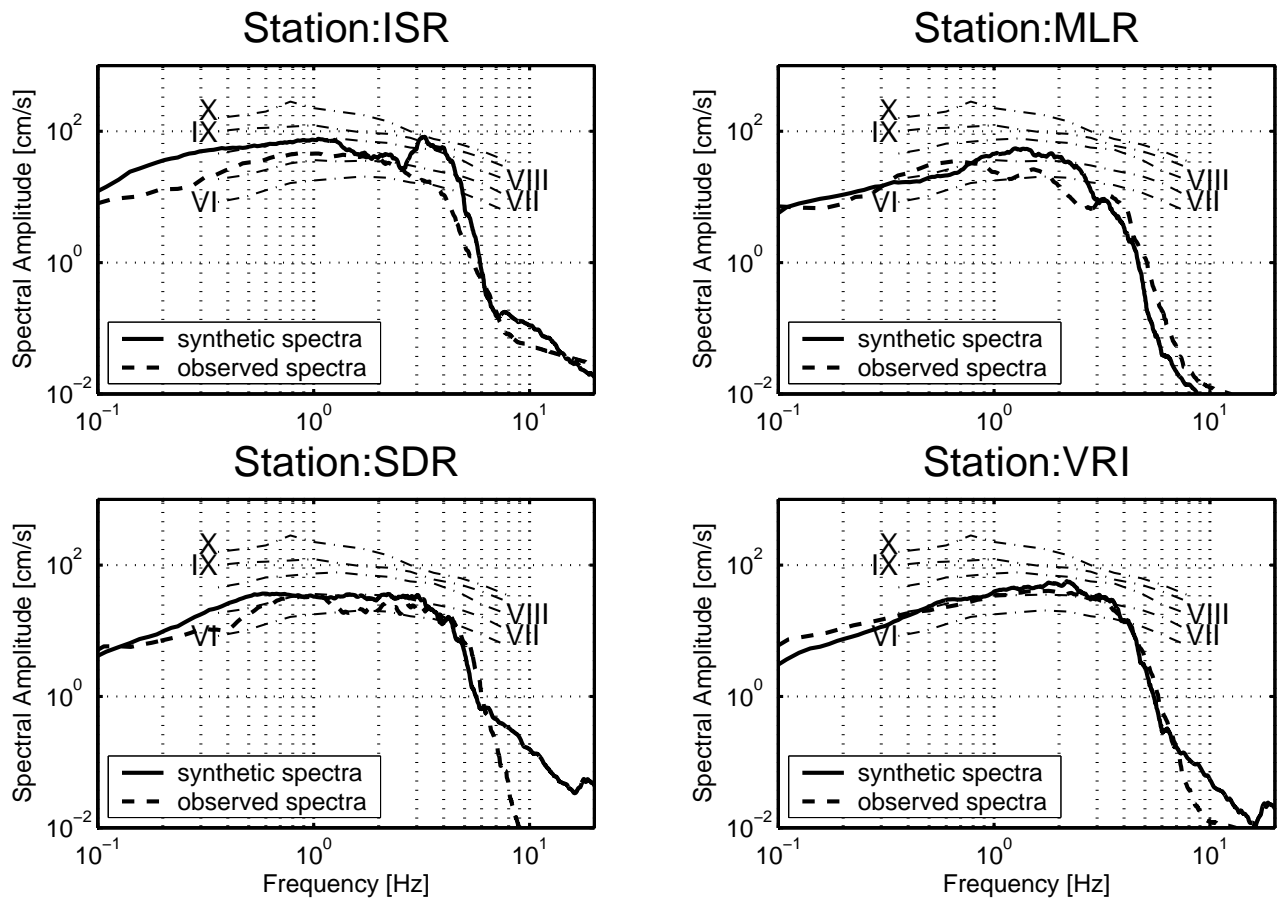


Figure 4.11: 2.5D modelling of the 1986 earthquake: Modelled and observed FAS at ISR, MLR, VRI and SDR and reference spectra for macroseismic intensities VI to X after Sokolov (2002). The modelling reproduces the observed FAS at VRI and SDR. At ISR modelling and observation show the same spectral amplitude between 1.4 and 2.8 Hz. Maximum intensity deviation of two units is found for ISR for frequencies larger than 2.8 Hz. However, for the whole frequency range the deviation is about one intensity unit. For MLR the comparison shows discrepancies between 0.9 and 2 Hz. But the overall intensity deviation is also about one intensity unit.

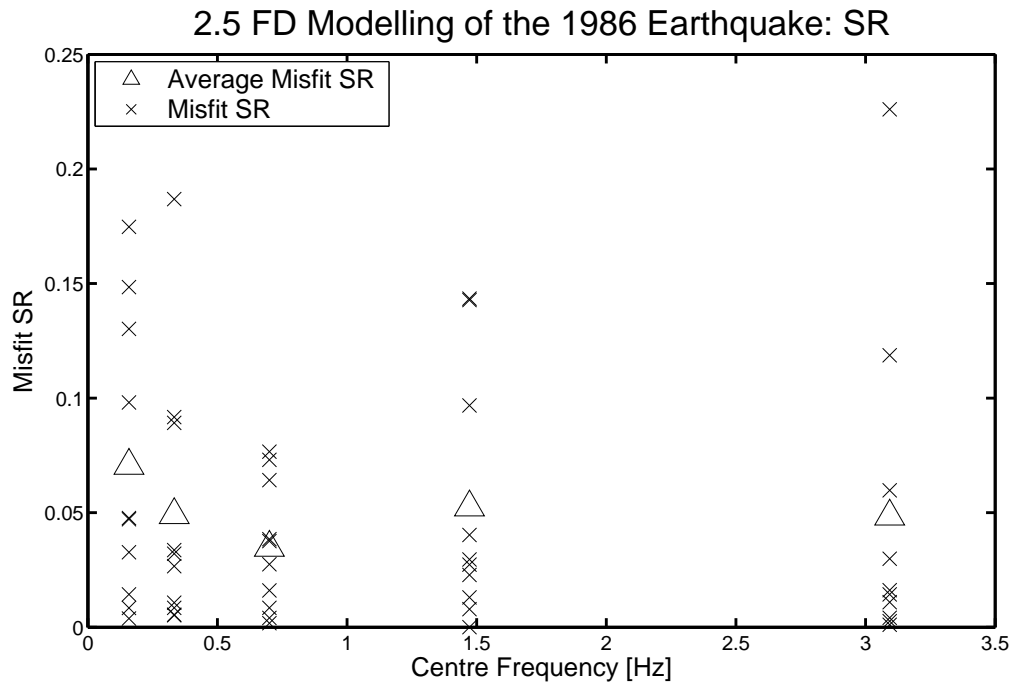


Figure 4.12: 2.5D modelling of the 1986 earthquake: Misfit SR of all ten stations plotted at the centre frequency. The values show no clear correlation with frequency. The average values within a frequency range are depicted by triangles. The frequency range between 0.48 and 1.02 Hz shows the lowest average value.

with the acceleration $a_r(t)$ in radial and $a_t(t)$ in transverse direction. The grey lines mark the regions for which the site amplification ratios are known (see 4.1). Outside these regions a frequency independent constant amplification ratio of 1, corresponding to "Very Hard Rock" (VHR), is applied. Large accelerations up to 700 cm/s^2 are found 30 to 60 km east of the epicentre. The overall PHA pattern is SW-NE orientated, which is the same distinctive form as shown by the macroseismic intensity distribution (see Fig. 3.2). The large accelerations of about 900 cm/s^2 in a narrow region south of the epicentre are most likely produced by the random model structure in combination with the basement features.

Next, the synthetic seismograms are translated into macroseismic intensities. This allows an area-wide comparison between modelling and observation and not only a pointwise comparison at the location of seismic stations. The relation between FAS and intensities are given by Sokolov (2002) and explained in chapter 2.4. The method proposed by Sokolov (2002) evaluates the frequency range up to 13 Hz with representative frequency ranges for each intensity value. Here, this procedure is not applicable because the maximum frequency of the modelling is 4.5 Hz. Therefore, the same procedure as used in section 2.4 and in Miksat et al. (2005) is applied. As each intensity value is assigned to a representative frequency range, the minimum intensity which can be evaluated for frequencies up to 4.5 Hz is about VI. The resulting calculated and observed intensity distributions of the 1986 earthquake are shown in Fig. 4.14. At a few points intensities up to X are simulated. A large pattern of intensities VIII is modelled about

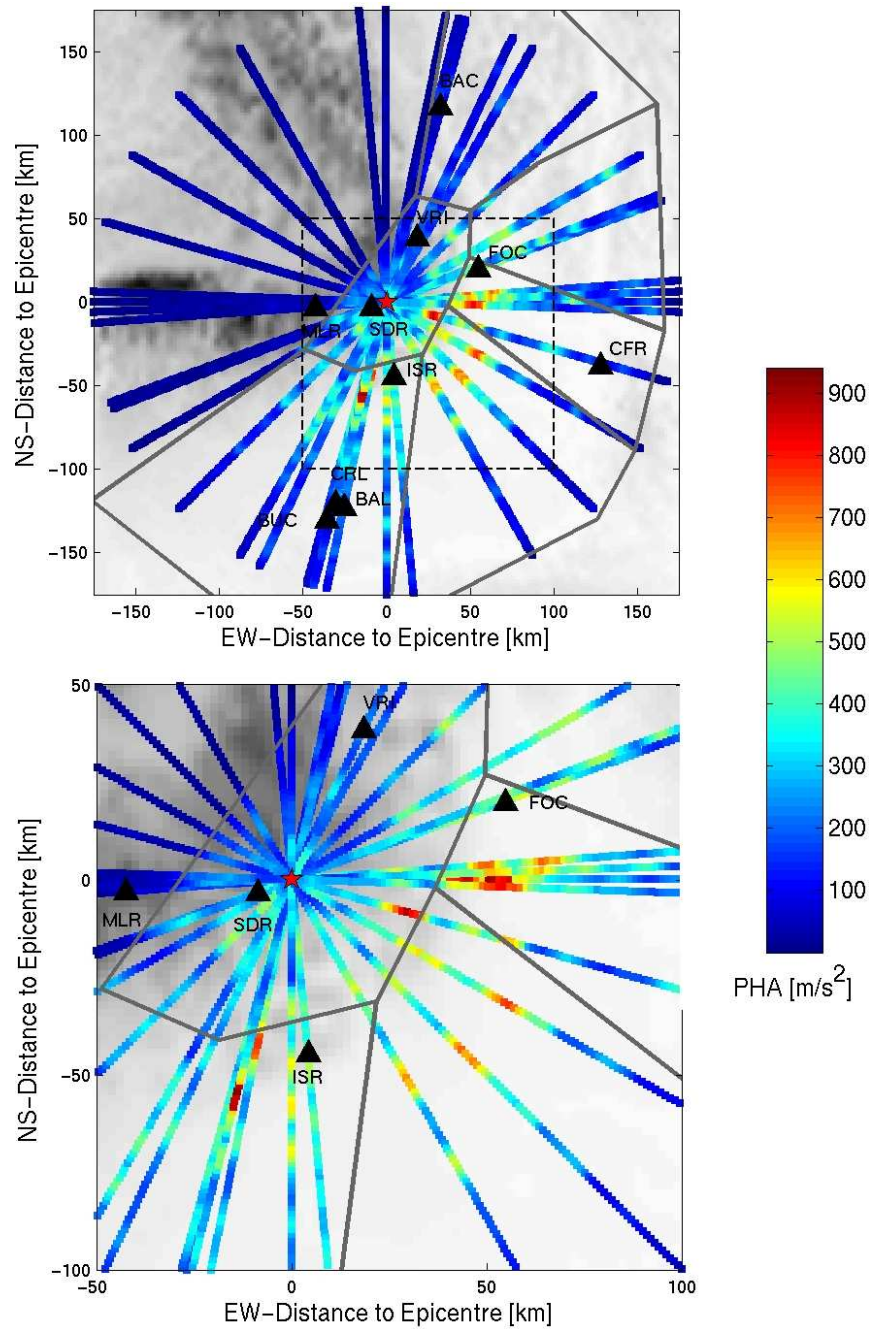


Figure 4.13: 2.5D modelling of the 1986 earthquake: Modelled PHA distribution for the 1986 earthquake. The grey lines mark the regions for which frequency dependent site amplification ratios are available. The red star indicates the epicentre of the 1986 earthquake. Station locations are marked by black triangles. The PHA distribution within the dashed rectangle (in the top image) is displayed in the bottom image. The overall PHA distribution shows the typical SW-NE orientation of the Vrancea earthquakes. Large PHA values up to about 700 cm/s^2 are calculated in a distance of 30 to 60 km east of the epicentre .

Station	CFR	FOC	ISR	SDR	VRI
SSR	0.33	0.02	0.27	0.10	0.10

Table 4.4: 3D modelling of the 1986 Earthquake: Summarised square residual (SSR) for all stations (see eq. 4.2). Lowest SSR are found for SDR and VRI.

25 to 70 km east of the epicentre. This pattern shows an overlap with the observed pattern of intensity VIII. Intensity of VIII is also modelled on small regions S to SE of the epicentre. For this regions the modelling overestimates the observation. East and SE of the epicentre the modelling reproduces the observed isoseismal of intensity VII. Towards the South, the intensity decrease of the observed values is stronger than the decrease of the modelled values. In N to NE direction, the modelled intensities are lower than the observed intensities. The modelling reproduces the overall SW-NE orientated pattern and absolute values. After the European Macroseismic Scale (EMS; Grünthal, 1998) macroseismic intensities are evaluated in a statistical sense such as 'intensity n is characterised by a high damage rate for most buildings of class X'. Consequently, it is likely that the small regions of modelled intensity IX and X would not be reproduced by macroseismic maps. Additionally, the shown intensity maps give the isoseismal lines, which represent a smoothed image of the original evaluation and therefore excludes very localised outliers. The modelled larger regions with intensity VIII south and SE of the epicentre suggest that the simplified procedure tends to overestimate the intensity values. Therefore, adoption of the intensity evaluation after Sokolov (2002) to the low frequency range should be performed. The quality of the modelling depends also on the azimuth. This suggests that a regional dependent Q structure would improve the modelling of strong ground motions for the Vrancea earthquakes.

4.3.2 3D Modelling of the 1986 Earthquake

3D modelling of ground motion is performed for a model that includes the stations CFR, ISR, FOC, SDR and VRI. The maximum frequency is 0.6 Hz. Fig. 4.15 shows the average FAS at CFR, ISR, FOC, SDR and VRI. At station CFR and FOC the modelling reproduces the observations. Also at VRI the observed frequencies between 0.2 and 0.6 Hz are reproduced by the modelling. At SDR and ISR the modelled amplitudes are larger than the observed spectra. Table 4.4 displays the summarised spectral residual (SSR; see eq. 4.2) for the first two frequency ranges between 0.11 and 0.48 Hz. The lowest SSR are given for station SDR and VRI. The modelled PHA distribution is displayed in Fig. 4.16. It shows the typically SW-NE orientated pattern. Maximum PHA of about 200 cm/s^2 occurs 40 km east of the epicentre. After Sokolov (2002) the frequency range up to 0.6 Hz only includes a small frequency band of the representative frequencies for intensity VII and IX. Therefore, the procedure used to evaluate intensities for the 2.5D modelling is not applicable for the low frequency 3D modelling.

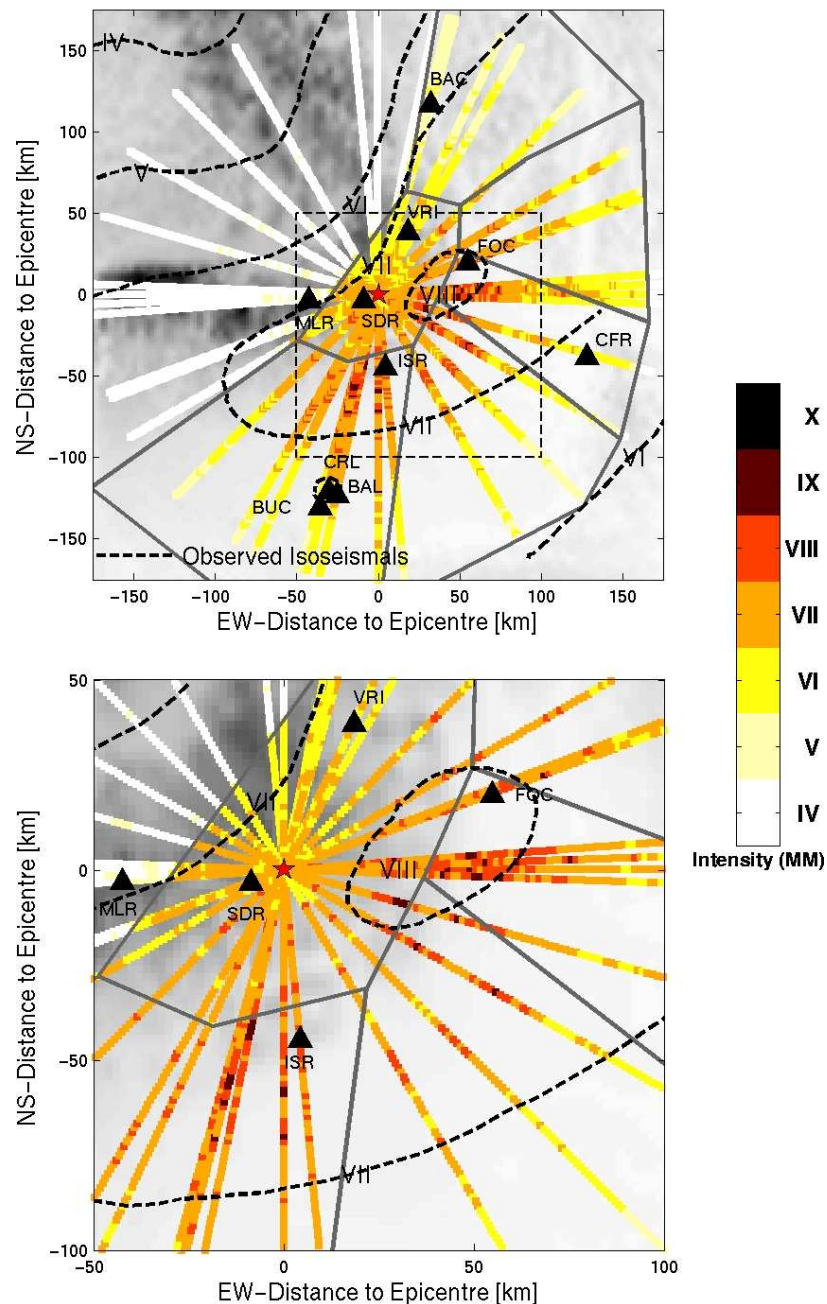


Figure 4.14: 2.5D modelling of the 1986 earthquake: The map shows the modelled macroseismic intensities for 20 profiles. The dashed lines indicate the observed isoseismal lines of the 1986 earthquake (see also Fig. 3.2). A detailed view of the intensities within the dashed rectangle indicated in the top image is shown in the bottom image. At a few locations intensities of X are calculated. Modelling and observation show in the same region about 25 to 75 km east of the epicentre an intensity of VIII. East and SE of the epicentre the modelled intensities reproduce the observed isoseismal of intensity VII. Towards the South the observed isoseismal of VII is overestimated. In northern to NE direction the modelled intensities are lower than the observed values of VII.

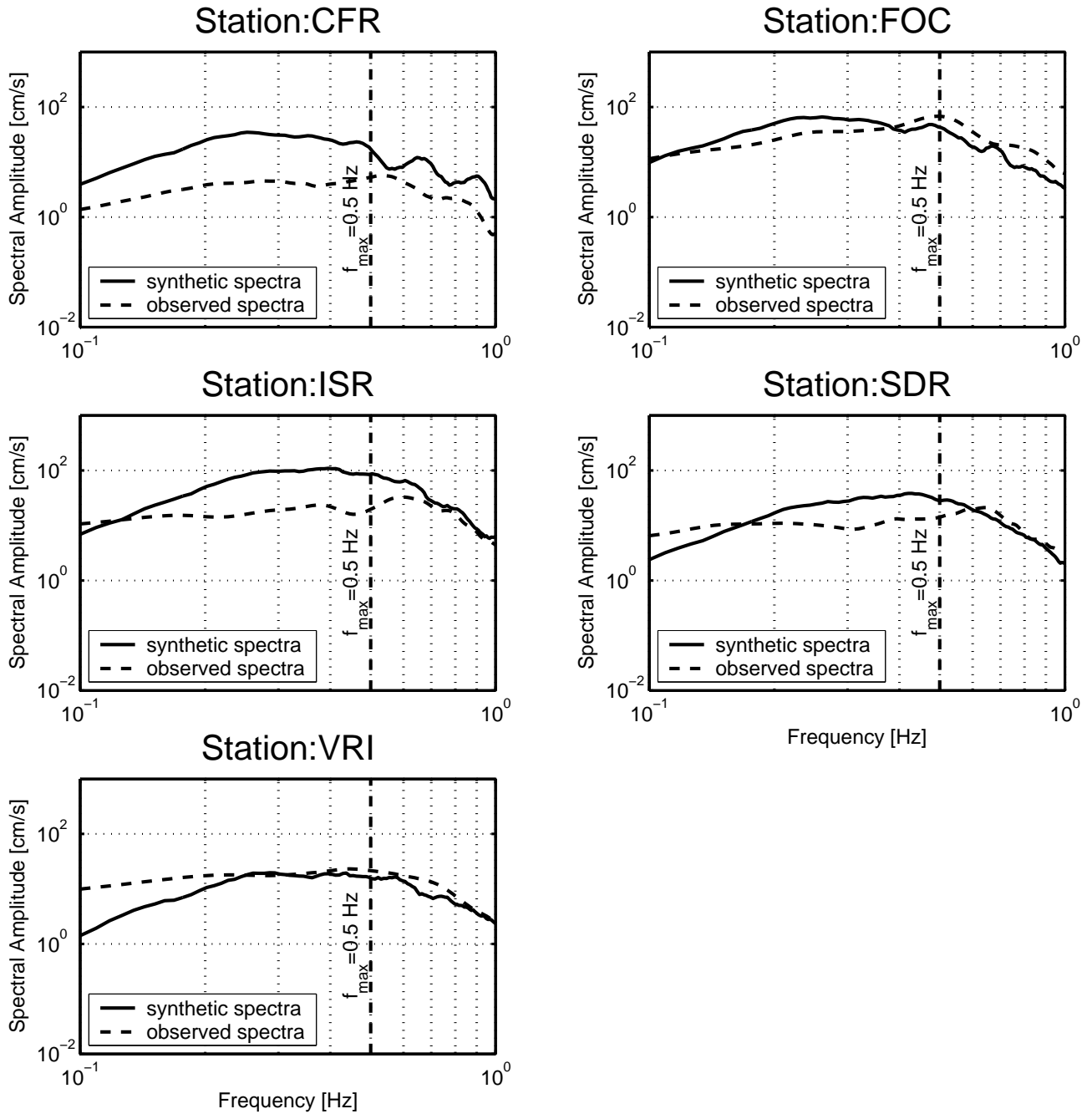


Figure 4.15: 3D modelling of the 1986 earthquake: The 3D modelling shows the best fit of the observed spectra FOC. At VRI the observed amplitudes between 0.2 and 0.6 Hz are reproduced by the modelling. At CFR, ISR and SDR the modelling overestimates the observed amplitudes. This indicates that the frequency content up to about 0.5 Hz of the applied source differs from the real earthquake source of the 1986 earthquake.

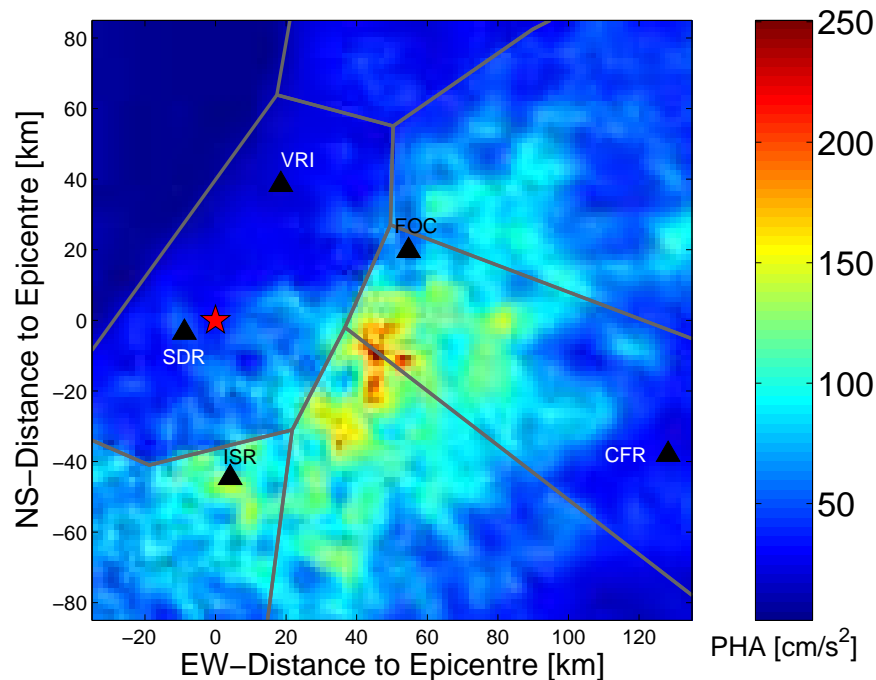


Figure 4.16: 3D modelling of the 1986 earthquake: PHA resulting from 3D modelling for frequencies up to 0.6 Hz. The red star marks the epicentre and the grey lines the boundaries of the regions for which amplification ratios are available (see Fig. 4.1). Strong motion stations are indicated by black triangles. Maximum PHA of about 200 cm/s^2 is modelled about 40 km east of the epicentre. The PHA distribution shows the distinctive SW-NE oriented pattern, typical for the intensity distributions of Vrancea earthquakes.

4.4 Modelling of the 2004 Earthquake ($M_w=5.9$)

On October 27th, 2004 a $M_w=5.9$ occurred in a depth of 98.6 km. Minor damage occurred in the Bucharest area. This event was the largest since the $M_w=6.9$ earthquake in 1990. The earthquake shows a thrust fault plane solution very similar to the other strong earthquakes. Unfortunately, no macroseismic intensity evaluation of this earthquake is published. However, the "Did you feel it?" programme of the USGS released intensity values based on an online questionnaire (<http://earthquake.usgs.gov/eqcenter/dyfi.php>). The distribution of evaluated intensities (Fig. 4.18) suggests a pattern very similar to previous earthquakes (see Fig. 3.2) with SW-NE elongated isoseismal lines. Due to the ambiguity of fault plane solutions, the Harvard centroid moment tensor catalogue (<http://www.seismology.harvard.edu/CMTsearch.html>) gives one fault plane with strike = 335° , dip = 19° and slip = 27° . The values for the second fault plane are similar to the values of the other larger Vrancea earthquakes with strike = 219° , dip = 81° and slip = 107° . Therefore, these values are adopted to simulate the earthquake. Fig. 4.17 shows the focal mechanism and the location of the epicentre. The source is modelled as a point source and it is scaled after section 1.5.1 with a stress drop of 150 MPa.

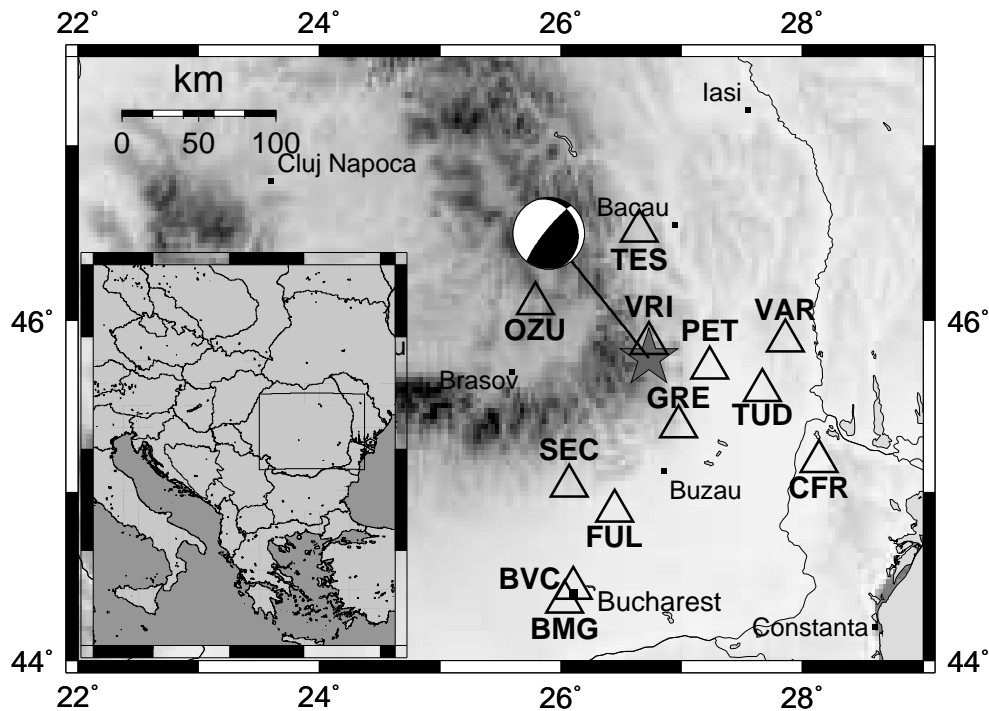


Figure 4.17: The map shows the epicentre and the focal mechanism after the Harvard centroid moment tensor catalogue. The triangles depict strong motion stations for which ground motion is modelled.

4.4.1 2.5D Modelling of the 2004 Earthquake

Ground motion is modelled for 20 profiles. Twelve profiles cross the location of seismic stations of the K2 network. Table 4.5 gives the azimuths of the slices and the corresponding station names. Fig. 4.19 and 4.20 display the observed and modelled FAS at these stations. At stations CFR, GRE, OZU, PET and TUD the modelling reproduces the observed spectra for the whole frequency range up to 4.5 Hz. At other stations the amplitudes of the real spectra are reproduced by the modelling for smaller frequency ranges. These are at BMG frequencies larger than 0.4 Hz, at FUL and TES frequencies smaller than 0.9 Hz and at VRI frequencies larger than 2 Hz. The modelled spectrum clearly underestimates the observed spectrum at SEC where unusual large accelerations up to 0.2 g were recorded for the frequency range up to 4.5 Hz. Fig. 4.21 displays the misfit SR (eq. 4.1) within the five frequency ranges listed in Table 4.2. Lowest average misfits SR is calculated for frequencies between 0.23 and 0.48 Hz. The average SR values for each frequency range are lower than 0.11, which is about the same as in the modelling of the 1986 earthquake (see Fig. 4.12). Only for stations SEC and FUL the misfit SR shows in more than one intensity range larger values than the maximum misfits for the 1986 earthquake. For station BMG only the SR of 0.41 within the first frequency range is larger than the maximum values for the 1986 earthquake. The summarised SSR are listed in Table 4.6, which are also in the same range as for the modelling of the 1986 earthquake (see Table 4.3). Lowest SSR are

USGS Community Internet Intensity Map (40 miles NNW of Buzau, Romania)
 ID:qqck_d4 20:34:37 GMT OCT 27 2004 Mag=5.9 Latitude=N45.70 Longitude=E26.56

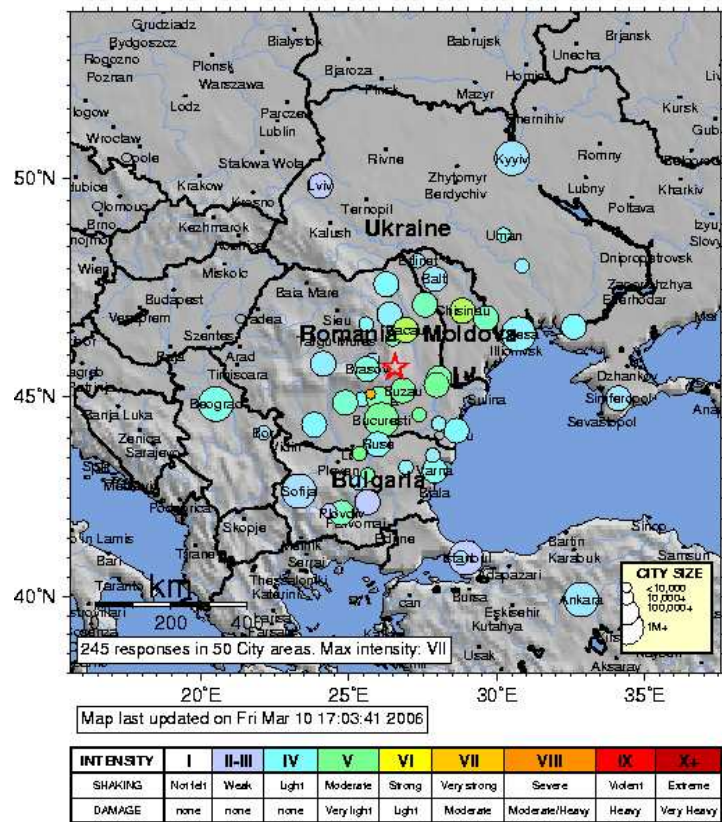


Figure 4.18: Macroseismic intensity map released by the USGS. The intensities are based on an online questionnaire in the frame of the USGS "Did you feel it?" programme. The intensity distribution indicates the same SW-NE elongated pattern as other strong Vrancea earthquakes (see Fig. 3.2)

calculated for PET and TUD. The deviation between the modelled and observed macroseismic intensities cannot be compared directly because the spectral values correspond to intensities with representative frequencies larger than 4.5 Hz. However, the modelling of the 2004 event produces SR and SSR values similar to the modelling of the 1986 earthquake, which suggests for the 2004 event also a maximum intensity deviation of one intensity unit. Fig. 4.22 shows the modelled PHA observations along the 20 profiles. Largest values of about 250 cm/s² occur E to SE of the epicentre.

Azimuth [°]	0.0	12.9	18.4	19.3	32.2	40.0	45.0	60.0	82.3	90.0
Station	-	FUL	BVC	BMG	SEC	-	-	-	VAR	-
Azimuth [°]	101.7	105.6	116.0	120.0	120.9	135.0	150.0	156.6	175.7	178.9
Station	FUL	TUD	OZU	-	CFR	-	-	GRE	TES	VRI

Table 4.5: Azimuths of the 2D slices used to model the 2004 earthquake. Ten slices cross the location of seismic stations.

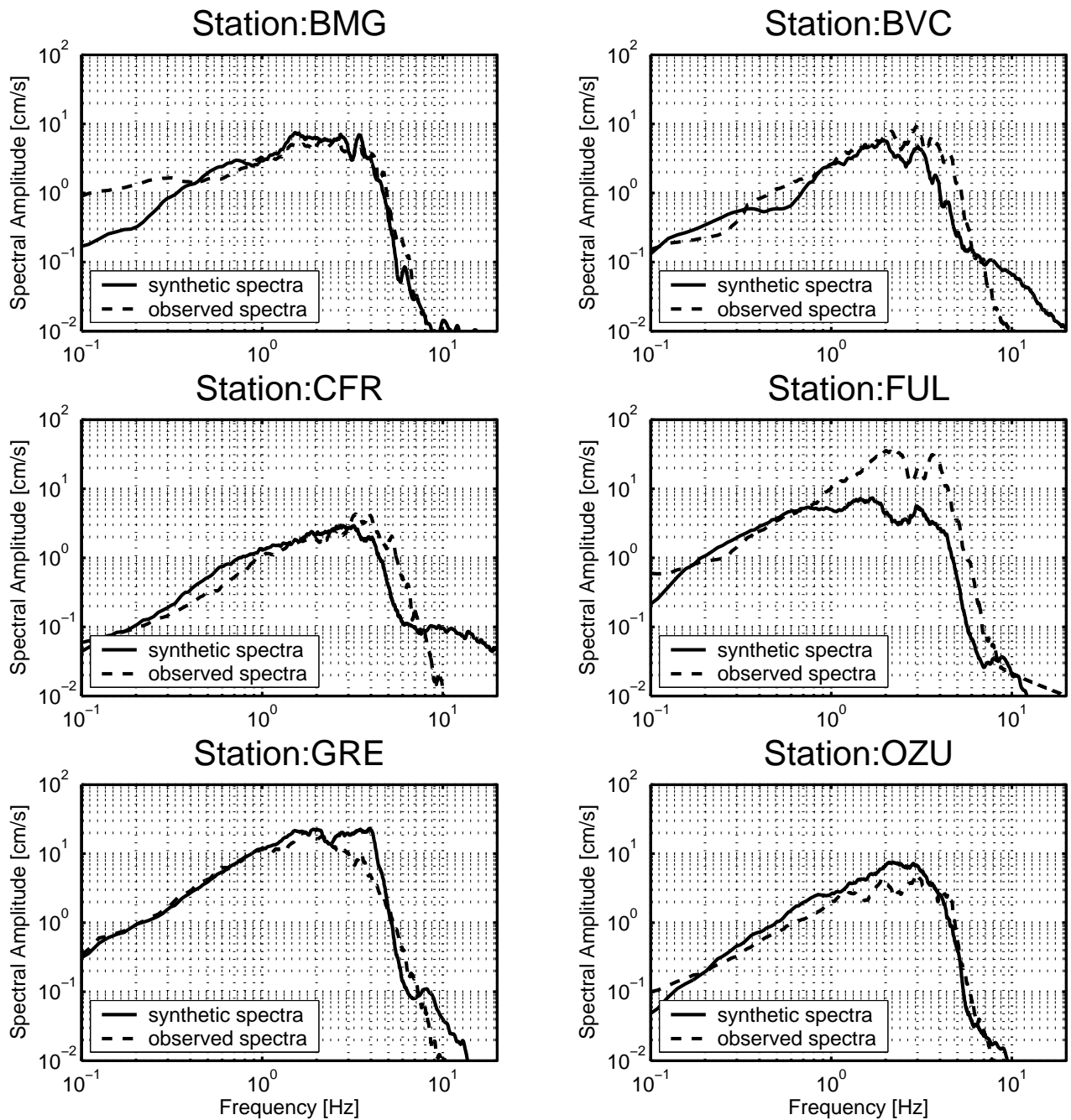


Figure 4.19: Observed and modelled (2.5D) spectra at BMG, BVC, CFR, FUL, GRE and OZU for the 2004 earthquake. At CFR, GRE and OZU the modelling reproduces the observed spectra for the whole frequency range up to 4.5 Hz. At FUL the modelling underestimates the observed spectrum for frequencies larger than 1 Hz.

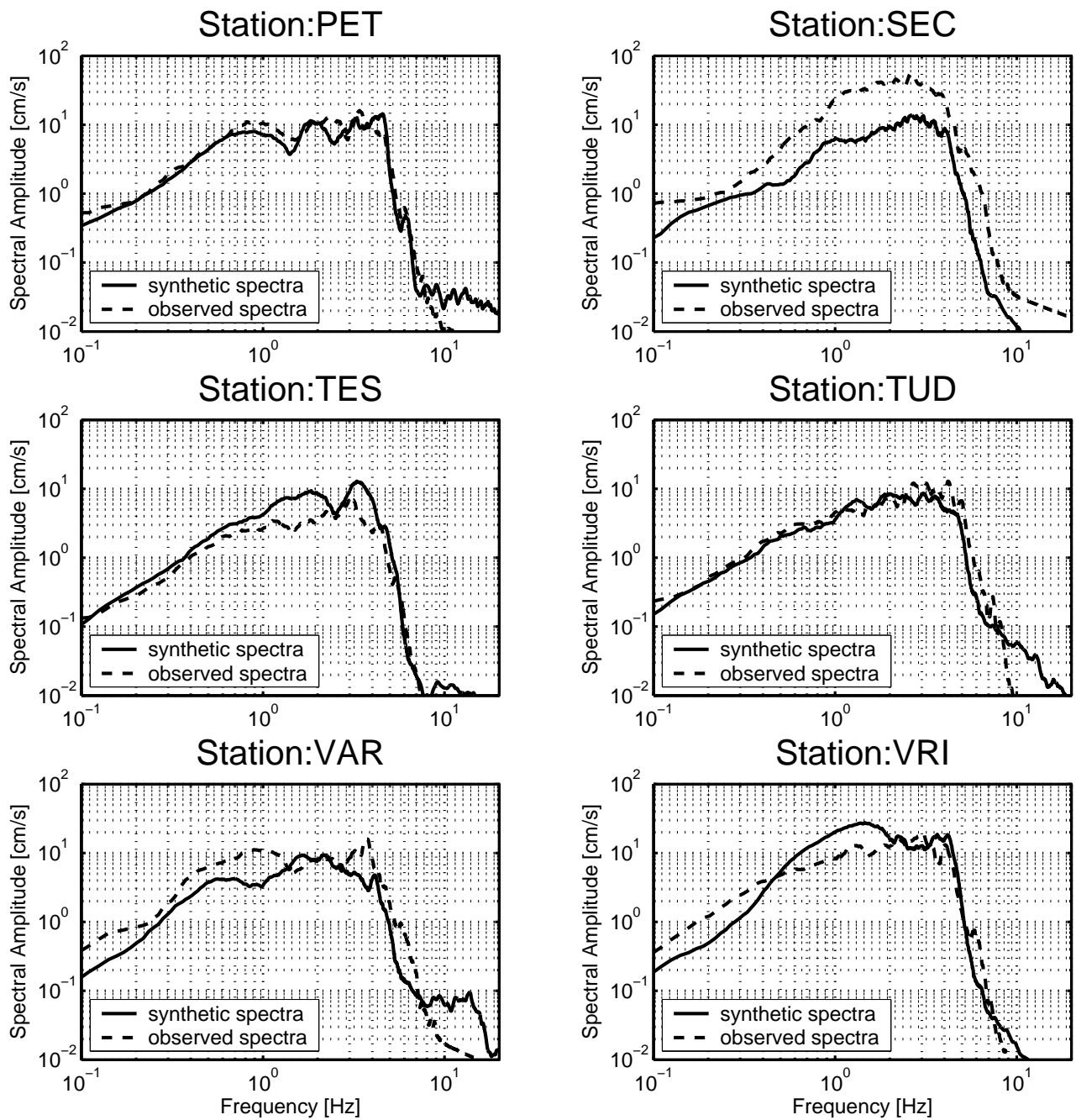


Figure 4.20: Modelled and observed spectra for the 2004 earthquake from the 2.5D modelling. Best fit is obtained at PET and TUD. At SEC and VAR the observed spectra are larger than the modelled spectra.

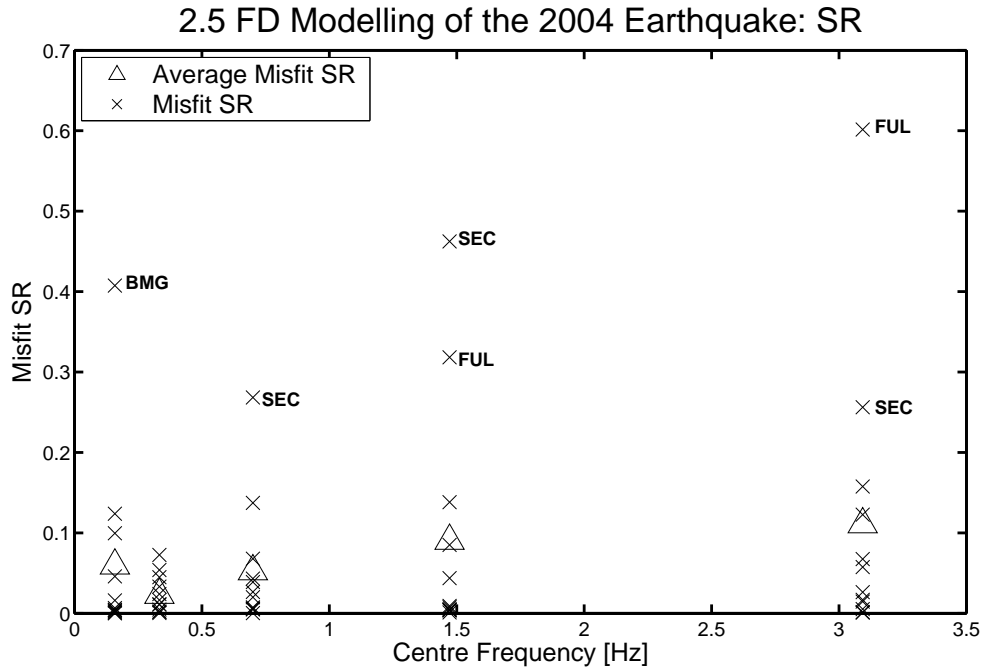


Figure 4.21: Misfit between the observed and modelled spectra of the 2004 earthquake. Misfit SR is plotted at the centre frequencies. The triangles give the average value for each frequency range. For the extreme outliers the corresponding station names are given. The misfits are similar to the misfits of the modelling of the 1986 earthquake (see Fig. 4.12). Only for stations SEC, FUL and BMG the misfit SR shows larger values than the maximum misfits for the modelling of the 1986 earthquake.

Station	BMG	BVC	CFR	FUL	GRE	OZU
SSR	0.091	0.040	0.018	0.188	0.027	0.024
Station	PET	SEC	TES	TUD	VAR	VRI
SSR	0.004	0.221	0.05	0.009	0.068	0.067

Table 4.6: 2.5D Modelling of the 2004 Earthquake: Summarised square residual (SSR) for all stations (see eq. 4.2). Lowest SSR values are obtained for CFR, PET and TUD.

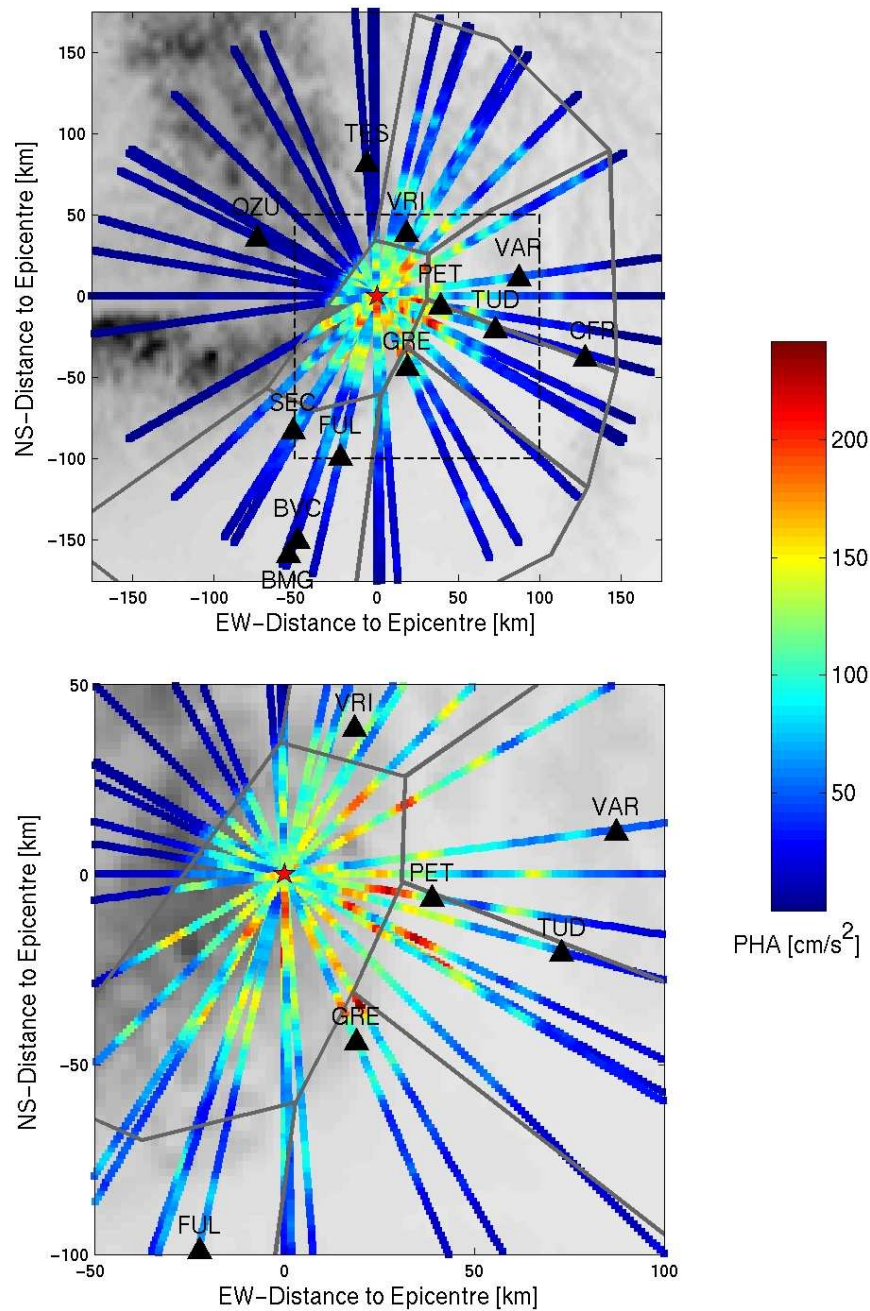


Figure 4.22: PHA distribution of the 2004 earthquake resulting from the 2.5D modelling. The grey lines give the regions for which amplification ratios are available. The bottom image shows the PHA distribution within the dashed area indicated in the top image. Accelerations up to 250 cm/s^2 occur E to SE of the epicentre.

Station	CFR	GRE	PET	TES	TUD	VAR	VRI
SSR	0.165	0.137	0.082	0.179	0.015	0.003	0.007

Table 4.7: 3D modelling of the 2004 earthquake: SSR (see eq. 4.2) for all stations between 0.1 and 0.46 Hz. Lowest values are found for VAR and VRI.

4.4.2 3D Modelling of the 2004 Earthquake

Seven stations (CFR, GRE, PES, TES, TUD, VAR and VRI) are located within the model region for the 3D FD modelling. Fig. 4.25 displays the modelled PHA for frequencies up to 0.6 Hz. Maximum values of about 250 cm/s^2 are calculated 20 km east of the epicentre. The modelled PHA distribution shows also the distinctive SW-NE orientated oval pattern. Fig. 4.23 and 4.24 display the observed and modelled FAS at the seven stations that are located within the model area. Station TUD, VAR and VRI show a good comparison between modelling and observation. At TES the modelling underestimates the observed amplitudes, whereas at CFR, GRE and PET the modelled amplitudes are larger than the observed values. The SSR for the first two frequency ranges between 0.11 and 0.48 Hz are given in Table 4.7. The values are about in the same range as for the 1986 earthquake (see Table 4.4). Lowest SSR is calculated for VAR and VRI.

4.5 Summary & Conclusions

This chapter describes a hybrid approach to simulate ground motions for SE Romania. 2.5D and 3D FD modelling of wave propagation is combined with the known site amplification characteristics of the region (Sokolov and Bonjer, 2006). By using FD the well known crustal and mantle structure of SE Romania is implemented into the modelling. Due to computational limits and the lacking knowledge of uppermost layers (several 100 meters) ground motion cannot be simulated by FD alone. Therefore, the known frequency dependent site amplification ratios (Sokolov et al., 2004; Sokolov and Bonjer, 2006) are applied to include the influence of the uppermost layers. As the modelled seismograms depend strongly on the locations of the random generated velocity fluctuations FAS are more appropriate to compare the modelled and observed earthquakes. Furthermore, the FAS of the ground motions give a measure of macroseismic intensity (Sokolov, 2002), and therefore of damage. FAS are also used by Gottschämmer et al. (2006) and Wenzel (2004) to invert for the free spectral parameters. The modelled FAS can also be used as an input for stochastic modelling (Boore, 2003). Therefore, the quality of the modelling is evaluated by comparing observed and modelled FAS. The 2.5D simulations of the 1986 ($M_W = 7.1$) earthquake result in a good fit between observed and modelled FAS with a maximum deviation of about one intensity unit. Area-wide comparison between observed and modelled macroseismic intensities of the 1986 earthquake showed the reliability of the presented method. The defined misfit function gives similar misfits values for the 1986 and 2004, which suggests for the modelling of the 2004 also a maximum deviation which corresponds only to one intensity unit. Consequently, the proposed 2.5D method is capable to simulate ground motions for SE Romania with an accuracy of about one intensity unit, which is the same accuracy as in intensity evaluations based

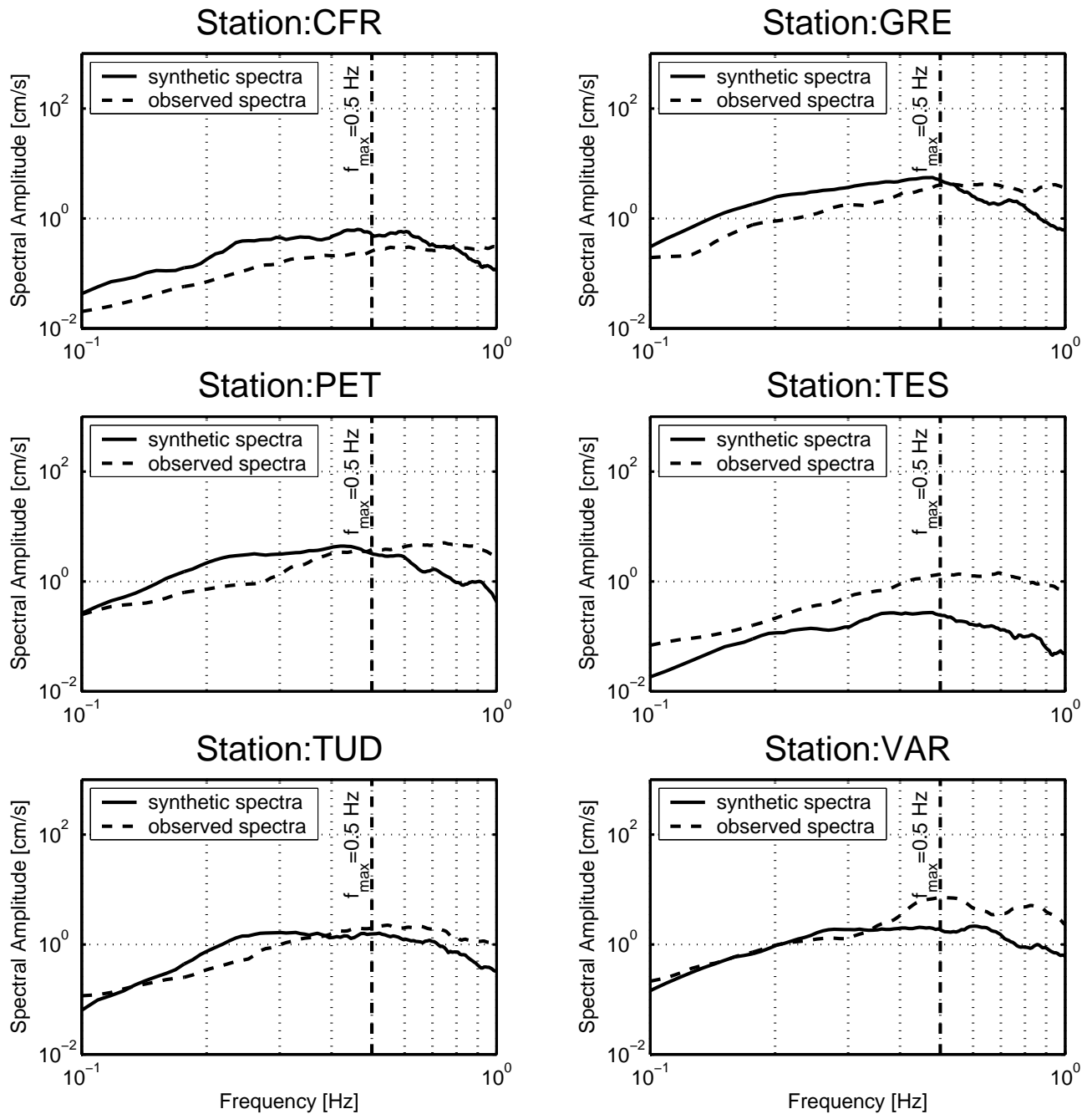


Figure 4.23: 3D modelling of the 2004 earthquake: Modelled (3D) and observed FAS at CFR, GRE, PET, TES, TUD and VAR. Best fit is found for stations TUD and VAR. At CFR and TES the modelled values are larger than the observed ones, whereas at TES the modelling underestimates the observed spectrum. The deviation between modelling and observation is lower than in the case of the 3D modelling of the 1986 earthquake (see Fig. 4.15).

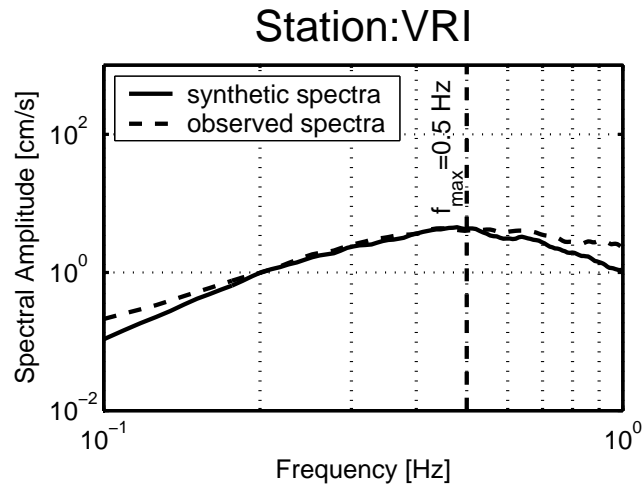


Figure 4.24: 3D modelling of the 2004 earthquake: Modelled and observed FAS at VRI. The modelling reproduces the observed spectra up to 0.5 Hz.

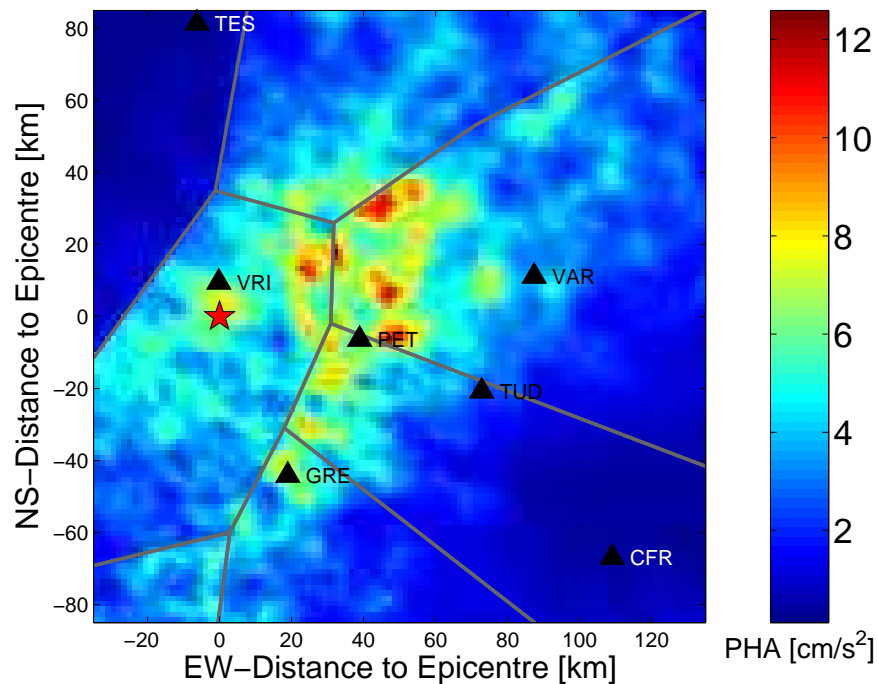


Figure 4.25: PHA resulting from 3D modelling of the 2004 earthquake. The red star marks the epicentre and the grey lines the boundaries of the regions for which amplification ratios are available (see Fig. 4.1). Strong motion stations are indicated by black triangles.

on observed macroseismic data (Sokolov and Wald, 2002). The application of the presented 3D method is only reasonable on larger computers, as the current maximum frequency of 0.5 Hz is far below the frequency range that is usually interesting for engineering purposes.

At this point it is necessary to mention that the modelling procedure is optimised to fit the observed spectra and intensities. The parameters chosen to achieve the fit cannot be uniquely determined as a trade-off between stress drop, Q structure and applied site amplification ratios exists. Especially, as the former two are not well constrained for SE Romania. By keeping the damping structure, which was also used by Sokolov et al. (2005), and choosing a realistic stress drop of 150 MPa for the Vrancea earthquakes (see section 1.5.1), it is necessary to use the mean plus one standard deviation instead of the mean values of the amplification ratios given by Sokolov and Bonjer (2006). This indicates that the real Q structure of SE Romania is not well known. Therefore, further research should concentrate on the Q structure of Romania, as this is the most uncertain parameter in the modelling. Current research addresses the stress drops for the Vrancea earthquakes (Oth et al., 2006) and the results will allow to model the Vrancea earthquakes with proper stress drop values. The improvement of the knowledge of the Q-structure and the stress drops is very important as this improves the quality of ground motion modelling method presented here and therefore allows a better hazard assesement for SE Romania in modelling scenario earthquakes consistently.

Summary & Conclusions

In this work ground motion was modelled for crustal and intermediate-depth earthquakes. As a crustal example the disastrous 1999 Kocaeli (Turkey) earthquake ($M_W = 7.4$) was simulated. The intermediate-depth Vrancea Strong earthquakes impose significant hazard on Romania, especially the Romanian capital Bucharest, and the neighbouring countries. Wave propagation was modelled in order to understand the influence of the source and the subsurface structure on the resulting ground motions. Furthermore, a method was developed to simulate strong ground motions for potential Vrancea earthquakes.

The 2D FD code of Karrenbach (1995) and 3D FD code of Olsen (1994) were utilised to simulate wave propagation. These FD codes apply the concept of FD to solve numerically the equation of motion and the corresponding stress-strain relationship, which govern wave propagation within elastic isotropic media. Numerical dispersion limits the maximum reliable frequency of the modelling, as the minimum grid spacing of the model region is limited by the available computer capacities. Therefore, not only 3D but also 2D simulations, which are less computer intensive than 3D calculations, were performed. However, in 2D a point source corresponds to a line source in 3D. Consequently, simulated 2D seismograms have to be corrected to generate proper 3D seismograms. Unfortunately, the correction given by Vidale and Helmberger (1987) is not applicable for the source implementation techniques of nowadays FD codes. Therefore, a correction was developed which can easily be applied on the 2D FD modelling. Comparison between 3D line source and corrected 2D seismograms displayed the reliability of the developed method. The key difference between the modelling of the 1999 Kocaeli and the Vrancea earthquakes is the utilised source in the modelling. In the case of the Kocaeli earthquake the fault plane is about 120 km long and 20 km deep. As rupture history inversions show, the rupture velocity, slip and rise time differ significantly on the fault. Therefore, it is necessary to include the extended fault and the complexity of the rupture process to model ground motions in the near fault area. In contrast, the Vrancea earthquakes are treated as point sources with an analytical source description after Beresnev and Atkinson (1997). These source simplifications of the Vrancea earthquakes is justified as the large stress drops of the Vrancea earthquakes correspond to small source extension compared to the minimal travel path of about 100 km up to the surface.

The very disastrous Kocaeli earthquake killed about 15,000 people, left about 400,000 homeless and produced a damage of 40 billions US\$. Six strong motion stations within 20 km to the fault recorded the earthquake. Macroseismic intensities up to X occurred along large regions near the fault rupture. The recorded accelerations seem to be low compared to the generated damage. Wave propagation from the Kocaeli earthquake up to 1.5 Hz was simulated by using 3D FD. A

simplified subsurface structure that contains the main sedimentary basins was constructed based on velocity and density values given by Ergin et al. (1998). Two different inverted rupture histories were implemented into the modelling (Bouchon et al., 2002; Sekiguchi and Iwata, 2002). The area-wide modelled PHV distribution showed a very complex pattern and it could be shown that this is strongly correlated to the details of the rupture process on the fault. Remarkably, no strong motion station was located within an area of maximum modelled PHV. Furthermore, synthetic seismograms were translated into macroseismic intensities following Sokolov (2002). Again, no strong motion station was located within a region of maximum modelled intensities of X. This suggests, that the few near fault strong motion stations were located in regions where no large ground motions occurred during the earthquake. Comparison of the modelled macroseismic intensity distributions and the observed intensities showed that the rupture process of Bouchon et al. (2002) reproduces the intensity distribution in the near fault area up to about 15 km, whereas the modelling with the rupture history of Sekiguchi and Iwata (2002) results in a complete different intensity distribution. This is a very interesting finding because both rupture processes reproduce the recorded seismograms at the stations used to invert the rupture process. The difference occurs probably due to the selection of stations which were applied for the inversions. Bouchon applied only near fault strong motion stations whereas Sekiguchi and Iwata (2002) included also data from stations with larger distances to the earthquake fault.

Wave propagation from the intermediate depth Vrancea earthquakes was modelled with 2D and 3D FD. 2D modelling was performed for many slices that were rotated around the hypocentre-epicentre axis. This 2.5D modelling procedure allowed an area-wide simulation of ground motions. Maximum frequency of the 2.5D FD and 3D modelling was 4.5 and 0.6 Hz, respectively. The subsurface structure of SE Romania is well known and was compiled by Martin et al. (2005, 2006). To produce realistic seismograms, stochastic velocity perturbations were added to the known underground structure. An exponential correlation function was used and the correlation length within the crust was 2 km with a RMS velocity perturbation of 5%. Within the mantle the used correlation length was 4 km with a RMS velocity perturbation of 2%. The earthquakes were simulated as point sources with the source time function after Beresnev and Atkinson (1997) and the source duration is scaled with a static stress drop of 150 MPa. All past strong Vrancea earthquakes produced similar intensity patterns, which are SW-NE elongated. To explore the origin of these patterns, FD simulations of the 1986 ($M_W = 7.1$) earthquake were carried out for varying underground models in order to fix the influence of the different subsurface structures. The modelling of the 1986 earthquake is representative for all Vrancea strong earthquakes as all earthquakes show similar focal mechanism and depths. The simulations showed that the combination of source radiation and location of the deep sedimentary basins produce the SW-NE oriented oval pattern because maximum S-wave amplitudes are radiated to the deep sedimentary basins SE to E of the Carpathian Arc. The influence of source radiation produce PGA variations up to a factor of four and the convex basin structures amplify the impinging S-waves up to a factor of 1.5. The source radiation is a critical factor as no large ground motions are modelled for regions with deep basins where the impinging S-waves have only small or intermediate amplitudes. However, the strong influence of the source radiation is not self evident and differs from case to case within the considered frequency range up to 4.5 Hz (Liu and Helmberger, 1985; Vidale, 1989; Castro et al., 2006; Takenaka et al., 2003; Siro and Chiaruttini, 1989; Sirovich, 1994). But in the case of the

Vrancea earthquakes, the discussed large stress drops and the consequently small fault sizes may produce a very coherent source signal compared to crustal earthquakes with large fault planes where rake rotation can disturb the radiation pattern (Spudich et al., 1998).

Numerical dispersion and the available computer power imposes strong limitations on the maximum reliable frequency of FD simulations. Therefore, it was necessary to simulate wave propagation from the Vrancea earthquakes within a model with a relatively large minimum S-wave velocity of about 1.7 km/s, which corresponds to hard rock conditions. Consequently, it is not possible to simulate realistic strong ground motion as the amplifications of the uppermost low velocity layers are not included into the modelling. Therefore, a hybrid modelling method was developed. First, FD modelling of wave propagation was performed within the subsurface structure after Martin et al. (2005, 2006). In a second step, the known frequency dependent site amplification ratios after Sokolov and Bonjer (2006) were applied on the results of the FD simulation. This method was applied on the 1986 and 2004 Vrancea earthquakes. The comparison between observed and modelled FAS displayed the reliability of the developed hybrid method. In the case of the 1986 earthquake macroseismic intensities were calculated following Sokolov (2002). The modelled intensity distribution reproduces the observed intensity pattern with its SW-NE oval shaped isoseismal lines. The comparison of modelled and observed FAS and intensities showed that the modelling is applicable to simulate strong ground motions for potential Vrancea strong earthquakes. Current research implements the developed method into the development of attenuation relationships for SE Romania (Wenzel, 2004; Gottschämmer et al., 2006).

List of Figures

1.1	Numerical Dispersion	9
1.2	Force Couples of the Seismic Moment Tensor	11
1.3	Strike ϕ , Dip δ and Rake λ of a Fault	13
1.4	Fault Orientation within a 2D Model	15
1.5	Modelling of the Vrancea Earthquakes: Moment Tensor Density Function	18
1.6	Modelling of the 1999 Kocaeli Earthquake: Moment Tensor Density Function	19
1.7	Snapshot of P- and S-Wave Radiation	20
1.8	Theoretical and Modelled P-Wave Radiation Pattern	21
1.9	Theoretical and Modelled S-Wave Radiation Pattern	21
1.10	Line Source Composed of an Infinite Number of Point Sources	22
1.11	Model Geometry Used to Verify the 2D to 3D Correction for Homogeneous Models	24
1.12	Source Wavelet Used to Validate the 2D to 3D Correction	24
1.13	Equivalence of a 3D Line Source Seismogram and a 2D Point Source Seimogram.	25
1.14	Comparison between a 3D Point Source Seismogram and a Corrected 2D Point Source Seimogram.	26
1.15	Model Used to Validate the 2D to 3D Correction for Layered Structures	27
1.16	Comparison between 3D FD Point Source Seismograms and Corrected 2D FD Seismograms for a Layered Model.	28
2.1	1999 Kocaeli Earthquake Fault and Near Fault Strong Motion Stations	30
2.2	Tectonic Map of Turkey	31
2.3	Fault Trace in Bouchon et al. (2002) and Fault Used for the Modelling	34
2.4	Fault Trace in Sekiguchi and Iwata (2002) and Fault Used for the Modelling	35

List of Figures

2.5	3D Subsurface Model	36
2.6	Representative Fourier Amplitude Spectra with Observed and Synthetic Spectra at IZT.	37
2.7	PHV Calculated from the Rupture Process of Bouchon et al. (2002)	38
2.8	Macroseismic Intensities Resulting from the Rupture of Bouchon et al. (2002) . .	38
2.9	Comparison Between Modelled and Observed Seismograms for the Rupture Process of Bouchon et al. (2002)	41
2.10	PHV Calculated from the Rupture Process of Sekiguchi and Iwata (2002)	42
2.11	Macroseismic Intensities Resulting from the Rupture of Sekiguchi and Iwata (2002)	42
2.12	Comparison of Modelled Seismograms and the Records at the Digital Station Used by Sekiguchi and Iwata (2002) for the Inversion	43
2.13	Modelled and Observed Seismograms at the Analog Stations Used by Sekiguchi and Iwata (2002) for the Inversion	44
3.1	Vrancea Earthquakes with Depths Larger than 70 km	48
3.2	Macroseismic Intensity Distributions for the 1977, 1986 and 1990 Earthquakes .	50
3.3	Basement Structure of SE Romania	51
3.4	Basement, Conrad and Moho Depths with Surface and Basement Velocities	52
3.5	Crustal structures after Martin et al. (2005) with the Slab Beneath the SE Carpathian Arc after Martin et al. (2006)	53
3.6	Observed and modelled seismograms at CFR	54
3.7	2D Slices through the Subsurface Structure with and without Stochastic Velocity Perturbations	56
3.8	Observed and modelled seismograms at CFR after Adding the Stochastic Velocity Perturbations	56
3.9	Damped and Undamped Seismogram at CFR	58
3.10	Seismograms Damped for Different Travel Times	58
3.11	2.5D Modelling Method	59
3.12	Moment Tensor Density Rate Function Used to Model the 1986 Vrancea Earthquake	60
3.13	2.5 FD Modelling of the 1986 Vrancea Earthquake: Modelled PGA Distribution .	61
3.14	Different Underground Structures of the SW-NE Slice	65

3.15	PGA along the SW-NE Slice for Varying Crustal Structures	66
3.16	PGA along the SW-NE for Varying Crustal and Mantle Structures	66
3.17	Snapshots of Wave Propagation within the SW-NE Slice	67
3.18	Different Underground Structures of the EW slice	68
3.19	PGA along the EW Slice for Varying Crustal Structures	69
3.20	PGA along the EW Slice for Varying Crustal and Mantle Structures	69
3.21	Different Underground Structures of the NW-SE Slice	70
3.22	PGA along the NW-SE Slice for Varying Crustal Structures	71
3.23	PGA along the NW-SE Slice for Varying Crustal and Mantle Structures	71
3.24	2.5D FD Modelling of the 1986 Earthquake: Modelled PGA Distribution after Adding Stochastic Velocity Perturbations	72
3.25	3D FD Modelling of the 1986 Earthquake: Modelled PGA Distribution	73
3.26	3D FD of the 1986 Earthquake: Modelled PGA Distribution for Model LAY	75
3.27	3D FD of the 1986 Earthquake: PGA Distribution for Model B	75
3.28	3D FD of the 1986 Earthquake: PGA along the SW-NE Slice	76
3.29	3D FD of the 1986 Earthquake: PGA along the EW Slice	76
3.30	3D FD of the 1986 Earthquake: PGA along the NW-SE Slice	77
3.31	3D FD of the 1986 Earthquake: PGA Distribution after Adding Stochastic Velocity Perturbations	77
3.32	Theoretical S-Wave Radiation Pattern of the 1986 Vrancea Earthquake at the Surface	78
3.33	Snapshots of the Wavefield in the Random Medium	81
3.34	Seismograms within the Homogeneous and Random Media	82
3.35	Peak Accelerations along Profiles through the Homogeneous and Random Models	83
3.36	Source Wavelet for Stress Drops between 50 and 350 MPa	84
3.37	Seismograms at BAL for Stress Drops between 50 and 350 MPa	84
3.38	Acceleration at BAL for Three Different Q Models.	85
4.1	Map with the Six Characteristic Regions for which Average Site Amplification Ratios are Given	89
4.2	Site Amplification Ratios between 0.2 and 10 Hz for the Six Characteristic Regions	90

List of Figures

4.3	Seismogram at CFR with and without Site Effects	91
4.4	1986 Strong Vrancea Earthquake: Focal Mechanism and Station Distribution . .	92
4.5	2.5D Modelling of the 1986 Earthquake: Seismograms at BAC and BAL	94
4.6	2.5D Modelling of the 1986 Earthquake: Seismograms at BUC and CFR	95
4.7	2.5D Modelling of the 1986 Earthquake: Seismograms at CRL and FOC	96
4.8	2.5D Modelling of the 1986 Earthquake: Seismograms at ISR and MLR	97
4.9	2.5D Modelling of the 1986 Earthquake: Seismograms at SDR and VRI	98
4.10	Modelled and Observed Fourier Amplitude Spectra (FAS) at BAC, BAL, BUC, CFR, CRL and FOC	99
4.11	Modelled and Observed FAS at ISR, MLR, VRI and SDR	100
4.12	2.5D Modelling of the 1986 Earthquake: Misfit SR	101
4.13	2.5D Modelling of the 1986 Earthquake: Modelled PHA Distribution	102
4.14	2.5D Modelling of the 1986 Earthquake: Modelled and Observed Macroseismic Intensities	104
4.15	3D Modelling of the 1986 Earthquake: Modelled and Observed FAS	105
4.16	3D Modelling of the 1986 Earthquake: Modelled PHA Distribution	106
4.17	Focal Mechanism and Station Location for the 2004 Earthquake	107
4.18	Macroseismic Intensities for the October 27, 2004 Earthquake Compiled by the USGS	108
4.19	2.5D Modelling of the 2004 Earthquake: FAS at BMG, BVC, CFR, FUL, GRE and OZU	109
4.20	2.5D Modelling of the 2004 Earthquake: FAS at PET, SEC, TES, TUD, VAR and VRI	110
4.21	2.5D Modelling of the 2004 Earthquake: Misfit SR	111
4.22	2.5 Modelling of the 2004: Modelled PHA Distribution	112
4.23	3D Modelling of the 2004 Earthquake: Modelled and Observed FAS at CFR, GRE, PET, TES, TUD and VAR	114
4.24	3D Modelling of the 2004 Earthquake: Modelled and Observed FAS at VRI . . .	115
4.25	3D Modelling of the 2004 Earthquake: Modelled PHA Distribution	115

List of Tables

1.1	Stability and Numerical Dispersion Constraints	10
2.1	Near Fault Strong Motion Stations	32
2.2	PGA according to Boore et al. (1997), Campbell (1997) and Sadigh et al. (1997) .	33
2.3	3D Elastic Model of the 1999 Kocaeli Earthquake Region	36
3.1	Vrancea Strong Earthquakes During the 20th Century	49
3.2	Parameters of the Stochastic Velocity Perturbations	55
3.3	Average Depths and Velocities of the Layered Model	62
3.4	Used Model Abbreviations	62
3.5	Used Q Models to estimate the Influence of the Q Structure	85
4.1	Azimuths of the 2D Slices used for the Modelling of the 1986 Earthquake	91
4.2	Frequency Ranges and Centre Frequencies Used to Calculate the Square Residual (SR)	93
4.3	2.5D Modelling of the 1986 Earthquake: Summarised Square Residual (SSR) . .	93
4.4	3D Modelling of the 1986 Earthquake: Summarised Square Residual SSR	103
4.5	Azimuths of the 2D slices Used for the Modelling of the 2004 Earthquake	108
4.6	2.5D Modelling of the 2004 Earthquake: SSR	111
4.7	3D Modelling of the 2004 Earthquake: SSR	113

Bibliography

- Aki, K. and Richards, P. G. (1980). *Quantitative seismology*. Freeman, San Francisco.
- Akkar, S. and Gülkan, P. (2002). A critical examination of near-field accelerograms from the Sea of Marmara region earthquakes. *Bull. Seism. Soc. Am.*, 92(1):428–447.
- Alex, C. M. and Olsen, K. B. (1998). Lens-effect in Santa Monica? *Geophys. Res. Lett.*, 25(18):3441–3444.
- Alford, R. M., Kelly, K. R., and Boore, D. M. (1974). Accuracy of finite-difference modeling of the acoustic wave equation. *Geophysics*, 39(6):834–842.
- Alterman, Z. and Karal, F. C. (1968). Propagation of elastic waves in layered media by finite difference methods. *Bull. Seism. Soc. Am.*, 58(1):367–398.
- Ambraseys, N., Smit, P., Berardi, R., Rinaldis, D., Cotton, F., and Berg-Thierry, C. (2000). Dissemination of European strong motion data. *CD-ROM Collection, European Council, Environment and Climate Research Programme*.
- Aptikaev, F. F. and Shebalin, N. V. (1983). The correlation between macroseismic effects and dynamic parameters of ground motion (in Russian). *Engineering Seismology Problems, issue 29*, pages 98–108. Nauka Publishing House, Moscow.
- Bakun, W. H., Aagaard, B., Dost, B., Ellsworth, W. L., Hardebeck, J. L., Harris, R. A., Ji, C., Johnston, M. J. S., Langbein, J., Lienkaemper, J. J., Michael, A. J., Murray, J. R., Nadeau, R. M., Reasenber, P. A., Reichle, M. S., Roeloffs, E. A., Shakal, A., Simpson, R. W., and Waldhauser, F. (2005). Implications for prediction and hazard assessment from the 2004 Park-field earthquake. *Nature*, 437:969–974.
- Barka, A., Akyüz, H. S., Altunel, E., Sunal, G., Cakir, Z., Dikbas, A., Yerli, B., Armijo, R., Meyer, B., Chabalier, J. B. D., ROckwell, T., Dolan, J. R., Hartleb, R., Dawson, T., Christoferson, S., Tucker, A., Fumal, T., Langridge, R., Stenner, H., Letttis, W., Bachhuber, J., and Page, W. (2002). The surface rupture and slip distribution of the 17 August 1999 Izmit earthquake (M 7.4), North Anatolian Fault. *Bull. Seism. Soc. Am.*, 92(1):43–60.
- Benites, R. and Olsen, K. B. (2005). Modeling strong ground motion in the Wellington metropolitan area, New Zealand. *Bull. Seism. Soc. Am.*, 95(6):2180–2196.

Bibliography

- Beresnev, I. A. and Atkinson, G. M. (1997). Modeling finite-fault radiation from ω^n spectrum. *Bull. Seism. Soc. Am.*, 87(1):67–84.
- Bonjer, K.-P. and Grecu, B. (2004). Data release 1996-2004 of the Vrancea K2 seismic network. one DVD with evt-files. Technical report.
- Bonjer, K.-P., Oncescu, M. C., Rizescu, M., Enescu, D., Driad, L., Radulian, M., Ionescu, C., and Moldoveanu, T. (2000). Source- and site-parameters of the April 28, 1999 intermediate depth Vrancea earthquake: First results from the new K2 network in Romania. In *Book of Abstracts and Papers, SSA-2-13-O*, page 53. XXVII General Assembly of the European Seismological Commission, Lisbon, Portugal.
- Boore, D. M. (2001). Comparisons of ground motions from the 1999 Chi-Chi earthquake with empirical predictions largely based on data from California. *Bull. Seism. Soc. Am.*, 91(5):1212–1217.
- Boore, D. M. (2003). Simulation of ground motion using the stochastic method. *Pure appl. geophys.*, 160:635–676.
- Boore, D. M., Joyner, W. B., and Fumal, T. E. (1997). Equations for estimating horizontal response spectra and peak acceleration from western North American earthquakes: A summary of recent work. *Seismol. Res. Lett.*, 68:128–153.
- Bouchon, M., Bouin, M.-P., Karabulut, H., Toksöz, M. N., Dietrich, M., and Rosakis, A. J. (2001). How fast is rupture during an earthquake? New insights from the 1999 Turkey earthquakes. *Geophys. Res. Lett.*, 28(14):2723–2726.
- Bouchon, M., Toksöz, M. N., Karabulut, H., Bouin, M.-P., Dietrich, M., Aktar, M., and Edie, M. (2002). Space and time evolution of rupture and faulting during the 1999 Izmit (Turkey) earthquake. *Bull. Seism. Soc. Am.*, 92(1):256–266.
- Brune, J. N. (1970). Tectonic stress and the spectra of seismic shear waves from earthquakes. *J. Geophys. Res.*, 75(26):4997–5009.
- Brune, J. N. (1971). Correction. *J. Geophys. Res.*, 76:5002.
- Campbell, K. W. (1997). Empirical near-source attenuation relationships for horizontal and vertical components of peak ground acceleration, peak ground velocity, and pseudo absolute acceleration response spectra. *Seismol. Res. Lett.*, 68:154–179.
- Castro, R. R., Franceschina, G., Pacor, F., Bindi, D., and Luzi, L. (2006). Analysis of the frequency dependence of the s-wave radiation pattern from local earthquakes in central Italy. *Bull. Seism. Soc. Am.*, 96(2):415–426.
- Cerjan, C., Kosloff, D., Kosloff, R., and Reshef, M. (1985). A nonreflecting boundary condition for discrete and elastic wave equations. *Geophysics*, 50(4):705–708.

- Chernov, Y. K. and Sokolov, V. Y. (1983). Relations between ground motion parameters and felt intensity. seismic hazard assessment (in Russian). *Engineering Seismology Problems, issue 24*, pages 96–111. Nauka Publishing House, Moscow.
- Cioflan, C. O., Apostol, B. F., Moldoveanu, C. L., Panza, G. F., and Marmureanu, G. (2004). Deterministic approach for the seismic microzonation of Bucharest. In Panza, G. F., Paskaleva, I., and Nunziata, C., editors, *Seismic Ground Motion in Large Urban Areas*, volume 161 of *Pageoph Topical Volumes*, pages 1149–1164.
- Cirpka, O. A. (2003). Generation of random, autocorrelated, periodic fields. Technical report, University of Stuttgart, Institute of Hydraulic Engineering. http://matlabdb.mathematik.uni-stuttgart.de/download.jsp?MC_ID=6&MP_ID=31.
- Clayton, R. and Enquist, B. (1977). Absorbing Boundary Conditions for Acoustic and Elastic Wave Equations. *Bull. Seismol. Soc. Amer.*, 67(6):1529–1540.
- Cohen, G. C. (2002). *Higher-Order Numerical Methods for Transient Wave Equations*. Springer Verlag Berlin, Heidelberg.
- Coutant, O., Virieux, J., and Zollo, A. (1995). Numerical source implementation in a 2D finite difference scheme for wave propagation. *Bull. Seism. Soc. Am.*, 85(5):1507–1512.
- Davis, P. M., and K. H. Liu, J. L. R., Gao, S. S., and Knopoff, L. (2000). Northridge earthquake damage caused by geologic focusing of seismic waves. *Science*, 289(5485):1746–1750.
- Delouis, B., Lundgren, P., Salichon, J., and Giardini, D. (2000). Joint inversion of InSAR and teleseismic data for the slip history of the 1999 Izmit (Turkey) earthquake. *Geophys. Res. Lett.*, 27(20):3389–3392.
- DeMets, C., Gordon, R. G., Argus, D. F., and Stein, S. (1994). Effect of recent revisions to the geomagnetic reversal time scale on estimate of current plate motions. *Geophys. Res. Lett.*, 21(20):2191–2194.
- Diehl, T., Ritter, J. R. R., and the CALIXTO group (2005). The crustal structure beneath SE Romania from teleseismic receiver functions. *Geophys. J. Int.*, 163(1):238–251.
- Durrant, D. R. (1999). *Numerical Methods for Wave Equations in Geophysical Fluid Dynamics*. Number 32 in Texts in Applied Mathematics. Springer-Verlag New York Inc.
- EERI (1999). The Chi-Chi Taiwan earthquake of September 21. *Earthquake Engineering Research Institute (EERI): Special Earthquake Report*.
- Erdik, M. (2001). Report on 1999 Kocaeli and Düzce (Turkey) earthquakes. Technical report, Bogazici University, Dept. of Earthquake Engineering, www.koeri.boun.edu.tr/deprenmuh/eqspecials/kocaeli/Kocaelireport.pdf.

Bibliography

- Ergin, M., Aktar, M., Bicmen, F., Yörük, A., Yalcin, N., and Kuleli, S. (1998). Izmit körfezi mikrodeprem calismasi. ATAG-1, ITÜ.
- FEMA (2003). The 2003 NEHRP recommended provisions for new buildings and other structures part 1: Provisions (FEMA 450). Technical report, Prepared for FEMA (Federal Emergency Management Agency) by the Building Seismic Safety Council (National Institute of Building Sciences), Washington DC.
- Frankel, A. (1993). Three-dimensional simulations of ground motions in the San Bernardino Valley, California, for hypothetical earthquakes on the San Andreas fault. *Bull. Seism. Soc. Am.*, 83(4):1020–1041.
- Frankel, A. and Clayton, R. W. (1984). A finite-difference simulation of wave propagation in two-dimensional random media. *Bull. Seism. Soc. Am.*, 74(6):2167–2186.
- Frankel, A. and Clayton, R. W. (1986). Finite difference simulations of seismic scattering: implications for the propagation of short-period seismic waves in the crust and models of crustal heterogeneity. *J. Geophys. Res.*, 91:6465–6489.
- Fuchs, K. and Müller, G. (1971). Computation of synthetic seismograms with the reflectivity method and comparison with observations. *Geophys. J. Roy. Astr. S.*, 23:417–433.
- Furumura, T. and Kennett, K. (2005). Subduction zone guided waves and the heterogeneity structure of the subducted plate: Intensity anomalies in northern Japan. *J. Geophys. Res.*, 110:B10302.
- Gao, S., Liu, H., Davis, P. M., and Knopoff, L. (1996). Localized amplification of seismic waves and correlation with damage due to the Northridge earthquake: Evidence for focusing in Santa Monica. *Bull. Seism. Soc. Am.*, 96(1B):S209–S230.
- Glaznev, V. N., Raevsky, A. B., and Skopenko, G. B. (1996). A three-dimensional integrated density and thermal model of the Fennoscandian lithosphere. *Tectonophysics*, 258:15–33.
- Görtz, A. (2002). *True amplitude multicomponent migration of elastic wavefields = Amplitudengetreue Mehrkomponentenmigration von elastischen Wellenfeldern*. PhD thesis, Karlsruhe University, Germany.
- Goto, H. and Sawada, S. (2004). Numerical simulation of strong ground motion on Adapazari basin during the 1999 Kocaeli, Turkey, earthquake. 13th World Conference on Earthquake Engineering Vancouver, B.C., Canada. Paper Number 720.
- Goto, H., Sawada, S., Morikawa, H., Kiku, H., and Ozalaybey, S. (2005). Modeling of 3D subsurface structure and numerical simulation of strong ground motion in the Adapazari Basin during the 1999 Kocaeli earthquake, Turkey. *Bull. Seism. Soc. Am.*, 95(6):2197 – 2215.

- Gottschämmer, E. and Olsen, K. B. (2001). Accuracy of the explicit planar free-surface boundary condition implemented in a fourth-order staggered-grid velocity-stress finite-difference scheme. *Bull. Seism. Soc. Am.*, 91(3):617–623.
- Gottschämmer, E., Oth, A., Miksat, J., and Wenzel, F. (2006). Hybrid modelling of ground motion. *First European Conference on Earthquake Engineering and Seismology (Geneva, Switzerland)*, (Paper Number 759).
- Graves, R. W. (1996). Simulating seismic wave propagation in 3D elastic media using staggered-grid finite differences. *Bull. Seism. Soc. Am.*, 86(4):1091–1106.
- Graves, R. W. (1998). 3D finite difference modeling of the San Andreas Fault: Source parameterization and ground motion levels. *Bull. Seism. Soc. Am.*, 88(4):881–897.
- Graves, R. W., Pitarka, A., and Somerville, P. G. (1998). Ground-motion amplification in the Santa Monica area: Effects of shallow basin-edge structure. *Bull. Seism. Soc. Am.*, 88(5):1224–1242.
- Grünthal, G., editor (1998). *European Macroseismic Scale 1998*.
- Guatteri, M., Mai, P. M., and Beroza, G. C. (2004). A pseudo-dynamic approximation to dynamic rupture models for strong ground motion prediction. *Bull. Seism. Soc. Am.*, 94(6):2051–2063.
- Guatteri, M., Mai, P. M., Beroza, G. C., and Boatwright, J. (2003). Strong ground-motion prediction from stochastic dynamic source models. *Bull. Seism. Soc. Am.*, 93(1):301–313.
- Gusev, A., Radulian, M., Rizescu, M., and Panza, G. F. (2002). Source scaling of intermediate-depth Vrancea earthquakes. *Geophys. J. Int.*, 151(3):879–889.
- Hanks, T. C. and Kanamori, H. (1979). A moment magnitude scale. *J. Geophys. Res.*, 84(B5):2348–2350.
- Hartzell, S. H. (1979). Analysis of the Bucharest strong ground motion record for the March 4, 1977 Romanian earthquake. *Bull. Seism. Soc. Am.*, 69(2):513–530.
- Haury, J. (2002). Statistische untersuchung zufallsverteilter Heterogenitäten an der KTB-Lokation. *Karlsruhe University*. Diploma thesis.
- Hauser, F., Prodehl, C., and the VRANCEA working group (2002). Seismic experiments target earthquake-prone region in Romania. *Trans. Am. Geophys. Un.*, 83:457, 462–463.
- Hauser, F., Raileanu, V., Fielitz, W., Bala, A., Prodehl, C., Polonic, G., and Schulze, A. (2001). Vrancea—the crustal structure beneath the southeastern Carpathians and the Moesian platform from a seismic refraction profile in Romania. *Tectonophysics*, 340(3-4):233–256.
- Hauser, F., Raileanu, V., Landes, Bala, A., Prodehl, C., and Fielitz, W. (2003). Properties of eastern Carpathian lithosphere, derived from two seismic refraction surveys in Romania - part 1. *Geophys. Res. Abstr.*, 5. EGS-AGU-EUG, EAE03-A-03359.

Bibliography

- Hock, S., Korn, M., Ritter, J. R. R., and Rothert, E. (2004). Mapping random lithospheric heterogeneities in northern and central Europe. *Geophys. J. Int.*, 157(1):251–264.
- Hock, S. and M. Korn, t. T. W. G. (2000). Random heterogeneity of the lithosphere across the Trans-European Suture Zone. *Geophys. J. Int.*, 141(1):57–70.
- Hubert-Ferrari, A., Barka, A., Jacques, E., Nalbant, S. S., Meyer, B., Armijo, R., Tapponnier, P., and King, G. C. P. (2000). Seismic hazard in the Marmara Sea region following the 17 August 1999 Izmit earthquake. *Nature*, 404:269–273.
- Hudson, J. A. (1980). *The excitation and propagation of elastic waves*. Cambridge University Press.
- Igel, H., Jahnke, G., and Ben-Zion, Y. (2002). Numerical simulation of fault zone guided waves: Accuracy and 3-D effects. *PAGEOPH*, 159(9):2067–2083.
- Jackson, J. and McKenzie, D. P. (1988). The relationship between plate motions and seismic moment tensors and the rates of active deformation in the Mediterranean and Middle East. *Geophys. J. Roy. Astr. S.*, 93:45–73.
- Jost, M. L. and Herrmann, R. B. (1989). A student's guide to and review of moment tensors. *Seismol. Res. Lett.*, 60:37–57.
- Joyner, W. B. (2000). Strong motion from surface waves in deep sedimentary basins. *Bull. Seism. Soc. Am.*, 90(6B):95–112.
- Karahan, A. E., Berckhemer, H., and Baier, B. (2001). Crustal structure at the western end of the North Anatolian Fault zone from deep seismic sounding. *Ann. Geofis.*, 44(1):49–68.
- Karrenbach, M. (1995). *Elastic tensor wave fields*. PhD thesis, Stanford University.
- Kawase, H. (1996). The cause of the damage belt in Kobe: "the basin-edge effect", constructive interference of the direct S wave with the basin-induced diffracted/Rayleigh waves. *Seismol. Res. Lett.*, 67:25–34.
- Kebeasy, T. R. M. and Husebye, E. S. (2003). A finite-difference approach for simulating ground responses in sedimentary basins: quantitative modelling of the Nile Valley, Egypt. *Geophys. J. Int.*, 154(3):913–924.
- Kelly, K. R., Ward, R. W., Treitel, S., and Alford, R. M. (1976). Synthetic seismograms: A finite-difference approach. *Geophysics*, 50(1):892–902.
- Kishon, E. (2001). *... und die beste Ehefrau von allen*. Lübbe Verlag.
- Lamb, H. (1904). On the propagation of tremors over the surface of an elastic solid. *Philos. T. Roy. Soc. A*, 203:1–42.

- Landes, M., Fielitz, W., Hauser, F., Popa, F., and group, C. (2004). 3D upper-crustal tomographic structure across the Vrancea seismic zone, Romania. *Tectonophysics*, 382:85–102.
- Lay, T. and Wallace, T. C., editors (1995). *Modern Global Seismology*. Academic Press, San Diego.
- Levander, A. R. (1988). Fourth-order finite-difference P-SV seismograms. *Geophysics*, 53(11):1425–1436.
- Li, X., Cormier, V. F., and Toksöz, M. N. (2002). Complex source process of the 17 August 1999 Izmit, Turkey, earthquake. *Bull. Seism. Soc. Am.*, 92(1):267–277.
- Liu, H.-L. and Helmberger, D. V. (1985). The 23:19 aftershock of the 15 October 1979 Imperial Valley earthquake: More evidence for an asperity. *Bull. Seism. Soc. Am.*, 75(3):689–708.
- Madariaga, R. (1976). Dynamics of an expanding circular fault. *Bull. Seism. Soc. Am.*, 66(1):639–666.
- Mai, P. M. and Beroza, G. C. (2002). A spatial random field model to characterize complexity in earthquake slip. *J. Geophys. Res.*, 107(B11):10–1 – 10–21.
- Mai, P. M., Hillers, G., Ben-Zion, Y., and Ampuero, J.-P. (2006). Earthquake scaling and near-source ground-motions from multi-cycle earthquake simulation (with heterogeneity in rate-and-state friction). In *Geophysical Research Abstracts, Vol. 8, 03323, 2006*. European Geosciences Union.
- Mandrescu, N. and Radulian, M. (1999). *Macroseismic Field of the Romanian Intermediate-Depth Earthquakes*, pages 163–174. Kluwer Academic Publishers, Dordrecht, Netherlands.
- Marcinkovich, C. and Olsen, K. B. (2003). On the implementation of perfectly matched layers in a 3D fourth-order velocity-stress finite-difference scheme. *J. Geophys. Res.*, 108(B5):E5E18–1 – E5E18–16.
- Marsal, D. (1989). *Finite Differenzen and Elemente*. Springer-Verlag Berlin, Heidelberg.
- Martin, M., Ritter, J. R. R., and the CALIXTO working group (2005). High-resolution teleseismic body-wave tomography beneath se romania - I. Implications for three-dimensional versus one-dimensional crustal correction strategies with a new crustal velocity model. *Geophys. J. Int.*, 162(2):448–460.
- Martin, M., Ritter, J. R. R., and the CALIXTO working group (2006). High-resolution teleseismic body wave tomography beneath SE-Romania - II. Imaging of a slab detachment scenario. *Geophys. J. Int.*, 164(3):579–595.
- McClusky, S., Balassanian, S., Barka, A., Demir, C., Ergintav, S., Georgiev, I., Gurkan, O., Hamburger, M., Hurst, K., Kahle, H., Kastens, K., Kekelidze, G., King, R., Kotzev, V., Lenk, O., Mahmoud, S., Mishin, A., Nadariya, M., Ouzounis, A., Paradissis, D., Peter, Y., Prilepin,

Bibliography

- M., Reilinger, R., Sanli, I., Seeger, H., Tealeb, A., Toksöz, M. N., and Veis, G. (2000). Global Positioning System constraints on plate kinematics and dynamics in the eastern Mediterranean and Caucasus. *J. Geophys. Res.*, 105(B3):5695–5720.
- Meade, B. J., Hager, B. H., McClusky, S. C., Reilinger, R. E., Ergintav, S., Lenk, O., Barka, A., and Ozener, H. (2002). Estimates of seismic potential in the Marmara Sea region from block models of secular deformation constrained by Global Positioning System measurements. *Bull. Seism. Soc. Am.*, 92(1):208–215.
- Miksat, J. (2002). 3D Finite-Differenzen Modellierung des Marmarabebens. *Karlsruhe University*. Diploma thesis.
- Miksat, J., Wenzel, F., and Sokolov, V. (2005). Low free-field accelerations of the 1999 Kocaeli earthquake? *Pure appl. geophys.*, 162(5):857–874.
- Moczo, P., Kristek, J., and Halada, L. (2000). 3D 4th-order staggered- grid finite-difference schemes: Stability and grid dispersion. *Bull. Seism. Soc. Am.*, 90(3):587 – 603.
- Moczo, P., Kristek, J., and Halada, L. (2004). *The Finite-Difference Method for Seismologists An Introduction*. Comenius University Bratislava.
- Müller, T. M. and Shapiro, S. A. (2001). Most probable seismic pulses in single realizations of two- and three-dimensional random media. *Geophys. J. Int.*, 144(1):83–95.
- Murphy, J. R. and O'Brien, L. J. (1977). The correlation of peak ground acceleration amplitude with seismic intensity and other physical parameters. *Bull. Seism. Soc. Am.*, 67:77–915.
- Olsen, K. B. (1994). *Simulation of three-dimensional wave propagation in the Salt Lake Basin*. PhD thesis, University of Utah, Salt Lake City.
- Olsen, K. B. (2000). Site amplification in the Los Angeles basin from three-dimensional modeling of ground motion. *Bull. Seism. Soc. Am.*, 90(6B):S77–S94.
- Olsen, K. B., Akinci, A., Rovelli, A., Marra, F., and Malagnini, L. (2006). 3D ground-motion estimation in Rome, Italy. *Bull. Seism. Soc. Am.*, 96(1):133–146.
- Olsen, K. B. and Archuleta, R. J. (1996). 3D simulation of earthquakes on the Los Angeles fault system. *Bull. Seism. Soc. Am.*, 86(3):575–596.
- Olsen, K. B., Archuleta, R. J., and Matarrese, J. R. (1995). Three-dimensional simulation of a magnitude 7.75 earthquake on the San Andreas Fault. *Science*, 270(5242):1628–1632.
- Olsen, K. B., Madariaga, R., and Archuleta, R. J. (1997). Three-dimensional dynamic simulation of the 1992 Landers Earthquake. *Science*, 278(5339):834 – 838.
- Olsen, K. B., Nigbor, R., and Konno, T. (2000). 3D viscoelastic wave propagation in the upper Borrego Valley, California, constrained by borehole and surface data. *Bull. Seism. Soc. Am.*, 90(1):134–150.

- Olsen, K. B., Pechmann, J. C., and Schuster, G. T. (1996). An analysis of simulated and observed blast records in the Salt Lake Basin. *Bull. Seism. Soc. Am.*, 86(3):1061–1076.
- Oncescu, M. C. (1989). Investigation of a high stress drop earthquake on August 30, 1986 in the Vrancea region. *Tectonophysics*, 163(1-2):35–43.
- Oncescu, M. C., Marza, V. I., Rizescu, M., and Popa, M. (1999). *The Romanian Earthquake Catalogue between 984-1997*, pages 43–47. Kluwer Academic Publishers, Dordrecht, Netherlands.
- Oth, A., Wenzel, F., and Radulian, M. (2006). Source parameters of intermediate-depth Vrancea (Romania) earthquakes from Empirical Green's Functions modeling. *submitted to Tectonophysics*.
- Panza, G. F. and Cuscito, M. (1982). Influence of focal mechanism on shape of isoseismals: Irpinia earthquake of November 23, 1980. *Pure appl. geophys.*, 120:577–582.
- Parsons, T., Toda, S., Stein, R. S., Barka, A., and Dietrich, J. H. (2000). Heightened odds of large earthquakes near Istanbul: An interaction-based probability calculation. *Science*, 288(5466):661–665.
- Peyrat, S., Olsen, K., and Madariaga, R. (2001). Dynamic modeling of the 1992 Landers earthquake. *J. Geophys. Res.*, 106(B11):26,467–26,482.
- Popa, M., Radulian, M., Grecu, B., Popescu, E., and Placinta, A. O. (2005). Attenuation in southeastern Carpathians area: Result of upper mantle inhomogeneity. *Tectonophysics*, 410:235–249.
- Radu, C., Polonic, G., and Apopei, I. (1979). Macroseismic field of the March 4, 1977 Vrancea earthquake. *Rev. Roum. de Geologie, Geophysique et Geographie GEOPHYSIQUE*, 23:19–26.
- Radu, C. and Utale, A. (1990). The May 30, 1990 Vrancea earthquake. Seismic intensity distribution. *National Institute for Earth Physics Report*, III,(A-4).
- Radu, C., Utale, A., and Winter, V. (1987). The August 30, 1986 Vrancea earthquake. Seismic intensity distribution. *National Institute for Earth Physics Report*, II(A-3).
- Radulian, M., Bonjer, K.-P., Popescu, E., Popa, M., Ionescu, C., and Grecu, B. (in print 2005). The october 27th, 2004 Vrancea (Romania) earthquake. *CSEM/EMSC Newsletter*.
- Ritter, J. R. R. and Rothert, E. (2000). Variations of the lithospheric seismic scattering strength below the Massif Central, France and the Frankonian Jura, SE Germany. *Tectonophysics*, 328:297–305.
- Ritter, J. R. R., Shapiro, S. A., and Schechinger, B. (1998). Scattering parameters of the lithosphere below the Massif Central, France, from teleseismic wavefield records. *Geophys. J. Int.*, 134(1):187–198.

Bibliography

- Rockwell, T. K., Lindvall, S., Dawson, T., Langridge, R., Lettis, W., and Klinger, Y. (2002). Lateral offsets on surveyed cultural features resulting from the 1999 Izmit and Düzce earthquakes, Turkey. *Bull. Seism. Soc. Am.*, 92(1):79–94.
- Sadigh, K., Chang, C.-Y., Egan, J. A., Makdisi, F., and Youngs, R. R. (1997). Attenuation relationships for shallow crustal earthquakes based on California strong motion data. *Seismol. Res. Lett.*, 68:180–189.
- Saenger, E. H. and Bohlen, T. (2004). Finite-difference modeling of viscoelastic and anisotropic wave propagation using the rotated staggered grid. *Geophysics*, 69(2):583–591.
- Saenger, E. H., Gold, N., and Shapiro, S. A. (2000). Modeling the propagation of elastic waves using a modified finite-difference grid. *Wave Motion*, 31:77–92.
- Sato, H. and Fehler, M. C. (1998). *Seismic wave propagation and scattering in the heterogeneous earth*, chapter 1+2. Springer Verlag New York.
- Sato, H., Nakahara, H., and Ohtake, M. (1997). Synthesis of scattered energy density for non-spherical radiation from a point shear-dislocation source based on the radiative transfer theory. *Phys. Earth. Planet. In.*, 104(1-3):1–13.
- Sato, T., Graves, R. W., and Somerville, P. G. (1999). 3-D finite-difference simulations of long-period strong motions in the Tokyo metropolitan area during the 1990 Odawara earthquake (mj 5.1) and the great 1923 Kanto earthquake (ms 8.2) in Japan. *Bull. Seism. Soc. Am.*, 89(3):579–607.
- Schmidt-Aursch, M. (1998). Zweidimensionale Modellierung von Wellenausbreitung bei Erdbeben mit Finiten Differenzen. *Karlsruhe University*. Diploma thesis.
- Sekiguchi, H. and Iwata, T. (2002). Rupture process of the 1999 Kocaeli, Turkey, earthquake estimated from strong-motion waveforms. *Bull. Seism. Soc. Am.*, 92(1):300–311.
- SFB461 (2005). Vrancea Earthquakes: Tectonics - Hazard - Risk Mitigation Research Program 2005 - 2007. <http://www-sfb461.physik.uni-karlsruhe.de/pub/web/sfb-www/main/events/downloads/brochure2005.pdf>.
- Shakal, A., Haddadi, H., Graizer, V., Lin, K., and Huang, M. (2006). Some key features of the strong-motion data from the m 6.0 Parkfield, California, earthquake of 28 September 2004. *Bull. Seism. Soc. Am.*, 96(4B):S90–S118.
- Shapiro, S. A. and Kneib, A. (1993). Seismic attenuation by scattering: theory and numerical results. *Geophys. J. Int.*, 114:373–391.
- Siro, L. and Chiaruttini, C. (1989). Source complexity of the 1980 southern Italian earthquake from the analysis of strong-motion S-wave polarization. *Bull. Seism. Soc. Am.*, 79(6):1810–1832.

- Sirovich, L. (1994). A case of the influence of radiation pattern on peak accelerations. *Bull. Seism. Soc. Am.*, 84(5):1658–1664.
- Sokolov, V. (2002). Seismic intensity and Fourier acceleration spectra: Revised relationship. *Earthq. Spectra*, 18:161–187.
- Sokolov, V. and Bonjer, K.-P. (2006). Modelling of distribution of ground motion parameters during strong Vrancea (Romania) earthquakes. *First European Conference on Earthquake Engineering and Seismology (Geneva, Switzerland)*, (Paper Number 363).
- Sokolov, V., Bonjer, K.-P., and Wenzel, F. (2004). Accounting for site effect in probabilistic assessment of seismic hazard for Romania and Bucharest: a case of deep seismicity in Vrancea zone. *Soil Dyn. Earthq. Eng.*, 24:929–947.
- Sokolov, V., Bonjer, K.-P., and Wenzel, F. (2005). Attenuation relations for engineering ground motion parameters an generalised site conditions based on Fourier amplitude spectra: intermediate-depth Vrancea earthquakes. In *Geophysical Research Abstracts, Vol. 7, 01747, 2005*. European Geosciences Union.
- Sokolov, V. and Wald, D. (2002). Instrumental intensity distribution for the Hector Mine, California, and the Chi-Chi, Taiwan, earthquakes: Comparison of two methods,. *Bull. Seism. Soc. Am.*, 92(6):2145–2162.
- Sperner, B., Lorenz, F., Bonjer, K., Hettel, S., Müller, B., and Wenzel, F. (2001). Slab break-off a abrupt cut or gradual detachment? New insights from the Vrancea region (SE Carpathians, Romania). *Terra Nova*, 13(3):172–179.
- Sperner, B. and the CRC 461 Team (2005). *Monitoring of Slab Detachment in the Carpathians*, pages 187–202. Lecture Notes in Earth Sciences, Vol. 105. Springer-Verlag Berlin Heidelberg.
- Spudich, P., Guatteri, M., Otsuki, K., and Minagawa, J. (1998). Use of fault striations and dislocation models to infer tectonic shear stress during the 1995 Hyogo-Ken Nanbu (Kobe) earthquake. *Bull. Seism. Soc. Am.*, 88(2):413–427.
- Stein, R. S., Barka, A. A., and Dietrich, J. H. (1997). Progressive failure on the North Anatolian fault since 1939 by earthquake stress triggering. *Geophys. J. Int.*, 128:594–604. <http://quake.wr.usgs.gov/research/deformation/modeling/papers/anatolia.html>.
- Stein, S. and Wysession, M. (2003). *An Introduction to Seismology, Earthquakes, and Earth structure*. Blackwell Publishing.
- Sule, M. R. (2004). *Seismic travel time tomography and elastic waveform modeling : Application to ore-dyke characterization*. PhD thesis, Karlsruhe University, Germany.
- Takenaka, H., Mamada, Y., and Futamura, H. (2003). Near-source effect on radiation pattern of high-frequency S waves: strong SH-SV mixing observed from aftershocks of the 1997 Northwestern Kagoshima, Japan earthquakes. *Phys. Earth. Planet. In.*, 137:31–43.

Bibliography

- Takeuchi, N. and Geller, R. J. (2003). Accurate numerical methods for solving the elastic equation of motion for arbitrary source locations. *Geophys. J. Int.*, 154(3):852–866.
- Thomas, J. W. (1995). *Numerical Partial Differential Equations, Finite Difference Methods*. Number 22 in Texts in Applied Mathematics. Springer-Verlag New York Inc.
- Tittgemeyer, M. (1999). *Streuung elastischer Wellen im oberen Erdmantel*. PhD thesis, Karlsruhe University, Germany.
- Trifunac, M. D. and Brady, A. G. (1975). On the correlation of seismic intensity scales with the peaks of recorded strong ground motion. *Bull. Seism. Soc. Am.*, 65(1):139–162.
- Tsai, Y. B. and Huang, M. W. (2000). Strong ground-motion characteristics of the Chi-Chi, Taiwan earthquake of September 21, 1999. *Earthq. Engin. and Engin. Seismol.*, 2:1–22.
- Udias, A. (1999). *Principles of Seismology*. Cambridge University Press.
- Vidale, J. and Helmberger, D. V. (1987). *Seismic Strong Motion Synthetics*, chapter Path effects in strong motion seismology, pages 267–319. Computational Techniques. Academic Press Inc, London.
- Vidale, J., Helmberger, D. V., and Clayton, R. W. (1985). Finite-difference seismograms for SH waves. *Bull. Seism. Soc. Am.*, 75(6):1765–1782.
- Vidale, J. E. (1989). Influence of focal mechanism on peak accelerations of strong motions of the Whittier Narrows, California, earthquake and an aftershock. *J. Geophys. Res.*, 94(B7):9607–9613.
- Virieux, J. (1984). SH-wave propagation in heterogeneous media: Velocity-stress finite-difference method. *Geophysics*, 49(11):1933–1943.
- Virieux, J. (1986). P-SV wave propagation in heterogeneous media: Velocity-stress finite-difference method. *Geophysics*, 51(4):889–901.
- Weidle, C., Widiyantoro, S., and the CALIXTO Working group (2005). Improving depth resolution of teleseismic tomography by simultaneous inversion of teleseismic and global P-wave traveltimes data - application to the Vrancea region in southeastern Europe. *Geophys. J. Int.*, 162(3):811–823.
- Wenzel, F. (2004). Prognose der Bodenbewegung bei Starkbeben. In *Starkbeben: Von geowissenschaftlichen Grundlagen zu Ingenieurmaßnahmen*, Finanzierungsantrag 2003-2005 des SFB 461, pages 141–168.
- Wenzel, F., Lorenz, F. P., Sperner, B., and Oncescu, M. C. (1999). Seismotectonics of the Romanian Vrancea area. In Wenzel, F., Lungu, D., and Novak, O., editors, *Vrancea Earthquakes: Tectonics, Hazard and Risk Mitigation*, pages 15–25. Kluwer Academic Publishers, Dordrecht, Netherlands.

- Wenzel, F. and Lungu, D. (2000). Earthquake risk assessment for Romania. Luxemburg. 2nd EuroConference on Global Change and Catastrophe Risk Management.
- Wessel, P. and Smith, W. H. F. (1998). New, improved version of Generic Mapping Tools released. *EOS Trans. Amer. Geophys. U.*
- Wirth, W. (2004). *Seismische Bodenbewegung in Bukarest (Rumänien) - Untersuchung lateraler Variationen und Modellierung mit empirischen Greenschen Funktionen*. PhD thesis, Karlsruhe University, Germany.
- Yagi, Y. and Kikuchi, M. (2000). Source rupture process of the Kocaeli, Turkey, earthquake of August 17, 1999, obtained by joint inversion of near-field data and teleseismic data. *Geophys. Res. Lett.*, 27(13):1969–1972.

Bibliography

Danksagungen/Acknowledgments

Prof. Dr. Friedemann Wenzel danke ich für die Betreuung der Arbeit und die interessante Aufgabenstellung. Die Diskussionen mit ihm und sein Blick für das Wesentliche schärften das Profil der Arbeit. Weiter ermöglichte er mir die Teilnahme an internationalen Konferenzen und Workshops, wodurch ich die Welt der Geowissenschaften kennenlernen und zahlreiche gute Kontakte knüpfen konnte.

Ich danke Prof. Dr. Karl Fuchs für die Übernahme des Korreferates. Während der gesamten Doktorandenzeit zeigte er sein Interesse in gelegentlichen Diskussionen und bei Seminarvorträgen.

Prof. Dr. Polat Gülkan (Middle East Technical University, Ankara, Turkey) kindly provided the original records of the strong-motion data of the 1999 Kocaeli earthquake. Discussions with him triggered this research.

Special thanks to Dr. Michel Bouchon and Dr. Haruko Sekiguchi for supplying their inversion results, which made the study on the 1999 Kocaeli earthquake possible.

I thank Dr. Kim Olsen for providing his 3D FD code.

Mein ganz besonderer Dank gilt Dr. Tobias Müller, der immer Zeit für Diskussionen über die FD Methode hatte und der mir geduldig die theoretische Seismologie nahe brachte. Ohne seine großzügige Unterstützung wären viele Fragen offen geblieben.

Vielen Dank an Dr. Ellen Gottschämmer für die hervorragende Zusammenarbeit und die Durchsicht des Manuskriptes. Ihre Vorschläge und Anregungen trugen wesentlich zur Verbesserung der Arbeit bei.

Special thanks to Dr. Vladimir Sokolov for his valuable ideas and the help with his intensity evaluation method.

Dipl.-Geophys. Adrien Oth danke ich für die vielen interessanten Diskussionen über Seismologie im Allgemeinen und über die Vrancea Erdbeben und deren Spannungsabfälle im Speziellen. Dadurch konnte meine Arbeit an vielen Punkten deutlich verbessert werden.

Besonders danken möchte ich Dr. Christian Weidle und Dr. Christoph Jäger mit welchen ich einen Großteil der Zeit als Student und Doktorand geteilt habe. Diese Zeit wird unvergesslich bleiben. Die Vorschläge von Dr. Christian Weidle verbesserten die sprachliche Qualität der vorliegenden Arbeit.

Die vielen Kaffeepausendiskussionen über die Quellen der Vrancea-Erdbeben mit Dr. Wolfgang Wirth trugen zur Implementierung der Quelle in die FD-Modellierungen bei.

Danken möchte ich Dr. Tim Müller für das Lesen des Manuskriptes. Seine Sicht der Arbeit als „Nicht-Seismologe“ ermöglichte wesentliche Verbesserungen.

Vielen Dank an Dr. Erik Saenger, der sich die Zeit nahm um das 2D FD Programm von Karrenbach (1995) zu diskutieren und der eine Version seines FD Programmes zur Verfügung stellte um Testrechnungen durchzuführen.

Ein großes Dankeschön geht an meine Familie. An meine Eltern, die mich auf vielerlei Weise unterstützt und meine Begeisterung an den Naturwissenschaften mitgetragen und gefördert haben. Meiner Schwester Dipl.-Phys. Deborah Brommler danke ich für die vielen ernsthaften, tief sinnigen und humorvollen Gespräche über die Physik und die Eigenheiten der physikalischen Welt. Außerdem danke ich ihr für die Durchsicht des Manuskriptes. Unvergesslich waren die jährlichen Besuche meines Bruders Jan in der Zeit als Student und Doktorand.

Mein ganz besonderer Dank gilt meiner Frau Stefanie, „der besten Ehefrau von allen“ (Kishon, 2001), die mich in jeder Hinsicht unterstützt und ermutigt hat. Während anstrengenden Zeiten, insbesondere in den letzten Monaten, verzichtete sie auf vieles und hielt mir den Rücken frei. Meine Kinder Lissy, Tom und Anika haben mich durch ihr Lachen und ihre fröhliche Art unterstützt und somit viel zum Gelingen meiner Arbeit beigetragen.

Lebenslauf

Persönliche Daten

Name: Joachim Miksat
Geburtsdatum: 13. Februar 1976
Nationalität: deutsch
Geburtsort: Riedlingen
Familienstand: verheiratet - 3 Kinder

Schulbildung

1982 - 1986 Grundschule Dürmentingen
1986 - 1995 Kreisgymnasium Riedlingen
27.06.1995 Allgemeine Hochschulreife

Hochschulausbildung

1996 - 2002 Studium der Geophysik
an der Universität Karlsruhe (TH)
03.05.2002 Diplom
seit Mai. 2002 Doktorand an der Fakultät für Physik
der Universität Karlsruhe (TH)



Hilfsmittel

Die FD Simulationen wurden auf einer SGI Origin 3200 des geophysikalischen Institutes durchgeführt. Die Auswertung der Ergebnisse und sonstige Berechnungen erfolgten mit Hilfe von Fortran 77/90 und MATLAB®. Zusätzliche Werkzeuge waren UNIX/LINUX spezifische Hilfsanwendungen wie shell Befehle/Programme.

Diese Dissertation wurde mit dem Formatierungsprogramm L^AT_EX erstellt. Weiter fanden die Grafikprogramme CorelDRAW®, OpenOffice, GIMP und Xfig Anwendung. Landkarten wurden mit GMT oder der Mapping Toolbox von MATLAB® erstellt.

Erklärung

Hiermit versichere ich, dass ich die vorliegende Arbeit selbstständig und nur mit den angegebenen Hilfsmitteln angefertigt habe.

Karlsruhe, den 21. November 2006